GDAŃSK UNIVERSITY OF TECHNOLOGY

The author of the doctoral dissertation: Małgorzata Nadolska-Dawidowska
Scientific discipline: Material Science

DOCTORAL DISSERTATION

Title of doctoral dissertation: Ammonium and potassium vanadates: synthesis, physicochemical characterization, and applications

Title of doctoral dissertation (in Polish): Wanadany amonu i potasu: synteza, charakterystyka fizykochemiczna oraz zastosowania

Supervisor *signature*	Auxiliary supervisor *signature*
dr hab. inż. Kamila Sadowska	dr inż. Marta Prześniak-Welenc

Gdańsk, year 2023

GDAŃSK UNIVERSITY OF TECHNOLOGY

STATEMENT

The author of the doctoral dissertation: Małgorzata Nadolska-Dawidowska

I, the undersigned, declare that I am aware that in accordance with the provisions of Art. 27 (1) and (2) of the Act of 4th February 1994 on Copyright and Related Rights (Journal of Laws of 2021, item 1062), the university may use my doctoral dissertation entitled: "Ammonium and potassium vanadates: synthesis, physicochemical characterization, and applications" for scientific or didactic purposes.[1]

Gdańsk,..... .....

signature of the PhD student

Aware of criminal liability for violations of the Act of 4th February 1994 on Copyright and Related Rights and disciplinary actions set out in the Law on Higher Education and Science(Journal of Laws 2021, item 478), 2as well as civil liability, I declare, that the submitted doctoral dissertation is my own work.

I declare, that the submitted doctoral dissertation is my own work performed under and in cooperation with the supervision of dr hab. inż. Kamila Sadowska and the auxiliary supervision of dr inż. Marta Prześniak-Welenc.

This submitted doctoral dissertation has never before been the basis of an official procedure associated with the awarding of a PhD degree.

All the information contained in the above thesis which is derived from written and electronic sources is documented in a list of relevant literature in accordance with Art. 34 of the Copyright and Related Rights Act.

I confirm that this doctoral dissertation is identical to the attached electronic version.

Gdańsk,..... .....

signature of the PhD student

I, the undersigned, agree to include an electronic version of the above doctoral dissertation in the open, institutional, digital repository of Gdańsk University of Technology.

Gdańsk,..... .....

signature of the PhD student

1 Art 27. 1. Educational institutions and entities referred to in art. 7 sec. 1 points 1, 2 and 4–8 of the Act of 20 July 2018 – Law on Higher Education and Science, may use the disseminated works in the original and in translation for the purposes of illustrating the content provided for didactic purposes or in order to conduct research activities, and to reproduce for this purpose disseminated minor works or fragments of larger works.

2 If the works are made available to the public in such a way that everyone can have access to them at the place and time selected by them, as referred to in para. 1, is allowed only for a limited group of people learning, teaching or conducting research, identified by the entities listed in paragraph 1.

DOCTORAL DISSERTATION

Ammonium and potassium vanadates: synthesis, physicochemical characterization, and applications

mgr inż. Małgorzata Nadolska-Dawidowska

Supervisor: dr hab. inż. Kamila Sadowska

Auxiliary Supervisor: dr inż. Marta Prześniak-Welenc

This work was carried out with the support of the National Science Centre grant – PRELUDIUM (UMO-2020/37/N/ST5/03697)

ABSTRACT

This doctoral thesis is devoted to the synthesis and investigation of ammonium/potassium vanadates, which constitute an interesting group of materials due to their potential applications in electrochemical devices and photocatalysis. The scope of the conducted experimental work included the synthesis of ammonium/potassium vanadates, their physicochemical characterization using various methods (spectroscopy, microscopy, thermal analysis and others), and evaluation of their use as cathode materials for Lithium-ion batteries (LIBs) or photocatalysts for the degradation of water contaminants. The main part of the thesis presents the conducted research and its analysis and consists of a collection of five articles [A1-A5] published in the following journals: Electrochimica Acta (IF 6.901, 100 pts. MEiN, 2020), Inorganic Chemistry (IF 5.436, 140 pts. MEiN, 2022), Materials (IF 3.057, 140 pts. MEiN, 2019), and Scientific Reports (IF 4.996, 140 pts MEiN, 2022 and 2023). This part is preceded by a brief introduction to the vanadate family, general motivation for the conducted research, and the current state of knowledge about ammonium/potassium vanadates, with special regard to their application as electrode materials for metal-ion batteries and photocatalysts. In the final section, the most significant achievements obtained within this thesis are summarized, and future research directions are presented. As part of the research, repeatable synthetic routes for uniform nanostructures of ammonium/potassium vanadates were developed. Notably, for the first time, the effect of precursor morphology and initial pressure on the hydrothermal synthesis of ammonium vanadates was studied. Furthermore, it has been proven that the obtained ammonium/potassium vanadates can be successfully used as efficient cathode materials for LIBs and as solar light-driven photocatalysts for decomposing water pollutants. In the case of the former application, hydrated vanadate compounds, i.e., $(NH_4)_2V_{10}O_{25}\cdot nH_2O$ and $K_2V_6O_{16}\cdot nH_2O$ were tested and described for the first time. For the latter, two new photocatalytic materials were proposed (KV_3O_8 and a composite based on $NH_4V_4O_{10}$ and reduced graphene oxide). In addition, more detailed studies (kinetics and mechanism of the photocatalysis process) were presented for $K_2V_6O_{16}\cdot nH_2O$ and $NH_4V_4O_{10}$.

Keywords: vanadates, nanomaterials, structural characterization techniques, cathode materials for ion-batteries, photocatalysts

STRESZCZENIE

Niniejsza praca doktorska poświęcona jest syntezie i badaniu wanadanów amonu/potasu, które stanowią interesującą grupę materiałów ze względu na ich potencjalne zastosowania w urządzeniach elektrochemicznych i fotokatalizie. Zakres przeprowadzonych prac eksperymentalnych obejmował syntezę wanadanów amonu/potasu, ich charakterystykę fizykochemiczną różnymi metodami (spektroskopia, mikroskopia, analiza termiczna i inne) oraz ocenę ich zastosowania jako materiałów katodowych do akumulatorów litowo-jonowych (LIBs) lub fotokatalizatorów do degradacji zanieczyszczeń wody. Zasadniczą część pracy, prezentującą przeprowadzone badania i ich analizę, stanowi zbiór pięciu artykułów [A1-A5] opublikowanych w następujących czasopismach: *Electrochimica Acta* (IF 6.901, 100 pkt MEiN 2020), *Inorganic Chemistry* (IF 5.436, 140 pkt MEiN 2022), *Materials* (IF 3.057, 140 pkt MEiN 2019), oraz *Scientific Reports* (IF 4.996, 140 pkt MEiN 2022 i 2023). Ta część została poprzedzona krótkim wprowadzeniem do rodziny wanadanów, ogólną motywacją prowadzonych badań oraz streszczeniem aktualnego stanu wiedzy na temat wanadanów amonu/potasu, ze szczególnym uwzględnieniem ich zastosowania jako materiałów elektrodowych do akumulatorów metalowo-jonowych i fotokatalizatorów. W ostatniej części podsumowano najważniejsze osiągniecia uzyskane podczas realizacji niniejszej pracy oraz przedstawiono dalsze kierunki badań. W ramach doktoratu opracowano powtarzalne procedury otrzymywania jednofazowych nanostruktur wanadanów amonu/potasu o jednorodnych rozmiarach i kształtach. Warto zauważyć, że po raz pierwszy zbadano wpływ morfologii prekursora i ciśnienia początkowego na morfologię wanadanów amonu otrzymywanych metodą hydrotermalną. Ponadto udowodniono, że uzyskane wanadany amonu/potasu mogą być z powodzeniem zastosowane jako wydajne materiały katodowe w LIBs oraz jako fotokatalizatory aktywowane światłem słonecznym do rozkładu zanieczyszczeń z wody. W przypadku zastosowań elektrochemicznych, po raz pierwszy przetestowano i opisano uwodnione związki wanadanów tj. $(NH_4)_2V_{10}O_{25}\cdot nH_2O$ oraz $K_2V_6O_{16}\cdot nH_2O$. Natomiast w przypadku drugiego zastosowania, zaproponowano dwa nowe materiały fotokatalityczne (KV_3O_8 oraz kompozyt na bazie $NH_4V_4O_{10}$ i redukowanego tlenku grafenu). Dodatkowo, przedstawiono rozszerzone badania dotyczące kinetyki i mechanizmu procesu fotokatalizy dla $K_2V_6O_{16}\cdot H_2O$ and $NH_4V_4O_{10}$.

Słowa kluczowe: wanadany, nanomateriały, metody badań strukturalnych, materiały katodowe do akumulatorów metalowo-jonowych, fotokatalizatory

TABLE OF CONTENTS

ABSTRACT **4**

STRESZCZENIE **5**

LIST OF ABBREVIATIONS **8**

1. INTRODUCTION **9**

1.1. The aim of work 13

2. LITERATURE REVIEW **16**

2.1. Current state of knowledge on Ammonium Vanadates 16

2.2. Current state of knowledge on Potassium Vanadates 21

3. OVERVIEW OF THE PUBLICATIONS CONSTITUTING THE DISSERTATION **27**

3.1. [A1] Tailoring size and shape- new path for ammonium metavanadate synthesis 28

3.1.1. Research background and objectives 28

3.1.2. Summary of main results 30

3.1.3. Full content of the article 32

3.2. [A2] Pressure in charge. Neglected parameter in hydrothermal synthesis turns out to be crucial for electrochemical properties of ammonium vanadates. 50

3.2.1. Research background and objectives 50

3.2.2. Summary of main results 51

3.2.3. Full content of the article 54

3.3. [A3] The valance state of vanadium-key factor in the flexibility of potassium vanadates structure as cathode materials in LIBs 66

3.3.1. Research background and objectives 66

3.3.2. Summary of main results 67

3.3.3. Full content of the article 70

3.4. [A4] Insight into Potassium Vanadates as Visible-Light-Driven Photocatalysts: Synthesis of V(IV)-Rich Nano/Microstructures for the Photodegradation of Methylene Blue 91

3.4.1. Research background and objectives 91

3.4.2. Summary of main results 92

3.4.3. Full content of the article 95

3.5. [A5] New light on the photocatalytic performance of $NH_4V_4O_{10}$ and its composite with rGO 114

3.5.1. Research background and objectives 114

3.5.2. Summary of main results 115

3.5.3. Full content of the article 119

4. CONCLUSIONS 136

5. REFERENCES 138

6. List of Figures 152

7. List of scientific achievements 153

LIST OF ABBREVIATIONS

CV - Cyclic Voltammetry

DRS - Diffuse Reflectance Spectroscopy

DSC - Differential Scanning Calorimetry

EIS - Electrochemical Impedance Spectroscopy

FTIR - Fourier-Transform Infrared Spectroscopy

GO - Graphene Oxide

KIBs - Potassium-Ion batteries

LIBs - Lithium-Ion batteries

MB - Methylene Blue

MS - Mass Spectrometry

PL – Photoluminescence

PPMS- Physical Property Measurement System

Raman - Raman Spectroscopy

RT - Room Temperature

TG – Thermogravimetry

UPLC–QTOF-MS/MS- ultra-performance liquid chromatography quadrupole time-of-flight mass spectrometry

UV–Vis - Ultraviolet-Visible

XAS - X-ray Absorption Spectroscopy

XPS - X-ray Photoelectron Spectroscopy

XRD - X-ray Diffraction

ZIBs - Zn-ion batteries

1. INTRODUCTION

Vanadium is a relatively widespread element in the Earth's crust with an estimated content of 0.02% by weight, exceeding the abundance of several other metals such as copper, cobalt, nickel, or zinc. This transition metal is known for its ability to exhibit variable oxidation states ranging from + 2 to + 5 and a wide spectrum of coordination polyhedra [1]. Such multiple oxidation states and rich coordination chemistry contribute to the vast array of vanadium compounds, which exhibit diverse physical and chemical properties and attract considerable interest across various scientific disciplines. Among various vanadium compounds, vanadates deserve special attention due to their promising applications in electrochemistry and photocatalysis.

Vanadates can be described as derivatives of vanadium oxides combined with cations, where the cation can be a metal ion or NH_4^+. They can also exist in hydrated form, where water molecules are additionally incorporated into their structure. The chemical composition of vanadates is highly varied, and to date, more than 30 types of vanadates with different cations have been reported. These cations include alkali metal ions (e.g., Li^+, Na^+, K^+), alkaline earth metal ions (e.g., Mg^{2+}, Sr^{2+}) [2], transition metal ions (e.g., Co^{2+}, Fe^{3+}, Ag^+) [3,4], rare earth metal ions (e.g., Nd^{3+}, Er^{3+}) [5,6] and other ions (e.g., Bi^{3+}, In^{3+} or NH_4^+) [7–9]. Vanadates can also be found in nature in the form of minerals such as Coulsonite (FeV_2O_4), Barnesite ($Na_2V_6O_{16}{\cdot}3(H_2O)$ or Carnotite ($K_2(UO_2)_2V_2O_8{\cdot}3(H_2O)$) [10,11]. Generally, vanadates are odourless crystalline solids (at RT) that come in a variety of colours from white through yellow, red, green to black. They present good chemical and thermal stability (hydrated metal vanadates and ammonium vanadates are stable up to ca. 150°C [12–15], while anhydrous metal vanadates often start to decompose much above 500°C [11]). Most of them crystallize in tetragonal, orthorhombic, or monoclinic structures. It is worth noting that many of them (e.g., $BiVO_4$, $FeVO_4$) exhibit polymorphism, and their phase transition (often irreversible) can be induced by high pressure and high temperature [16–18]. The structure of vanadates, in addition to cations, consists of a vanadium oxide framework composed of V-O polyhedra. These polyhedra can link to each other by corners, edges and faces, resulting in a plethora of different vanadate structures, such as chain structures, layered structures or 3D-tunnel structures (examples are presented in Figure 1a). V-O polyhedra occur in diverse forms that are closely related to the oxidation state of vanadium and vary from VO_4 tetrahedron through VO_5 trigonal bipyramid and square pyramid to VO_6 distorted and regular octahedra (see Figure 1b). The oxidation state of vanadium in tetrahedral coordination is always +5 and any attempts to change it led to significant structural modifications. Therefore, compounds with tetrahedral V-O frameworks (e.g., chain structures) do not favour reversible redox reactions making them unsuitable for metal-ion battery applications. Trigonal bipyramids and square pyramids can be formed from tetrahedra by adding an extra oxygen atom (this fifth oxygen atom can come from adjacent tetrahedra chain). Further addition of a sixth oxygen atom from a neighbouring pyramid chain can transform square pyramids into distorted or regular octahedra. In such configurations, vanadium is found in a mixed oxidation state of +5 and +4, and

also +3 or lower (in regular octahedra). Trigonal bipyramids, square pyramids, and octahedra are typical building blocks observed in layered/3D tunnel structures [19,20].

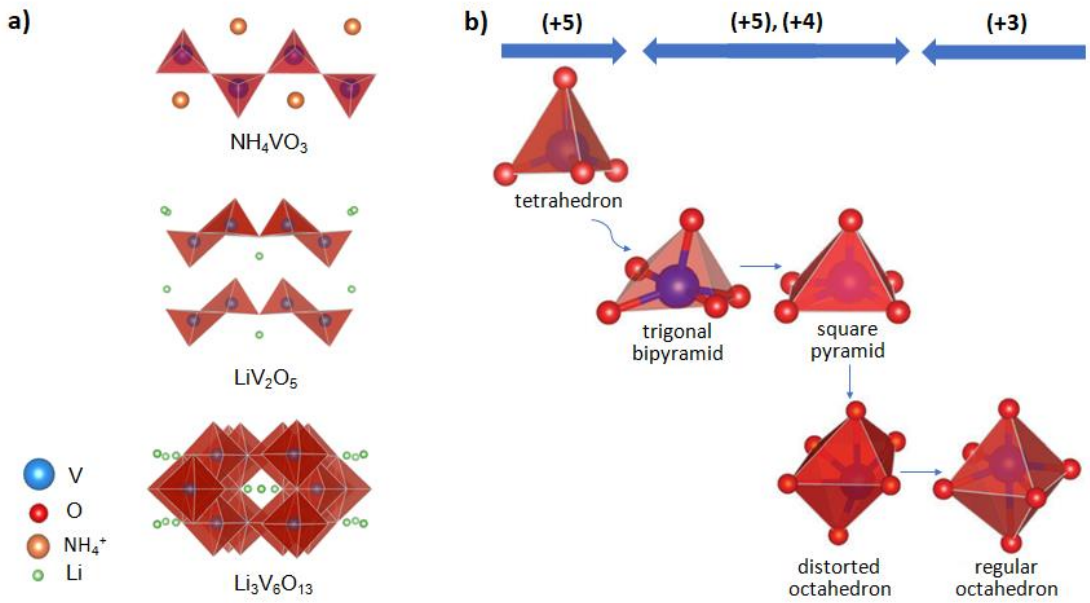

Figure 1. Representative examples of chain, layered and 3D-tunnel structure of vanadates (a). Types of the V-O polyhedra, horizontal axis represents the oxidation state of vanadium (b). Figure was drawn using VESTA software.

Unique layered/tunnel structures together with the multivalence of vanadium, make vanadates potential candidates for energy storage applications, particularly as electrode materials in rechargeable metal-ion batteries. The layered/tunnel arrangement provides well-defined channels for the diffusion of ions, which are crucial for efficient ion intercalation/deintercalation processes during the charging and discharging of a battery. It also allows the accommodation of a substantial number of guest ions, contributing to the high charge storage capacity of vanadates. The extensive interlayer spaces or tunnels have also been proven to be suitable for host ions with large radii (such as hydrated ions), making them attractive in emerging battery technologies [21]. Vanadates usually exhibit enhanced electrochemical performance compared to pure vanadium oxides. This is closely related to the presence of cations in the structure of vanadates, which offer the following advantages. First, embedded cations expand interlayer and tunnel spaces, providing more sites for guest ions and resulting in larger storage capacities [22–25]. Second, these cations contribute to improved electronic conductivity within the material, facilitating efficient charge transfer during electrochemical processes. Finally, they can act as pillars that strengthen the structural framework, preventing collapse and ensuring the stability of the material during repeated charge/discharge cycles [26]. In addition to metal and ammonium cations, water molecules can also be present in the structure of vanadates. Like cations, structural water exhibits a “pillar effect” and leads to structural expansion and improved stability of vanadates. In addition, it works as a charge shield for the metal guest ions, decreasing their effective charges through solvation, which reduces the electrostatic interaction between them and the host framework and improves diffusion kinetics [27,28]. Due to all the above advantages, vanadates have become a subject of extensive investigation as electrode materials across a variety of battery systems and have been tested both in nonaqueous and aqueous electrolytes [29–34]. The first reports on their

use in metal-ion batteries date back to the late 20th century and were devoted to conventional LIBs [35]. Over time, researchers have expanded their focus to other mono- and multivalent ion batteries and vanadates have been successfully applied in Na [36], K [37], NH_4 [38], Mg [39], Ca [40], Zn [41], Al [42], Ni [43,44]-ion batteries. Despite LIBs remaining the most studied application, recent research has shown a growing interest in vanadates for aqueous Zn-ion batteries (ZIBs) and has been summarized in many reviews [45–47]. The vast majority of reports discuss vanadates as cathode materials, although examples of their application as anodes can also be found in the recent literature [48]. The most commonly studied compounds are alkali metal vanadates (mainly those with lithium and sodium) and transition metal vanadates (especially zinc, iron and cobalt vanadates). Additionally, much attention has been given to ammonium vanadates, which, instead of metallic ions, possess ammonium cations in their structure. Nonmetal cations bring many benefits, such as lower density and molecular weight (resulting in higher gravimetric and volumetric storage capacities) and reduced costs. In the field of cathode materials for LIBs, vanadates typically exhibit a specific capacity ranging from 100 to 250 $mAhg^{-1}$ and an average working potential range of 2 to 4 V vs Li/Li^+. However, their practical developments still remain at a relatively early experimental stage, and challenges related to cycling stability, rate capability, and cost-effectiveness continue to be areas of active investigation. As a result, a wide variety of strategies have been employed to improve the electrochemical performance of vanadates, including composition optimization, structure engineering, morphology tuning, and surface modification or functionalization. Ongoing research is focused on various strategies to improve the electrochemical performance of vanadates, which include composition optimization, structure engineering, morphology tuning, and surface modification or functionalization. Recently, many efforts have been made to obtain single-phase vanadate nanostructures. Single-phase electrode materials ensure consistent and predictable electrochemical behaviour, while the presence of secondary phases or impurities can introduce side reactions, leading to capacity loss, decreased cycling stability, and even safety concerns. Interfaces between different phases can also hinder the movement of ions and electrons within the material, resulting in higher resistance, slower ion diffusion kinetics, and reduced overall battery performance. Like single-phase materials, nanostructures also present several advantages, such as a high specific surface area with good accessibility to electroactive sites or shortened diffusion paths, which contribute to improved charge capacity and rate capability [49,50].

Another important area of application of vanadates is photocatalysis. Most vanadates exhibit semiconducting behaviour, and their band gaps typically fall within the range of 2 to 3 eV [51]. This range corresponds to the energy levels of visible and ultraviolet light, making vanadates capable of efficiently absorbing sunlight and harnessing its energy for various applications, including environmental remediation [52] and clean energy production [53]. Among vanadates, bismuth vanadate ($BiVO_4$) definitely stands out as one of the most frequently studied photocatalysts. However, in recent years, increasing attention has also been paid to alternative vanadate-based photocatalysts, with particular emphasis on transition metal vanadates (e.g., $AgVO_3$ [54], $Cu_3V_2O_8$ [55], $FeVO_4$ [56]). $BiVO_4$ (specifically its monoclinic scheelite

polymorph) is an n-type semiconductor with a direct band gap of 2.4 eV. It exhibits great photo and chemical stability, nontoxicity and good dispersibility in water. These features, together with appropriate band edge potentials, make $BiVO_4$ a promising candidate for applications in solar-driven photocatalytic wastewater treatment. To date, numerous reports have presented the successful utilization of $BiVO_4$ for the degradation of various organic compounds, such as dyes (mainly Methylene Blue (MB) and Rhodamine B [57]) or pharmaceuticals (e.g., ibuprofen [58], antibiotics: ciprofloxacin, tetracycline [59]). Unfortunately, in many cases, the photocatalytic efficiency of pristine $BiVO_4$ is limited by the fast recombination of photoinduced carriers. Hence, to address this limitation and further improve the photocatalytic performance of $BiVO_4$, several methods have been proposed, such as morphology tuning, surface modification (elemental doping, defect engineering), and the formation of heterojunctions or composites [60,61]. For instance, numerous reports can be found in the literature, which prove that nanometric dimensions are favourable for the excitation, separation, and migration of photocatalytic electron-hole pairs [62,63]. Reducing the particle size to the nanoscale also increases the specific surface area, leading to a greater number of available active sites for photocatalysis and adsorption (adsorption is an essential process in photocatalysis, enriching pollutants around the catalyst surface and improving photocatalytic performance). For the same reason, the porous structure characterized by a well-developed surface area is of particular interest. Additionally, the interconnected pores and open channels enable efficient migration of pollutants to active sites, accelerating the photocatalysis reaction. Such a hierarchical structure also ensures structural integrity, which is important in terms of photocatalyst reusability. Moreover, porous structures can effectively scatter and trap incident light, resulting in enhanced light harvesting. The implementation of other strategies, such as surface modification, can further enhance the photoactivity of vanadates [64,65]. Notably, defects (e.g., oxygen vacancies, V^{4+} surface species) have a profound impact on the material's electronic structure. They introduce new energy levels within the bandgap, expanding the range of light absorption. Simultaneously, they increase the carrier concentration and thus conductivity, facilitating the efficient migration of charge carriers within the material. Furthermore, defects promote surface charge separation and inhibit the recombination of photogenerated electron-hole pairs. Finally, defects significantly impact the adsorption capability and can enhance the binding of pollutant molecules onto the surface of photocatalysts [66].

In summary, vanadates hold enormous potential in the energy storage and photocatalysis fields. While significant progress has been made in recent years, vanadate-based cathodes and photocatalysts are still in the early stages of development, and their practical utilization is limited. In addition to improving the electrochemical/photocatalytic properties of established vanadate materials, there is a growing emphasis on the exploration of novel vanadate compounds.

1.1. The aim of work

This dissertation focuses on two types of vanadates: ammonium vanadates and potassium vanadates. Despite their intriguing properties and potential in the field of electrochemistry, these compounds have not received as much scientific attention as other vanadates. Moreover, there is a clear gap in the use of such vanadates in photocatalytic applications, and only a few single studies can be found on this topic. On the other hand, potassium and ammonium are widely available and less expensive than many other metal ions, such as lithium and zinc (most frequently used in vanadate-based electrode materials) or bismuth (extensively studied for photocatalytic applications). This makes ammonium/potassium vanadates suitable for large-scale applications and provides additional motivation for their studies.

In terms of structural characteristics, ammonium and potassium vanadates exhibit many similarities, which determine their potential application. The first noteworthy similarity is observed in the size of cations, which, along with vanadium oxide framework, are the main building blocks of their structure. The reported ionic radius size of NH_4^+/K^+ ions falls within the range of 1.3–1.6 Å and is relatively large when compared to other metallic ions. Second, NH_4^+ ions are often considered analogous to alkali metal cations. Both NH_4^+ and K^+ ions exhibit similar electronic structures, sharing an identical number of electrons in their outermost electron shell (8 e) and a single positive charge [67]. The size and electronic structure of NH_4^+/K^+ ions are crucial factors contributing to their comparable chemical behaviour. For example, they are able to bond multiple water molecules with the same hydration enthalpy (c.a. 300 $kJmol^{-1}$) and size of hydrated radius (3.31 Å) [68]. The similarities between the NH_4^+/K^+ ions also translate into similarities in the crystallographic structures of ammonium/potassium vanadates. This was first observed over 70 years ago by Howard and Evans [69], who reported that the dimensions of the tetrahedral chains and the lengths of V-O bonds in NH_4VO_3 and KVO_3 are virtually identical. The combination of NH_4^+ or K^+ ions with a vanadium-oxide framework usually results in the formation of a layered structure, which is observed in the majority of described ammonium/potassium vanadates. The intercalated NH_4^+ or K^+ ions act as structural supports that physically separate the V-O layers. Notably, due to the relatively large size of these cations, the interlayer spaces of ammonium/potassium vanadates often reach 10 Å or more. Such large interlayer spaces offer significant advantages, especially in the context of rechargeable batteries, by enabling efficient storage and rapid transport of guest metal ions. Furthermore, the positively charged NH_4^+/K^+ ions interact with the negatively charged V-O layers and ensure structural stability. This so-called “pillar effect” is often emphasized in the context of cathodes based on ammonium/potassium vanadates, which can endure numerous charge/discharge cycles without significant degradation of their structure or performance.

Such unique structural features of ammonium/potassium vanadates as well as the relatively limited literature on these compounds were the main motivation for starting the research presented in this thesis.

The primary objective of the thesis was the investigation of the possibilities of using ammonium/potassium vanadates in electrochemistry (as cathode materials for LIBs) and

photocatalysis (for the degradation of water contaminants). The conducted research was focused on the synthesis and examination of ammonium/potassium vanadates with diverse compositions and structures, which have not yet been reported or fully described in the literature. Special attention was given to obtaining uniform samples with nanostructured morphology and layered compounds with a high content of V^{4+} surface species. It was assumed that these specific features should lead to the good electrochemical/photocatalytic properties of ammonium/potassium vanadates. Additionally, given the frequently reported limitations regarding the stability of vanadates, it was decided to focus on hydrated compounds for cathodic application. In the case of photocatalytic application, it was proposed to synthesize the composite and combine the vanadate compound (specifically ammonium vanadate) with reduced graphene oxide (rGO).

Based on the above, the following research hypotheses were proposed:

1. Nanostructures of hydrated ammonium/potassium vanadates exhibit favourable properties for use as cathode materials in LIBs.

2. Nanostructures of ammonium/potassium vanadates show photocatalytic activity and are suitable for the solar light-driven photodegradation of water contaminants.

The investigation of novel ammonium/potassium vanadate structures with desired properties is closely connected to the development of their synthesis method and is the first step toward their practical utilization. Therefore, additional hypotheses regarding this topic were formulated:

3. The precursor morphology and initial pressure in the hydrothermal synthesis of ammonium vanadates significantly influence their morphology and phase composition.

4. The hydrothermal synthesis of the ammonium vanadate/rGO composite, which involves the simultaneous hydrothermal reduction of NH_4VO_3 and graphene oxide, results in a hierarchical/porous structure of the final product.

To verify the formulated hypotheses, the following research tasks were undertaken:

- Development of the repeatable synthesis of ammonium/potassium vanadates that allow structures with desired properties to be obtained. Herein, two different methods were employed. Ammonium vanadates were obtained by hydrothermal synthesis, while potassium vanadates were synthesized via a method based on liquid-phase exfoliation with ion exchange.

- Physicochemical characterization of samples by means of various methods, which included spectroscopic methods (Fourier-Transform Infrared Spectroscopy (FTIR),

Raman Spectroscopy, X-ray Photoelectron Spectroscopy (XPS), X-ray Absorption Spectroscopy (XAS), Photoluminescence (PL), and Ultraviolet-Visible Diffuse Reflectance Spectroscopy (UV-vis DRS)), microscopic methods (Scanning Electron Microscopy (SEM), Transmission Electron Microscopy (TEM)), X-ray Diffraction (XRD), thermal analysis (Thermogravimetry-Mass Spectrometry (TG-MS), Differential Scanning Calorimetry (DSC)), and N_2 adsorption. Full physicochemical analysis allowed us to determine the structural, morphological, and optical properties of the obtained ammonium/potassium vanadate structures and to evaluate the relationship between the synthesis conditions and the final product.

- Utilization of the obtained ammonium/potassium vanadate structures as cathode materials for nonaqueous LIBs.

- Utilization of the obtained ammonium/potassium vanadate structures as photocatalyst materials for the degradation of water pollutants. Samples were tested in the form of powder, in deionized water and under simulated solar light. The photocatalytic activity of samples was investigated by the oxidation of a model organic dye: MB. In addition, for the ammonium vanadates, the reduction of Cr(VI) was evaluated.

2. LITERATURE REVIEW

2.1. Current state of knowledge on Ammonium Vanadates

Ammonium vanadates (general formula: $(NH_4)_xV_yO_z$) were first described in 1938 by Dubois and Breton [70], and since then, more than ten different forms of ammonium vanadates with various stoichiometries have been investigated. Among them, NH_4VO_3 is the most common representative, which is widely used in industry and plays an important role in the synthesis of vanadium oxides, various metal vanadates, or other ammonium vanadates [71]. It is also employed for vanadium recovery and as the main component of Mandelin reagent, which finds widespread application in the detection of toxic drugs or psychoactive substances. Further examples include dyeing and printing on woollens, staining wood black and usage as a drier for paints and inks or photographic developer [72].

In addition to NH_4VO_3, which is commercially available, other ammonium vanadates have been reported in the literature. Such compounds have attracted considerable research attention due to their potential application as electrode materials for rechargeable metal-ion batteries. Here, $NH_4V_4O_{10}$ is most commonly described; however, other phases can be found, both with a single ($NH_4V_3O_8$, $(NH_4)_2V_4O_9$, $(NH_4)_2V_4O_{11}$) and mixed ($(NH_4)_2V_7O_{16}$, $NH_4V_3O_7$, $(NH_4)_2V_3O_8$) valence state of vanadium. Most of them exist in both hydrated and anhydrous forms. Other phases that have been reported only in hydrated form can also be listed, such as $(NH_4)_2V_{10}O_{25}\cdot 8H_2O$ or $(NH_4)6V_{10}O_{28}\cdot 6H_2O$.

Similar to simple metal oxides, a wide variety of synthesis methods have been proposed to obtain ammonium vanadates, such as precipitation, solvothermal methods, solid-state synthesis, thermal decomposition or electrosynthesis. Synthesis of NH_4VO_3 deserves special attention, as it is the most frequent precursor of other ammonium vanadates. One of the first synthesis protocols was described in 1950 by Baker et al [73]. The method is based on the precipitation of NH_4VO_3 from an aqueous solution of $NaVO_3$ by adding NH_4Cl. First, $NaVO_3$ is obtained by boiling a solution of V_2O_5 and Na_2CO_3 until CO_2 is completely released, and then $KMnO_4$ is added. The undissolved by-products (V_2O_5 and MnO_2) are filtered off, and the filtrate is washed with water until H_2O_2 no longer gives a positive reaction for vanadium. This purified supernatant is heated to 60°C and poured in one portion into a hot aqueous NH_4Cl solution. Precipitation of NH_4VO_3 starts immediately and is completed after a few hours. After filtration, washing with water, and drying, an almost pure white powder of ammonium metavanadate is obtained. The efficiency of the method is 80%, and the product still contains some Na (0.3% NaCl). A simplified procedure was presented by Vezina and Gow [74]. Briefly, an aqueous solution of $NaVO_3$ and Na_2CO_3 is prepared by leaching V_2O_5 with an excess of Na_2CO_3 (for the concentration of V_2O_5 ≥100 g, it is necessary to heat the solution to boiling temperature and agitate for 1 h). Then, the precipitation of NH_4VO_3 is carried out at room temperature by adding crystalline NH_4Cl to the stirred V_2O_5-Na_2CO_3. After 24 h, the precipitates are collected by vacuum filtering and washed with ethyl alcohol. The yield under these conditions is greater than 99%.

Preparation of NH_4VO_3 is also the subject of few patents [75,76]. For example, the invention from 1961 relates to the recovery of NH_4VO_3 directly from acidic solvent strip solutions, which are used in the process of vanadium extraction from ore [75]. The acidic vanadyl starting solutions contain tetravalent vanadium; thus, at the beginning, it is necessary to treat them with $NaClO_3$ to oxidize vanadium to the pentavalent state. Then, the oxidized vanadium solution is added to the aqueous solution of sodium carbonate. During this step, the pH should be kept in the range of 7-8 by adjusting it with ammonia. Next, the resulting solution is purified by heating it at 70-90°C and subsequent filtration of precipitated impurities. Finally, as in the aforementioned protocols, NH_4VO_3 is precipitated by the addition of NH_4Cl. In this method, the recovery of vanadium is approximately 95%. In regard to the synthesis of other ammonium vanadate compounds (e.g., $NH_4V_4O_{10}$ and $NH_4V_3O_8$), the hydrothermal method is the most commonly used approach. In recent years, there has been a significant increase in research on the synthesis of such compounds, mainly driven by their potential use as cathode materials. Unfortunately, most reports present only individual synthesis protocols (often focusing on the synthesis of ammonium vanadates with specific morphologies to enhance their electrochemical properties), and there is a lack of reviews that summarize the synthesis of ammonium vanadates. Thus, an attempt to systematize this subject was made by the author of this dissertation and published as a post-conference short chapter in a monograph [77]. Generally, the hydrothermal synthesis of ammonium vanadates is based on heating an acidified aqueous solution of NH_4VO_3 under elevated pressure. In this method, three main steps can be distinguished. The first stage involves the preparation of the reaction mixture, which is an aqueous solution containing the precursor (i.e., source of NH_4 cations and vanadate ions), pH adjusters, surfactants, and other compounds to facilitate the chemical reaction. As previously mentioned, NH_4VO_3 is the principal precursor due to its cost-effectiveness and commercial availability, while the composition of the reaction mixtures can vary significantly. The reaction mixture is prepared by thoroughly mixing the components until they are completely dissolved; usually, this process is aided by ultrasound or elevated temperature. The second stage includes the actual hydrothermal process; the prepared reaction mixture is placed in a tightly sealed reactor (autoclave), where it is heated (usually above 140°C and less than 200°C) and maintained at an elevated temperature for several hours to several dozen hours. Finally, the obtained product is washed with deionized water/ethanol and dried (below 100°C).

To date, dozens of protocols for the synthesis of ammonium vanadates have been reported, which vary in reaction time, heating temperature, and pH of the precursor solution. Such diverse synthesis parameters resulted in the formation of structures with varying stoichiometric compositions (over 10 compounds in hydrated/non-hydrated form are known) and morphologies (from nano to micro-structures with shapes of belts, rods, spheres, square/hexagonal plates, and others). The versatility of hydrothermal synthesis is illustrated in the Figure 2, which shows SEM images of different ammonium vanadate compounds ($NH_4V_3O_8$, $NH_4V_4O_{10}{\cdot}nH_2O$, $(NH_4)_2V_6O_{16}{\cdot}nH_2O$) with various morphologies obtained by adjusting the pH of precursor solution [78], reaction time [79] and heating temperature [80]. Another commonly employed practice for

controlling the morphology of ammonium vanadates is the utilization of templates. Available examples include both soft templates (such as β-cyclodextrin [81], carboxymethyl cellulose [82], sodium dodecyl benzene sulfonate [83]) and hard templates (Ti foil [84] or Ni foam [85]). As depicted in Figure 3, template-assisted synthesis leads to the formation of organized and more uniform structures.

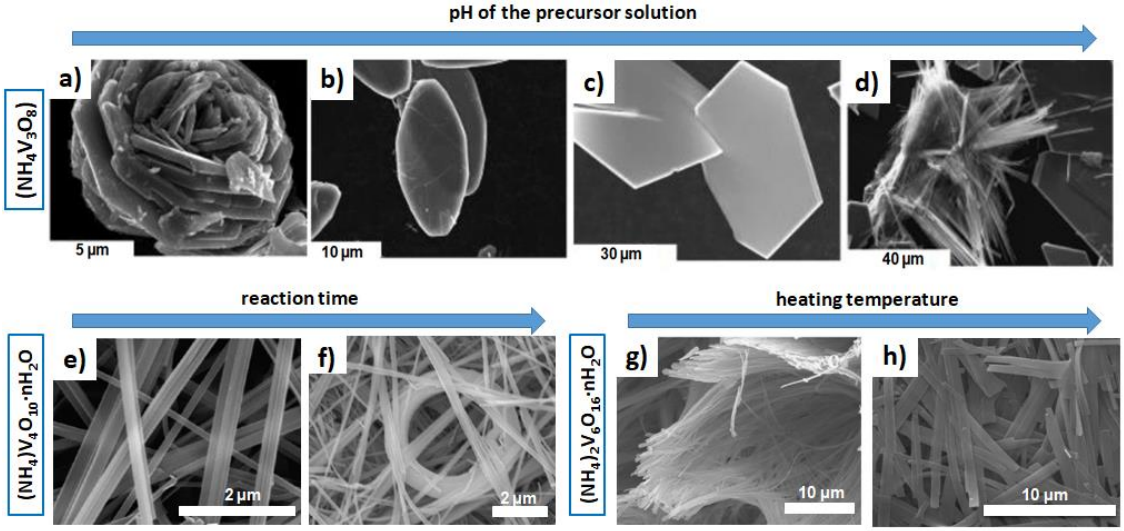

Figure 2. SEM images of: $NH_4V_3O_8$ obtained at pH = 2.5 (a), 3 (b), 4.5 ÷ 5.5 (c), 6 (d) [78]*; $NH_4V_4O_{10}·nH_2O$ obtained after 24 h (e) and 48h (f)* [79]*; $(NH_4)_2V_6O_{16}·nH_2O$ obtained at 130°C (g) and 160°C (h)* [80]

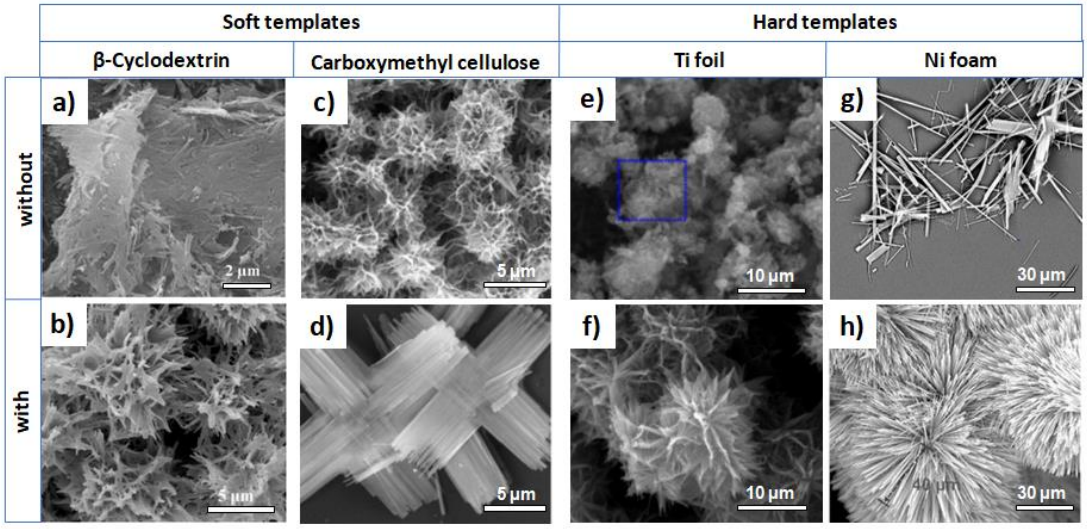

Figure 3. SEM images of $NH_4V_4O_{10}$ (a-f) and $(NH_4)_2V_{10}O_{25}·8H_2O$ (g-h) obtained without and with the utilization of the following templates: β-cyclodextrin (a-b) [81]*, carboxymethyl cellulose (c-d)* [82]*, Ti foil (e-f)* [84] *or Ni foam (g-h)* [85].

Ammonium vanadates typically crystallize in orthorhombic (e.g., NH_4VO_3) and monoclinic systems (e.g., $NH_4V_4O_{10}$ [81], $NH_4V_3O_8$ [86], $(NH_4)_2V_{10}O_{25}·8H_2O$ [87], $(NH_4)_2V_6O_{16}·1.5H_2O$ [88]); however, other systems, such as tetragonal (e.g., $(NH_4)_2V_3O_8$ [89]) or triclinic systems (e.g., $(NH_4)_2V_7O_{16}$ [90]), have also been reported. Representative crystal structures are presented in Figure 4 on the example of NH_4VO_3 and $NH_4V_4O_{10}$. NH_4VO_3 crystallizes in the orthorhombic Pbcm (no. 57) space group (a=4.9 Å, b=11.8 Å, c=5.8 Å, α=β= ɣ=90°). The structure is composed of corner-sharing VO_4 tetrahedra that form VO_3^- chains extending along the c-axis. All chains are

parallel, and NH_4^+ cations are situated in the voids between these chains. Each cation in the crystal interacts with four symmetry-related [VO_4] tetrahedra, forming two strong and two weak hydrogen bonds. $NH_4V_4O_{10}$ crystallizes in the monoclinic C12/m1 (no. 12) space group (a=11.71 Å, b= 3.76, c=9.81 Å, α= ɣ=90°, β=101°). The structure of $NH_4V_4O_{10}$ consists of double layers of V_4O_{10} built from VO_5 trigonal bipyramids and VO_6 distorted octahedra. Each layer is formed by single sheets with short vanadyl bonds (V=O, 1.6–1.7 Å) on either side of each layer, and the two sheets in each layer are connected via long trans bonds (V···O, 2.2–2.5 Å).

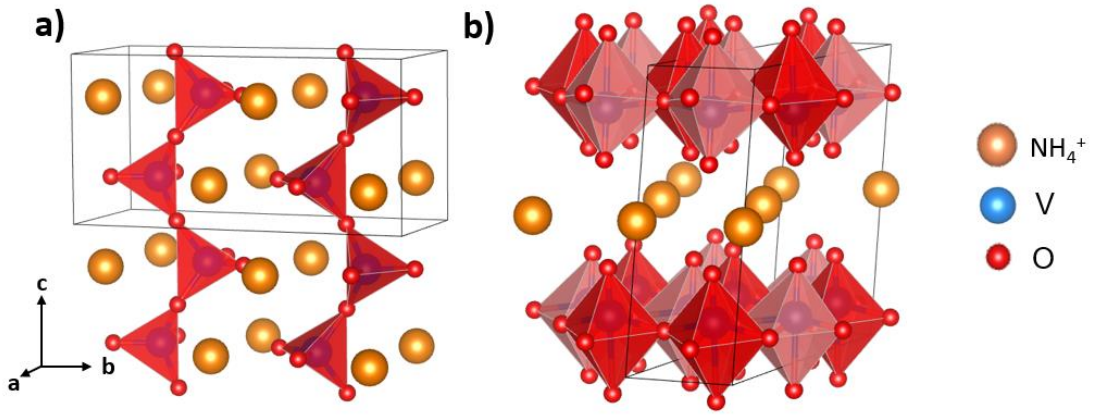

Figure 4. Representative crystal structures of ammonium vanadates on the example of NH_4VO_3 (Crystal system, space group: orthorhombic, Pbcm) and $NH_4V_4O_{10}$ (Crystal system, space group: monoclinic, C12/m1). Figure was drawn using VESTA software.

Specific AVO structures with large interlayer spacings (ca. 10 Å) together with multivalence of vanadium make them promising candidates for cathode materials in mono- [83,91,92] and multi-valent ion batteries [43,93,94]. As mentioned in the introduction, the layered structure of vanadium oxides, with high theoretical charge storage capacity, can accommodate a large number of metal ions. Furthermore, intercalated NH_4^+ ions increase the intrinsic conductivity and extend the interlayer spacing, improving the diffusion rate of metal ions. The embedded NH_4^+ cations also stabilize the crystal structure (due to the presence of N–H···O hydrogen bonds). The idea of employing ammonium vanadate in rechargeable ion batteries was introduced in 2002 by Torardi and Miao [95]. Despite the unsatisfactory stability, the pioneering work was the inspiration for further study, and since then, $NH_4V_4O_{10}$ has been widely investigated as the cathode not only for LIBs but also for sodium- [96], calcium- [97], zinc- [94], nickel- [43], and magnesium- [98] ion batteries. Recently, Yang and co-workers reported the synthesis of ammonium vanadate/rGO composites for the first time [99]. Such a composite was obtained by facile hydrothermal synthesis (150°C, 6 h), which includes simultaneous reduction of graphene oxide and ammonium vanadate and growth of one-dimensional $NH_4V_3O_8$ nanobelts on the rGO sheets. Compared with pure $NH_4V_3O_8$ nanobelts, the $NH_4V_3O_8$/rGO composite revealed an improvement in the electrochemical performance of the LIBs, as shown by its highly reversible capacities and good rate capabilities. Another example was presented by Qiu et al. [100]. Scientists employed similar hydrothermal routes but different synthesis conditions (180°C, 3 h, different precursor solution compositions). They obtained flower-like $NH_4V_4O_{10}$ structures

anchored on rGO sheets. Finally, the as-prepared $NH_4V_4O_{10}$/rGO composite was successfully applied as a high-performance electrode material for hybrid capacitive deionization.

The above examples demonstrate the great potential of ammonium vanadates as electrode materials in rechargeable ion batteries. In contrast, the usage of ammonium vanadates in photocatalytic applications is much more rarely reported. Only three publications can be found in this topic, and all of them are devoted to the $NH_4V_4O_{10}$ phase. The first experiments reported in 2012 by Abbood et al. revealed poor photoactivity of $NH_4V_4O_{10}$ [82]. The studied cross-like $NH_4V_4O_{10}$ nanobelt arrays did not show any catalytic action for the degradation of Rhodamine B after 210 min under visible light. However, the authors proposed that photoactivity can be induced by calcination (above 400°C) of the as-obtained structures and their transformation to a mixed-phase product consisting of V_2O_5 and a small amount of VO_2. It was observed that the energy band gap changed from 2.25 eV to 1.98 eV after calcination, which is explained by the presence of some V^{4+} species. It is also suggested that the calcination process increases the surface area of the sample, which together with a wider optical absorption range results in increased photocatalytic performance. Another two works are devoted to the heterojunction of $NH_4V_4O_{10}$ with quantum dots (CdS and C-dot) and their utilization in the degradation of antibiotics. In 2021, S. Le et al. reported a CdS/$NH_4V_4O_{10}$ composite for the decomposition of the widely used antibiotic amoxicillin [101]. The fabrication process of the composite included two steps: the hydrothermal synthesis of $NH_4V_4O_{10}$ nanobelts and further intercalation of CdS QDs into the $NH_4V_4O_{10}$ interlayer space with the heating reflux method. Four various composites were obtained that varied in the mass percentage of CdS (2-8 wt%), and the best photoactivity was obtained for the composite with 6 wt% CdS, which was further studied in detail. This composite degraded 90.6% of amoxicillin within 120 min under simulated sunlight. For comparison, bare $NH_4V_4O_{10}$ nanobelts degraded 51.2% of antibiotic. For both samples, the adsorption of antibiotic molecules was similar and reached 25% after 60 min in the dark. The introduction of CdS QDs does not significantly influence the band gap, which equals 2.21 eV for $NH_4V_4O_{10}$ nanobelts and 2.34 eV for the CdS/$NH_4V_4O_{10}$ composite. Moreover, the introduction of CdS QDs expands the interlayer space of $NH_4V_4O_{10}$ (which increases the accessible active sites) but also prevents CdS quantum dot agglomeration and shedding. The second work devoted to the $NH_4V_4O_{10}$-based photocatalyst was published in 2022 by Y. Zhang and co-workers [102]. Scientists designed an efficient ternary C-dots/$SrTiO_3$/$NH_4V_4O_{10}$ catalyst for the removal of antibiotic residues (sulfamethoxazole, aureomycin hydrochloride and ciprofloxacin) from the aqueous environment. The reported photocatalytic degradation efficiency of antibiotics for pure $NH_4V_4O_{10}$ was below 20%, which was 4-5 times lower than that for heterojunctions. S. Le prepared an intercalated CdS/$NH_4V_4O_{10}$ composite that degraded 90% of amoxicillin within 120 min under simulated sunlight, while pure $NH_4V_4O_{10}$ could degrade 50% [101].

2.2. Current state of knowledge on Potassium Vanadates

Potassium vanadates (general formula: $K_xV_yO_z$) are less studied than ammonium vanadates. The most known are KVO_3 and K_3VO_4, which are used as catalysts in the oil and gas industry or corrosion inhibitors in fertilizer production. They are also components of dyes, inks, laundry compounds, and intermediates in glass manufacturing [103]. Potassium vanadates have received great interest from the scientific community due to their potential application as electrode materials, and the vast majority of publications are devoted to this topic. Accordingly, many various potassium vanadates have been reported in the literature: both compounds in which the nominal valence state of vanadium atoms is +5 (e.g., KV_3O_8 [104], $K_2V_8O_{21}$ [105], $K_3V_5O_{14}$ [106], $K_4V_2O_7$ [107], $K_5V_3O_{10}$ [108]) and mixed-valence potassium vanadates such as $K_2V_3O_8$, $K_{0.5}V_2O_5$ [109], $K_{0.25}V_2O_5$ [110]. Hydrated forms of potassium vanadates are also known, i.e., $K_{0.5}V_2O_5 \cdot nH_2O$ [111] and $K_2V_6O_{16} \cdot nH_2O$ [112].

There are no systematic studies on the synthesis of potassium vanadates. Precipitation is the simplest synthesis method of potassium vanadates. Such compounds can also be obtained via a hydrothermal method, which is very useful in the synthesis of nanostructured potassium vanadates. These are the two most popular methods; however, other approaches can be found, such as solid-state reactions [107,113], sol-gel processes [114,115] or electrosynthesis [105,116]. Generally, both V_2O_5 and NH_4VO_3 are employed as vanadium sources, while many various compounds can act as potassium sources, e.g., KOH, KCl, KNO_3, KVO_3, and K_2CO_3. Based on the published experimental details, it can be seen that the synthesis time is rather long and usually exceeds 24 h. In the case of precipitation, there is no need for heating, and synthesis is carried out at RT, while the hydrothermal reaction is carried out in the range of 180-210°. It was also demonstrated that the use of sonication pre-treatment or microwave heating can greatly decrease the synthesis time, even to a few hours [117]. Frequently, additional heating (above 250°C) is applied as the post-synthesis treatment, which allows different phases to be obtained by changing the atmosphere and temperature of the process [118]. The vast majority of potassium vanadates are obtained in the form of randomly arranged elongated structures. However, well-organized structures have also been reported. For example, hierarchical microspheres built from interconnected nanosheets can be obtained in the solvothermal reaction when ethanol is used as a solvent [110]. In another work, scientists proposed using potassium bicarbonate as a precursor in hydrothermal synthesis, which resulted in a 3D architectural nanofiber network and porous hydrogel structure [119].

Potassium vanadates can crystallize in the tetragonal, orthorhombic or monoclinic system. Representative crystal structures are presented in Figure 5 on the example of KVO_3 and KV_3O_8. K_3VO_4 crystallizes in the tetragonal $I\bar{4}2m$ space group (a=b=6.0 Å, c=8.7 Å, α=β= ɣ=90°) Its structure can be described as alternating $[K_2O_2]^{2-}$ and $[KVO_2]^{2+}$ layers, and the following building units can be listed: VO_4 tetrahedra, KO_4 tetrahedra and distorted KO_4 trigonal pyramids. KVO_3 crystallizes in the orthorhombic Pbcm space group (a=5.2 Å, b=5.7 Å, c=10.7 Å, α=β= ɣ=90°). Its structure is characterized by VO_3^- chains extending along the c-axis, with adjacent chains linked by the potassium cation [120]. VO_3^- chains are formed by corner-sharing VO_4

tetrahedra, while K^+ is bonded in an 8-coordinate geometry to eight oxygen atoms. Finally, KV_3O_8 crystallizes in the monoclinic P21/m space group (a=5.0 Å, b= 8.4, c=7.7 Å, α= ɣ=90°, β=98.1°). It exhibits a layered structure consisting of edge-sharing distorted VO_6 octahedra and edge-sharing pairs of VO_5 square pyramids. The potassium cations occupy positions between the layers in irregular 12-fold coordination with neighbouring oxygen atoms [121].

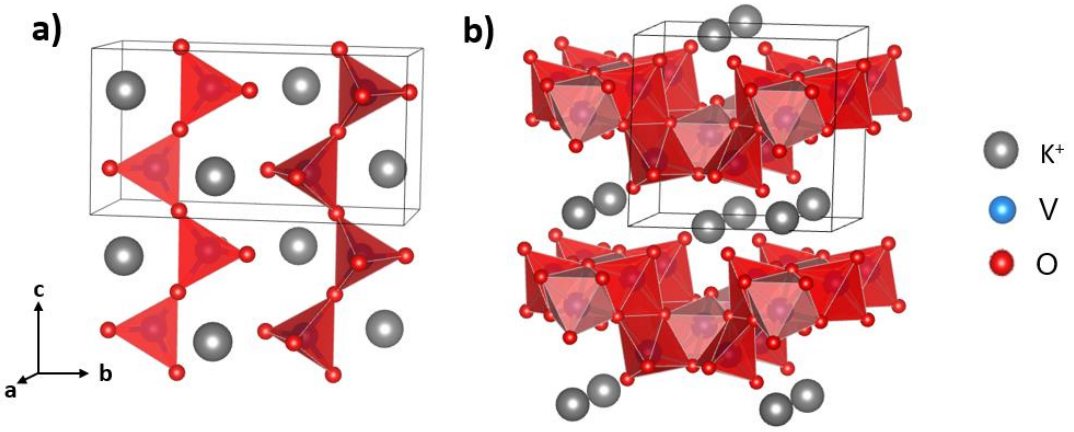

Figure 5. Representative crystal structures of ammonium vanadates on the example of KVO_3 (Crystal system, space group: orthorhombic, Pbcm) and KV_3O_8. (Crystal system, space group: monoclinic, P21/m). Figure was drawn using VESTA software.

The unique layered structure of potassium vanadates makes them potential candidates for electrode materials in rechargeable ion batteries. The existence of K ions between the vanadium oxygen layers provides a large spacing for reversible ion intercalation/deintercalation during the charge/discharge process. Moreover, K^+ ions can strongly interact with oxygen from vanadium oxide layers, which greatly enhances the structural stability of potassium vanadates during cycling [122–124]. Additionally, the incorporation of K^+ ions between the vanadium oxide layers can efficiently introduce oxygen vacancies and V^{4+} species, which are beneficial for the electrical conductivity of the electrode material and enhance its ion diffusion kinetics [125]. The electrochemical properties of potassium vanadates were investigated for the first time in 1984 by Raistrick and Huggins, who studied the thermodynamics and kinetics of the Li insertion reactions of $K_{0.25}V_2O_5$ [126]. Since then, many potassium vanadates with various stoichiometries and morphologies have been investigated as cathode materials in mono- and multivalent ion batteries. Among them, $K_xV_2O_5$ (x in the range of 0.2-0.5) are still the most commonly studied. For instance, $K_{0.5}V_2O_5$ has been tested as a cathode material in lithium [109], sodium [127], potassium [118,122,128], calcium [117] and zinc [129] ion batteries, while $K_{0.25}V_2O_5$ has been tested in lithium [110,130], sodium [131] and zinc [132] ion batteries. Interesting studies were carried out by Baddour-Hadjean et al. [122], in which scientists prepared a series of potassium vanadates with varied K/V ratios and compared their electrochemical properties as Li-ion cathodes. KV_3O_8, $K_{0.5}V_2O_5$, and $K_{0.25}V_2O_5$ compounds were synthesized by the precipitation method by simply adjusting the stoichiometric ratios of K/V of precursors. The electrochemical performance of the obtained samples strongly depends on the crystalline structure of each compound. As presented in the Figure 6a, $K_{0.25}V_2O_5$ exhibits a tunnel framework, while KV_3O_8

and $K_{0.5}V_2O_5$ possess layered structures. The potassium-poorer compound $K_{0.25}V_2O_5$ reveals the highest initial discharge capacity of 230 $mAhg^{-1}$ (4-2 V, at C/10 rate); however, its tunnel structure is not stable during cycling, and the discharge capacity continuously decreases (66% of the initial capacity recovered after 70 cycles). In contrast, potassium vanadates with layered structures exhibit excellent capacity retention (less than a 5% decrease within 70 cycles). The first discharge capacity equals 70 $mAhg^{-1}$ and 210 $mAhg^{-1}$ for KV_3O_8 and $K_{0.5}V_2O_5$, respectively (Figure 7b). The structural stability of such compounds is provided by K^+ ions, which stabilize the stacking of double-sheet V_2O_5 layers and ensure a reversible Li accommodation–extraction process. The high delivered capacity originates from the large interlayer spacing of 7.7 Å observed for $K_{0.5}V_2O_5$.

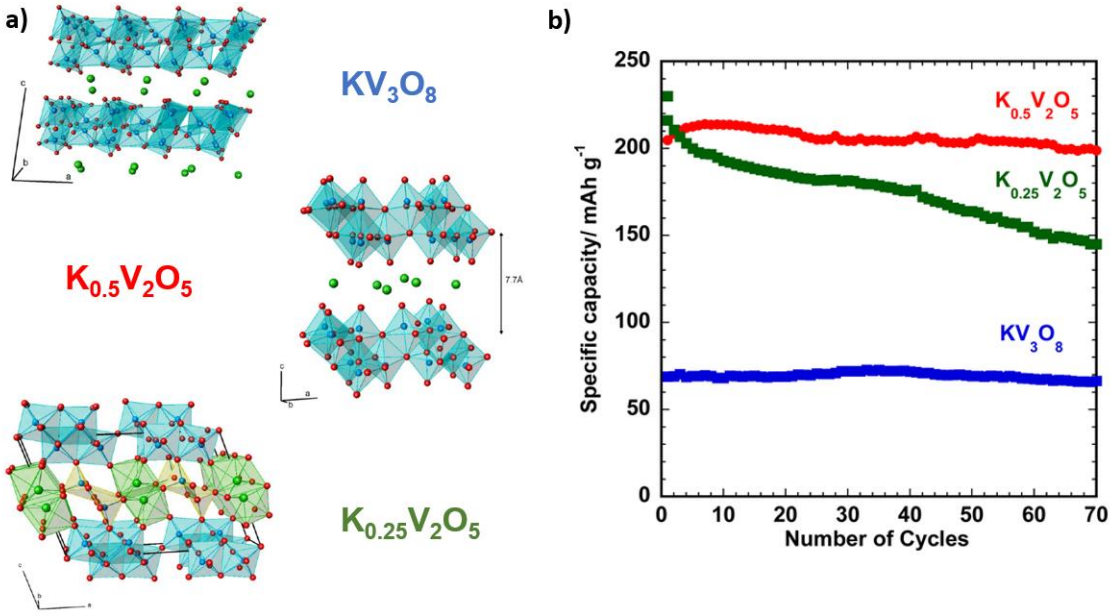

Figure 6. Comparison of KV_3O_8, $K_{0.5}V_2O_5$, and $K_{0.25}V_2O_5$: a) crystal structure b) electrochemical performance as cathode materials for LIBs (at C/10 rate in the 4−2 V potential range) [122].

The beneficial effect of the presence of K ions between V_2O_5 is well presented in [129]. The stability of the electrodes based on V_2O_5 and $K_{0.5}V_2O_5$ was compared in aqueous $ZnSO_4$ (3 M), which was further applied as an electrolyte in ZIBs. In the case of V_2O_5, the colour of the electrolyte turned yellow after one day, while for $K_{0.5}V_2O_5$, it remained colourless throughout the testing period of 8 days (Figure 7a). The change in colour indicates the dissolution process of vanadium from the electrode and was further confirmed by inductively coupled plasma optical emission spectroscopy. After 8 days, the content of vanadium in the electrolyte was 4.968 mgL^{-1} for V_2O_5 and 0.861 mgL^{-1} for $K_{0.5}V_2O_5$. It was also shown that after 1 month in the electrolyte, the V_2O_5 electrode was seriously damaged, while the $K_{0.5}V_2O_5$ electrode remained unchanged and showed no difference from its original appearance (Figure 7b). The improved stability of $K_{0.5}V_2O_5$ was further confirmed in electrochemical measurements. When applied as a cathode in ZIBs, the $K_{0.5}V_2O_5$ electrode exhibits good rechargeability with a capacity of 92.2 $mAhg^{-1}$ at the 150th cycle under a current density of 1 Ag^{-1}. In contrast, V_2O_5 delivered an initial capacity of 56.8

$mAhg^{-1}$, which quickly faded to 7.5 $mAhg^{-1}$ after 50 cycles (Figure 7c). More impressively, even after 3000 cycles at a current density of 5 Ag^{-1}, $K_{0.5}V_2O_5$ delivers 140.3 $mAhg^{-1}$. Such high rate capability and cyclic stability are ascribed to the crystal structure of potassium vanadates, particularly the existence of K-O bonds between V-O layers. In the same work, scientists investigated the effect of the K^+ intercalation amount on the electrochemical performance. In addition to $K_{0.5}V_2O_5$, two other potassium vanadates with higher potassium amounts were investigated. However, the stoichiometry of the samples was not fully determined, and only a small sector of XRD diffraction patterns and ICP analysis for K (without vanadium) were published. Nevertheless, the XRD diffraction peak of the (100) crystal plane shifts to higher diffraction angles with increasing amounts of K^+. This indicates a decrease in interlayer spacing in the potassium vanadate structure and can be explained by the enhanced interaction between positively charged K ions and negatively charged O ions upon K-ion intercalation. A smaller interlayer spacing can inhibit the diffusion of metal ions during charging/discharging and thus negatively affect the electrochemical performance of the material. Such a tendency was also observed for the tested ZIBs cathodes, and the higher the amount of K^+ in the potassium vanadates was, the lower the specific capacity. In summary, it can be concluded that the intercalation of K ions into V_2O_5 could inhibit the active material from dissolving in the aqueous electrolyte. On the other hand, an excessive amount of K ions in the potassium vanadate structure could be unfavourable to their electrochemical performance. However, it should be noted here that the evaluated potassium vanadates varied in morphology, which can also strongly influence the electrochemical properties of the active material. A comprehensive study was published by Meng et al., who prepared V_2O_5, $K_{0.25}V_2O_5$ and KV_3O_8 in the form of nanowires and tested them as cathode materials for lithium- and sodium- ion batteries [131]. Compared with V_2O_5, the potassium vanadate nanowires exhibit great improvement in electrochemical performance. Moreover, $K_{0.25}V_2O_5$ displays better rate performance and cycling stability than KV_3O_8. When tested at a current density of 100 mAg^{-1} and for 100 cycles, the discharge capacities of V_2O_5, KV_3O_8 and $K_{0.25}V_2O_5$ were 71, 165 and 270 $mAhg^{-1}$ in LIBs and 8, 41 and 82 $mAhg^{-1}$ in sodium-ion batteries, respectively. It should be noted that the initial discharge capacity of potassium vanadates was lower than that of V_2O_5 and can be explained by the partial occupation of K ions in the available ion intercalation sites. However, fast capacity loss occurs for V_2O_5 after the first 5 cycles. A similar phenomenon can be observed for KV_3O_8 after ca. 20 cycles, while for the second potassium vanadate phase-$K_{0.25}V_2O_5$, the capacity remains stable. The differences in cyclic stability result from the different crystal structures of the studied compounds and were confirmed by in situ XRD measurements and *ex situ* ICP analysis. The intercalation of lithium/sodium ions into the interlayer structure of V_2O_5 leads to irreversible structural transformation and severe structural degradation in the initial cycles. Such fast capacity loss is often observed for V_2O_5-based cathodes and limits their practical utilization in rechargeable ion batteries. In the case of potassium vanadates, the K ions between vanadium oxide layers can bond with oxygen atoms and act as pillars, protecting the structure from collapse during the charge/discharge processes. The vanadium oxide layers of $K_{0.25}V_2O_5$ are composed of

single-connected oxygen atoms, while KV_3O_8 is composed of both single-connected and tri-connected oxygen atoms. However, tri-connected oxygen atoms cannot provide strong interactions with the K ions, and thus, after several cycles, partial K ions are extracted from the crystal structure of KV_3O_8. This leads to the weakening of the pillar effect and structural degradation in further cycles. The vanadium oxide layers of $K_{0.25}V_2O_5$ consist of only single-connected oxygen atoms, which can form strong interactions with K ions and ensure structural integrity and consequently lead to excellent cycling performance during the charge/discharge process.

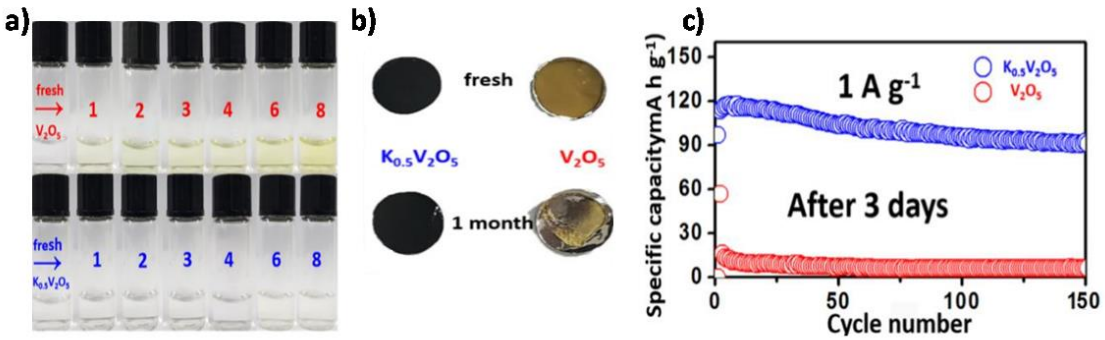

Figure 7. Stability measurements of V_2O_5 and $K_{0.5}V_2O_5$. a) Control of the 3 M $ZnSO_4$ electrolyte (over an 8-day period with soaked electrodes. b) Comparison of pristine electrodes and electrodes after one month in $ZnSO_4$ electrolyte (3 M). c) The electrochemical performance of $K_{0.5}V_2O_5$ and V_2O_5 as cathode materials in ZIBs [129].

Recently, Su et al. demonstrated that potassium vanadates can work even at low temperatures. Scientists investigated hydrothermally obtained $K_{0.5}V_2O_5$ nanobelts and tested them as ZIBs cathode materials at room temperature and -20°C [133]. Electrodes exhibit high reversible capacities of 251 $mAhg^{-1}$ and 115 $mAhg^{-1}$ at 5 Ag^{-1} at room temperature and -20°C, respectively. In both cases, no capacity fading was observed through 1000 cycles. In addition, Liu et al. reported that potassium vanadates can also be suitable as anode materials [134]. $K_{0.23}V_2O_5$ was obtained via a simple hydrothermal method with a post-calcination process and investigated as a negative electrode for LIBs and KIBs. Materials were tested in the potential range of 0.01–3 V versus M/M^+ (M = Li, K). When used in LIBs, $K_{0.23}V_2O_5$ exhibits good reversible capacity: 480 $mAhg^{-1}$ at 20 mAg^{-1} after 100 cycles and 440 $mAhg^{-1}$ at 200 mAg^{-1} after 300 cycles. Even at a higher current density of 800 mAg^{-1}, the discharge capacity remains at a stable level of 200 mAh g^{-1} during 10 cycles. In KIBs, $K_{0.23}V_2O_5$ maintains a capacity of 120 $mAhg^{-1}$ after 150 cycles at 20 mAg^{-1} and 100 $mAhg^{-1}$ at 100 mAg^{-1} after 100 cycles. The same material was investigated by Xu et al. as a cathode material for LIBs (potential range: 1.5 and 3.8 V versus Li^+/Li) and delivers 240 $mAhg^{-1}$ at 50 mAg^{-1} (76% capacity retention after 100 cycles) and 80 $mAhg^{-1}$ at a high current density of 1800 mAg^{-1} [135]. For both examples, such excellent electrochemical performance is ascribed to the specific layered crystal structure of $K_{0.23}V_2O_5$ (which buffers the volume changes during ion insertion/deinsertion) and flower-like morphology (which provides many open channels for the access of electrolyte and facilitates fast diffusion of Li^+/K^+ during cycling).

Similar to the case of ammonium vanadates, the application of potassium vanadates as photocatalysts is scarce. Only one report (published in 2015) can be found that presents the utilization of hydrated $K_2V_6O_{16}$ for the photodegradation of Methyl Orange [136]. Unfortunately, authors focus more on the synthesis part than the application and neither mechanism/kinetics of photocatalysis process nor the electronic band structure is discussed. Briefly, Kong et al. proposed a hydrothermal synthesis in which the morphology and content of crystalline water of $K_2V_6O_{16}$ were controlled by adjusting the reaction time and pH of the process. This allowed to obtain two types of micrometric crystals: $K_2V_6O_{16}\cdot 2.7H_2O$ plates and $K_2V_6O_{16}\cdot 1.5H_2O$ fibres. UV–vis DRS revealed that the energy band gap in both samples is similar and equal to 2.15 eV for $K_2V_6O_{16}\cdot 2.7H_2O$ and 2.20 eV for $K_2V_6O_{16}\cdot 1.5H_2O$. There were also no differences in the photocatalytic performance of these two samples, and 90 min of visible light irradiation resulted in approximately 40% degradation of Methyl Orange.

3. OVERVIEW OF THE PUBLICATIONS CONSTITUTING THE DISSERTATION

This chapter presents the publications that comprise the dissertation. Each publication was included in a separate subsection and is preceded by research background, description of research problems and aims. Next, the main results were summarized and discussed with regard to the formulated hypotheses.

The content of this chapter consists of the following research articles:

[A1] M. Prześniak-Welenc, **M. Nadolska**, B. Kościelska, K. Sadowska. Tailoring the size and shape –new path for ammonium metavanadate synthesis, *Materials*, 2019, 12(20), 3446.

[A2] M. Prześniak-Welenc, **M. Nadolska**, A. Nowak, K. Sadowska. Pressure in charge. Neglected parameter in hydrothermal synthesis turns out to be crucial for electrochemical properties of ammonium vanadates, *Electrochimica Acta*, 2020, 339, 135919.

[A3] M. Prześniak-Welenc, **M. Nadolska**, K. Jurak, J. Li, K. Górnicka, A. Mielewczyk-Gryń, M. Rutkowska, A. P. Nowak. The valance state of vanadium-key factor in the flexibility of potassium vanadates structure as cathode materials in LIBs, *Scientific Reports*, 2022, 12, 18751.

[A4] **M. Nadolska**, M. Szkoda, K. Trzciński, P. Niedziałkowski, J. Ryl, A. Mielewczyk-Gryń, K. Górnicka, M. Prześniak-Welenc. Insight into Potassium Vanadates as Visible-Light-Driven Photocatalysts: Synthesis of V(IV)-Rich Nano/Microstructures for the Photodegradation of Methylene Blue, *Inorganic Chemistry*, 2022, 61, 25, 9433-9444.

[A5] **M. Nadolska**, M. Szkoda, K. Trzciński, J. Ryl, A. Lewkowicz, K. Sadowska, J. Smalc-Koziorowska, M. Prześniak-Welenc. New light on the photocatalytic performance of $NH_4V_4O_{10}$ and its composite with rGO, *Scientific Reports*, 2023, 13, 3946.

3.1. [A1] Tailoring size and shape- new path for ammonium metavanadate synthesis

3.1.1. Research background and objectives

Ammonium metavanadate (NH_4VO_3) is a versatile compound with a wide range of applications across various scientific and industrial fields. It deserves special attention due to its use in chemistry as the principal precursor for the synthesis of diverse vanadium compounds, including the hydrothermal synthesis of other ammonium vanadates. Due to its versatility, ammonium metavanadate is a relatively common chemical compound that is readily available from many chemical suppliers. Additionally, it is typically more affordable than other vanadate compounds. The production of NH_4VO_3 involves the addition of ammonium salts to solutions containing vanadate ions, obtained by the dissolution of V_2O_5 in alkaline aqueous solutions [137]. It is important to note that different manufacturers may employ variations of this method or additional steps based on their capabilities and quality standards.

It is known that the reactivity of precursors can differ based on their source, synthesis method, or even production series. Variations in reactivity can subsequently affect reaction kinetics, yields, and final product properties. Thus, if the purity, consistency, and reproducibility of synthesized materials are critical, it may be advisable to use specific precursors from a single source. Such an issue is especially important in scientific research, as it minimizes the variability of experiments and the possibility of potential mistakes and inaccurate conclusions. On the other hand, precursors can serve as valuable tools that enable control over the characteristics of the final product, and the literature abounds in numerous studies devoted to the influence of precursor properties on the synthesis processes of diverse materials. The vast majority of research focuses on precursor morphology. For example, certain precursor shapes may be more prone to surface oxidation or contamination, which can impact the chemical composition of the final product. Different precursor shapes may also lead to materials with varying levels of crystallinity and can result in preferential crystal growth along certain crystallographic directions. Precursor size influences the kinetics of chemical reactions during synthesis. Smaller particles or finely divided precursors offer higher surface areas, resulting in faster reaction rates and improved yields in various synthesis methods. As the precursor size decreases, the size of the final material is also reduced. Special attention has been given to nanosized precursors, whose properties can differ significantly from their bulk counterparts. Usually, nanosized precursors offer increased solubility and enhanced dispersion. This can lead to better homogeneity of samples and is helpful in the synthesis of composites [138]. In many cases, nanostructures exhibit distinct thermal properties, such as reduced thermal stability or decreased melting point; thus, the usage of nanosized precursors can initiate and promote chemical reactions at lower temperatures compared to bulk materials. In summary, the precursor morphology is a pivotal parameter in material synthesis and directly affects the morphology and structure of the final product. It should be emphasized here that both the morphology and structure define the properties of materials and determine the possibility of their future utilization in various

applications. Interesting research has been presented by Zhang et al., who studied the relations between the morphologies of V_2O_5 and their electrochemical properties as battery-type electrode materials for supercapacitors [139]. The morphology-controlled synthesis of V_2O_5 was realized with the usage of butterfly like, rhombohedral, and flower-like NH_4VO_3 microcrystals and their calcination in ambient air. Obtaining such precursors with different morphologies was possible thanks to the development of an innovative method that combines the hydrothermal treatment of commercial NH_4VO_3 aqueous solution and further drowning-out crystallization in the presence of ethanol. To obtain pure V_2O_5, the as-synthesized NH_4VO_3 was calcined at 400°C for 4 h in an ambient air atmosphere. The V_2O_5 crystals preserved the original sizes and shapes of the NH_4VO_3 precursors; however, their structure became porous, and some cracks on the surface were observed. Finally, the electrochemical properties of V_2O_5 were studied as battery-type electrodes for supercapacitors using 1 M $LiClO_4$/propylene carbonate as the electrolyte. All samples demonstrated impressive initial capacitances and exceeded most of the values previously reported for V_2O_5-based electrodes. Rhombohedral V_2O_5 showed the highest initial specific capacitance (641 Fg^{-1}at 0.5 Ag^{-1}) with excellent rate capability (540 Fg^{-1}at 10 Ag^{-1}) and cycling stability, retaining over 110% of its initial capacitance after 3000 cycles. In contrast, the more complex morphologies of the butterfly like and flower-like V_2O_5 led to higher degrees of electrode polarization, higher resistance, and lower specific capacitance (556 $Fg^{-1}$and 609 Fg^{-1}at 0.5 Ag^{-1}, respectively). In addition, the structure of flower-like V_2O_5 was less stable than the other two morphologies, and for this sample, a decline to only 61% of the initial capacitance was observed after 3000 cycles.

The above example is just one of many illustrating that the precise control of precursor morphology enables the design of materials with specific (often unique) properties and consequently enhanced performance. Understanding how the morphology of starting materials impacts the synthesis process and resultant materials has become a fundamental aspect of materials science. Keeping that in mind, the study presented in [A1] was designed to explore the influence of NH_4VO_3 morphology on the hydrothermal synthesis of ammonium vanadates. The investigations focused on two distinct morphologies, namely, micro- and nanostructures of NH_4VO_3. Selected morphological varieties displayed a significant difference in both particle size and shape, providing an excellent basis for the research. Microstructures of NH_4VO_3 are commercially available, while nanostructures can be obtained by a facile synthesis method. Utilizing an "in-house synthesized" precursor offers the advantage of enhanced synthesis reproducibility. Furthermore, it is expected that nanostructured NH_4VO_3 should result in smaller and thinner structures of ammonium vanadate. It is highly probable that in this case, the resulting material will exhibit an organized structure with a well-developed surface. The nanostructured precursor should also contribute to increased sample homogeneity compared to the microstructured precursor.

The aim of the study was to determine the influence of the NH_4VO_3 morphology on the hydrothermal synthesis of ammonium vanadates. Two different NH_4VO_3 were studied: commercially available microstructures and synthesized nanostructures, and employed as

precursors for the synthesis of ammonium vanadates [A1]. The resulting products were characterized by means of XRD, FTIR, Raman and SEM analysis.

3.1.2. Summary of main results

Ammonium vanadates were obtained via a hydrothermal method in an autoclave. Commercially available microstructured NH_4VO_3 and synthesized nanostructured NH_4VO_3 were used as precursors. All other parameters (i.e., temperature, time, volume, reagent concentration) were kept constant and were chosen according to the literature review [77] and preliminary studies.

First, nanostructured NH_4VO_3 was synthesized according to the novel method described in the first part of the manuscript. The proposed method is based on liquid-phase exfoliation accompanied by ion exchange. It includes a one-step procedure carried out at room temperature, wherein V_2O_5 (transition metal anion source) is added to a solution of organic ammonium salt (NH_4 cation source) in an appropriate solvent (delamination agent). One of the main advantages of such a method is the possibility of controlling the size and shape of obtained NH_4VO_3 crystals by changing the type of ammonium salt (ammonium formate or ammonium acetate) and the solvent (water or formamide). When ammonium formate and formamide were used, nanocrystalline structures with a flower-like morphology could be obtained. Thus, such parameters were chosen for further studies. Moreover, the synthesis procedure was repeated three times, which confirmed the good reproducibility of the proposed method. The phase purity and chemical composition of the as-synthesized NH_4VO_3 were confirmed by XRD, FTIR and Raman spectroscopy, and all the results were in agreement with databases and reference spectra of NH_4VO_3. Next, the morphology of the synthesized and commercial NH_4VO_3 was compared by SEM analysis. The synthesized NH_4VO_3 exhibited a flower-like microstructure with an average diameter of 1.5 µm. The observed spherical structures were built of uniform crystals with lengths in the range of 0.5–1 µm and widths in the range of 0.2–0.5 µm. Their thickness was on the nanoscale and equal to ca. 20–80 nm. In contrast, commercial NH_4VO3 was characterized by irregularly shaped crystals and a broad size distribution. Their length was between 80-200 µm, width: 50-120 µm, and thickness: 5-25 µm.

Next, synthesized nanostructured and commercial microstructured NH_4VO_3 were used as precursors in the hydrothermal synthesis of ammonium vanadates. The XRD results disclosed that hydrothermally obtained materials were a mixture of $(NH_4)V_4O_{10}{\cdot}H_2O$ and $(NH_4)_{0.76}V_4O_{10}$. Spectroscopic analysis (FTIR and Raman) further confirmed the chemical structure and mixed valence of vanadium in the obtained samples. The splitting of V═O bands in the FTIR spectra, arising from distortions in the vanadium oxide layers, is more pronounced for the sample obtained from the nanostructured precursor. On the other hand, in the spectrum of the sample prepared from the microstructured precursor, significant splitting of the characteristic band for NH_4^+ was observed, which reflects various chemical environments of $NH_4^{+\cdot}$ In conclusion, all the obtained results indicated that the contribution of the hydrated $(NH_4)V_4O_{10}{\cdot}H2O$ phase was higher for the sample prepared from synthesized nanostructured NH_4VO_3 than for the sample prepared from

commercial microstructured NH_4VO_3. Moreover, significant differences were observed in the morphology of the hydrothermally obtained samples. Samples prepared from commercial microstructured NH_4VO_3 consisted of uneven, variably shaped tiles with rounded edges. Tiles were randomly arranged and formed many irregular aggregates. The individual tile sizes ranged from hundreds of nanometers to a few microns. In contrast, the sample obtained from the nanostructured precursor exhibited a high degree of morphological uniformity, with similar structural features observed throughout the entire sample. In this case, the fundamental building blocks consisted of thin, jagged flakes that self-assembled into a porous, interconnected structure. Such a complex structure made it difficult to estimate the dimensions of individual flakes. Nevertheless, the thickness of the flakes was on the order of several dozen nanometers.

In conclusion, the above results demonstrate the significance of precursor morphology in shaping the properties of hydrothermally synthesized ammonium vanadates. This influence is particularly visible in the differences in the morphology of the final product. As expected, the nanostructured precursor facilitated the production of ammonium vanadate materials with well-controlled size attributes. Specifically, the final product exhibited flower-like microstructures consisting of uniform crystals with nanoscale thickness. In contrast, the employment of commercial microstructured NH_4VO_3 results in irregularly shaped crystals with a broad size distribution. It should be noted that precursor morphology is just one of many parameters in the hydrothermal synthesis of ammonium vanadates. Other parameters, such as reaction time, temperature, or precursor solution composition, are usually well described in synthesis protocols, and their impact on the obtained ammonium vanadates has been the subject of extensive research. Unfortunately, precursor morphology is practically never taken into consideration. Studies presented in the publication [A1] highlight the need for careful precursor selection and quality control in achieving desired characteristics in the obtained ammonium vanadates. Furthermore, the investigated precursor compound, NH_4VO_3, is one of the most frequently used precursors, not only in the synthesis of ammonium vanadates but also in the synthesis of other vanadates and vanadium oxides. It is believed that the presented results together with the facile, repeatable synthesis of nanostructured NH_4VO_3 will motivate and inspire other scientists to further research within the broader context of materials science.

3.1.3. Full content of the article

Title: Tailoring the size and shape –new path for ammonium metavanadate synthesis

Authors: M. Prześniak-Welenc, M. Nadolska, B. Kościelska, K.Sadowska

Journal: Materials, 2019, 12(20), 3446

Impact factor: 3.057 (2019)

Ministerial Points: 140 pts

DOI: 10.3390/ma12203446

I was responsible for the part devoted to the synthesis of mixed-valence ammonium vanadates, which included: the synthesis of nanostructured precursor NH_4VO_3, proposition and realization of the hydrothermal synthesis of mixed-valence ammonium vanadates from nanostructured and microstructured NH_4VO_3, physicochemical characterization of the obtained samples, data analysis and visualization, preparation of the part of the manuscript corresponding to the above.

materials

MDPI

Article

Tailoring the Size and Shape—New Path for Ammonium Metavanadate Synthesis

Marta Prześniak-Welenc *, Małgorzata Nadolska, Barbara Kościelska and Kamila Sadowska

Faculty of Applied Physics and Mathematics, Gdansk University of Technology, Narutowicza 11/12, 80-233 Gdansk, Poland

* Correspondence: marta.welenc@pg.edu.pl; Tel.: +48-583-486-606

Received: 23 September 2019; Accepted: 17 October 2019; Published: 21 October 2019

Abstract: Ammonium metavanadate, NH_4VO_3, plays an important role in the preparation of vanadium oxides and other ammonium compounds, such as $NH_4V_3O_8$, $(NH_4)_2V_3O_8$, and $NH_4V_4O_{10}$, which were found to possess interesting electrochemical properties. In this work, a new route for the synthesis of NH_4VO_3 is proposed by mixing an organic ammonium salt and V_2O_5 in a suitable solvent. The one-step procedure is carried out at room temperature. Additionally, the need for pH control and use of oxidants necessary in known methods is eliminated. The mechanism of the NH_4VO_3 formation is explained. It is presented that it is possible to tailor the morphology and size of the obtained NH_4VO_3 crystals, depending on the combination of reagents. Nano- and microcrystals of NH_4VO_3 are obtained and used as precursors in the hydrothermal synthesis of higher ammonium vanadates. It is proven that the size of the precursor particles can significantly affect the physical and chemical properties of the resulting products.

Keywords: ammonium vanadates; hydrothermal synthesis; morphology control

1. Introduction

Ammonium metavanadate (NH_4VO_3) plays an important role in the preparation and purification of vanadium compounds, including, for example, $NH_4V_3O_8$, $NH_4V_4O_{10}$, $(NH_4)_{0.6}V_2O_5$, and V_2O_5, V_6O_{13} [1–7]. These vanadium oxides and their derivatives are of huge interest, mainly due to their Li-ion intercalation properties. Therefore they are considered as a favorable cathode material inthe secondary Li-ion batteries (LIBs) [1,4,7]. Recent studies have shown that vanadium oxide derivatives can also be successfully used in multivalent ion batteries, such as calcium-ion [8], magnesium-ion [9], and zinc-ion [10–12] batteries. Moreover NH_4VO_3 is used as an efficient and mild catalyst for the synthesis of α-hydroxyphosphonate derivatives, which act as inhibitors of a diverse group of enzymes e.g. HIV protease [13]. Ammonium metavanadate can also be used as an electrolyte additive in the electrochemical anodization of magnesium alloy surface to improve its corrosion resistance [14]. However, one of the main drawbacks connected with the commercial usage of ammonium metavanadate in the mentioned applications is the cost of the synthesis of this precursor. The industrial production of NH_4VO_3 is usually a multi-step procedure, carried out under harsh conditions (oxidizing agents, alkalines) and elevated temperature [15,16]. Moreover, ammonium chloride or other inorganic salts, serving as an ammonium ions source, need to be used in the substantial excess to enable the efficient precipitation of the desired product. Therefore, next to the high cost of the production, the obtained NH_4VO_3 suffers from poor particle size distribution and possibly high concentration of impurities. The morphology of the precursor strongly affects the properties of the final product, especially the electrochemical performance, which is of the priority, when referring to LIBs. Therefore, novel methods of ammonium metavanadate synthesis are sought, with particular interest to approaches enabling NH_4VO_3 crystals size and shape control. Controllable synthesis of ammonium metavanadate is of

importance not only due to the potential electrochemical applications. Here, it should be noted that several examples of NH_4VO_3 use as catalyst can be found in the literature [17–19]. It is known that the size of the catalyst particles strongly influences its catalytic performance [20,21]. Therefore, simple and efficient synthesis of uniform and nano-sized NH_4VO_3 particles would pave the way for their wider application spectrum.

In this paper, we report a simple, low temperature, one-pot approach for ammonium metavanadate synthesis, while using V_2O_5 and chosen organic ammonium salt as substrates and suitable solvent. Beneficially, the size and shape of the obtained NH_4VO_3 crystals can be simply controlled by choosing type of the solvent and type of the organic ammonium salt. Therefore, the properties of the synthesized material can be tailored for a specific purpose.

2. Materials and Methods

2.1. Materials

Formamide (99.5%, ACROS Organics, New Jersey, NJ, USA), ammonium formate (99%, ACROS Organics, New Jersey, NJ, USA), ammonium acetate (97%, Alfa Aesar, Kandel, Germany), V_2O_5 (99.2%, Alfa Aesar, Kandel, Germany), NH_4VO_3 (99%, Sigma Aldrich, Saint Louis, MO, USA), and oxalic acid dihydrate ($C_2H_2O_4{\cdot}2H_2O$, L.P P-H "OH") were used without further purification. MiliQ water (0.05 μS cm^{-1}) was used in all experiments.

The general procedure was as follows. To 50 mL of 1.25 mol/L solution of ammonium organic salt (ammonium formate or ammonium acetate) in appropriate solvent (water or formamide) 50 mg of V_2O_5 was added. The mixture was agitated for several minutes at RT and then left for 12 h. From the initially yellow solution, white solids precipitated, which were separated by centrifugation (2 min, 14000 rpm). After washing several times with ethanol, the white crystalline product was dried overnight at RT under reduced pressure (0.01 bar). The obtained samples were denoted, as presented in Table 1.

Table 1. Nomenclature of obtained samples.

Solvent	Salt	
	Ammonium Formate	**Ammonium Acetate**
Water	AF/W	AA/W
Formamide	AF/F	AA/F

Hydrothermal Synthesis of Ammonium Vanadates

In a typical procedure, 0.2 g NH_4VO_3 (commercial or AF/F) and 0.2 g $C_2H_2O_4{\cdot}2H_2O$ were dissolved in 7 mL of deionised water under magnetic stirring (300 rpm). Subsequently, the obtained solutions were placed into a stainless-steel autoclave (Series 4680, Parr Instrument Co., Moline, IL, USA) with a capacity of 1800 mL and then kept for 72 h at 180 °C. After that time, the autoclave was evacuated with a rate of ca. 1 bar/min and then cooled to room temperature naturally. Finally, the obtained precipitates were washed several times with deionised water and then dried at 40 °C under vacuum.

2.2. Methods

The phase composition of obtained samples was examined by X-ray diffraction method (XRD) by Philips X'Pert diffractometer system (Royston, UK) while using CuKα radiation in range of 5–80° of 2Θ. The FT-IR spectra were recorded at room temperature while using a Perkin-Elmer spectrometer (model Frontier FTIR MIR/FIR) (Waltham, MA, USA). The FT-IR spectra of the samples that were pressed into KBr pellets with constant measure material concentration (0.5%) were collected in the wave number range 4000–400 cm^{-1} (mid IR region) while using the KBr beam splitter. The surface morphologies of the samples were studied by a FEI Company Quanta FEG 250 scanning electron microscope (SEM) (Waltham, MA, USA), mounting the analyzed sample on a carbon conductive

tape The thermogravimetric analysis (TGA) was performed under argon atmosphere (flow rate 60 cm^3 min^{-1}) with heating rate 10 °C/min. from 40 °C to 550 °C while using Netzsch STA 449 F1 Jupiter®(Netzsch, Selb, Germany). Constant sample mass (6 ± 0.5 mg) was used. The thermal behavior has also been studied with mass spectrum (MS). The gases that come out from sample during heating were monitored by the quadruple mass spectrometer Netzsch QMS 403 Aëolos (Netzsch, Selb, Germany).Raman spectra were recorded while using Renishaw InVia spectroscope (Renishaw, UK) with argon ion laser operating at 514.5 nm focused through a 50× objective. Collected light was dispersed through a triple monochromator and detected with a charge-coupled device. The spectra were collected in the dark, with a resolution of 2 cm^{-1} in the range of 100–3000 cm^{-1}.

3. Results and Discussion

3.1. Structural Analysis

Ammonium metavanadate was obtained in a simple, low cost, and one-step method. In the first experiment, ammonium formate was used as a source of ammonium ion and formamide as a solvent. According to the literature, formamide is as an effective delaminating agent that is used in the liquid-phase exfoliation of V_2O_5 [22]. Therefore, it was considered to be a solvent of choice. Ammonium formate possessing the same structural core as a formamide was an apparent selection. Analogously, the reaction was carried out while using water as a solvent, keeping the same ratio of reagents. Water was used as a cheaper and environmentally friendly solvent. It was found out that the reaction proceeded in both solvents. However, it was visible by the naked eye, whereby the morphology of the obtained products differs dramatically. Fine, white powder was collected from the reaction that was carried out in the formamide, whereas bulky, uniform crystals were obtained in the aqueous environment.

X-ray diffraction patterns were recorded to confirm the phase purity and crystallinity of the obtained samples. Figure 1 illustrates the part of XRD patterns (10–70° of 2θ) of AF/F, AF/W, AA/F, and AA/W. The observed diffractions peak for all samples match very well with JCPDS Card no. 00-025-0047, which corresponds to the NH_4VO_3 orthorhombic structure with a space group of Pmab (No. 57) with lattice parameter values of a = 5.827 Å, b = 11.782 Å, and c = 4.905 Å. Moreover, no signals of other phases were detected, which indicated the high purity of obtained NH_4VO_3 micro- and nanocrystals.

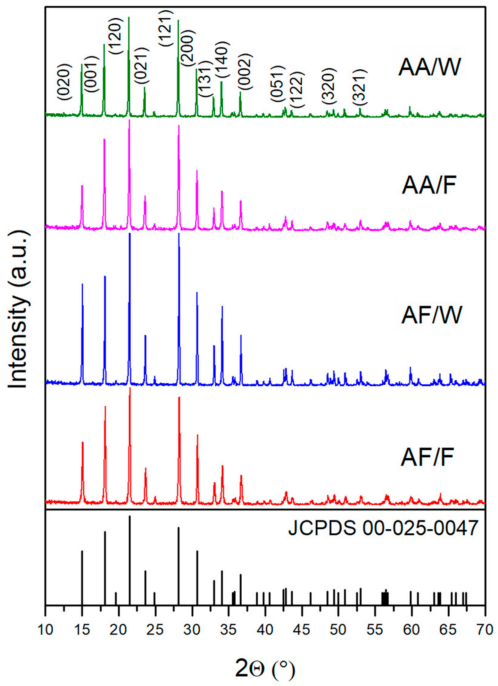

Figure 1. X-ray diffraction method (XRD) patterns of samples AF/F, AF/W, AA/F, and AA/W.

FTIR spectroscopy was used to further analyze the obtained samples. Figure 2 presents the FTIR spectra of four analyzed samples. The spectra recorded for all samples are identical and they are in agreement with the reference spectrum of ammonium metavanadate (NIST Chemistry WebBook, SRD 69), which confirms the identity of the synthesized products (see Supplementary Materials, Figure S1). The bands centered at 3200, 2945, and 2796cm^{-1} are assigned to the stretching vibration of bonds in the NH_4^+. Next, the characteristic band for NH_4^+, located at 1414 cm^{-1}, is due to N-H in plane vibration mode. The strong band at 919 cm^{-1} refers to V=O stretching and other bands that are visible in the region between 860 cm^{-1} and 500 cm^{-1} are attributed to V-O-V bonds vibrations [23,24].

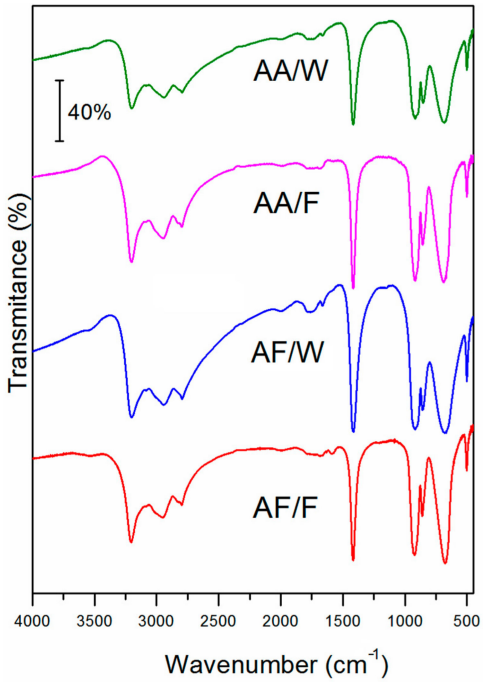

Figure 2. FTIR spectra of samples AF/F, AF/W, AA/F, and AA/W.

Being complementary to FTIR, Raman spectroscopy was also used to confirm the structure of the samples. All spectra, as presented in Figure 3, conform to the NH_4VO_3 spectrum (see Figure S2). The main peak, positioned at 926 cm^{-1} corresponding to VO_2 symmetrical vibrations, is followed by a smaller band at 895 cm^{-1} that arises from asymmetrical VO_2 vibrations. The other visible bands at 647 and 495 cm^{-1} are connected with V-O-V asymmetric and symmetric stretching, respectively. At lower frequency region (400–200 cm^{-1}), several bands of low intensity can be observed, and they refer to VO_2 bending and NH_4^+ stretching [24]. Below 200 cm^{-1}, the Raman bands are assigned to the lattice modes and they are generally observed for layered structures. The different intensities may be due to the different morphologies of the analyzed samples.

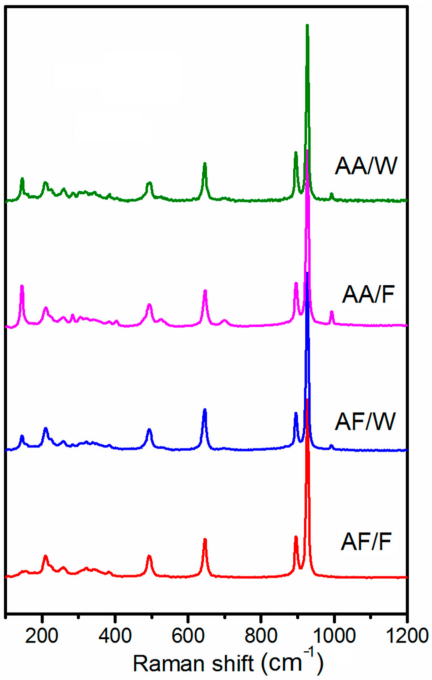

Figure 3. Raman spectra of samples AF/F, AF/W, AA/F, and AA/W.

The SEM analysis further revealed morphological differences. As can be seen in Figure 4a, the AF/F sample adopted flower-like structure, with dimensions between 1.5 µm and 3 µm. The length of single crystals forming a flower-like structure was in the range of 0.5–1 µm, their width was c.a. 0.2–0.5 µm, and their thickness was in the nanoscale and equal to 20–80 nm. Much bigger crystals can be seen in Figure 4b, presenting the morphology of AF/W sample. The obtained crystals were casketoids in shape, with a length of 7–10 µm, width 4.5–5.5 µm, and thickness 0.5–1.5 µm.

The same protocol was performed in both solvents (that is formamide and water), using, however, ammonium acetate instead of ammonium formate in order to verify whether the procedure can be broadened to other salts. Again, both of the approaches succeeded in NH_4VO_3 preparation (see XRD results, Figure 1), and again they lead to different morphologies. When the reaction was carried out in formamide, using ammonium acetate as an ammonium cations source (AA/F sample), conglomerated crystals of elongated shape were prepared, as can be seen in Figure 4c. Their average length was between 0.3 µm and 0.7 µm, width: 0.1–0.4 µm, and thickness: 0.1–0.2 µm. In the case of the reaction that was conducted in water, the casketoidal shape of crystals was also observed, however the crystals were agglomerated (Figure 4d). They were 3–10 µm long, 1.5–2 µm wide, and 0.4–0.8 µm thick.

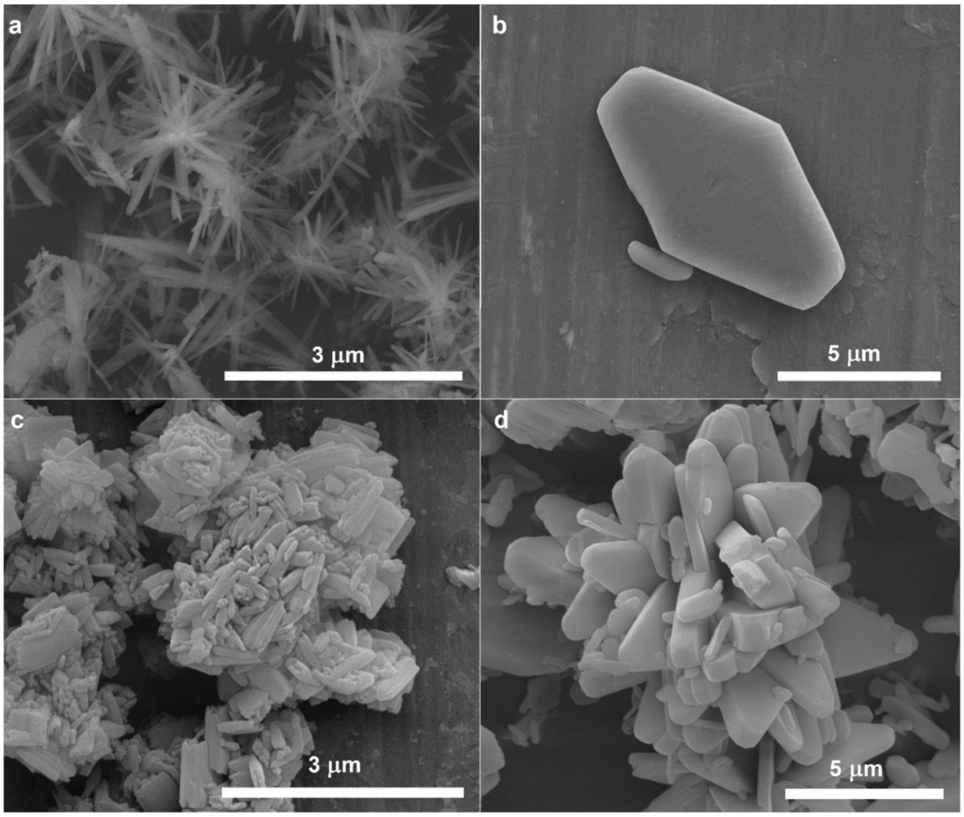

Figure 4. Scanning electron microscope (SEM) images of (**a**) AF/F; (**b**) AF/W; (**c**) AA/F and (**d**) AA/W.

The SEM images clearly show that the morphology of the end product can be nicely tuned by changing the type of ammonium salt and the solvent. It can be concluded that the used solvent affected crystal shapes and their size was more salt-type dependent. Moreover, the use of ammonium acetate resulted in more agglomerated samples. Additionally, mixtures of the solvents (water and formamide) and mixture of the salts (ammonium acetate and formate) were used, respectively (Supplementary Materials, Figures S3–S6). The SEM images (Figure 4a,c, Supplementary Materials, Figures S3d–f and S5) demonstrated that formamide, regardless of the salt type used, caused the delamination of starting oxide and enhanced the formation of elongated structures. Formamide was previously reported to be an effective solvent for V_2O_5 liquid exfoliation. Analyzing the SEM images, it can be stated that the intercalation of formamide molecules into V_2O_5 is the first step in the proposed synthesis. In Figure S3d, it can be clearly seen that the monolith of V_2O_5 flakes off, which results in the detachment of thin elongated shavings. Simultaneously, ammonium cations are dragged into the vanadium-oxide layers by means of the formate anions, forming ammonium metavanadate nanorods. Figure 5 presents the scheme of the process.

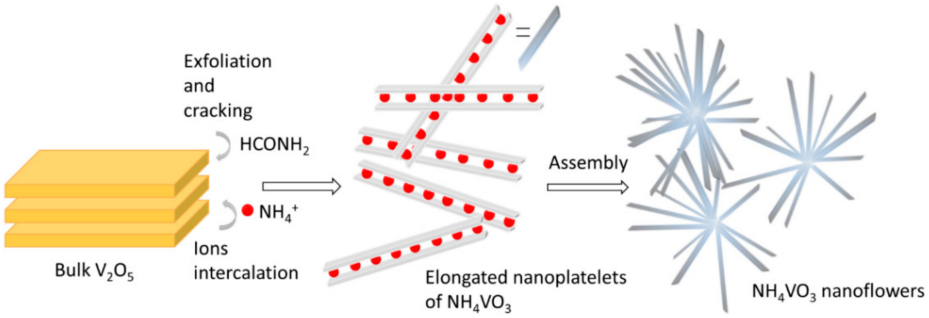

Figure 5. Scheme of proposed mechanism of NH_4VO_3nanoflowers formation.

The observation of initial solutions that were prepared in formamide and water supports the mechanism described above. If the precursor V_2O_5 was added into the solution of organic salt in formamide, the yellow slurry was formed, which, in time, changed color to white. The yellow color due to V_2O_5 disappeared, as solid vanadium oxide underwent delamination and ammonium ion intercalation to produce white ammonium metavanadates crystals. In contrast, when the V_2O_5 is added to the mixture of organic salt and water, the normally water-insoluble V_2O_5 creates a clear yellow solution. In aqueous solution, dioxovandium(V) ions VO_2^+ are formed, which undergo hydrolysis and dissociation, as follows, Equations (1) and (2):

$$VO_2^+ + H_2O \rightarrow VO(OH)_3aq + H^+ \quad (1)$$

$$VO(OH)_3aq \rightarrow VO_2(OH)_2^- + H^+ \quad (2)$$

Protonation of VO_2^+ is a limiting step of the reaction and it requires the presence of strong acids. This restriction is negligible if complexing ligands are involved. If carboxylates are present in the solution, the $RCOO^-$ might replace the OH^- to produce soluble complexes of structure $VO(RCOO)_3$ and$VO_2(RCOO)_2^-$, where R is CH_3- or H- in our case. The formation of surface complexes, followed by the dissolution of acetate- or formate-vanadium(V) species, makes the aqueous solution homogenous. A similar observation was reported for vanadium-oxalate complexes [25]. The next step is the precipitation of the ammonium metavanadate from the reaction mixture, which results in bigger crystals of different shapes, as compared to the delamination product.

3.2. Hydrothermal Synthesis of Higher Ammonium Vanadates from NH_4VO_3

As discussed before, the morphology and structure of the materials have great influence on their properties, which determine their potential usage. Ammonium metavanadate is a most frequently used precursor in the hydrothermal synthesis of other vanadates [26–28]. Therefore, hydrothermal synthesis was carried out in order to investigate an effect of the precursor morphology on the final product, while using commercial NH_4VO_3 and sample AF/F. Figure S7 presents the SEM image of commercial NH_4VO_3. Two aqueous solutions were prepared, keeping the same concentration of ammonium metavanadate (commercial or synthesized) and oxalic acid. Stirring the reaction mixtures before inserting them into autoclave revealed the first differences. The solution containing commercial NH_4VO_3 darkened to reddish-orange after one hour of stirring, whereas the solution of AF/F was pale yellow. After 72 h of hydrothermal reaction under 180 °C, the solids were separated and analyzed. The sample that was obtained from commercial NH_4VO_3 was denoted as HydroSigma and the latter one was denoted as HydroAF/F.

The XRD results disclosed that synthesized material is a mixture of $(NH_4)V_4O_{10}{\cdot}H_2O$ (JCPDS no. 00-031-0075) and $(NH_4)_{0.76}V_4O_{10}$ (JCPDS no. 00-027-1019). As displayed in Figure 6a, diffractograms match well with the references, with the exclusion of the first peak of HydroSigma. Shifting of the first peak is well-known in the case of hydrated ammonium vanadates and is attributed to the water intercalation [12].

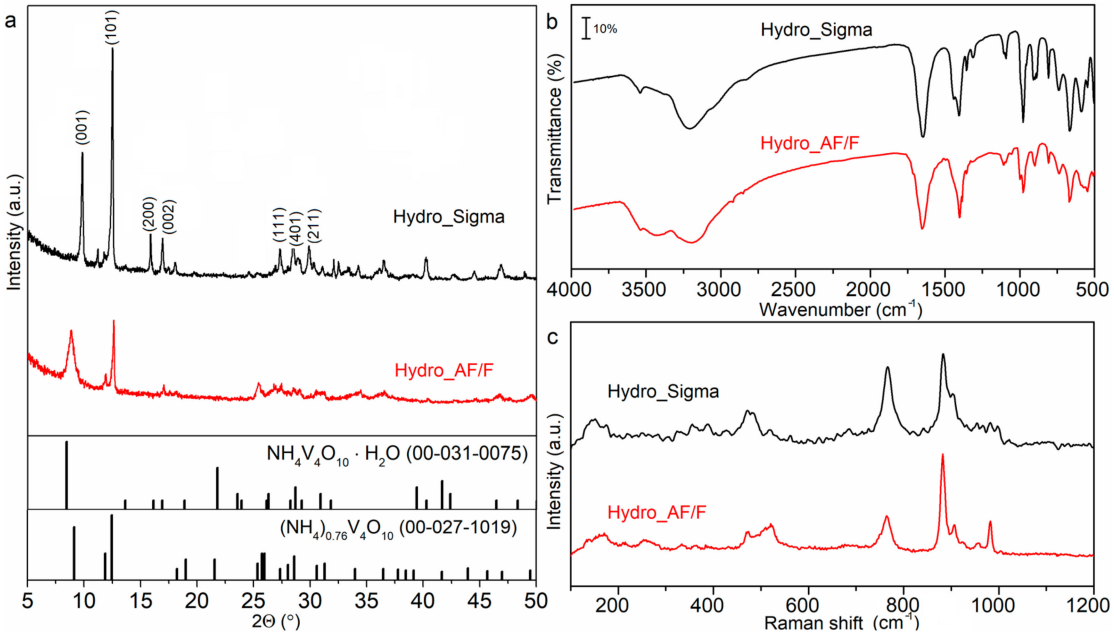

Figure 6. Structural analysis results: (**a**) XRD patterns of samples HydroSigma and HydroAF/F; (**b**) FTIR spectra of samples HydroSigma and HydroAF/F and (**c**) Raman spectra of samples HydroSigma and HydroAF/F.

By comparing the XRD patterns for both samples, it can be seen that the diffraction peaks of HydroAF/F are wider and less intense, which is typical for nanomaterials. Moreover, the average crystallite size of samples was calculated from the first diffraction peak while using the Scherrer equation, with the Sherrer constant of 0.9. As expected, the calculated average crystallite sizes are much smaller for HydroAF/F (14 nm) than for HydroSigma (150 nm), which is in accordance with SEM results (Figure 7). Analogously to the previous studies, FTIR and Raman spectroscopy measurements were carried out. In Figure 6b, the FTIR spectra of both samples are presented. Broad band centered at 3200 cm^{-1} and sharp band at 1412 cm^{-1}, referring to NH_4^+ vibrations are observed for both samples. Characteristic for vanadium compounds bands are visible in the range of 1000–600 cm^{-1}. The presence of crystalline water is revealed as a small band at 3540 cm^{-1} and strong band at 1645 cm^{-1}. When comparing the intensities of V=O stretching band at ~1000 cm^{-1} with band of H_2O stretching at 1645 cm^{-1} in two analyzed samples, it can be concluded that HydroAF/F contains more water. It is in agreement with XRD results, which showed that the percentage contribution of $(NH_4)V_4O_{10}{\cdot}H_2O$ was higher in the HydroAF/F sample, as compared to HydroSigma. Raman spectra revealed further differences. Figure 6c depicts the normalized Raman spectra. The main bands in HydroAF/F and HydroSigma spectra are positioned at 990, 880, 760, and 520 cm^{-1} and they correspond to VO_2 symmetrical and asymmetrical vibrations and V-O-V asymmetric and symmetric stretching. Several bands of low intensity can be seen in the range of 150–500 cm^{-1}, referring to VO_2 bending and NH_4^+ stretching. The HydroSigma spectrum is more affected by the presence of non-stoichiometric phase, as the overlapping or quenching of some bands is observed. Moreover, the signals intensities were much lower in the case of Hydro Sigma sample. Neither, $(NH_4)V_4O_{10}{\cdot}H_2O$ nor $(NH_4)_{0.76}V_4O_{10}$ Raman spectrum has been reported so far.

Figure 7 presents the SEM images of the manufactured materials. The morphological differences can be clearly seen. The sample HydroSigma is composed of uneven, differently shaped tiles with rounded edges. In the case of HydroAF/F thin, jagged flakes were created, assembling into porous structure. The time and temperature of the reaction were chosen based on the previously published papers. The reaction that was conducted within 72 h in 180 °C was found to be the most frequently used in the literature [26–29]. However, the influence of the precursor morphology on the final product has not been thoroughly studied. Our results proved that this factor cannot be neglected.

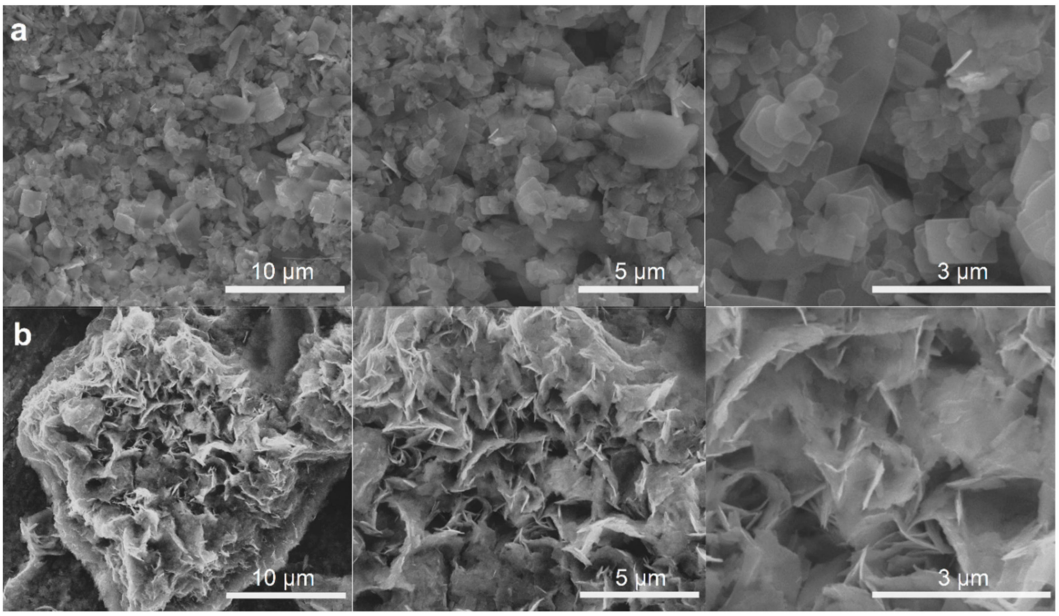

Figure 7. SEM images of (**a**) HydroSigma sample and (**b**) HydroAF/F sample with different magnifications.

In summary, there are many methods for producing ammonium vanadium compounds; however, regardless of the technique, numerous synthesis parameters must be considered. In the production of nanomaterials, the precursor morphology is important, as it strongly affects the type and the properties of the final product.

4. Conclusions

A novel method of ammonium metavanadate synthesis was presented. The NH_4VO_3 was successfully obtained from V_2O_5, while using organic ammonium salt and formamide or water as a solvent. Diffractometry, Raman, and FTIR spectroscopy and SEM imaging analyzed all of the materials. Depending on the reaction parameters, differently sized and shaped structures were obtained. Micro- and nanocrystals were manufactured. Micro- and nanocrystalline NH_4VO_3 served as a precursor in hydrothermal reaction for higher ammonium vanadates synthesis. A mixture of $(NH_4)V_4O_{10}{\cdot}H_2O$ and $(NH_4)_{0.76}V_4O_{10}$ was obtained in both cases, however the contribution of each phase was different for the samples that were obtained from different precursor. The morphology was also strongly affected by the type of the precursor used.

Supplementary Materials: (FTIR, Raman, SEM of NH_4VO_3) is available in the online version of this article at http://www.mdpi.com/1996-1944/12/20/3446/s1, Figure S1: FTIR spectrum of ammonium metavanadate, Figure S2: Raman spectrum of ammonium metavanadate, Figure S3: SEM images presenting the structure of V_2O_5 used as a precursor (a and b) and intermediates formed in the reaction of V_2O_5 with ammonium formate in formamide (c and d), leading to flower-like nanostructural crystals of NH_4VO_3 (e and f), Figure S4: SEM images presenting structures of NH_4VO_3 obtained from V_2O_5 in water using ammonium formate (a and b), ammonium acetate (c and d), and equimolar mixture of ammonium formate and ammonium acetate (e and f), Figure S5: SEM images presenting structures of NH_4VO_3 obtained from V_2O_5 in formamide using ammonium formate (a), ammonium acetate (b), and equimolar mixture of ammonium formate and ammonium acetate (c and d), Figure S6: SEM images presenting structures of NH_4VO_3 obtained in the reaction of V_2O_5 and ammonium formate carried out in the 1:1 (*v*/*v*) mixture of water and formamide, Figure S7: SEM image of commercial NH_4VO_3 used in a hydrothermal synthesis.

Author Contributions: Conceptualization, M.P.-W., investigation, M.P.-W, M.N., B.K. and K.S.; writing—original draft preparation, M.P.-W., M.N. and K.S; visualization M.N.; supervision M.P.-W.

Funding: This research was funded by National Science Centre, Poland, grant number DEC-2017/01/X/ST5/01415 and 2016/23/D/ST5/02800. The APC was funded by National Science Centre, Poland, grant number 2016/23/D/ST5/02800.

Conflicts of Interest: The authors declare no conflict of interest.

References

1. Liu, Y.; Xu, M.; Shen, B.; Xia, Z.; Li, Y.; Wu, Y.; Li, Q. Facile synthesis of mesoporous $NH_4V_4O_{10}$ nanoflowers with high performance as cathode material for lithium battery. *J. Mater. Sci.* **2018**, *53*, 2045–2053. [CrossRef]
2. Mai, L.Q.; Lao, C.S.; Hu, B.; Zhou, J.; Qi, Y.Y.; Chen, W.; Gu, E.D.; Wang, Z.L. Synthesis and electrical transport of single-crystal $NH_4V_3O_8$ nanobelts. *J. Phys. Chem. B* **2006**, *110*, 18138–18141. [CrossRef] [PubMed]
3. Chen, Q.; Xia, Q.; Xu, Y.; Wang, P.; Tan, Q. $NH_4V_4O_{10}$ micro-flowers as cathode material for high performance hybrid magnesium-lithium-ion batteries. *Mater. Lett.* **2019**, *247*, 178–181. [CrossRef]
4. Wang, H.; Ren, Y.; Wang, W.; Huang, X.; Huang, K.; Wang, Y.; Liu, S. $NH_4V_3O_8$ nanorod as a high performance cathode material for rechargeable Li-ion batteries. *J. Power Sources* **2012**, *199*, 315–321. [CrossRef]
5. Ma, Y.; Ji, S.; Zhou, H.; Zhang, S.; Li, R.; Zhu, J.; Li, W.; Guo, H.; Jin, P. Synthesis of novel ammonium vanadium bronze $(NH_4)_{0.6}V_2O_5$ and its application in Li-ion battery. *RSC Adv.* **2015**, *5*, 90888–90894. [CrossRef]
6. Cheng, Y.; Huang, J.; Li, J.; Cao, L.; Xu, Z.; Wu, J.; Cao, S.; Hu, H. Structure-controlled synthesis and electrochemical properties of $NH_4V_3O_8$ as cathode material for Lithium ion batteries. *Electrochim. Acta* **2016**, *212*, 217–224. [CrossRef]
7. Tian, X.; Xu, X.; He, L.; Wei, Q.; Yan, M.; Xu, L.; Zhao, Y.; Yang, C.; Mai, L. Ultrathin pre-lithiated V_6O_{13} nanosheet cathodes with enhanced electrical transport and cyclability. *J. Power Sources* **2014**, *255*, 235–241. [CrossRef]
8. Vo, TN.; Kim, H.; Hur, J.; Choi, W.; Kim, T. Surfactant-assisted ammonium vanadium oxide as a superior cathode for calcium-ion batteries. *J. Mater. Chem. A* **2018**, *6*, 22645–22654. [CrossRef]
9. Esparcia, E.; Chae, M.; Ocon, J.; Hong, S. Ammonium Vanadium Bronze ($NH_4V_4O_{10}$) as a High-Capacity Cathode Material for Nonaqueous Magnesium-Ion Batteries. *Chem. Mater.* **2018**, *30*, 3690–3696. [CrossRef]
10. Wei, T.; Li, Q.; Yang, G.; Wang, C. Highly reversible and long-life cycling aqueous zinc-ion battery based on ultrathin $(NH_4)_2V_{10}O_{25}{\cdot}8H_2O$ nanobelt. *J. Mater. Chem. A* **2018**, *6*, 20402–20410. [CrossRef]
11. Yang, G.; Wei, T.; Wang, C. Self-Healing Lamellar Structure Boosts Highly Stable Zinc-Storage Property of Bilayered Vanadium Oxides. *ACS Appl. Mater. Interfaces* **2018**, *1041*, 35079–35089. [CrossRef] [PubMed]
12. Lai, J.; Zhu, H.; Zhu, X.; Koritala, H.; Wang, Y. Interlayer-Expanded V_6O_{13} n H_2O Architecture Constructed for an Advanced Rechargeable Aqueous Zinc-Ion Battery. *ACS Appl. Energy Mater.* **2019**, *2*, 1988–1996. [CrossRef]
13. Sonar, S.S.; Kategaonkar, A.H.; Ware, M.N.; Gill, C.H.; Shingate, B.B.; Shingare, M.S. Ammonium metavanadate: An effective catalyst for synthesis of α hydroxyphosphonates. *Arkivoc* **2009**, *2*, 138–148.
14. Si, Y.; Xiong, Z.; Zheng, X.; Li, M.; Yang, Q. Improving the Anti-Corrosion Ability of Anodization Film of AZ31B Magnesium Alloy by Addition of NH_4VO_3 in the Electrolyte. *Int. J. Electrochem. Sci.* **2016**, *11*, 3261–3268. [CrossRef]
15. Brauer, G. *Handbook of Preparative Inorganic Chemistry*, 2nd ed.; Brauer, G., Ed.; Academic Press Inc.: New York, NY, USA, 1965.
16. Du, G.; Sun, Z.; Xian, Y.; Jing, H.; Chen, H.; Yin, D. The nucleation kinetics of ammonium metavanadate precipitated by ammonium chloride. *J. Cryst. Growth* **2016**, *441*, 117–123. [CrossRef]
17. Mandhane, P.G.; Joshi, R.S.; Ghawalkar, A.R.; Jadhav, G.R.; Gill, C.H. Ammonium metavanadate: A mild and efficient catalyst for the synthesis of coumarins. *Bull. Korean Chem. Soc.* **2009**, *30*, 2969–2972. [CrossRef]
18. Jadhav, G.R.; Shaikh, M.U.; Kale, R.P.; Gill, C.H. Ammonium metavanadate: A novel catalyst for synthesis of 2-substituted benzimidazole derivatives. *Chin. Chem. Lett.* **2009**, *20*, 292–295. [CrossRef]
19. Niralwad, K.S.; Shingate, B.B.; Shingare, M.S. Microwave-assisted one-pot synthesis of octahydroquinazolinone derivatives using ammonium metavanadate under solvent-free condition. *Tetrahedron Lett.* **2010**, *51*, 3616–3618. [CrossRef]
20. Wu, D.; Wang, C.; Chao, Y.; He, P.; Ma, J. Porous bowl-shaped VS_2 nanosheets/graphene composite for high-rate lithium-ion storage. *J. Eng. Chem.* **2020**, *43*, 24–32. [CrossRef]
21. Xie, X.; Mao, M.; Qi, S.; Ma, J. ReS_2-Based electrode materials for alkali-metal ion batteries. *Cryst. Eng. Commun.* **2019**, *21*, 3755–3769. [CrossRef]
22. Rui, X.; Lu, Z.; Yu, H.; Yang, D.; Hng, H.H.; Lim, T.M.; Yan, Q. Ultrathin V_2O_5 nanosheet cathodes: Realizing ultrafast reversible lithium storage. *Nanoscale* **2013**, *5*, 556–560. [CrossRef] [PubMed]

23. Heyns, A.M.; Venter, M.W.; Range, K.J. The vibrational spectra of NH_4VO_3 at elevated temperatures and pressures. *Z. Naturforsch. B* **1987**, *42*, 843–852. [CrossRef]
24. Onodera, S.; Ikegami, Y. Infrared and Raman spectra of ammonium, potassium, rubidium, and cesium metavanadates. *Inorg. Chem.* **1980**, *19*, 615–618. [CrossRef]
25. Bruyère, V.I.; Morando, P.J.; Blesa, M.A. The dissolution of vanadium pentoxide in aqueous solutions of oxalic and mineral acids. *J. Colloid Interface Sci.* **1999**, *209*, 207–214. [CrossRef] [PubMed]
26. Zhang, K.F.; Zhang, G.Q.; Liu, X.; Su, Z.; Li, H.L. Large scale hydrothermal synthesis and electrochemistry of ammonium vanadium bronze nanobelts. *J. Power Sources* **2006**, *157*, 528–532. [CrossRef]
27. Wang, N.; Chen, W.; Mai, L.; Dai, Y. Selected-control hydrothermal synthesis and formation mechanism of 1D ammonium vanadate. *J. Solid State Chem.* **2008**, *181*, 652–657. [CrossRef]
28. Vernardou, D.; Apostolopoulou, M.; Louloudakis, D.; Katsarakis, N.; Koudoumas, E. Hydrothermal growth and characterization of shape-controlled $NH_4V_3O_8$. *New J. Chem.* **2014**, *38*, 2098–2104. [CrossRef]
29. Kou, L.; Cao, L.; Huang, J.; Yang, J.; Wang, Y. Facile synthesis of $NH_4V_3O_8$ nanoflowers as advanced cathodes for high performance of lithium ion battery. *J. Mater. Sci. Mater. Electron.* **2018**, *29*, 4830–4834. [CrossRef]

materials

MDPI

Article

Tailoring the Size and Shape—New Path for Ammonium Metavanadate Synthesis

Marta Prześniak-Welenc *, Małgorzata Nadolska, Barbara Kościelska and Kamila Sadowska

Faculty of Applied Physics and Mathematics, Gdansk University of Technology, Narutowicza 11/12, 80-233 Gdansk, Poland; malgorzata.nadolska@pg.edu.pl (M.N.); barkosci@pg.edu.pl (B.K.); kamsadow@pg.edu.pl (K.S.)

* Correspondence: marta.welenc@pg.edu.pl; Tel: +48 583486606

Received: 23 September 2019; Accepted: 17 October 2019; Published: 21 October 2019

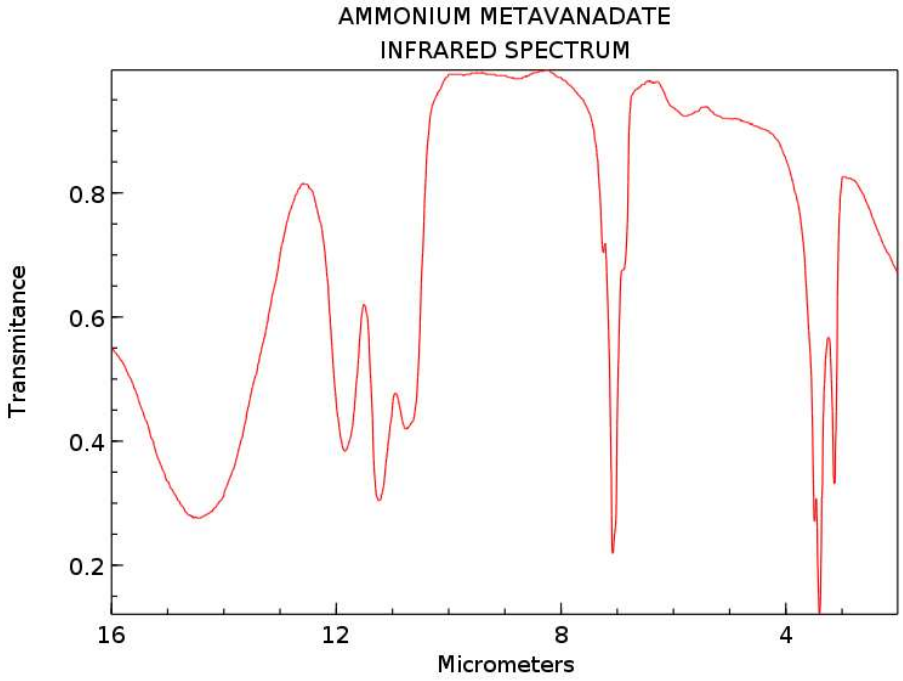

Figure S1. FTIR spectrum of ammonium metavanadate [1].

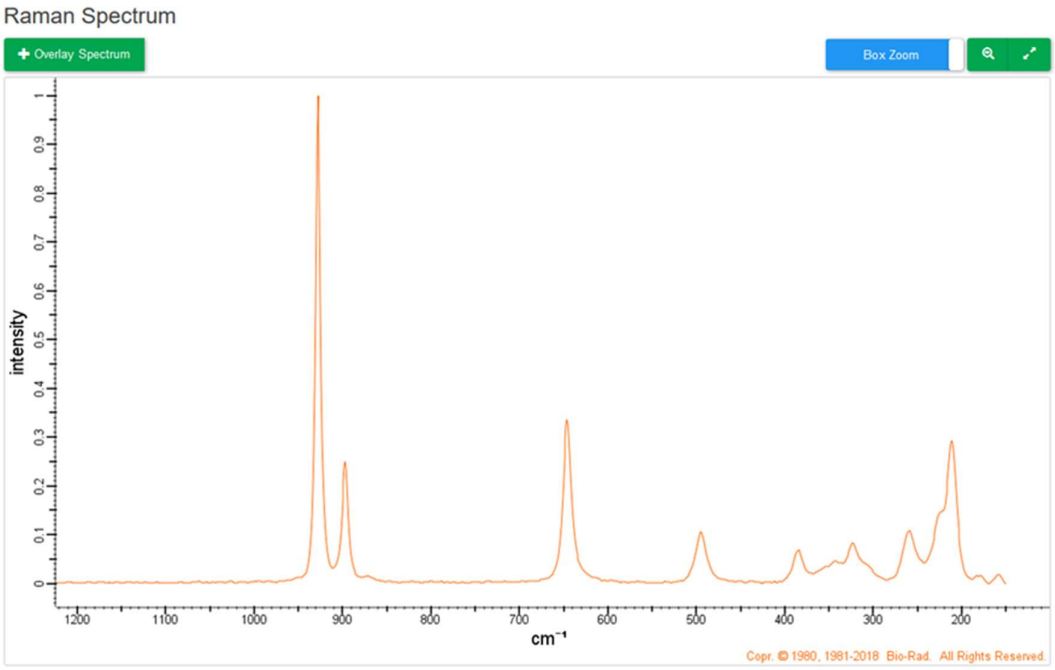

Figure S2. Raman spectrum of ammonium metavanadate.

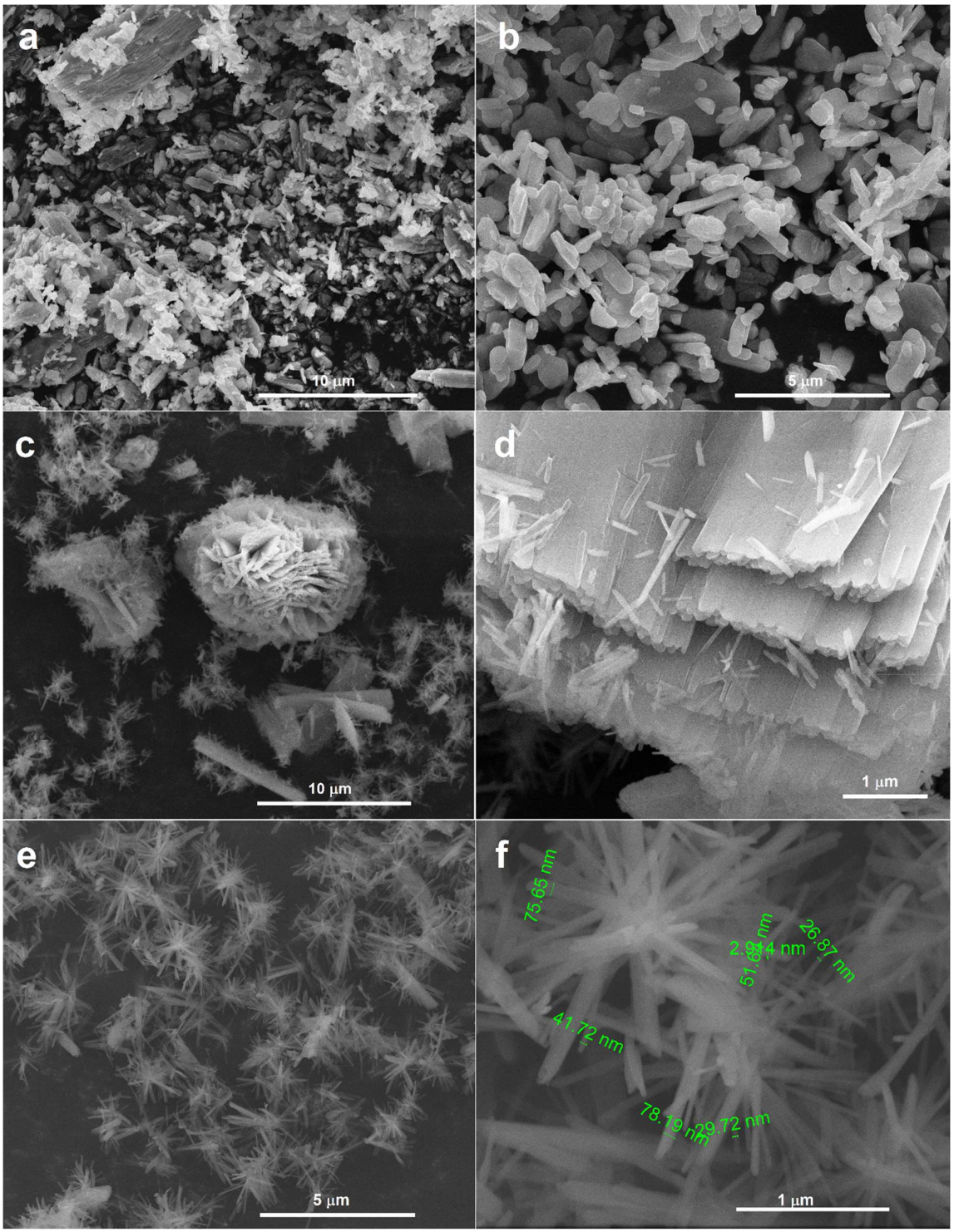

Figure S3. SEM images presenting the structure of V_2O_5 used as a precursor (**a**,**b**) and intermediates formed in the reaction of V_2O_5 with ammonium formate in formamide (**c**,**d**), leading to flower-like nanostructural crystals of NH_4VO_3 (**e**,**f**).

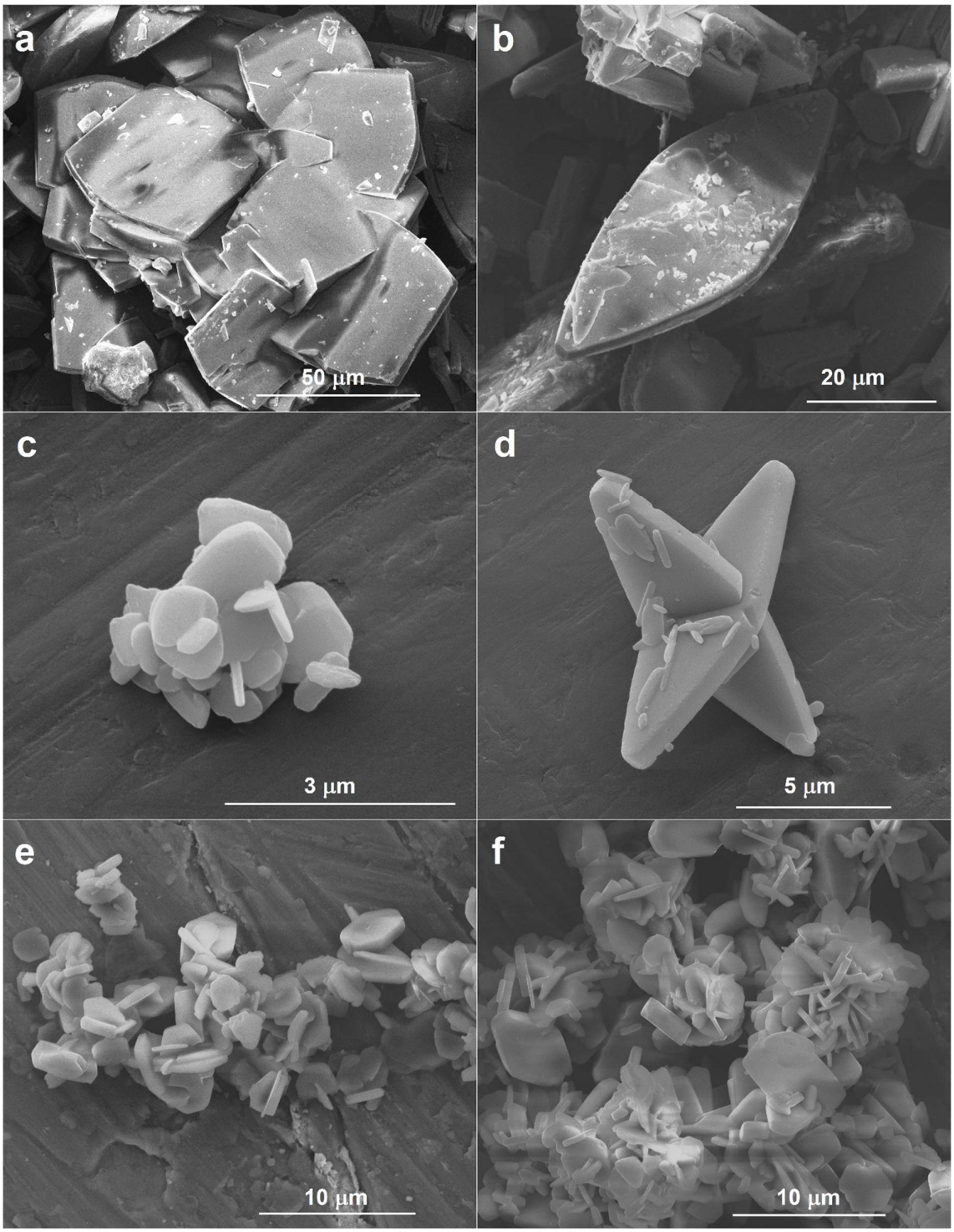

Figure S4. SEM images presenting structures of NH_4VO_3 obtained from V_2O_5 in water using ammonium formate (**a**,**b**), ammonium acetate (**c**,**d**), and equimolar mixture of ammonium formate and ammonium acetate (**e**,**f**).

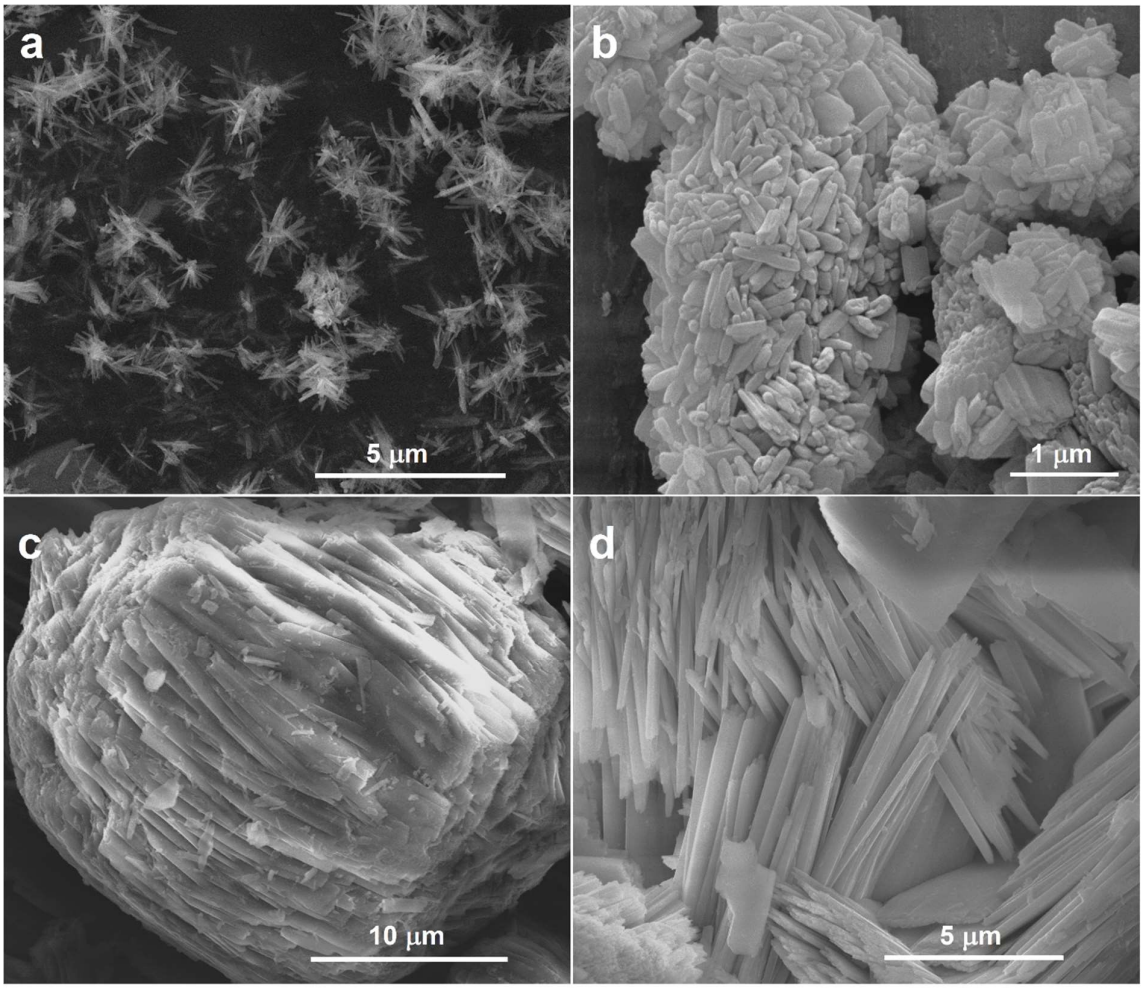

Figure S5. SEM images presenting structures of NH_4VO_3 obtained from V_2O_5 in formamide using ammonium formate (**a**), ammonium acetate (**b**), and equimolar mixture of ammonium formate and ammonium acetate (**c**,**d**).

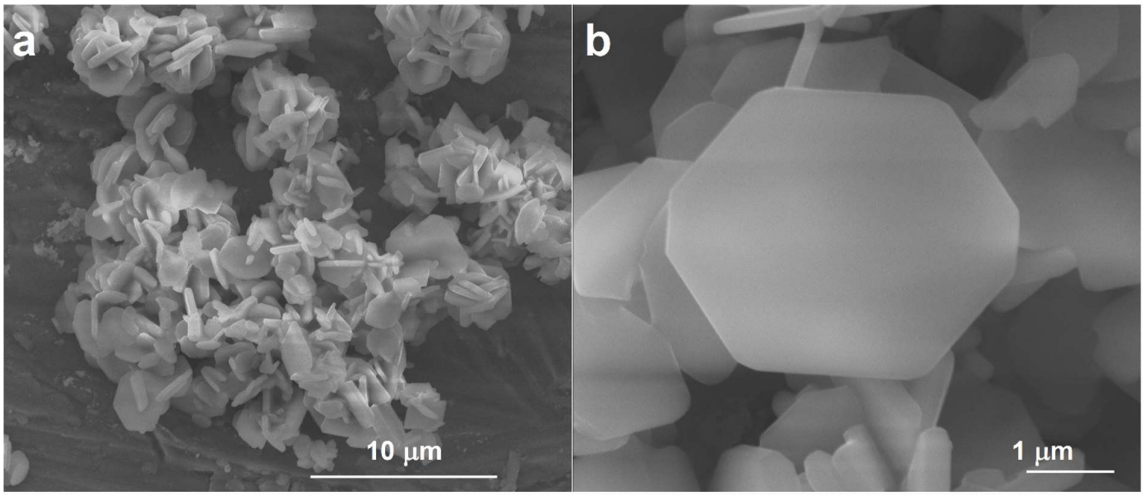

Figure S6. SEM images presenting structures of NH_4VO_3 obtained in the reaction of V_2O_5 and ammonium formate carried out in the 1:1 (*v*/*v*) mixture of water and formamide.

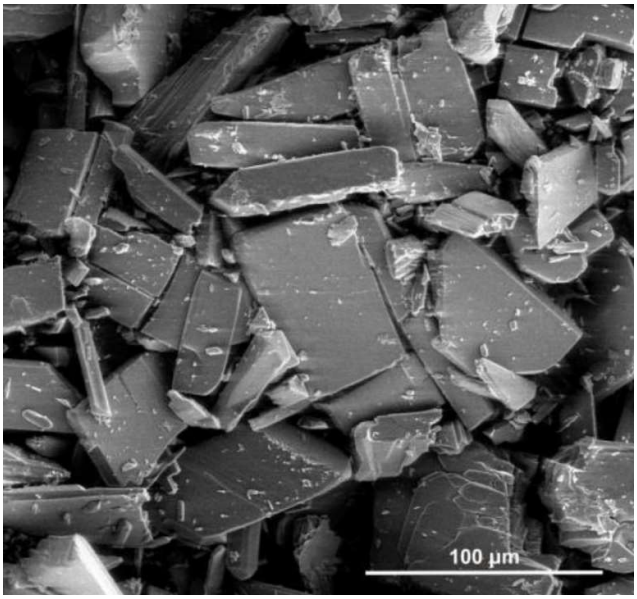

Figure S7. SEM image of commercial NH_4VO_3 used in a hydrothermal synthesis.

References:

1. NIST Chemistry WebBook; Available online: https://webbook.nist.gov/chemistry (accessed on 27 July 2019).

3.2. [A2] Pressure in charge. Neglected parameter in hydrothermal synthesis turns out to be crucial for electrochemical properties of ammonium vanadates.

3.2.1. Research background and objectives

A hydrothermal method is a well-known technique and is widely used for the synthesis of various types of materials, such as metal oxides, carbides, sulfides, or nitrides [140,141]. It is also the most popular method for the synthesis of vanadates. In recent years, much attention has been given to the synthesis of ammonium vanadates, which are promising electrode materials for rechargeable ion batteries. To date, dozens of protocols for the synthesis of ammonium vanadates have been reported, which result in various stoichiometries (more than 10 compounds in hydrated/non-hydrated form have been described in the literature) and different morphologies (from thin nanowires through 3D nanoflowers up to micrometric platelets) [77]. It is known that the morphology and structure of materials have a great influence on their electrochemical properties. Recently, many efforts have been made to obtain single-phase ammonium vanadate nanostructures.

As discussed in the introduction, both the chemical composition and morphology of ammonium vanadates can be tailored by controlling the hydrothermal synthesis parameters. Despite extensive research into synthesis protocols involving various conditions, such as reaction time, temperature, or precursor solution composition, there is a noticeable lack of studies on the effect of pressure on the hydrothermal synthesis of ammonium vanadates. On the other hand, in additon to temperature, pressure is one of the most essential physical parameters needed for hydrothermal conditions, and it plays a pivotal role in the synthesis process of various materials. For example, pressure generally increases the solubility of reactants in the solvent. The improved solubility leads to more homogenous solutions, assuring a comparable environment in the whole reaction mixture, which is essential for producing materials with consistent composition and properties. Elevated pressure may accelerate nucleation, facilitating the formation of smaller particles. It also influences the growth process and thus the morphology of the final product. Additionally, pressure can impact the crystal structure and promote the formation of specific phases or polymorphs. It has also been reported that high-pressure hydrothermal conditions favor the incorporation of water molecules into the crystal lattice and the synthesis of hydrate compounds.

All the abovementioned factors served as the driving force behind the studies presented in the publication [A2]. It was proposed to evaluate the effect of the initial pressure on the hydrothermal synthesis of ammonium vanadates. The hypothesis is that the presence of initial pressure will promote the formation of ammonium vanadates with a hydrated structure and nanometric particle sizes. Additionally, the initial pressure should have a beneficial effect on sample homogeneity, including phase purity and narrow particle size distribution. Consequently, the resulting ammonium vanadates are expected to exhibit improved electrochemical properties.

The aim of the study was to determine the influence of the initial hydrothermal synthesis pressure on the ammonium vanadate phase and morphology. Physicochemical characterization of the synthesized samples included XRD, FTIR, XPS, TGA-MS, SEM, and TEM. Moreover, samples obtained without and with the highest studied pressure (50 bar) were tested as cathode materials for non-aqueous LIBs.

3.2.2. Summary of main results

Ammonium vanadates were obtained via a typical hydrothermal method carried out in an autoclave. To study the pressure effect, the reaction was carried out in a pre-pressurized autoclave under 5, 25, and 50 bar (versus ambient pressure) and without initial pressure. The needed initial pressure was adjusted by filling the autoclave with N_2. All other parameters (i.e., temperature, time, volume, reagent concentration) were kept constant and were chosen according to the literature review and preliminary studies.

XRD analysis revealed that the obtained ammonium vanadates differed in crystallographic structure and phase composition. The sample obtained without initial pressure contained two phases, $(NH_4)_2V_{10}O_{25}\cdot 8H_2O$ and $(NH_4)_2V_6O_{16}$, with the dominance of the first phase characterized by much more intense reflexes. Further analysis indicated that the contribution of the $(NH_4)_2V_{10}O_{25}\cdot 8H_2O$ phase increased with increasing initial pressure, and finally, the sample obtained with the highest studied pressure (50 bar) was single-phase. The existence of two various phases was also confirmed by FTIR and TG analysis. In the FTIR spectra, splitting of bands arising from V-O bond vibrations was observed. This indicates the presence of different structural units, varied in geometries and bond lengths: VO_5 square pyramids in $(NH_4)_2V_{10}O_{25}\cdot 8H_2O$ and VO_6 octahedrons in $(NH_4)_2V_6O_{16}$. Thermogravimetric analysis coupled with mass spectrometry allowed us to estimate the crystalline water content, which was two times higher for the sample obtained with the highest pressure compared to the sample obtained without initial pressure. Considering the stoichiometry of the obtained phases, the mean valence of vanadium is equal to 5.0 for $(NH_4)_2V_6O_{16}$ and 4.8 for $(NH_4)_2V_{10}O_{25}\cdot 8H_2O$. Additional XPS analysis (see Figure 8) revealed that in all samples, vanadium existed on the surface in both the V^{4+} and V^{5+} valence states. The relative share of vanadium V^{4+} in the samples varied from ca. 30-45% and increased with increasing initial pressure.

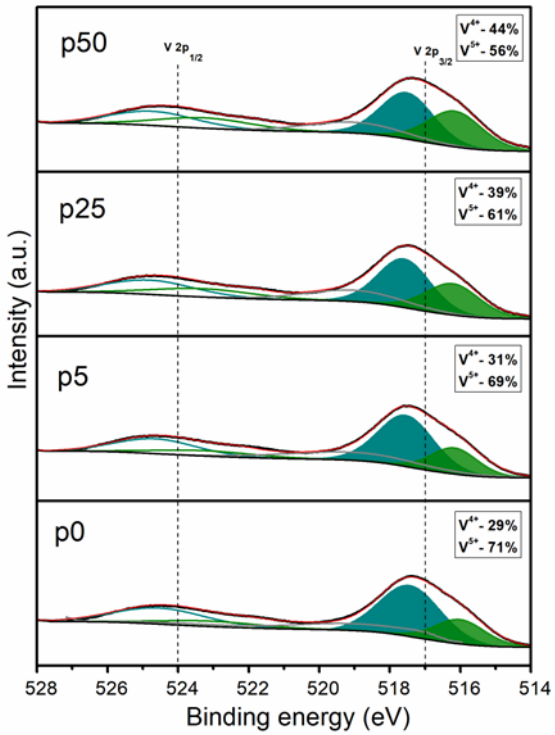

Figure 8. High-resolution XPS spectra of the V2p regions for samples obtained without applying initial pressure (p0) and with the application of 5, 25, and 50 bar (p5, p25, p50, respectively. XPS measurements were performed with Omicron NanoTechnology spectrometer with Mg Kα as an excitation source. The binding energies were corrected using the background C1s (285.0 eV) line as a reference. XPS spectra were analysed with Casa-XPS software using Shirley background subtraction and Gaussian-Lorentzian curve as a fitting algorithm.

Finally, the electrochemical properties of samples obtained without (p0) and with the highest studied pressure (50 bars, sample named p50) were compared as cathode materials for LIBs. The electrodes were tested in the potential range from 2.0 V to 4.0 V and in sequence, which involved six cycles at varying current rates (50 mAg^{-1}, 100 mAg^{-1}, 150 mAg^{-1}, 200 mAg^{-1}, 150 mAg^{-1}, 100 mAg^{-1}, and 50 mAg^{-1}). At a current density of 50 mAg^{-1}, the material obtained without initial pressure exhibited an initial discharge capacity of 167 $mAhg^{-1}$, while the material obtained with 50 bars demonstrated a higher capacity of 261 $mAhg^{-1}$. The final capacities decreased to 44 $mAhg^{-1}$ and 229 $mAhg^{-1}$, resulting in capacity retentions of 26% and 87%, respectively. Upon increasing the current density to 200 mAg^{-1}, the discharge capacity dropped to only 39 $mAhg^{-1}$ for the sample obtained without initial pressure, whereas it maintained a high level of 191 $mAhg^{-1}$ for the sample obtained with 50 bar.

In summary, the obtained results demonstrate that the initial pressure of hydrothermal synthesis affects both the morphology and the structure of ammonium vanadates. The conducted studies underline the positive impact of the initial pressure on the homogeneity of the samples. As expected, higher pressure leads to the synthesis of thinner and more uniform structures of ammonium vanadates. Additionally, initial pressure facilitates the formation of three-dimensional flower-like architectures. It was also found that the initial pressure is a crucial factor for the final phase composition of the synthesized ammonium vanadates. High pressure was necessary to obtain a single-phase sample: $(NH_4)_2V_{10}O_{25}\cdot 8H_2O$. Furthermore, XPS analysis

indicated a relatively high content of V^{4+} species on the surface of all samples. Such V^{4+} surface species have been proven to be beneficial for the electrochemical properties of vanadates, and their presence depends on several factors, including not only material composition but also synthesis methods. One of the common approaches to introduce V^{4+} species on the surface of vanadates includes the incorporation of a reducing agent during the synthesis process [142,143] or post-treatment (e.g., annealing under different atmospheres [144,145], plasma modification [146]). In the described studies, oxalic acid, which is a mild reducing agent, was added during the synthesis of ammonium vanadates. Furthermore, higher pressure results in a higher content of V^{4+} surface species, which was consistent with XRD analysis and the predominance of the $(NH_4)_2V_{10}O_{25}\cdot 8H_2O$ phase. This indicates that the initial pressure promotes the reduction of V^{5+} to V^{4+} and the synthesis of mixed valence ammonium vanadates. Further electrochemical measurements revealed substantial differences between samples obtained under different pressures. As described, the p50 material was a pure $(NH_4)_2V_{10}O_{25}\cdot 8H_2O$ phase, while p0 was composed of $(NH_4)_2V_{10}O_{25}\cdot 8H_2O$ and $(NH_4)_2V_6O_{16}$. The former phase has not been previously investigated as a cathode material for LIBs, while the latter is known to be suitable for such applications. Interestingly, p50 delivered good specific capacity with relatively high-capacity retention, demonstrating that the structure of $(NH_4)_2V_{10}O_{25}\cdot 8H_2O$ enables reversible lithium-ion intercalation/deintercalation. In contrast, p0, composed of two phases, exhibited significantly lower capacity and degradation during cycling. Thus, it is suggested that in this case, the additional phase acts as a blocking agent for the lithium-ion insertion process. Such a phenomenon is known from the literature. The interfaces between different phases hinder the rapid diffusion of lithium ions. They can also promote undesirable side reactions. Generally, mixed-phase materials often show insufficient stability due to structural differences with varying degrees of volume expansion upon lithiation, which can lead to deformation, particle cracking, and loss of electrical contact.

The presented studies fill a gap regarding the influence of initial pressure on the hydrothermal synthesis of ammonium vanadates. The results reveal that the initial pressure is one of the key parameters in the synthesis, which affects both the morphology and phase of ammonium vanadates and ultimately determines their electrochemical properties. Publication [A2] also extends the current knowledge on the utilization of ammonium vanadates as electrode materials in metal-ion batteries. Herein, $(NH_4)_2V_{10}O_{25}\cdot 8H_2O$ was investigated for the first time as a cathode material for LIBs, and the results indicated its promising potential in such applications. The good electrochemical performance can be ascribed to the unique crystal structure of $(NH_4)_2V_{10}O_{25}\cdot 8H_2O$ (layered structure with large interlayer spacing, presence of NH_4^+ cations and H_2O molecules, which act as structural pillars), morphology of the obtained sample (flower-like microspheres built from nanobelts) and presence of V^{4+} species on the surface. The obtained results also highlight the necessity of utilizing pure-phase materials for efficient lithium-ion storage.

3.2.3. Full content of the article

Title: Pressure in charge. Neglected parameter in hydrothermal synthesis turns out to be crucial for electrochemical properties of ammonium vanadates

Authors: M. Prześniak-Welenc, M. Nadolska, A. Nowak, K. Sadowska

Journal: Electrochimica Acta, 2020, 339, 135919

Impact factor: 6.901 (2020)

Ministerial Points: 100 pkt

DOI: 10.1016/j.electacta.2020.135919

I contributed to this work by conceptualizing experiments under the supervision of dr Marta Prześniak-Welenc. In particular, based on the literature review, I proposed to study the effect of initial pressure on the hydrothermal synthesis of ammonium vanadates for the first time. I planned and carried out hydrothermal syntheses, participated in electrode preparation, characterized the obtained samples (XRD, FTIR, TGA) and discussed the results. I prepared the figures and the first version of the manuscript.

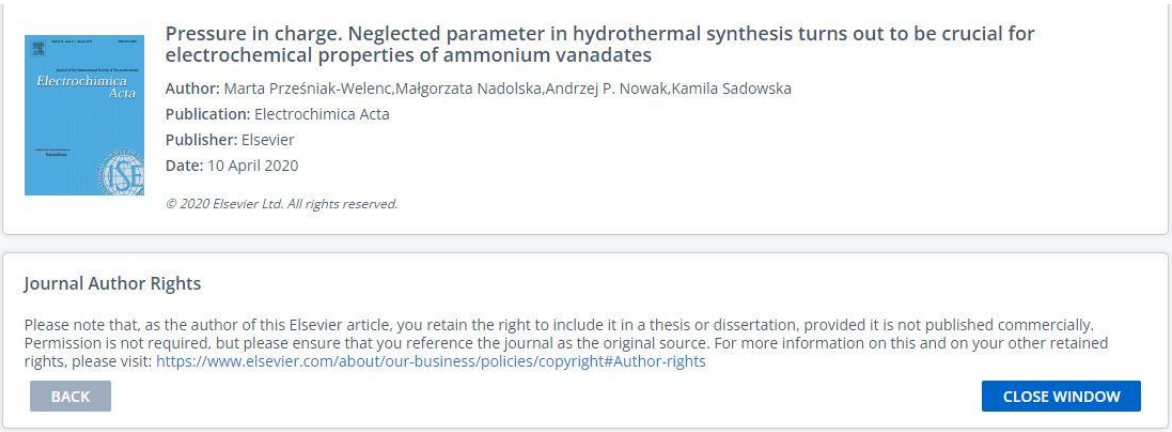

Electrochimica Acta 339 (2020) 135919

Contents lists available at ScienceDirect

Electrochimica Acta

journal homepage: www.elsevier.com/locate/electacta

Pressure in charge. Neglected parameter in hydrothermal synthesis turns out to be crucial for electrochemical properties of ammonium vanadates

Marta Prześniak-Welenc [a, *], Małgorzata Nadolska [a], Andrzej P. Nowak [b], Kamila Sadowska [a, 1]

[a] Faculty of Applied Physics and Mathematics, Gdansk University of Technology, Narutowicza St. 11/12, 80-233, Gdansk, Poland
[b] Faculty of Chemistry, Gdansk University of Technology, Narutowicza St. 11/12, 80-233, Gdansk, Poland

ARTICLE INFO

Article history:
Received 6 November 2019
Received in revised form
9 February 2020
Accepted 16 February 2020
Available online 17 February 2020

Keywords:
Ammonium vanadate
Solvothermal method
Electrochemical characterization
Li-ion battery

ABSTRACT

Ammonium vanadates are of great interest as they exhibit unusual electrical and sensory properties. $(NH_4)_2V_6O_{16}$ and $(NH_4)_2V_{10}O_{25}\cdot 8H_2O$ with various morphology were obtained in the hydrothermal synthesis under controlled temperature and pressure. It was shown, that the pure $(NH_4)_2V_{10}O_{25}\cdot 8H_2O$ was obtained under 50 bar of initial pressure, whereas lower pressure lead to the mixture of two compounds. The influence of the pressure was studied for the first time, and the results demonstrated its utmost importance. Moreover, the electrochemical performance of synthesized $(NH_4)_2V_{10}O_{25}\cdot 8H_2O$ was studied, revealing its excellent behavior as cathode material for Li-ion batteries. To the best of our knowledge, there is no information available on using this structure in such application.

1. Introduction

Ammonium vanadates are of great interest because of their structural diversity, rich chemistry and remarkable properties. Owing to the multivalence of vanadium, up to now, more than ten different forms with various stoichiometry have been investigated [1–9]. Moreover, ammonium vanadates are promising candidates for cathode material in lithium-ion batteries [10–14]. Some papers also report their usage as novel gas sensing material [15] or cathode material in multivalence-ion batteries [16–18]. The broad family of ammonium vanadates, with the general formula $(NH_4)_xV_yO_z$, are composed of vanadium oxide layers and NH_4^+ ions intercalated between them. The layered structure of vanadium oxides, with high theoretical charge storage capacity, can accommodate a large number of lithium ions. Furthermore, intercalated NH_4^+ ions increase the intrinsic conductivity and extend the interlayer spacing, improving the diffusion rate of lithium ions [19]. The embedded cations also stabilize the crystal structure (due to the presence of N–H···O hydrogen bonds), which is beneficial for the long-term cyclability of the electrode materials [20].

So far, many synthesis protocols have been reported leading to the formation of ammonium vanadates with diverse structures and morphologies [10,21–26]. It is well-known, that both the structure and morphology of materials have a significant influence on their properties and consequently on their further utilization. Therefore, many efforts have been undertaken to control these features, mainly in order to enhance the electrochemical properties of ammonium vanadates. For example, nanostructures with large active surface areas shorten diffusion pathways and provide high charge capacity [24,25]. Recently, Liu et al. have obtained uniform mesoporous $NH_4V_4O_{10}$ nanoflowers which exhibited high capacity (242.8 mA h/g at a current density of 200 mA/g) and a long life cycle (65% retention capacity after 200 cycles) [26]. Wang et al. showed that $NH_4V_3O_8$ with a flower-like morphology deliver a maximum discharge capacity of 365 mA h/g at 15 mA/g with 84% retention after 50 cycles [24]. In the literature, most syntheses are based on the facile hydrothermal method where an acidulated NH_4VO_3 solution is treated in a raised temperature (above 140 °C) in a closed system. By varying the reaction time and temperature, various nanomaterials, such as $NH_4V_3O_8$ nanoflowers [24], $NH_4V_4O_{10}$ nanobelts or $(NH_4)_{0.6}V_2O_5$ square bricks [4] were obtained. In

* Corresponding author.
E-mail address: marta.welenc@pg.edu.pl (M. Prześniak-Welenc).
[1] Present address: Nalecz Institute of Biocybernetics and Biomedical Engineering, Polish Academy of Sciences. Ks. Trojdena St. 4; 02–109 Warsaw, Poland.

https://doi.org/10.1016/j.electacta.2020.135919
0013-4686/

contrast, Zakharova et. al showed that these parameters affect only the size of the resulting particles - with increasing temperature and time particles decreased in size [27]. Indubitably, the acidity of the feed solution has a profound effect on the final hydrothermal product [28]. For instance, by changing the pH from 2.5 to 1.5 and then to 0.5, the obtained products were $NH_4V_4O_{10}$ nanobelts, $(NH_4)_2V_6O_{16}\cdot$ $1{,}5H_2O$ nanowires $(NH_4)_6V_{10}O_{28}\cdot 6H_2O$ nanobundles, respectively [6]. It should be noticed that the pH value of the solution can be adjusted by various chemical reagents (such as, oxalic acid [23–25,29,30], hydrochloric acid [6,22] and others [27,31,32]), which sometimes act also as forming agents. According to the literature, required structure growth can also be assisted by additional templating agents, e.g. sodium dodecyl benzene sulfonate [13], chitosan [33], and sodium carboxymethyl cellulose [34]. Although, synthesis protocols with different conditions (i.e. reaction time and temperature, pH of the growth solution, proper pH control compounds, surfactants and their molar ratio to the precursor), were thoroughly studied, the pressure effect has not yet been reported. Next to temperature, pressure is one of the most essential physical parameters required for hydrothermal conditions, and therefore its influence cannot be neglected in the synthesis.

To the best of our knowledge, presented in this paper $(NH_4)_2V_{10}O_{25}\cdot 8H_2O$ material has never been utilized as a cathode material for lithium-ion batteries. In the literature, one may find information about the utilization of $(NH_4)_2V_{10}O_{25}\cdot 8H_2O$ for Zn-ion batteries [18] and in supercapacitors [8]. However, both examples describe the electrochemical performance of $(NH_4)_2V_{10}O_{25}\cdot 8H_2O$ in aqueous electrolyte. The specific capacity of such cathode material in the zinc-ion battery was equal to 229 mA h/g for a current density of 100 mA/g. However, it must be remembered that it is difficult to compare the results obtained in aqueous and non-aqueous electrolytes. In the case of aqueous systems, one should be aware of parasitic processes, which lead to loss of water, a decrease of energy, and continuous battery degradation. Such parasitic processes are not observed in non-aqueous systems consisted of one single cell. However, more than one cell is usually present in the battery. It may lead to the overcharge reactions and may become a considerable factor affecting battery performance.

In this work, the effect of the initial synthesis pressure on the ammonium vanadates phase and morphology have been studied for the first time. In the literature, the influence of temperature and pH on the obtained structures morphology and properties are frequently studied. However, there is a lack of study on the significance of the pressure during synthesis. Our results show, that this parameter cannot be neglected. As proof, we report the differences in the electrochemical behavior of samples synthesized under different initial pressures. It must be mentioned that comparing the results presented in the literature is difficult without the information of all synthesis parameters such as temperature, composition, pH, and pressure. Therefore, the studies about the influence of pressure are crucial in the development of the hydrothermal synthesis of ammonium vanadates and their further applications. Therefore, in this paper, samples have been prepared using a simple hydrothermal method without initial pressure and under 5, 25, and 50 bars. The resulting products were fully characterized by means of X-ray diffraction (XRD), scanning (SEM) and transmission electron microscopy (TEM), Fourier transform infrared spectroscopy (FTIR) and thermogravimetric analysis (TG). Moreover, the electrochemical properties have been compared and assessed for application in lithium-ion battery.

2. Experimental

2.1. Material preparation

Ammonium metavanadate (NH_4VO_3, 99%) was purchased in Sigma Aldrich. Oxalic acid dihydrate ($C_2H_2O_4\cdot 2H_2O$) was received from L.P P–H "OH". In all synthesis Mili-Q deionised water was used.

All samples were prepared *via* hydrothermal method in the autoclave. In a typical procedure, 0.250 g NH_4VO_3 and 0.250 g $C_2H_2O_4\cdot 2H_2O$ were dissolved in 25 ml of deionised water under magnetic stirring. Then the obtained yellow solution (pH = 1) was placed into a stainless-steel autoclave with a capacity of 1800 ml and kept for 8 h at 180 °C. After that time, the autoclave was evacuated with a rate of ca. 1 bar/min and then cooled to room temperature naturally. Finally, the obtained bluish-green precipitate was several times washed with deionised water and dried at 40 °C under vacuum. In order to study the pressure effect, this procedure was repeated in pre-pressurized autoclave under 5, 25, or 50 bars. Required initial pressure was adjusted by filling the autoclave with N_2. Sample synthesized without initial pressure was denoted as p0 and samples obtained under initially set pressure were labelled as p5, p25, and p50, respectively.

2.2. Apparatus

X-ray diffraction patterns (XRD) were collected on a Philips X'PERT PLUS diffractometer with Cu Kα radiation (λ = 1.5406 Å) and 2θ ranging from 5 to 70°. The FullProf Suite program was used to perform LeBail refinements using Thompson-Cox-Hastings pseudo-Voigt peak shapes. The Fourier transform infrared (FTIR) spectra were recorded on PerkinElmer Frontier spectrophotometer, with a resolution of 2 cm^{-1} in the range of 400–4000 cm^{-1}. In order to make measurements in transmittance mode, all samples were mixed with KBr and pressed to pellets. The surface morphology and fine grain structure of the samples were studied also at room temperature by a FEI Company Quanta FEG 250 scanning electron microscope (SEM) and a FEI TECNAI G2 F20 transition electron microscopy (TEM). Thermogravimetric analysis (TG) was carried out under argon atmosphere from 40 °C to 560 °C (with a heating rate 10 °C/min) using Netzsch STA 449 F1. The first derivative of TGA, denoted as DTG, was calculated using Netzsch Proteus ThermalAnalysis program. The thermal behavior was also studied with mass spectrum (MS). The gases that come out from the samples during heating were monitored by the quadruple mass spectrometer Netzsch QMS 403C Aëolos.

2.3. Electrochemical measurements

The electrodes were prepared from a slurry containing 7:2:1 wt ratio of p0 or p50, carbon black as conducting agent and 10 wt% vinylidiene fluoride (PVDF) as a binder. After being blended in N-methylpyrrolidone, the slurry was spread on the thin aluminium foil. Next the discs were cut off dried under dynamic vacuum in an oven (Glass Oven B-595, Büchi, Germany) for 24 h at 60 °C. Dried disc electrodes were used in two-electrode Swagelok® cells with lithium foil as a counter and reference electrodes (99.9% purity, 0.75 mm thickness, AlfaAesar, USA), 1 M $LiPF_6$ in EC:DMC ratio 1:1 (LP30 Merck, Germany) as the electrolyte, and glass fibre (Schleicher & Schüll, Germany) as the separator. The battery tests of the samples were performed using the ATLAS 0961 MBI (Poland)

multichannel battery testing system with different current densities. Cyclic voltammetry measurements (CV) were carried out on a PGSTAT204 galvanostat/potentiostat over the potential range from 2.0 V to 4.0 V vs. Li/Li^+ with a scanning rate of 0.1 mV/s.

3. Results and discussion

3.1. Material characterization

The phase composition and crystallographic structure of the obtained samples were determined by XRD analysis (Fig. 1). The XRD pattern of the sample p0 revealed, that it is composed of two phases $(NH_4)_2V_{10}O_{25}\cdot 8H_2O$ and $(NH_4)_2V_6O_{16}$, with the dominance of the first one. The presence of the $(NH_4)_2V_6O_{16}$ is revealed by its main diffraction peak located at 11.32° (star in Fig. 1). The lattice parameters were determined from LeBail refinement (see ESI) and the obtained values are in good agreement with those reported in the literature [8,18,21]. Analysing the diffractograms of the samples p5, p25 and p50, it can be noticed, that the intensity of the diffraction peaks ascribed to $(NH_4)_2V_6O_{16}$ decreased as compared to p0 and was not observed in the case of p50, obtained under the highest initial pressure among studied. Generally, a higher pressure may lead to more homogenous solutions, assuring a comparable environment in the whole reaction mixture, which is beneficial for phase purity. It can also speed up the rate of a synthesis reaction, facilitating the reduction process. This suggests that $(NH_4)_2V_6O_{16}$ is an intermediate phase in the reaction and demonstrates that the phase structure of the final product is strongly dependent on the initial pressure of the reaction.

Fig. 2 shows the FTIR spectra of the obtained samples. Several distinct absorption bands appeared, which can be assigned to the different vibrational modes of N—H and V—O bonds. The absorption bands observed at ~3150 cm^{-1} and ~1400 cm^{-1} are due to the stretching and bending vibrations of the N—H in the NH_4^+ group.

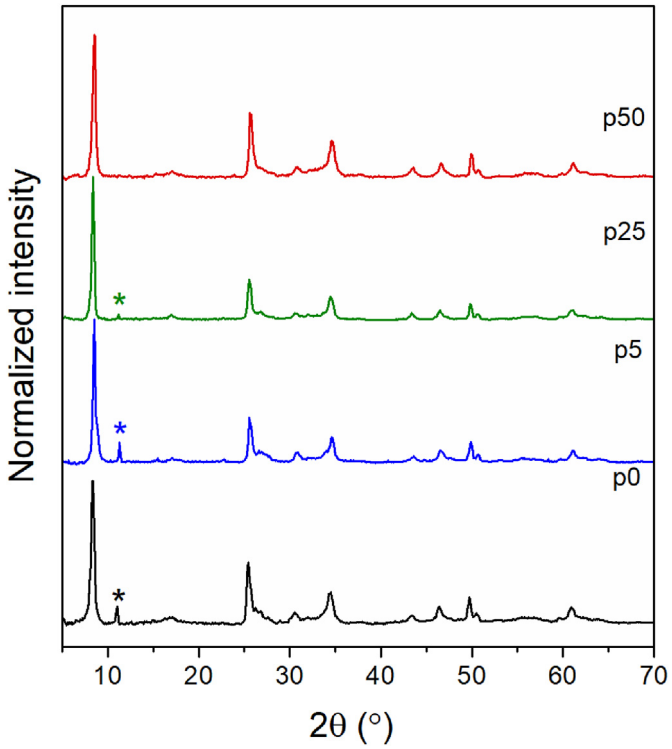

Fig. 1. Normalized XRD patterns of p0, p5, p25 and p50.

The sharp band centred at ~1000 cm^{-1} corresponds to V═O stretches. Bands present in the lower frequency region (765 cm^{-1} and 535 cm^{-1}) are characteristic for the symmetric and asymmetric stretching vibrations of the V—O—V bond. Furthermore, two bands at 3450 cm^{-1} and 1640 cm^{-1}, referring to the O—H stretching and bending vibration of the crystal water, confirmed the hydrated structure of analysed crystals [15]. Similarly to XRD results, the p0 revealed differences in spectroscopic data as compared to other samples. Splitting of bands arising from V—O (at 1000 cm^{-1}) and V—O—V (in the range 765—500 cm^{-1}) observed in the p0 spectrum, indicates the presence of two inequivalent V═O groups [19]. According to the XRD results all samples exhibit two phases: the main one $(NH_4)_2V_{10}O_{25}\cdot 8H_2O$ and additional $(NH_4)_2V_6O_{16}$. The first one is composed of VO_5 square pyramids and the second one of VO_6 octahedrons, which differ in bond lengths and in consequence oscillate with different frequencies. Due to the fact that in the p0 sample contribution of the additional phase is the highest, the most distinct splitting of the bands is observed in the p0 spectrum.

The morphology of the synthesized samples were investigated using SEM and TEM. As can be seen in Fig. 3, different initial pressures in the hydrothermal synthesis lead to diverse samples morphologies. In the absence of the initial pressure the final product was the most heterogeneous-sample was a mixture of thick microplatelets as well as thin nanobelts. Moreover, microplatelets and nanobelts were randomly orientated and tended to agglomerate. In contrast, when the initial pressure was given, the obtained products were uniform and composed of only one kind of nanostructures. In addition, the nanostructures self-assemble into flower-like structures. It should be noticed here that usually to obtain such three-dimensional structures additional soft or hard templates must be used [8,11,24]. In the case of sample obtained with 5 bars, flowers are built from nanoflakes with thickness up to 150 nm. Along with the further increase of the initial pressure nanoflakes elongate to thinner nanobelts. The obtained results show that initial synthesis pressure is a valuable tool for the synthesis of homogenous three-dimensional nanostructures.

Further investigation using high-resolution TEM (HRTEM) and the corresponding selected-area electron diffraction pattern (SAED) revealed differences in the samples microstructure. A TEM and HRTEM images of the nanobelts obtained without initial pressure during synthesis (p0) are shown in Fig. 4a and b respectively. It can be seen, that single nanobelt has poly-crystalline structure. White circles (Fig. 4b), indicate areas of different lattice fringes orientations (inset in Fig. 4b). It may be due to the fact that the p0 material is a mixture of two phases. According to XRD results, when the initial pressure increases to 50 bar, mostly phase $(NH_4)_2V_{10}O_{25}\cdot 8H_2O$ was obtained. Fig. 4c shows a TEM image of typical nanobelt (sample p50) obtained at the highest pressure. The corresponding SAED pattern (inset of Fig. 4c, black dot corresponds to the area where SAED pattern was recorded) exhibited very sharp diffraction spots, indicating a single crystal structure of this nanostructure. The observed lattice spacing in the HRTEM image (Fig. 4d) was calculated to be 0.344 nm and it matches well with the (003) plane of monoclinic $(NH_4)_2V_{10}O_{25}\cdot 8H_2O$.

In order to determine thermal stability of the obtained samples, thermogravimetric analysis (TG) with evolved gas analysis using mass spectrometry (MS) were performed. The mass spectra were measured from *m/z* 2 to 60. After the experiments, the measured peaks intensity were analysed as a function of the reaction time. The background of carrier gas was subtracted from *m/z* ion currents. The largest intensities of ion current were registered for the fragments corresponding to NH_3 and H_2O ions: *m/z* 14 (N^+), 15 (NH^+), 16 (NH_2^+, O^+) 17 (NH_3^+, OH^+), and 18 (H_2O^+). Fig. 5a and b shows TG and DTG (TG 1st derivative expressed in %/min, it determines rate of mass change) curves of p0 and p50 samples

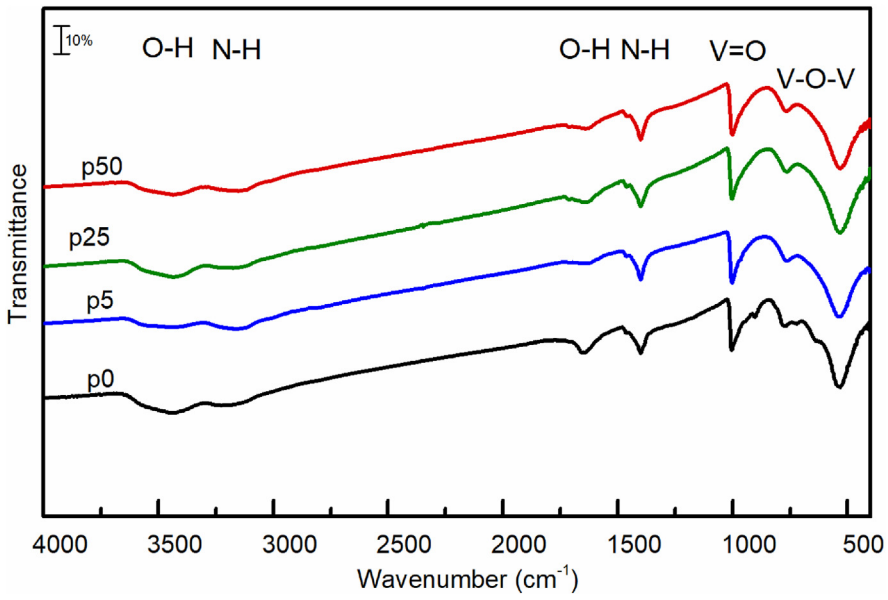

Fig. 2. FTIR spectra of samples p0, p5, p25 and p50.

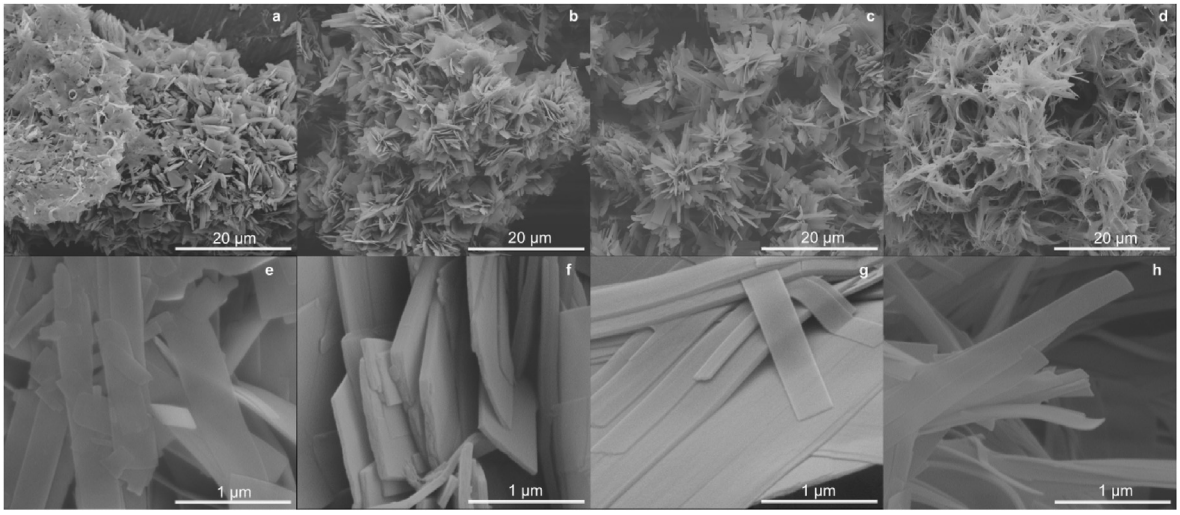

Fig. 3. SEM images of samples p0 (a, e), p5 (b, f), p25 (c, g), p50 (d, h).

respectively with registered ion currents.

The thermal decomposition of measured samples occurred in three stages. From the TG/DTG plots, it is seen that the first thermal decomposition stage caused by the removal of the adsorbed water, occurred slightly in different temperature range for each sample. For sample p0 the first decomposition was observed between 40 and 205 °C and for p50 in the range of 40–118 °C, with a mass loss of 0.76% and 0.57%, respectively. The second weight loss of 7.22% between 205 and 362 °C (with DTG peak at 336 °C) and 7.20% between 118 and 314 °C (with DTG peak at 272 °C) for p0 and p50 samples respectively was resulted mostly by the release of NH_3 and water formed as a result of the separation of the ammonium group. It is known that during the decomposition of vanadium ammonium compounds, equimolar amounts of NH_3 and H_2O are formed according to the equation:

$$n\ (NH_4)_xV_yO_z \rightarrow m\ (NH_4)_aV_bO_c + NH_3 + H_2O$$

For this reason, the curves presenting the ion current for *m*/*z* 18 (H_2O^+) and 15 (NH^+) are overlapping in this temperature range (Fig. 5a and b). The last decomposition stage with mass loss of 3.16% (with DTG peak at 410 °C) for p0 and 5.95% (with DTG peak at 340 °C) for p50 was caused by the release of NH_3 and deintercalation of strongly-bounded water (the clearly visible shoulder on *m*/*z* 18 ion current). The visible differences in thermal stability result from phase composition, morphology, and microstructure of samples. According to TEM and XRD results, sample p0 is composed of two phases ($(NH_4)_2V_6O_{16}$ and $(NH_4)_2V_{10}O_{25}\cdot 8H_2O$) and nanobelts have poly-crystalline structure (Fig. 4b) and probably for this reason, the release of NH_3 occurs above 205 °C. On the other hand, sample p50 consists of $(NH_4)_2V_{10}O_{25}\cdot 8H_2O$ phase and therefore weight loss associated with deintercalation strongly-bounded water (last decomposition stage) is almost twice as large.

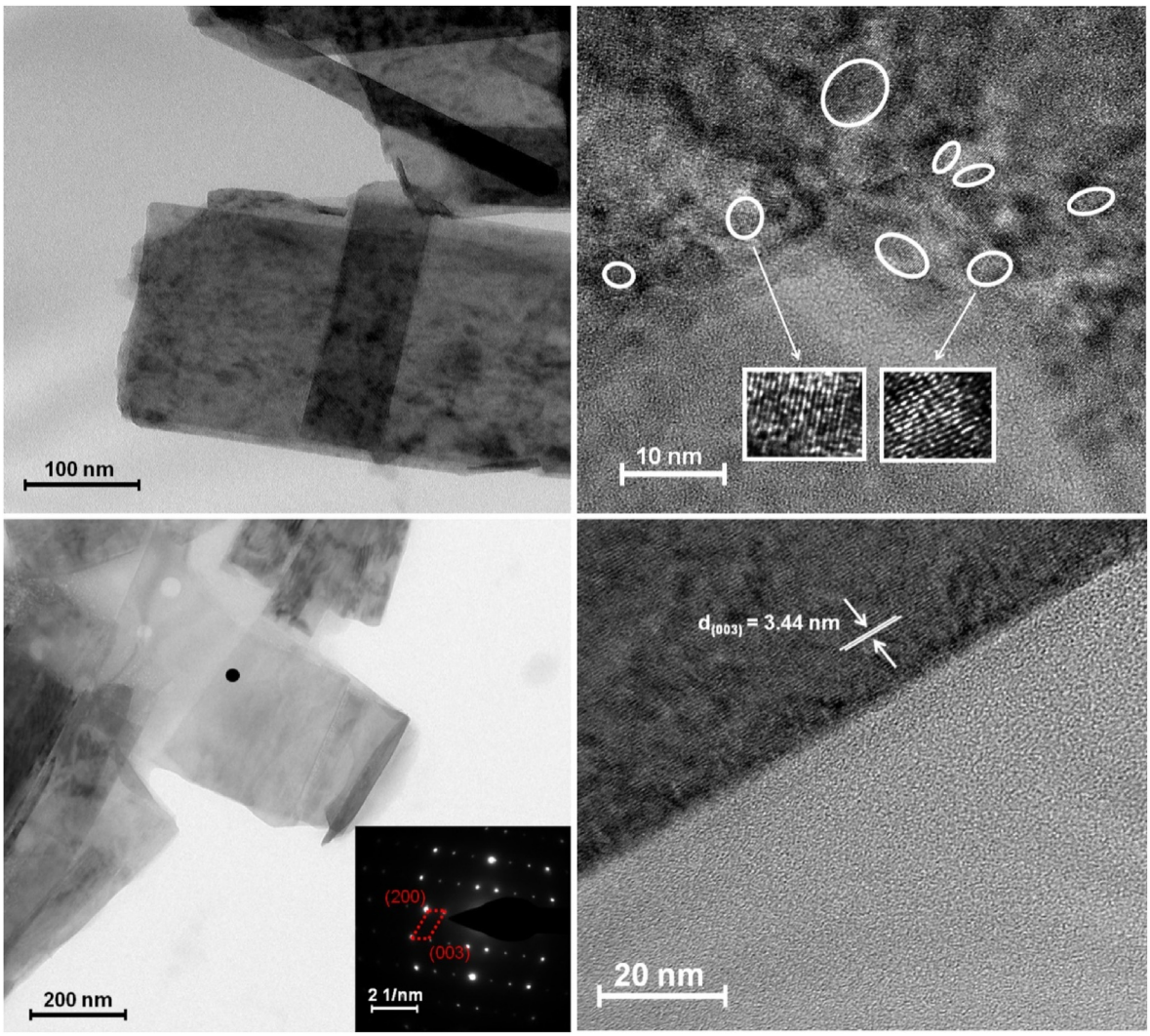

Fig. 4. TEM (a,c) and HRTEM (b,d) images of samples p0 (a,b) and p50 (c,d). The inset in (c) is the SAED pattern.

3.2. Electrochemical performance

Ammonium vanadates are promising cathodic materials for Li-ion batteries. As it was mentioned before, $(NH_4)_2V_{10}O_{25}\cdot 8H_2O$ has not been studied in such application, so far. Fig. 6 shows galvanostatic curves for 1st, 2nd, 3rd and 42nd charge/discharge cycle of p0 and p50 electrode material at 2–4 V at current density of 50 mA/g. The first discharge capacity for p0 and p50 recorded at 50 mA/g equals to 167 mA h/g and 261 mA h/g, respectively. The final specific capacity was 44 mA h/g and 229 mA h/g for p0 and p50, respectively. It gave capacity retention of 26% for p0 and 87% for p50. Thus, it is shown that p50 electrode material exhibits higher specific capacity with higher capacity retention in comparison with p0 material. The shape of the chronopotentiometric curve of p0 and p50 is similar.

One may see that the first three discharging cycles exhibit plateau at ~3.0 V, ~2.8 V and 2.5 V. In the reverse process one may see plateau at ~2.7 V. However, the shape of the curve for the 42nd cycle for p0 is totally different. It is very likely that material undergoes irreversible changes during lithium ion insertion/extraction process. The differences between p0 and p50 electrode material are well visible on the cyclic voltammetry curves in Fig. 7. Both materials have two cathodic maxima at very close potentials, ~3.0 V (I) and 2.8 V (II). The third and fourth cathodic maxima are recorded at 2.61 V (III) and 2.52 V (III*) for p0, 2.56 V (III) and 2.44 V (III*) for p50. These cathodic maximum are coupled with only one anodic current maximum at 2.66 V (iii) for p0 and 2.75 V (iii) for p50. We assume that the presence of two cathodic maxima is due to step reversible intercalation of lithium ions in the solid phase of both p0 and p50 electrode materials. Such phenomenon was observed for $NH_4V_3O_8\cdot 0.2H_2O$ by Wang et al. [3]. It is noteworthy to mention that the anodic maximum for p50 at 2.66 V (iii) hinders detection the anodic maximum at with 2.91 V (ii).

The p0 electrode material is a mixture consisting of $(NH_4)_2V_6O_{16}$ and $(NH_4)_2V_{10}O_{25}\cdot 8H_2O$ while the p50 is a pure $(NH_4)_2V_{10}O_{25}\cdot 8H_2O$ phase only. Further, the $(NH_4)_2V_{10}O_{25}\cdot 8H_2O$ is composed of double layer δ-MV_2O_5 type structure known in the literature as δ-$M_xV_4O_{10}$ [36]. Thus, in the studied case one may conclude that $(NH_4)_2V_{10}O_{25}\cdot 8H_2O$ is built of two molecules of $NH_4V_4O_{10}\cdot 4H_2O$ and one molecule of V_2O_5. The presence of water in $NH_4V_4O_{10}\cdot 4H_2O$ origins from the synthesis method. Hence, the difference in the composition of the electrode affects reaction with lithium ions regarding reversibility of Li^+ intercalation/deintercalation.

The distance between the vanadium oxide layers in p50 seems to be more suitable for stabilization the structure during charging/

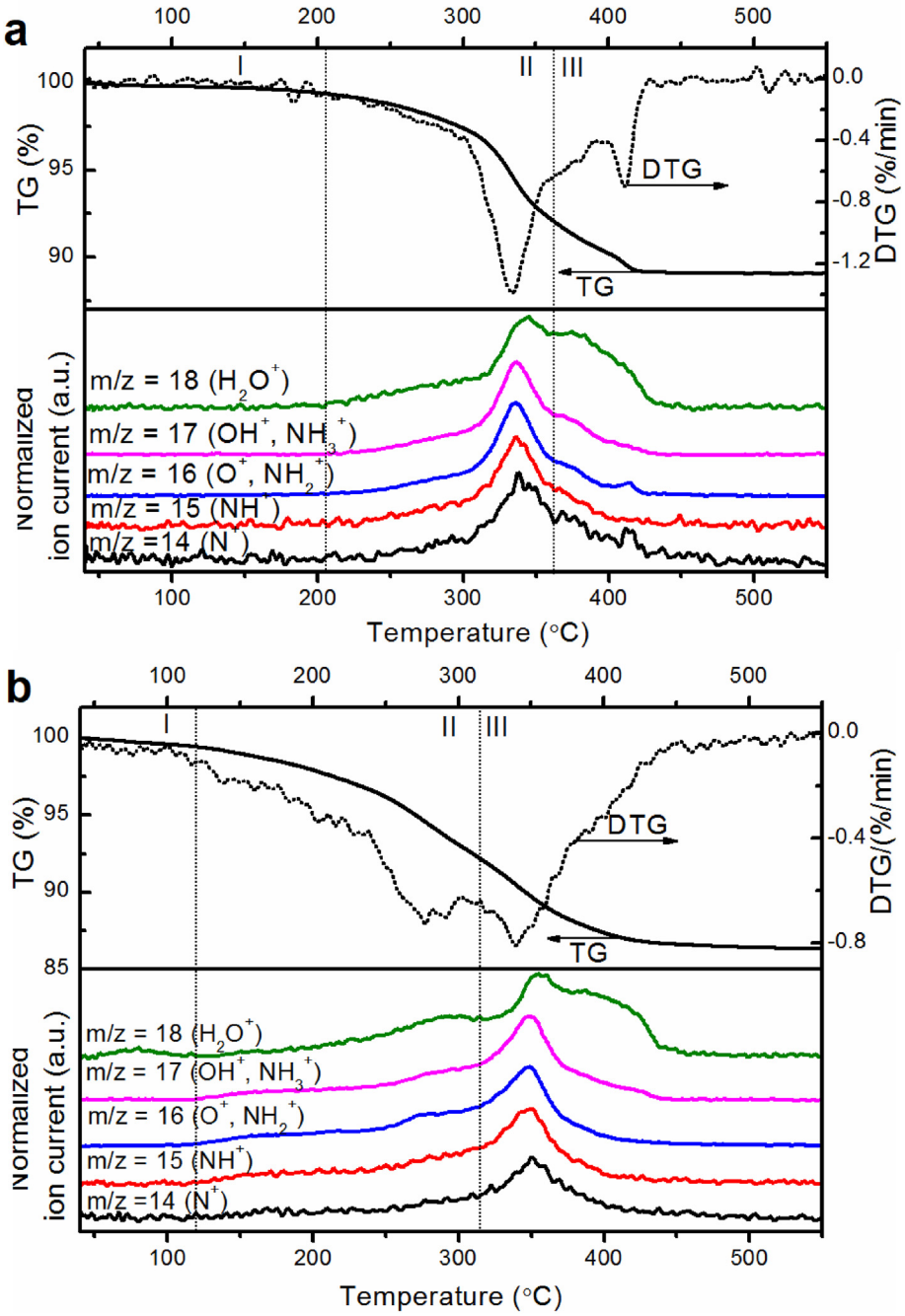

Fig. 5. The TG and DTG curves of a) p0 and b) p50 sample with registered ion currents for NH_3 and H_2O ions in the evolved gas during the samples decomposition.

discharging as it was already observed for lithium-rich layered materials [37,38]. It might be due to fact that $NH_4V_4O_{10}$ may inhibit lithium insertion between V_2O_5 layers of $(NH_4)_2V_{10}O_{25}\cdot 8H_2O$. Thus, the presence of three plateau during discharge (see Fig. 6) and three cathodic maxima recorded on CV curve (see Fig. 7) might be identified as lithium-ion intercalation process into ammonium vanadate structure according to equation [28,39]:

$$NH_4V_4O_{10} + (3\text{-}x)Li^+ + (3\text{-}x)e^- = Li_{3\text{-}x}NH_4V_4O_{10}$$

The theoretical capacity of $Li_{3\text{-}x}NH_4V_4O_{10}$ is of ~211 mA h/g. Taking into account the presence of two double layers of the $NH_4V_4O_{10}$ structure with V_2O_5 layer the theoretical amount of lithium ions able to be inserted into $(NH_4)_2V_{10}O_{25}\cdot 8H_2O$ is no less than 9 giving theoretical capacity at least 221 mA h/g. The rate performance of p0 and p50 electrode materials at varying current rates is shown in Fig. 8. Electrode materials were tested in the sequence 50 mA/g → 100 mA/g → 150 mA/g → 200 mA/g → 150 mA/g →100 mA/g → 50 mA/g for six cycles in a sequence. The p0 electrode material exhibited stable electrochemical performance up to 12 cycles with specific charge and discharge capacities of 137 ± 7 mA h/g and 141 ± 2 mA h/g at 100 mA/g for the 12th cycle, respectively. The 4 mA h/g difference in the specific capacity for charge/discharge process is due to open circuit potential (OCP) procedure applied between discharge and charge stages. During that time lithium ions migrate from host material to the electrolyte.

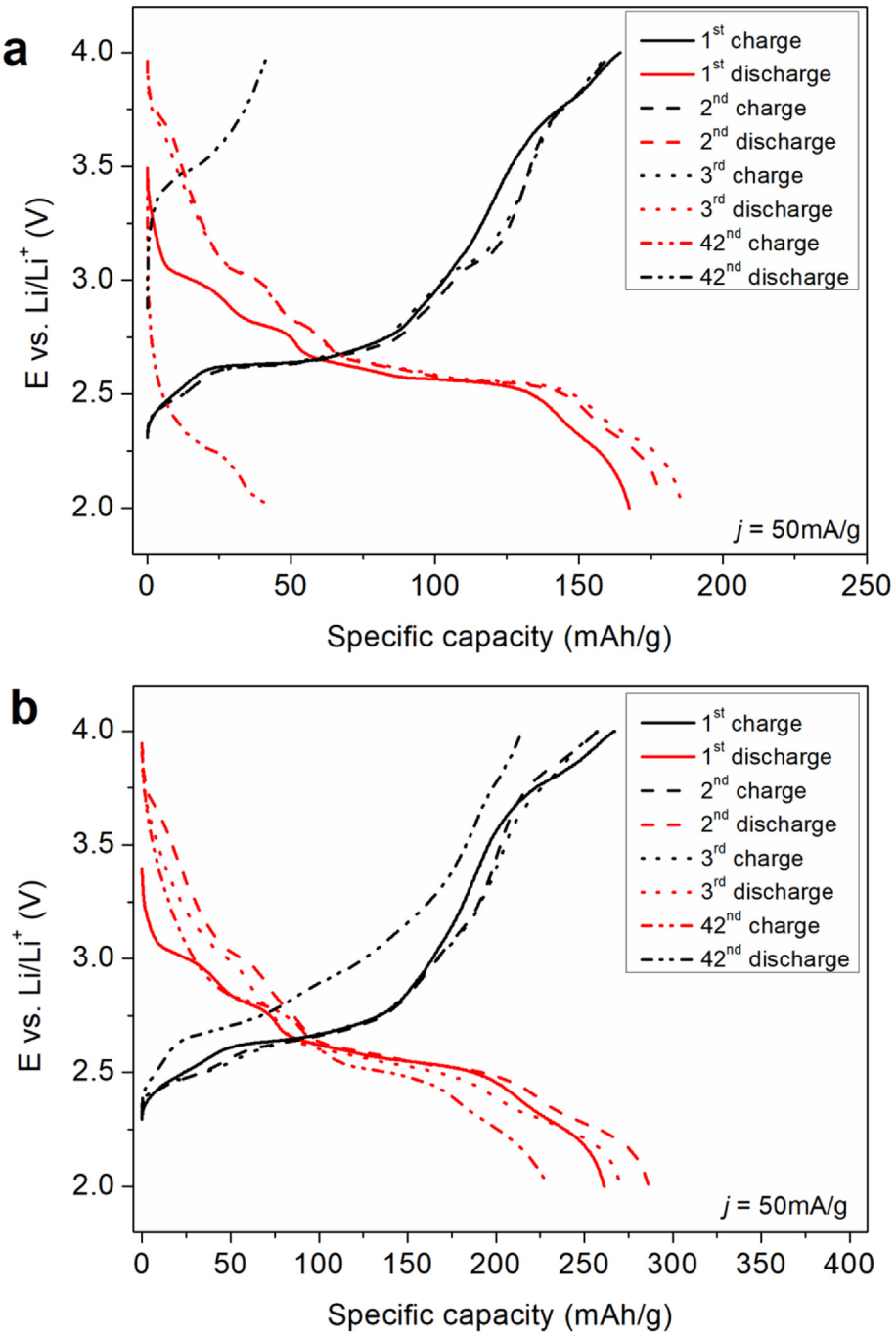

Fig. 6. The first three and last 42 nd cycles of charge/discharge profiles of a) p0 and b) p50 electrode material.

Hence, for oxidation process less lithium ions can be extracted from an electrode material. The OCP procedure was applied to reach equilibrium state of the electrode material after discharging process.

The increase in current density to 150 mA/g caused capacity drop to 84 ± 10 mA h/g for the 18th discharge cycle. Even worse results were obtained for current density equal to 200 mA/g. The discharge capacity for the 24th cycle was 39 ± 6 mA h/g. It seemed that high current densities had an irreversible negative effect on the capacity of p0 electrode material. The p0 electrode material did not recover if the initial current density (50 mA/g) was applied. The discharge capacity for the 42nd cycle was only 49 ± 4 mA h/g. It is very likely that material underwent structural changes during applying high current density that did not allow lithium ions to be inserted into the host structure. The p0 electrode material seems to be inappropriate for lithium-ion storage because it possesses lower specific capacitance and is degrading during cycling. The additional intermediate phase $(NH_4)_2V_6O_{16}$, which is present in the p0 sample, is known to be suitable as cathode material for lithium-ion batteries. However, results showed that sample p0 had much lower capacity than values reported in the literature [24]. It should be noticed here that p0 is composed of two phases $(NH_4)_2V_{10}O_{25}\cdot 8H_2O$ and $(NH_4)_2V_6O_{16}$ with the dominance of the first one, and it cannot be treated as pure $(NH_4)_2V_6O_{16}$. It is

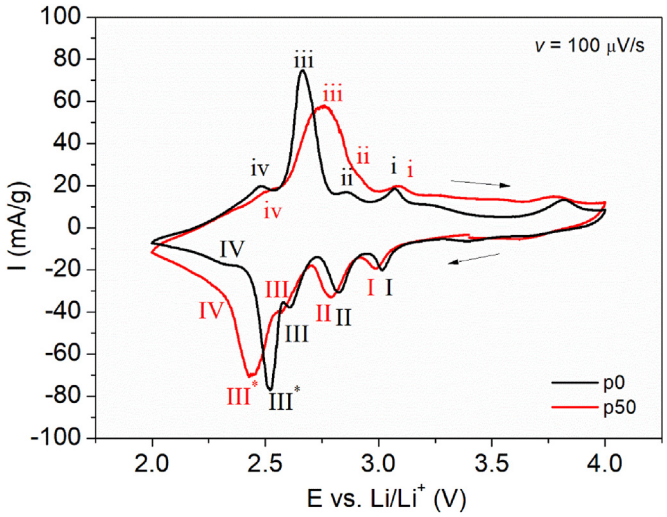

Fig. 7. Cyclic voltammetry curves of the p0 and p50 electrode materials, scan 3.

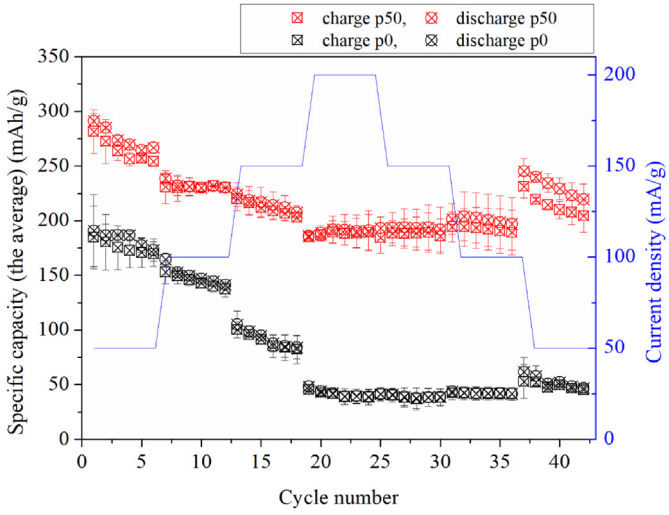

Fig. 8. The rate capability of p0 and p50 electrodes in the potential range from 2.0 V to 4.0 V.

suggested that in this case, the additional phase acts as a blocking agent for the lithium-ion insertion process. Moreover, it should not be forgotten that electrochemical performances of vanadium oxide-based materials are also strongly affected by the preparation method [40].

Much better results were obtained for p50 positive electrode material. One may see that during the continuous cycling with increasing and decreasing current densities, the specific capacity did not change significantly. The specific charge capacity at 50 mA/g was 254 ± 4 mA h/g and 204 ± 15 mA h/g for the 6th and the 42nd cycle, respectively. The specific discharge capacity was slightly higher with the values of 266 ± 5 mA h/g and 220 ± 14 mA h/g for the 6th and the 42nd cycle, respectively. It gives a capacity retention of 82.7% for the discharge process.

During increase of current density one may see the capacity decrease. However, this decrease is not so drastic as it was observed for p0 electrode material. The discharge capacity for p50 for $j = 200$ mA/g was 191 ± 18 mA h/g, and did not change much when the current density increased to 100 mA/g (197 ± 24 mA h/g for the 36th cycle). It shows that also for p50 high currents are very likely to change the crystallographic structure of p50. This change seems to be irreversible as the material did not reach values of specific capacities from the initial cycles. However, the high currents do not affect the specific capacity as much it was observed for p0 electrode material. In the all cases for p50 one may see capacity difference of about 10–15 mA h/g between charge and discharge process. This phenomenon is of the same origin as it was already described for p0 electrode material.

It is noteworthy that the specific discharge capacity for the 6th cycle is 45 mA h/g higher in comparison with the theoretical capacity (221 mA h/g) which suggests that $(NH_4)_2V_{10}O_{25}\cdot 8H_2O$ structure can uptake more than 9 lithium ions during lithium insertion process. Moreover, the discharge capacity of 191 ± 18 mA h/g for $j = 200$ mA/g is only slightly lower than theoretical one. It can be concluded that p50 electrode material is a suitable for lithium-ion batteries.

4. Conclusions

Effect of the initial pressure on the final product was studied in the hydrothermal reaction of ammonium metavanadate and oxalic acid. The morphology and chemical structure of ammonium vanadates obtained with different initial pressure values (0, 5, 25, and 50 bar) were characterized by SEM, TEM, XRD, FTIR, TG and MS. Results indicate that the initial pressure affects both the morphology and the structure of the samples and cannot be omitted during the synthesis. It was found, that higher pressure results in more homogenous and thinner structures. Moreover, it facilities the formation of three-dimensional flower-like structures. It was also shown that the initial pressure is a key factor for the final phase composition of the samples. High pressure was necessary to obtain pure-phase $(NH_4)_2V_{10}O_{25}\cdot 8H_2O$. The electrochemical measurements revealed substantial differences between samples obtained under different pressure. The $(NH_4)_2V_{10}O_{25}\cdot 8H_2O$ was studied as a cathodic material for Li-ion batteries, showing great performance. The specific capacity of 191 mA h/g at 200 mA/g evidenced that the electrode material is stable during cycling at high current densities. This phenomenon is attributed to unique $(NH_4)_2V_{10}O_{25}\cdot 8H_2O$ structure that allows reversible lithium ion intercalation/deintercalation.

Author contributions

The manuscript was written through contributions of all authors. All authors have given approval to the final version of the manuscript

Funding sources

Marta Prześniak-Welenc thanks National Science Centre, Poland for grant number 2017/01/X/ST5/01415. Kamila Sadowska (Żelechowska) thanks National Science Centre, Poland for grant number 2016/23/D/ST5/02800. Andrzej P. Nowak thanks Ministry of Science and Higher Education, Poland (DS no. 030893/003).

CRediT authorship contribution statement

Marta Prześniak-Welenc: Conceptualization, Supervision, Writing - original draft, Investigation, Funding acquisition. **Małgorzata Nadolska:** Writing - original draft, Investigation, Visualization. **Andrzej P. Nowak:** Writing - original draft, Investigation. **Kamila Sadowska:** Writing - original draft, Investigation, Funding acquisition.

Appendix A. Supplementary data

Supplementary data to this article can be found online at https://doi.org/10.1016/j.electacta.2020.135919.

References

[1] G.S. Zakharova, I.V. Baklanova, A.Y. Suntsov, Y. Liu, Q. Zhu, W. Chen, $NH_4V_3O_7$: synthesis, morphology, and optical properties, Russ. J. Inorg. Chem. 61 (2016) 1584–1590, https://doi.org/10.1134/S0036023616120214.

[2] G.Q. Zhang, S.T. Zhang, Charge-discharge mechanisms of ammonium vanadium bronze $NH_4V_4O_{10}$ nanobelts as cathode for lithium-ion battery, Asia-Pacific power, Energy Eng. Conf. APPEEC. 5 (2009) 2–5, https://doi.org/10.1109/APPEEC.2009.4918215.

[3] H. Wang, K. Huang, S. Liu, C. Huang, W. Wang, Y. Ren, Electrochemical property of $NH_4V_3O_8 \cdot 0.2H_2O$ flakes prepared by surfactant assisted hydrothermal method, J. Power Sources 196 (2011) 788–792, https://doi.org/10.1016/j.jpowsour.2010.07.022.

[4] H. Fei, X. Wu, H. Li, M. Wei, Novel sodium intercalated $(NH_4)_2V_6O_{16}$ platelets: high performance cathode materials for lithium-ion battery, J. Colloid Interface Sci. 415 (2014) 85–88, https://doi.org/10.1016/j.jcis.2013.10.025.

[5] M.A. Teplonogova, A.D. Yapryntsev, A.E. Baranchikov, V.K. Ivanov, Selective hydrothermal synthesis of ammonium vanadates(V) and (IV,V), Transit. Met. Chem. (2018) 2–7, https://doi.org/10.1007/s11243-018-0265-x.

[6] N. Wang, W. Chen, L. Mai, Y. Dai, Selected-control hydrothermal synthesis and formation mechanism of 1D ammonium vanadate, J. Solid State Chem. 181 (2008) 652–657, https://doi.org/10.1016/j.jssc.2007.12.036.

[7] H.K. Park, G. Kim, Ammonium hexavanadate nanorods prepared by homogeneous precipitation using urea as cathodes for lithium batteries, Solid State Ionics 181 (2010) 311–314, https://doi.org/10.1016/j.ssi.2010.01.011.

[8] Y. Jiang, L. Jiang, Z. Wu, P. Yang, H. Zhang, Z. Pan, et al., In situ growth of $(NH_4)_2V_{10}O_{25} \cdot 8H_2O$ urchin-like hierarchical arrays as superior electrodes for all-solid-state supercapacitors, J. Mater. Chem. A. 6 (2018) 16308–16315, https://doi.org/10.1039/c8ta05706k.

[9] T.Z. Ren, Z.Y. Yuan, X. Zou, Crystal growth of mixed-valence ammonium vanadates, Cryst. Res. Technol. 42 (2007) 317–320, https://doi.org/10.1002/crat.200610821.

[10] Y. Cheng, J. Huang, J. Li, L. Cao, Z. Xu, J. Wu, et al., Structure-controlled synthesis and electrochemical properties of $NH_4V_3O_8$ as cathode material for Lithium ion batteries, Electrochim. Acta 212 (2016) 217–224, https://doi.org/10.1016/j.electacta.2016.07.008.

[11] D. Fang, Y. Cao, R. Liu, W. Xu, S. Liu, Z. Luo, et al., Novel hierarchical three-dimensional ammonium vanadate nanowires electrodes for lithium ion battery, Appl. Surf. Sci. 360 (2016) 658–665, https://doi.org/10.1016/j.apsusc.2015.11.038.

[12] Y. Ma, S. Ji, H. Zhou, S. Zhang, R. Li, J. Zhu, et al., Synthesis of novel ammonium vanadium bronze $(NH_4)_{0.6}V_2O_5$ and its application in Li-ion battery, RSC Adv. 5 (2015) 90888–90894, https://doi.org/10.1039/c5ra18074k.

[13] H. Wang, Y. Ren, W. Wang, X. Huang, K. Huang, Y. Wang, et al., $NH_4V_3O_8$ nanorod as a high performance cathode material for rechargeable Li-ion batteries, J. Power Sources 199 (2012) 315–321, https://doi.org/10.1016/j.jpowsour.2011.10.069.

[14] H. Wang, K. Huang, C. Huang, S. Liu, Y. Ren, X. Huang, $(NH_4)_{0.5}V_2O_5$ nanobelt with good cycling stability as cathode material for Li-ion battery, J. Power Sources 196 (2011) 5645–5650, https://doi.org/10.1016/j.jpowsour.2011.02.046.

[15] S.G. Leonardi, P. Primerano, N. Donato, G. Neri, Behavior of sheet-like crystalline ammonium trivanadate hemihydrate $(NH_4V_3O_8 \times 0.5H_2O)$ as a novel ammonia sensing material, J. Solid State Chem. 202 (2013) 105–110, https://doi.org/10.1016/j.jssc.2013.03.028.

[16] E.A. Esparcia, M.S. Chae, J.D. Ocon, S.T. Hong, Ammonium vanadium bronze $(NH_4V_4O_{10})$ as a high-capacity cathode material for nonaqueous magnesium-ion batteries, Chem. Mater. 30 (2018) 3690–3696, https://doi.org/10.1021/acs.chemmater.8b00462.

[17] T.N. Vo, H. Kim, J. Hur, W. Choi, I.T. Kim, Surfactant-assisted ammonium vanadium oxide as a superior cathode for calcium-ion batteries, J. Mater. Chem. A. 6 (2018) 22645–22654, https://doi.org/10.1039/C8TA07831A.

[18] C. Wang, T. Wei, Q. Li, G. Yang, Highly reversible and long-life cycling aqueous zinc-ion battery based on ultrathin $(NH_4)_2V_{10}O_{25}{}^*8H_2O$ nanobelts, J. Mater. Chem. (2018), https://doi.org/10.1039/C8TA06626D.

[19] S.H. Lee, J.M. Koo, S.G. Oh, S.S. Im, Facile synthesis of ammonium vanadate nanofibers by using reflux in aqueous V_2O_5 solution with ammonium persulfate, Mater. Chem. Phys. 194 (2017) 313–321, https://doi.org/10.1016/j.matchemphys.2017.03.053.

[20] A. Ottmann, G.S. Zakharova, B. Ehrstein, R. Klingeler, Electrochemical performance of single crystal belt-like $NH_4V_3O_8$ as cathode material for lithium-ion batteries, Electrochim. Acta 174 (2015) 682–687, https://doi.org/10.1016/j.electacta.2015.06.027.

[21] K.J. Range, C. Eglmeier, A.M. Heyns, D. Waal, Ammonium hexavanadate, $(NH_4)_2V_6O_{16}$: preparation, crystal structure, infrared spectra and high-pressure reactions, Zeitschrift fur Naturforsch. - Sect. B J. Chem. Sci. 45 (1990) 31–38, https://doi.org/10.1515/znb-1990-0108.

[22] D. Vernardou, M. Apostolopoulou, D. Louloudakis, N. Katsarakis, E. Koudoumas, Hydrothermal growth and characterization of shape-controlled $NH_4V_3O_8$, New J. Chem. 38 (2014) 2098–2104, https://doi.org/10.1039/c3nj01446k.

[23] H.K. Park, G. Kim, Ammonium hexavanadate nanorods prepared by homogeneous precipitation using urea as cathodes for lithium batteries, Solid State Ionics 181 (2010) 311–314, https://doi.org/10.1016/j.ssi.2010.01.011.

[24] L. Kou, L. Cao, J. Huang, J. Yang, Y. Wang, Facile synthesis of $NH_4V_3O_8$ nanoflowers as advanced cathodes for high performance of lithium ion battery, J. Mater. Sci. Mater. Electron. 29 (2018) 4830–4834, https://doi.org/10.1007/s10854-017-8438-5.

[25] T.N. Vo, H. Kim, J. Hur, W. Choi, I.T. Kim, Surfactant-assisted ammonium vanadium oxide as a superior cathode for calcium-ion batteries, J. Mater. Chem. A. 6 (2018) 22645–22654, https://doi.org/10.1039/C8TA07831A.

[26] Y. Liu, M. Xu, B. Shen, Z. Xia, Y. Li, Y. Wu, et al., Facile synthesis of mesoporous $NH_4V_4O_{10}$ nanoflowers with high performance as cathode material for lithium battery, J. Mater. Sci. 53 (2018) 2045–2053, https://doi.org/10.1007/s10853-017-1619-z.

[27] G.S. Zakharova, C. Täschner, T. Kolb, C. Jähne, A. Leonhardt, B. Büchner, Morphology controlled $NH_4V_3O_8$ microcrystals by hydrothermal synthesis, Dalt, OR Trans. 42 (2013) 4897, https://doi.org/10.1039/c3dt32550d.

[28] S. Sarkar, P.S. Veluri, S. Mitra, Morphology controlled synthesis of layered $NH_4V_4O_{10}$ and the impact of binder on stable high rate electrochemical performance, Electrochim. Acta 132 (2014) 448–456, https://doi.org/10.1016/j.electacta.2014.03.144.

[29] X. Tian, X. Xu, L. He, Q. Wei, M. Yan, L. Xu, et al., Ultrathin pre-lithiated V_6O_{13} nanosheet cathodes with enhanced electrical transport and cyclability, J. Power Sources 255 (2014) 235–241, https://doi.org/10.1016/j.jpowsour.2014.01.017.

[30] K.F. Zhang, G.Q. Zhang, X. Liu, Z.X. Su, H.L. Li, Large scale hydrothermal synthesis and electrochemistry of ammonium vanadium bronze nanobelts, J. Power Sources 157 (2006) 528–532, https://doi.org/10.1016/j.jpowsour.2005.07.043.

[31] G.S. Zakharova, A.P. Tyutyunnik, Q. Zhu, Y. Liu, W. Chen, Hydrothermal synthesis and thermal stability of self-assembling $NH_4V_3O_7$ microcrystals, Russ. J. Inorg. Chem. 60 (2015) 653–657, https://doi.org/10.1134/S0036023615060194.

[32] L. Liu, Q. Liu, W. Zhao, L. Wang, G. Li, L. Chen, Facile synthesis of $NH_4V_3O_8$ micro/nanoplates and the effects of cutoff potential on electrochemical performance, Int. J. Electrochem. Sci. 12 (2017) 11754–11762, https://doi.org/10.20964/2017.12.19.

[33] Y. Liu, B. Shen, X. Liu, Y. Wu, X. He, Q. Li, High-yield and eco-friendly fabrication of ultra-long $(NH_4)_2V_6O_{16} \cdot 1.5H_2O$ nanowires and their electrochemistry performances, Int. J. Electrochem. Sci. 12 (2017) 5483–5491, https://doi.org/10.20964/2017.06.31.

[34] H.A. Abbood, H. Peng, X. Gao, B. Tan, K. Huang, Fabrication of cross-like $NH_4V_4O_{10}$ nanobelt array controlled by CMC as soft template and photocatalytic activity of its calcinated product, Chem. Eng. J. 209 (2012) 245–254, https://doi.org/10.1016/j.cej.2012.08.027.

[36] P.Y. Zavalij, M.S. Whittingham, Structural chemistry of vanadium oxides with open frameworks, Acta Crystallogr. B 55 (1999) 627–663, https://doi.org/10.1107/S0108768199004000.

[37] S. Taminato, M. Hirayama, K. Suzuki, K. Kim, Y. Zheng, K. Tamura, Mechanistic studies on lithium intercalation in a lithium-rich layered material using Li_2RuO_3 epitaxial film electrodes and in situ surface X-ray analysis, J. Mater. Chem. A. 2 (2014) 17875–17882, https://doi.org/10.1039/c4ta02795g.

[38] K. Ghatak, S. Basu, T. Das, V. Sharma, H. Kumar, D. Datta, Effect of cobalt content on the electrochemical properties and structural stability of NCA type cathode materials, Phys. Chem. Chem. Phys. 20 (2018) 22805–22817, https://doi.org/10.1039/c8cp03237h.

[39] C. Wang, H. Liu, M. Jiang, Y. Wang, R. Liu, Z. Luo, Applied Surface Science Ammonium vanadate@polypyrrole@manganese dioxide nanowire arrays with enhanced reversible lithium storage, Appl. Surf. Sci. 416 (2017) 402–410, https://doi.org/10.1016/j.apsusc.2017.04.069.

[40] H.Y. Xu, H. Wang, Z.Q. Song, Y.W. Wang, H. Yan, M. Yoshimura, Novel chemical method for synthesis of LiV_3O_8 nanorods as cathode materials for lithium ion batteries electrochim, Acta 49 (2004) 349–353, https://doi.org/10.1016/j.electacta.2003.08.017.

Supporting information

Pressure in charge. Neglected parameter in hydrothermal synthesis turns out to be crucial for electrochemical properties of ammonium vanadates

Marta Prześniak-Welenc[a], Małgorzata Nadolska[a], Andrzej P. Nowak[b] and Kamila Żelechowska[a*]

[a]*Faculty of Applied Physics and Mathematics, Gdansk University of Technology, Narutowicza St. 11/12, 80-233 Gdansk, Poland*

[b]*Faculty of Chemistry, Gdansk University of Technology, Narutowicza St. 11/12, 80-233 Gdansk, Poland*

*Corresponding author; e-mail: kamila.zelechowska@pg.edu.pl, tel: +48 583486616, fax: +48 583471705

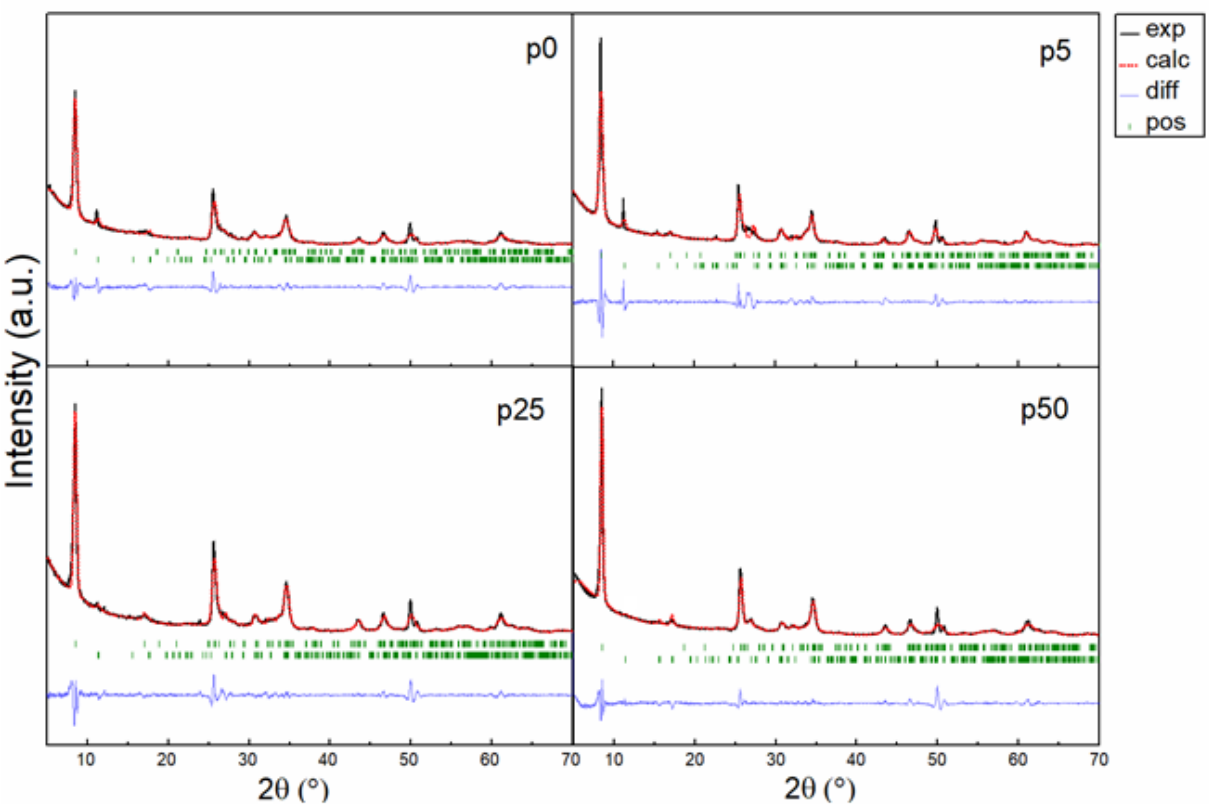

Fig. S1. Le Bail refeinment of $(NH_4)_2V_{10}O_{25} \cdot 8H_2O$ and $(NH_4)_2V_6O_{16}$ for p0,p5,p25 and p50. The experimentally obtained data are shown with a black line, calculated pattern is shown with a red dots and the green vertical marks indicate expected Bragg reflections. The blue line at the bottom shows the difference between the observed and calculated data

Phase 1: $(NH_4)_2V_{10}O_{25} \cdot 8H_2O$ (JCPDS 00-26-0097)

Phase 2: $(NH_4)_2V_6O_{16}$ (JCPDS 01-079-2051).

Tab. 1. The lattice parameters obtained from LeBail refinement

		a	b	c	α	β	γ
p0	phase 1	11,73	3,54	11,25	90	112,39	90
	phase 2	7,86	8,24	5,04	90	96,62	90
P5	phase 1	11,69	3,66	11,13	90	110,12	90
	phase 2	7,85	8,4	5,00	90	96,49	90
p25	phase 1	11,69	3,59	11,24	90	112,27	90
	phase 2	7,83	8,33	5,21	90	97,03	90
P50	phase 1	11,67	3,65	11,15	90	111,13	90
	phase 2	--	-	-	-	-	-

3.3. [A3] The valance state of vanadium-key factor in the flexibility of potassium vanadates structure as cathode materials in LIBs

3.3.1. Research background and objectives

Layered vanadium oxides have been the subject of extensive research as promising cathode materials for LIBs due to their high specific capacities, relatively low cost, and adequate safety characteristics [147,148]. Unfortunately, the practical application of vanadium oxides is hindered by low electrical conductivity and structural degradation during battery cycling [149,150]. Therefore, in recent years, the attention of scientists has shifted towards other vanadium-based compounds, more precisely vanadates, as a potential solution to these challenges. Compared to vanadium oxides, vanadates contain additional cations in their structure. The presence of these cations is pivotal in shaping their electrochemical properties. As was already highlighted in the first part of the thesis, embedded cations stabilize the crystal structure and enhance the electrical conductivity. Moreover, they offer enlarged interlayer spacing, providing more space for guest ions, facilitating their mobility, and reducing structural strain during cycling [151]. To date, numerous different vanadates that vary in the type and quantity of cations, have been investigated as electrode materials for metal-ion batteries [152,153]. Among them, potassium vanadates offer distinct advantages due to the large of potassium ions, resulting in a greater expansion of the structure while still maintaining a relatively low mass, thus contributing to higher gravimetric capacities. Furthermore, potassium is a relatively abundant and low-cost element, which is particularly important in large-scale applications. Despite these advantages, potassium vanadates appear to be underrated, and there is limited literature available regarding their utilization as a cathode material in LIBs.

In this field, the primary focus of research has been on $K_xV_2O_5$ compounds (x in the range of 0.2-0.5 [119,130,131,154]); however, single studies have also been reported for KV_3O_8 [131], $K_2V_8O_{21}$ [105], $K_3V_5O_{14}$, and KV_5O_{13} [155]. In addition, most studies present potassium vanadates in the form of elongated structures with thicknesses in the nanometer range and lengths reaching several micrometres. As expected, the incorporation of potassium ions within the vanadate structure, along with downsizing to nanodimensions, leads to a high specific capacity and excellent cyclic stability. The obtained specific capacities at a current density of 100 mAg^{-1} typically exceed 200 $mAhg^{-1}$, while those at a current density of 1000 mAg^{-1} are slightly higher than 100 $mAhg^{-1}$. The capacity retention after 100 cycles is greater than 90%, although a few exceptions can be observed. For instance, the highest initial discharge capacity of 301 $mAhg^{-1}$ (at 100 $mAg^{-1)}$ was reported for the sample (KV_3O_8 nanowires) with the lowest capacity retention (55% after 100 cycles) [131]. The observed capacity fading was attributed to the weakening of the pillar effect, which is caused by the partial removal of potassium ions from the crystal structure during successive charge-discharge cycles. Further literature analysis revealed that in most cases, the synthesis process of potassium vanadates is complex and involves several steps, with at least one of them requiring heating to temperatures exceeding 400°C. Furthermore, there is

a noticeable lack of research on hydrated potassium vanadates in the literature, while structural water can offer benefits such as improved structural stability and faster ion diffusion.

The remarkable performance of cathodes utilizing potassium vanadates and the clear research gap and complicated synthesis methods served as the motivation for conducting the studies presented in [A3]. This study aimed to synthesize nanostructures of hydrated potassium vanadates and assess their electrochemical performance as cathode materials for LIBs. The structural and morphological properties of the obtained samples were characterized using XRD, FTIR, TG, MP-AES, XPS, XAS, N_2 adsorption, SEM and TEM. Next, samples were tested as cathode materials for nonaqueous LIBs. The battery tests were carried out in two potential ranges (2.0 - 4.0 V and 1.5 - 4.0 vs Li/Li^+). In addition, *ex situ* measurements (XRD, MP-AES, XPS, XAS) of discharged electrodes were performed.

3.3.2. Summary of main results

Potassium vanadates were synthesized by the LPE-IonEX method (liquid-phase exfoliation with ion exchange), which was proposed in [A1]. Herein, two samples were studied, which were obtained at two different temperatures: 20°C (denoted as KVO-20) and 40°C (denoted as KVO-40).

XRD analysis revealed that both samples were single-phase, and the obtained diffraction patterns corresponded well with the monoclinic hydrated potassium hexavanadate phase. Further TGA and MP-AES analysis indicated that the chemical composition was $K_{2.44}V_6O_{16}{\cdot}0.65H_2O$ for KVO-20 and $K_{2.54}V_6O_{16}{\cdot}0.76H_2O$ for KVO-40. The chemical structure of potassium vanadates and crystal water was also confirmed by FTIR spectroscopy and the presence of characteristic bands associated with the vibrations of specific bonds, including V═O, V–O···K, and O-H. Insights into the valence states of vanadium ions in the samples were obtained through XAS and XPS analysis. The former refers to the bulk oxidation state, while the latter is a surface-sensitive method. The XAS results were consistent for both samples, indicating a vanadium oxidation state of +5. In contrast, XPS analysis showed the presence of V^{4+} species on the sample surfaces and revealed distinct differences between both samples. For KVO-20, the relative share of vanadium V^{4+} reached 10% and was 5 times higher than that for KVO-40.

The obtained samples were in the form of nanostructures and exhibited uniform belt-like morphology. It was observed that a higher synthesis temperature led to notably narrower and thinner structures. The widths of individual nanobelts ranged from 50 to 200 nm for KVO-20 and from 30 to 50 nm for KVO-40. The thickness varied from 10 to 40 nm for the sample obtained at 20°C and was below 10 nm for the sample obtained at higher temperature. In both samples, the length of the nanobelts reached a few micrometres. Differences in dimensions contributed to differences in specific surface area, and as expected, the specific surface area of KVO-40 (S_{BET} = 36.3 m^2g^{-1}) was significantly higher than that of KVO-20 (S_{BET} = 15.6 m^2g^{-1}). Subsequent TEM analysis revealed that the nanobelts were composed of alternating crystalline and amorphous regions, and for both samples, "fringe-free" domains were observed between clearly visible lattice fringes. Furthermore, "fringe-free" domains were more frequently observed in

KVO-20 than in KVO-40. The results from TEM analysis also indicated that the obtained nanobelts exhibit a preferred [010] growth orientation direction (b-axis) and width along the [100] direction (a-axis).

Finally, the obtained samples were tested as cathode materials for non-aqueous LIBs. The electrochemical performance was assessed within two potential ranges, 1.5–4.0 V and 2.0-4.0 V, at current densities ranging from 100 to 1000 mAg^{-1}. In the broader potential range, both KVO-20 and KVO-40 displayed similar specific discharge capacities, with values of 260 $mAhg^{-1}$ at 100 mAg^{-1} and 181 $mAhg^{-1}$ at 1 Ag^{-1}. In the narrower potential range, the specific capacity of KVO-20 was approximately 50 $mAhg^{-1}$ higher than that of KVO-40 and was equal to 225 $mAhg^{-1}$ at 100 mAg^{-1} and 153 $mAhg^{-1}$ at 1 Ag^{-1}. The cycling performance of the samples was further evaluated over 100 cycles at a current density of 1 Ag^{-1}. In the 1.5–4.0 V potential range, KVO-20 exhibited a high capacity retention of 99.9%, whereas KVO-40 showed a retention of 84.1%. In the narrower potential range, the specific capacity for KVO-20 increased from 153 to 164 $mAhg^{-1}$, while for KVO-40 decreased from 106 to approximately 90 $mAhg^{-1}$, with a capacity retention of 83.0%.

In summary, hydrated potassium vanadate nanostructures were successfully synthesized by the novel LPE-IonEx method. The proposed method offers easy operation (reaction temperature below 40°C, water as a reaction medium, no need for complicated equipment) and excellent repeatability. Most importantly, it enabled the synthesis of single-phase, uniform nanobelts of $K_2V_6O_{16}\cdot nH_2O$, which were further used as cathode materials for LIBs. Two different samples obtained at two distinct temperatures (20°C and 40°C) were evaluated. These samples shared consistent layered structures (with almost identical lattice parameters), comparable water contents, and similar shapes and sizes of nanobelts. Samples varied significantly in terms of V^{4+} contribution (the relative share of vanadium V^{4+} surface species was 5 times higher for the sample obtained at 20°C and reached 10%) and specific surface area, which was more than two times higher for the sample obtained at 40°C.Generally for both samples, the determined specific surface area exceeded 10 m^2g^{-1}, which is considered a good level when compared to other vanadates commonly used in cathodes. Among these two factors, the first was pivotal for the electrochemical properties of the obtained potassium vanadates. The analysis revealed that during the subsequent charge/discharge cycle, the potassium ions in the $K_2V_6O_{16}\cdot nH_2O$ structure are replaced by lithium. It is assumed that this process occurs faster in the broader potential range and for the sample obtained at 20°C and finally leads to the formation of two phases: $K_{0.25}V_2O_5$ and $Li_{0.30}V_2O_5$. In the narrower potential range and for the sample obtained at 40°C, the structural changes are more gradual, which probably leads to the formation of the intermediate, unstable phase $Li_xK_yV_6O_{16}$. The sample obtained at 20°C was more stable during electrochemical tests and exhibited higher specific capacity values, which was associated with a significantly higher contribution of V^{4+} surface species. These V^{4+} surface species are believed to improve the electronic conductivity and enhance ion diffusion kinetics. In addition, their existence is probably connected with the formation of "fringe-free" domains, which further prevents the structure

of potassium vanadates from collapsing while replacing potassium with lithium within subsequent charge/discharge cycles.

Publication [A3] extends the current knowledge on the utilization of potassium vanadates as cathode materials in LIBs. Herein, the Li-ion storage performance of $K_2V_6O_{16}\cdot nH_2O$ was investigated for the first time. The obtained samples delivered a remarkable capacity of 260 $mAhg^{-1}$ at 100 mAg^{-1} and 181 $mAhg^{-1}$ at 1 Ag^{-1}. The obtained values are comparable to those reported for potassium vanadates and generally higher than those for recently described vanadates with other metal ions (e.g., $Na_2V_6O_{16}\cdot nH_2O$ nanowires [156] and $CaV_6O_{16}\cdot nH_2O$ nanoribbons [157]). The observed good electrochemical performance is attributed to the single-phase layered structure of the obtained potassium vanadates (with large interlayer spaces and the presence of K^+ ions and water molecules, which act as pillars) and elongated nanosized structures with well-developed surface areas and high uniformity. Moreover, the conducted studies confirm the importance of V^{4+} species on the electrochemical properties of vanadates and emphasize their beneficial effects on cycle stability and rate capability when used as cathode materials for LIBs. Importantly, the presented potassium vanadates were obtained using a facile synthesis method, which is highly advantageous compared to the previously reported, complicated synthesis methods that require high temperatures and multiple steps. Both, simple preparation method and interesting electrochemical performance makes $K_2V_6O_{16}\cdot nH_2O$ nanostructures valuable candidates for electrodes in LIBs.

3.3.3. Full content of the article

Title: The valance state of vanadium-key factor in the flexibility of potassium vanadates structure as cathode materials in LIBs

Authors: M. Prześniak-Welenc, M. Nadolska, K. Jurak, J. Li, K. Górnicka, A. Mielewczyk-Gryń, M. Rutkowska, A. P. Nowak.

Journal: Scientific Reports, 2022, 12, 18751

Impact factor: 4.996 (2022)

Ministerial Points: 140 pts

DOI: https://doi.org/10.1038/s41598-022-23509-x

I contributed by participating in samples synthesis and electrodes preparation. I carried out measurements using XRD, FTIR and N_2 adsorption measurements. I analysed the obtained results (e.g., Le Bail refinement, BET method) and correlated them with other techniques and electrochemical performances. I also assisted in XAS measurements. My contribution included preparation and development of the last manuscript version, response to the reviewers and funding acquisition.

scientific reports

Check for updates

OPEN

The valance state of vanadium-key factor in the flexibility of potassium vanadates structure as cathode materials in Li-ion batteries

M. Prześniak-Welenc[1]✉, M. Nadolska[1], K. Jurak[2], J. Li[3], K. Górnicka[1], A. Mielewczyk-Gryń[1], M. Rutkowska[2] & A. P. Nowak[2]

Potassium hexavanadate ($K_2V_6O_{16}{\cdot}nH_2O$) nanobelts have been synthesized by the LPE-IonEx method, which is dedicated to synthesis of transition metal oxide bronzes with controlled morphology and structure. The electrochemical performance of $K_2V_6O_{16}{\cdot}nH_2O$ as a cathode material for lithium-ion batteries has been evaluated. The KVO nanobelts demonstrated a high discharge capacity of 260 mAh g^{-1}, and long-term cyclic stability up to 100 cycles at 1 A g^{-1}. The effect of the vanadium valence state and unusual construction of the nanobelts, composed of crystalline and amorphous domains arranged alternately were also discussed in this work. The ex-situ measurements of discharged electrode materials by XRD, MP-AES, XAS and XPS show that during the subsequent charge/discharge cycle the potassium in the $K_2V_6O_{16}{\cdot}nH_2O$ structure are replacing by lithium. The structural stability of the potassium hexavandate during cycling depends on the initial vanadium valence state on the sample surface and the presence of the "fringe free" domains in the $K_2V_6O_{16}{\cdot}nH_2O$ nanobelts.

Over the past decades, vanadium-based oxides[1–8], and vanadium bronzes, in particular vanadium oxide bronzes[9–12] have been extensively studied, due to their high specific capacity, low cost, and better safety characteristics, as potential cathode materials for rechargeable lithium-ion batteries. Most vanadium bronzes with the general formula $A_xV_yO_z$, where A is virtually any cation of an alkali or earth alkali metal, have a stable structure for intercalation of Li^+ and Na^+. Therefore, they have been applied to non-aqueous and aqueous LIBs or Sodium-ion batteries[13,14], especially nanostructured form. The nanostructural morphology can shorten the diffusion path of ions and increase the contact area between the electrolyte and active materials[15]. The potassium vanadates are considered as positive electrode materials for LIBs since the 1980s when Raistrick and Huggins for the first time examined their electrochemical performance[16,17]. Since then, many potassium vanadates compounds have been investigated as cathode materials. Manev et al. have reported the electrochemical performance of series of potassium vanadates such as KV_3O_8, $K_2V_8O_{21}$, $K_3V_5O_{14}$, and KV_5O_{13}, and among them, the last one exhibits the best specific capacity of about 210 mAh g^{-1}, and good cyclability[18]. Baddour-Hadjean et al.[19], investigated the influence of local structure on electrochemical performance of KV_3O_8 and $K_{0.5}V_2O_5$ with layered structures, and $K_{0.25}V_2O_5$ with a tunnel framework isomorphic structure. They demonstrated, that the potassium-richer compound KV_3O_8 has good rechargeability despite a low discharge capacity (70 mAh g^{-1}), while the potassium-poorer bronze $K_{0.25}V_2O_5$ exhibits the high specific capacity (230 mAh g^{-1}) but slow and continuous capacity fade with cycling, meanwhile the $K_{0.5}V_2O_5$ combined the remarkable specific capacity 210 mAh g^{-1} with excellent capacity retention. It should be underlined, that the present studies of potassium vanadates electrochemical performance are mostly focus on $K_{0.25}V_2O_5$[20–23] and $K_{0.5}V_2O_5$[24–26] in hydrated or non-hydrated form. Recently, the $K_2V_6O_{16}{\cdot}nH_2O$ has attracted much attention as positive electrode material in metal-ion batteries. The crystal structure of potassium hexavanadates can be described as a hewettite type structure where the layered V_3O_8 backbone is formed by two basic structural units of VO_6 and V_2O_8 polyhedrons. In addition, the hydrated K ions are located between the layers, which stabilize the structure and facilitate intercalation/deintercalation of guest ions and act as "pillars"[27–30]. Furthermore, water molecules inside the potassium hexavanadate expand the

[1]Institute of Nanotechnology and Materials Engineering, Gdansk University of Technology, Narutowicza 11/12, 80-233 Gdansk, Poland. [2]Faculty of Chemistry, Gdansk University of Technology, Narutowicza 11/12, 80-233 Gdansk, Poland. [3]Key Laboratory for Thin Film and Microfabrication of Ministry of Education, Department of Micro/Nano-Electronics, Shanghai Jiao Tong University, Shanghai 200240, China. ✉email: marta.welenc@pg.edu.pl

interlayer distance, and promote ion diffusion[31]. Above mentioned features led to studies of $K_2V_6O_{16}{\cdot}nH_2O$ as a cathode material for calcium-ion[27] or zinc-ion[28,32] batteries. However, to the best of our knowledge, it has never been considered for lithium-ion batteries.

In this work, a comprehensive study of $K_2V_6O_{16}{\cdot}nH_2O$ as a cathode material for LIBs is reported for the first time. We investigated the influence of the vanadium valence state on the electrochemical performance in two potential ranges (2.0–4.0 V and 1.5–4.0 V). The hydrated potassium vanadate was obtained by an innovative method, based on the Liquide-Phase Exfoliation with Ion Exchange (LPE-IonEx)[33]. This method is dedicated to the synthesis of transition metal oxide bronzes with controlled morphology and structure, moreover opposite to the other synthesis method, allows obtain the single-phase compounds. The stability of potassium hexavanadate was explored based on ex-situ characterization involving the phase as well as the change in vanadium valence after cycling performance. We have demonstrated that the valence state of vanadium on the sample surface plays a crucial role in the structural flexibility and electrochemical performance of $K_2V_6O_{16}{\cdot}nH_2O$. Moreover, this compound is a promising candidate for a positive electrode for rechargeable lithium batteries and exhibits a remarkable specific capacity of 260 mAh g^{-1} combined with excellent capacity retention (> 99% after 100 cycles) among the potassium–vanadium bronzes.

Experimental

Synthesis. Potassium formate (99%, Sigma Aldrich), V_2O_5 (99.2%, Alfa Aesar) were used as reagents without further purification. Samples were prepared via the LPE-IonEx method. To 50 mL of 1 M solution of potassium formate in deionized water (DIW), 500 mg of V_2O_5 was added. The mixture was vigorously stirred for 48 h at two temperatures: RT (sample KVO-20) and 40 °C (sample KVO-40). From the initial solution, rusty red solid residues were collected by centrifugation. After washing several times with DIW, the product was dried overnight at 40 °C under reduced pressure (0.01 bar).

Characterization. X-ray diffraction patterns (XRD) were collected in the range 2θ of 5°–70° by a D2 Phaser diffractometer (Bruker) with CuK_α radiation (λ = 1.5404 Å). The FullProf Suite program was used to perform Le Bail refinements using Thompson–Cox–Hastings pseudo-Voigt peak shapes. The Fourier transform infrared (FTIR) spectra were recorded in the range of 400–4000 cm^{-1} on Perkin Elmer Frontier spectrophotometer. The surface morphology and fine grain structure were studied by a FEI Company Quanta FEG 250 scanning electron microscope (SEM) and an FEI TECNAI G2 F20 transition electron microscopy (TEM). Nitrogen adsorption–desorption isotherms were measured on a surface area analyser NOVAtouch™ 2 (Quantachrome Instruments) at 77 K. Prior to the measurements, samples were degassed at 40 °C for 12 h under dynamic vacuum. The specific surface area was calculated using the Brunauer–Emmett–Teller (BET) linear equation in the relative pressure range (p/p_0) from 0.1 to 0.3 from six points. The correlation coefficient of the linear regression was not less than 0.99. Thermogravimetric analysis (TG) was carried out under argon atmosphere with a flow rate of 60 ml/min in the temperature range 40–350 °C (heating rate 5 °C/min) using STA 449 F1 (Netzsch). The high-resolution X-ray photoelectron spectroscopy (XPS) analysis was performed using an Escalab 250Xi device (ThermoFisher Scientific), equipped with a mono-chromatic AlKα source. Measurements were carried out at 25 eV pass energy with 0.05 eV energy step size. The X-ray spot size was 250 µm. The calibration of the XPS spectrum was done using the characteristics peak of adventitious carbon C1s at 284.6 eV[34]. The X-ray absorption (XAS) measurements were performed at the ASTRA beamline at SOLARIS National Synchrotron Radiation Centre, Cracow, Poland. The V K-edge XANES of powder samples and after-cycled electrodes were obtained in transmission mode in the range 5265 to 5550 eV. Concentration of the elements in the samples determined using atomic emission spectrometry with microwave plasma atomisation (MP-AES) supplied by Agilent. K, Li, V standard solution were obtained from Sigma Aldrich, Ms Spectrum and J.T. Baker, respectively. The determination of the elements in the samples was carried out at specific wavelengths (Li—670.784 nm, K—766.491 nm, and V—437.923 nm).

Electrochemical measurements. The electrodes were prepared from a slurry containing a 7:2:1 weight ratio of KVO-20 or KVO-40, carbon black (Super P®, Timcal) as conducting agent, and 10 wt% polyvinylidene fluoride (Solef® 6020) as a binder in N-methylpyrrolidone (AlfaAesar). The slurry was spread on the aluminum foil. The foil was dried under a dynamic vacuum in an oven (Glass Oven B-595, Büchi) for 24 h at 90 °C. Next, the discs of 10 mm diameter were cut from the film. The average loading mass of electrode material was ~ 0.5 mg. Dried disc electrodes were used in two-electrode pouch cells with lithium foil as a counter and reference electrodes (99.9% purity, 0.75 mm thickness, Alfa Aesar) in 1 M $LiPF_6$ in EC:DMC ratio 1:1 (LP30 Merck) as the electrolyte, glass fiber (Schleicher & Schüll) as the separator, and polyester film as an adhesive tape (RD-697, PPI, Ireland). The battery tests, including galvanostatic polarization as well as cyclic voltammetry were performed using the ATLAS 0961 MBI (Poland) multichannel battery testing system within the potential range from 1.5 to 4.0 V, and from 2.0 to 4.0 V vs. Li/Li^+ with a scanning rate of 0.01, 0.02, 0.05 and 0.1 mV s^{-1}. Galvanostatic intermittent titration technique (GITT) was applied after for the first charge/discharge cycle with a current density of 100 mA g^{-1}, pulse duration of 1800s and 2 h relaxation time. The cut-off potential was 1.5 V for charging and 4.0 V for discharging.

Results and discussion

Structural analysis. The XRD patterns of sample KVO-20 and KVO-40 (Fig. S1, ESM) can be indexed within the monoclinic $K_2V_6O_{16}{\cdot}1.5H_2O$ phase (JCPDS no. 00-051-0379). The lattice parameters, determined from Le Bail refinement, are given in Supporting Information (Fig. S2, Table S1, ESM).To confirm the lattice water presence in the samples, TG analysis was performed (Fig. S3). The weight loss between 40 and 100 °C is attributed to the evaporation of physisorbed water and between 100 and 350 °C to chemisorbed structural

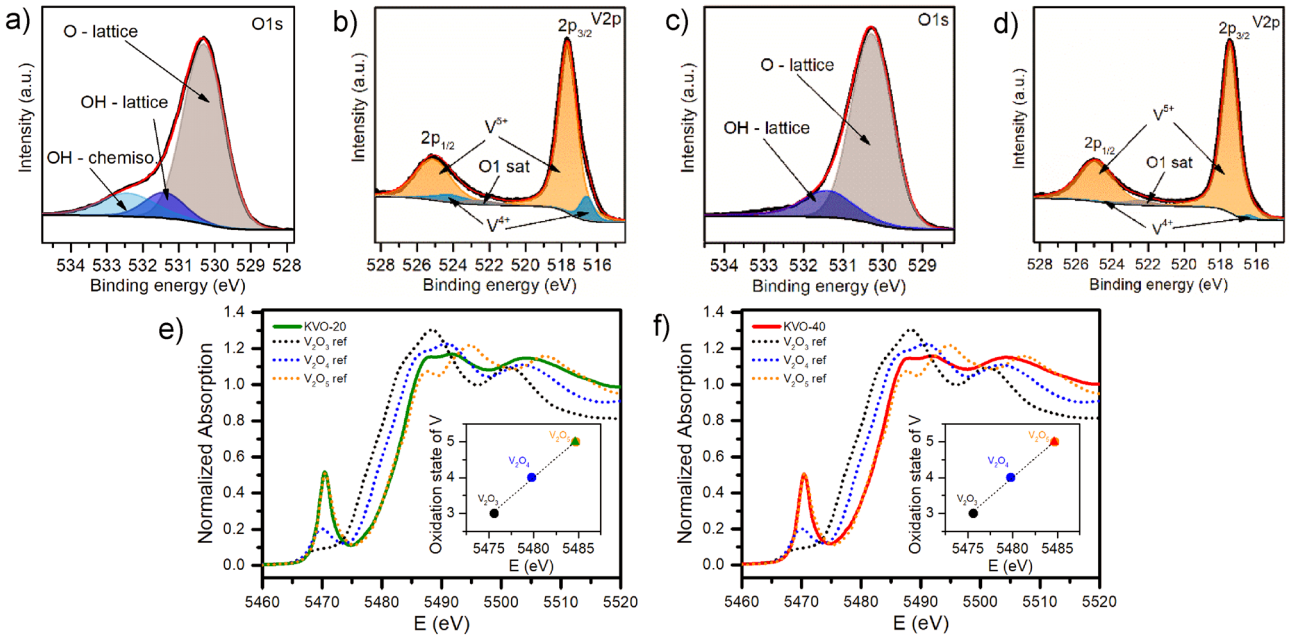

Figure 1. (**a–d**) High resolution XPS spectra of the O 1s and V 2p regions for KVO-20 (**a,b**) and KVO-40 (**c,d**), (**e,f**) V K-edge the XANES for KVO-20 (**e**) and KVO-40 (**f**), respectively (the insets show the relation between vanadium oxidation state and the edge position).

water[14]. The lattice water attributed loss for KVO-20 is 1.75 wt% and 2.05 wt% for KVO-40, which corresponds to 0.65 and 0.76 molecules of water per $K_2V_6O_{16}$ formula unit, respectively. The FTIR spectra of the samples are shown in Fig. S4 in the ESM. The bands at ~ 1005 and ~ 970 cm^{-1} can be assigned to V=O vibrations, while those at 525 and 590 cm^{-1} to the symmetric and asymmetric stretching of V–O–V[30]. The band at 730 cm^{-1} corresponds to bridging V–O···K stretching[35]. The band at 950 cm^{-1} visible for both samples, suggests the existence of the OH bridge between two metals, likely vanadium[36]. In addition, bands related to the water molecules (stretching and bending vibrations at ~ 3450 cm^{-1} and ~ 1620 cm^{-1}, respectively) can be observed for both samples[30]. Next, the XPS technique was used to investigate the chemical composition and the valence state of vanadium ions in the samples. The O 1s core-level spectra show deconvoluted peaks (530–532 eV), three for sample KVO-20 (Fig. 1a), and two for KVO-40 (Fig. 1c). The lower binding energy at 530.3 eV corresponds to O–lattice[27]. The second peak centered at 531.4 eV is attributed to the loosely bounded oxygen ions on the surface, namely, OH^- groups[37]. The third peak centered at 532.5 eV, observable only for sample KVO-20, is ascribed to chemisorbed OH^- ions on the surface[38]. The XPS for V 2p (Fig. 1b,d) shows two peaks located around 525 and 517.7 eV, which are attributed to V $2p_{1/2}$ and $V2p_{3/2}$, respectively. The $V2p_{3/2}$ band for both samples shows asymmetry shaped with a very weak shoulder line on the lower binding energy side, two different components of $V2p_{3/2}$ are apparent. The strong peak around 517.5 eV and the weak peak around 516.5 eV were corresponding to the V^{5+} and V^{4+} respectively[39]. These components are also present for V $2p_{1/2}$ peak, the two peaks centered at 525 eV and 524 eV were assigned to the V^{5+} and V^{4+},respectively (the Fig. S5a,b, ESM). The peak located around 522 eV was attributed to the O1s satellite[40]. Based on the area of the fitted curves, the relative atomic ratio of V^{4+}/V^{5+} present on the sample surface were estimated to be 0.10 for sample KVO-20 and 0.02 for sample KVO-40. The surface vacancies interact with the H_2O molecules, which leads to water chemisorption[41]. Therefore, due to the 5-times smaller concertation of V-vacancy on the KVO-40 sample surface, the peak centered at 532.5 eV (chemisorbed OH^- ions) is very likely to be overlapped with the peak located at 531.4 eV (OH–lattice).

The XPS spectrum in K 2p core level binding energy (Fig. S5c,d, ESM) show two characteristic peaks of the $2p_{3/2}$ and $2p_{1/2}$ spin–orbit of K^+ coupled energy states, centered at 292.9 eV and 295.7 eV, respectively, with an energy separation of 2.8 eV. The BE of potassium ions strongly depends on the degree of hydration, with increased concentration of water, i.e. the K 2p BE in KOH is known to be shifted to the lower energy[37]. The $2p_{3/2}$ spin–orbit for $K_2V_6O_{16}{\cdot}2.7H_2O$ is centered at 291.3 eV[27], while for $K_2V_6O_{16}{\cdot}1.5H_2O$ is located at 292.6 eV[30]. The position of the K^+ spin–orbit for both samples confirms the presence of fewer than 1.5 molecules of water in the structure, which is in good agreement with TG results. The survey spectra show that both samples consist only K, V, and O, and no other elements were detected (Fig. S5e,f, ESM). The analysis of the vanadium valence state in the bulk were characterized by the X-ray absorption spectroscopy. Figure 1e,f show the X-ray absorption near-edge structure (XANES) spectra of the V K-edge for KVO-20 and KVO-40, respectively. Both samples have the same pre-edge adsorption peak position, which is attributed to the forbidden electronic transition 1 s → 3d[42]. The vanadium K-edge position for vanadium oxides (V_2O_3, V_2O_4, and V_2O_5) show near to linear relation between the V oxidation state and the edge position (see insets on Fig. 1e,f). With for higher oxidation state the edge position shifts to a higher energy. The relative contributions in a mixed system can be estimated by performing a fit with a linear combination of known references. The determination of the oxidation state typically refers to a shift of the absorption edge[43]. To determine the "edge position", the maximum of the first derivative of the XANES spectrum

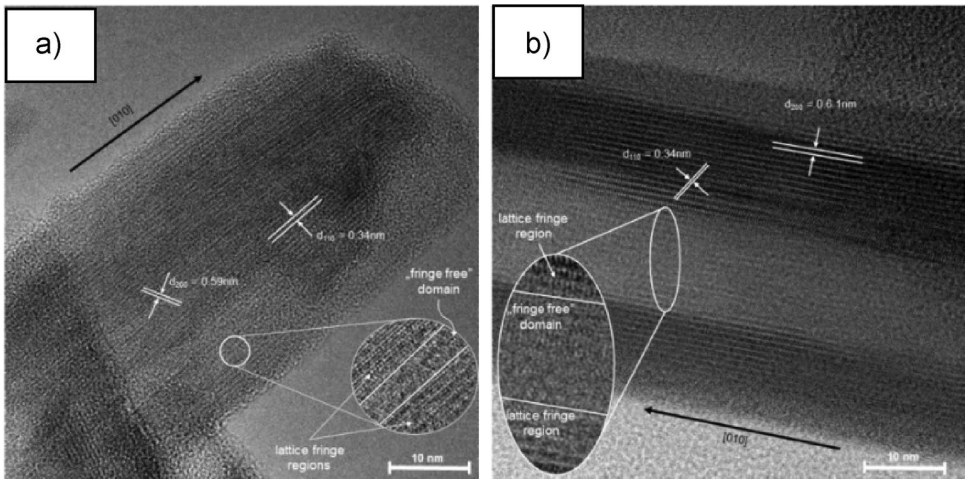

Figure 2. High-resolution TEM image of KVO-20 (**a**) and KVO-40 (**b**).

was used[44]. The maximum of the first derivative of the KVO-20 and KVO-40 XANES spectra were observed near to the maximum of the V_2O_5 reference (Fig. 1). This suggest that the valance state of vanadium is 5+. It should be noticed that the transmission mode XAS analysis gives information about the bulk, while the XPS is surface-sensitive method, which explain the differences in the obtain results. It is commonly reported that the amount of V^{4+} can reach up to 10% of the total amount of vanadium ions on the surface, especially when the synthesis is performed by wet-chemical method[6]. Summarizing, the chemical formula of the KVO samples based on MP-AES, XPS, XAS and TGA results is for KVO-20: $K_{2.44}V_6O_{16}{\cdot}0.65H_2O$ and for KVO-40: $K_{2.54}V_6O_{16}{\cdot}0.76H_2O$.

The sample KVO-20 shows a belt-like structure, where single nanobelts have a width 50–200 nm, a thickness of 10–40 nm, and a length of few micrometers (Fig. S6a). With increasing synthesis temperature, the nanobelts become thinner, and their cross-section decreases. The width of sample KVO-40 (Fig. S6b) nanostructures are between 30 and 50 nm, and the thickness is below 10 nm. Thinner and narrower belts result in a more developed surface area: the specific surface area was more than two times higher for KVO-40 ($S_{BET} = 36.3\ m^2\ g^{-1}$) than for KVO-20 ($S_{BET} = 15.6\ m^2\ g^{-1}$) (Fig. S6c). The TEM images of a single nanobelt of KVO-20 (Fig. 2a) and KVO-40 (Fig. 2b) reveal a region of "fringe-free" domains between clearly distinguishable lattice fringe regions. A similar structure with fringe-free domains was observed previously for $Na_2V_6O_{16}{\cdot}3H_2O$ nanorods[45]. This suggests that the nanobelts are composed of crystalline and amorphous domains arranged alternately. Moreover, the "fringe-free" domains were observed more often for KVO-20 than KVO-40. However, the hydrous layered potassium hexavanadates are unstable under the strong electron beam irradiation condition, leading to the destruction of their crystallines[29]. Therefore, to confirm that these are not artefacts, the picture was taken at the same position in the interval of about 10 s.

The regions with the fringe lattice and the "fringe-free" domain arranged alternately are present before and after irradiating with the electron beam (Fig. S7a,b, respectively, ESM). The formation of crystalline/amorphous structure is probably caused by the delamination process during sample synthesis. The structural defects present lead to structure collapse during this process, and the fringe-free domains creation. The concentration of fringe-free domains is dependent on synthesis temperature. At higher temperatures, it will be smaller because a more uniform crystal structure will be created. The observed lattice spacing for the crystalline region was calculated to be 0.34 nm and 0.59 nm for sample KVO-20 and 0.34 nm and 0.61 nm for sample KVO-40, which closely correspond to the (110) and (200) planes of the monoclinic $K_2V_6O_{16}{\cdot}1.5H_2O$, respectively. Thus, the hydrated potassium vanadate nanobelts show a preferred [010] growth orientation direction (b-axis) and the width along the [100] direction (a-axis). The surface of the nanobelts is mainly formed by the (001) and (110) planes (Fig. S8b in the ESM). The structure of $K_2V_6O_{16}{\cdot}1.5H_2O$ (see Fig. S8a, ESM) consists of the infinite V–O chains along the b-axis with a short V–V distance of 0.18 nm. This is indicating the high-anisotropic internal structure with the highest stacking density along this direction. In comparison, the a-and c-axis have longer average V–V distances close to 0.30 and 1.12 nm, respectively and are characterized by a lower stacking density. Therefore, the growth rates for the a-and c-axis are slower than for the b-axis. As a result, the hydrated potassium vanadate nanobelts grow along the [010] direction. Additionally, along the c-axis, connected double chains have loosely-packed tunnel-interoperating structures, and considerably large interlayer distances form along the a-axis[46].

Electrochemical properties. Cyclic voltammetry of the KVO-20 and KVO-40 electrodes at a sweep rate of $V = 100\ \mu V\ s^{-1}$ is shown in Fig. 3a,b. One may see that during the reduction process, two current maxima are observed for both electrode materials. The position of those maxima depends on the type of electrode material: 2.37 V, 2.57 V (Fig. 3a) or 2.61 V (Fig. 3b) (with a shoulder at 2.78 V) for KVO-20 and 2.27 V, 2.53 V (Fig. 3a) or 2.52 V (Fig. 3b) (with a shoulder at 2.80 V) for KVO-40. The peaks located between 2.6 V and 2.8 V are attributed to the reduction of vanadium ions from V^{5+} to V^{4+}. The current maximum at ~ 2.4 V is originating to vanadium V^{5+} to V^{4+} reduction and partial reduction of V^{4+} to V^{3+}[20]. The former reaction is a dominant process. The shift in position is very likely to be attributed to the difference in the vanadium valence state of active mate-

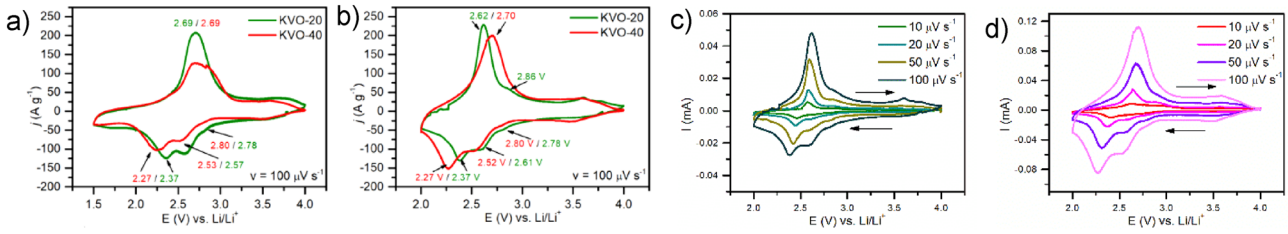

Figure 3. Cyclic voltammetry curves of KVO-20 and KVO-40 electrode materials at a scan rate of 100 μV s^{-1} over 1.5–4.0 V (**a**) and 2.0–4.0 V (**b**) potential window. Cyclic voltammetry curves at different scan rates for (**c**) KVO-20 and (**d**) KVO-40.

rial. The reduction of V^{5+} to V^{4+} occurs for the sample KVO-20 at the lower potentials since the concentration of V^{4+} ions in this sample is five times greater than for KVO-40. The presence of two well-defined current maxima is related to the insertion of two lithium ions atoms into the KVO-20 and KVO-40 layers. It is very interesting that during the oxidation process there is only one anodic maximum for both electrode materials. The anodic current maximum is at potential ca. 2.70 V. It might be attributed to the fact that during oxidation the lithium ions are removed from vanadium oxide layers simultaneously. To determine the charge storage mechanism the method proposed by Liu et al. was performed[47]. In general, two electrode processes occur during the examination of the sweep-rate dependence of the current response during cyclic voltammetry procedure: capacitive (a surface mechanism) and diffusion dependent. The total current response of an electrode is a mixture of these mechanisms:

$$i(\mathrm{V}) = \mathrm{k}_1 \cdot v + \mathrm{k}_2 \cdot v^{1/2}, \tag{1}$$

where $k_1 \cdot v$ is the capacitance related process while $k_2 \cdot v^{1/2}$ is attributed to diffusion-controlled mechanism. One should take into account that in a real system simple mechanism does not occur[48]. To evaluate the charge storage contribution the analysis of the sweep-rate of voltammetric currents was performed, see Fig. 3c,d. Detailed analysis is presented in Fig. S9. The shaded regions show the percentage contribution of capacitive currents in the total charge storage. It is seen that even for low sweep rates the charge storage is mainly attributed to the surface mechanism, and equal to about 80%. We also performed the GITT measurements to calculate diffusion coefficient of KVO-20 and KVO-40 electrode materials (Fig. S10). For KVO-20 (Fig. S10a, ESM) and KVO-40 (Fig. S10b, ESM) during reduction process the value of diffusion coefficient continuously increases. During oxidation, the increase is seen for KVO-20 in the full range while for the KVO-40 only till 2.6 V followed gradual decrease with the increase of the voltage. There is a visible relation between the values of diffusion coefficient and redox couple activity of electrode materials. The current responses related to redox/oxidation couple activity is in the potential range from around 2.1 to 2.8 V. There is an increase in the diffusion coefficient within this range for both processes. It shows that the structure of KVO seems to be flexible for lithium insertion/extraction. Such flexibility may be attributed to inclination of potassium ions to be replaced by lithium ions to obtain an equilibrium. The KVO-20 and KVO-40 materials were tested over two potential ranges 1.5–4.0 V and 2.0–4.0 V, at current density ranging from 100 to 1000 mA g^{-1}. The relation between specific capacity and applied current density is given in Fig. 4a,b). One may see that during the first five cycles at current density $j = 100$ mA g^{-1} for both electrode materials the value of specific capacity slightly increases. Comparing the specific capacity of electrode materials charged/discharged in the two potential ranges, obtained values are about 50 mAh g^{-1} higher for 1.5–4.0 V in than for the 2.0–4.0 V. The specific discharge capacity of KVO-20 and KVO-40 electrode material for $j = 1$ A g^{-1} is 181 mAh g^{-1} for both materials investigated in the potential range from 1.5 to 4.0 V (Fig. 4a). The obtained value is higher than specific discharge capacity reported recently for similar vanadium oxide- based materials such as $Na_2V_6O_{16}{\cdot}xH_2O$ nanowires[49,50], and $CaV_6O_{16}.3H_2O$ nanoribbons[51]. In the narrower potential range, the specific discharge capacity was equal to 153 mAh g^{-1} and 110 mAh g^{-1} for KVO-20 and KVO-40, respectively (Fig. 4b). It is noteworthy that there are no significant differences in specific capacities for KVO-20 and KVO-40 electrode material polarized in 1.5–4.0 V potential range for different current densities. Moreover, after applying the current density of 1 A g^{-1}, both electrode materials showed similar remarkable specific capacity values for the current density of 100 mA g^{-1} (cycles from 21 to 25) equal to 260 mAh g^{-1}.

Unfortunately, the KVO-40 electrode material exhibited much worse electrode performance for the potential range 2.0–4.0 V. It is In analogy to similar described compounds i.e. $Na_{2+x}V_6O_{16}$ system[52], it is possible that only up to 2 lithium ions can be up taken by KVO. During intercalation lithium ions move into the structure according to reactions:

$$\mathrm{K}_{2.44}\mathrm{V}_6\mathrm{O}_{16} \cdot 0.65\mathrm{H}_2O + \mathrm{Li}^+ + 2e^- = \mathrm{Li}_2\mathrm{K}_{2.44}\mathrm{V}_6\mathrm{O}_{16} \cdot 0.65\mathrm{H}_2O \text{ for KVO} - 20, \tag{2}$$

$$\mathrm{K}_{2.54}\mathrm{V}_6\mathrm{O}_{16} \cdot 0.76\mathrm{H}_2O + \mathrm{Li}^+ + 2e^- = \mathrm{Li}_2\mathrm{K}_{2.54}\mathrm{V}_6\mathrm{O}_{16} \cdot 0.76\mathrm{H}_2O \text{ for KVO} - 40. \tag{3}$$

Consequently, the theoretical capacity is 80 $mAhg^{-1}$ and 79 $mAhg^{-1}$ for KVO-20 and KVO-40, respectively. In the studied case the specific capacity for both cathode materials is much higher than the theoretical value. Thus, the comparison of theoretical capacity with obtained capacity is misleading. The theoretical capacity refers to insertion of lithium ions while the total capacity is a sum of capacities originating from intercalation (diffusion

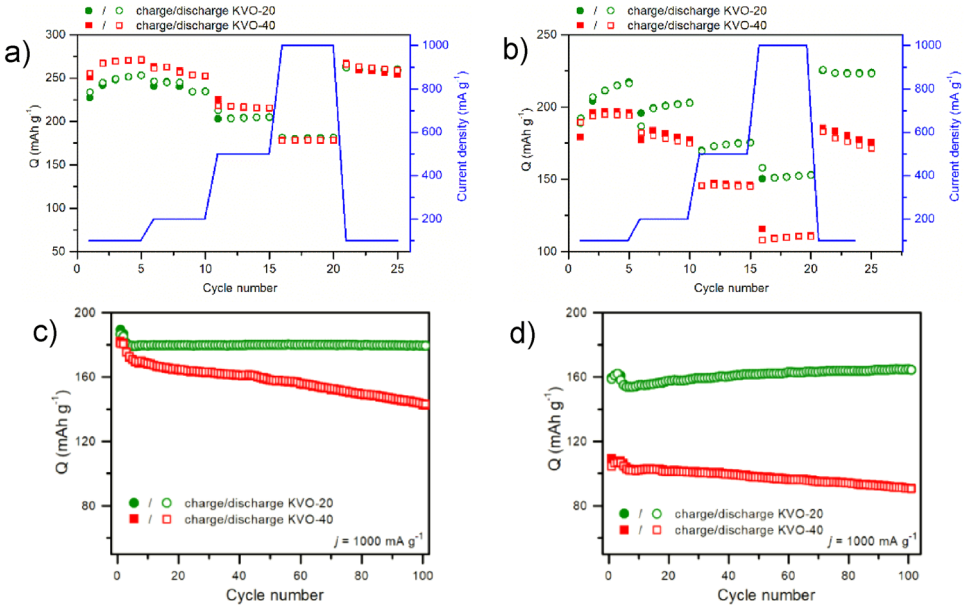

Figure 4. Electrochemical performance of KVO-20 and KVO-40 electrode materials: Galvanostatic tests over the voltage range of (**a**) 1.5–4.0 V and (**b**) 2.0–4.0 V. The charge/discharge tests at j = 1 A g^{-1} for 100 cycles in (**c**) 1.5-4 V and (**d**) 2.0–4 V.

of lithium ions into the material structure) and charge storage on the surface of the material (pseudofaradaic). The obtained results evidenced that a surface mechanism is a dominant process, and is equal to about 80%, see Fig. S9 in the ESM.

The charge storage mechanism by KVO system is pseudofaradaic origin where the charge is stored via redox reaction mainly at the surface[53] and not into the structure of the material. The charge storage contribution is almost the same for KVO-20 and KVO-40 electrode materials. It evidences that in terms of chemical formula both materials are similar. Moreover, the differences in specific surface area (15.6 m^2 g^{-1}, and 36.3 m^2 g^{-1} for KVO-20 and KVO-40, respectively) do not influence the charge storage mechanism. Thus, the obtained differences of the specific capacity values are rather due to the differences in the crystallographic structure than in the difference in chemical composition. In other words, the slight differences in chemical composition affect the crystallographic structure that has a huge impact on electrochemical performance. Such difference might likely be due to the differences in the initial vanadium valence state on the sample surface of KVO-20 and KVO-40 samples. It was reported that the valence state of vanadium plays a crucial role in the electrochemical performance of vanadium oxide as cathode materials[31]. The presence of V^{4+} is beneficial for ion insertion/extraction, as that the presence of an appropriate number of tetravalent vanadium would is beneficial for the electronic transfer[54]. Considering the high values of the specific capacity at 1 A g^{-1}, extended cycles at a given current density were performed to investigate the cycling performance (Fig. 4c,d).The electrochemical behavior of KVO-20 and KVO-40 electrode materials for 100 charge/discharge cycles suggests that charge storage might be of capacitive origin in both cases. The KVO-20 electrode material seems to be more stable during electrochemical tests in both potential ranges and additionally exhibit higher specific capacity values. The 5th cycle discharge capacity in the 1.5–4.0 V potential range is 179 mAh g^{-1}, and the capacity retention is 99.89% for the 101st cycle (Fig. 4c). In the narrower potential range, the specific capacity shows an increasing trend between the 5th and 101st cycle, from 154 to 164 mAh g^{-1}. This phenomenon might be attributed to structural changes in the sample during cycling. In the case of KVO-40 electrode material for the 1.5–4.0 V potential range, the specific capacity equals 170 mAh g^{-1} for the 5th discharge cycles and the 101st cycle drops to 143 mAh g^{-1} with the capacity retention of about 85% (Fig. 4d). In the narrower potential range, where the initial discharge capacity is 106 mAh g^{-1}, the capacity retention between the 5th and 101st discharge cycle is similar and equals 83%. Intercalation of two Li ions into vanadium compounds, results in a series of crystalline-to-crystalline transitions. The intercalation of the first Li-ion, brings only minor structural changes, while the insertion of the second Li-ion leads to significantly different structures, often irreversible[55]. We assume that such process may led to off-stoichiometric defects that affects lithium intercalation/extraction process and specific capacity of the material. Similar phenomenon was previously observed for $LiFePO_4$ by Ceder et al.[56]. They noticed that cycling at higher current density affects the specific capacity of studied electrode materials. The presence of plateau on both galvanostatic profiles is typical for the faradaic reaction taking place in both systems even after cycles (Fig. S12). The position of the plateau agrees with the current maxima observed in cyclic voltammetry curves (Fig. 3a,b). Nevertheless, the investigation of the structural changes of cathode material after cycling with the utilization of the ex-situ XPS, XAS, XRD, MP-AES were performed. The electrodes were examined at a fully discharged (oxidized) state. Figure 5 shows the XRD pattern of fresh electrode material and after 100 galvanostatic tests cycles in both potential ranges. The structure of the KVO-20 and KVO-40 samples did not preserve pristine crystal structures after cycling. However, the clear

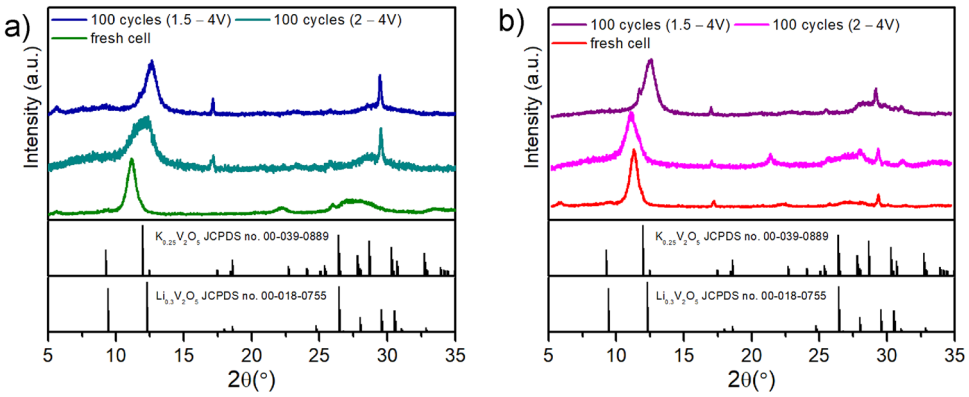

Figure 5. Ex-situ XRD pattern of the (**a**) KVO-20 and (**b**) KVO-40 electrode at the pristine state and a fully discharged state electrode after 100 charges/discharge test at j = 1 Ag^{-1} in two potential ranges.

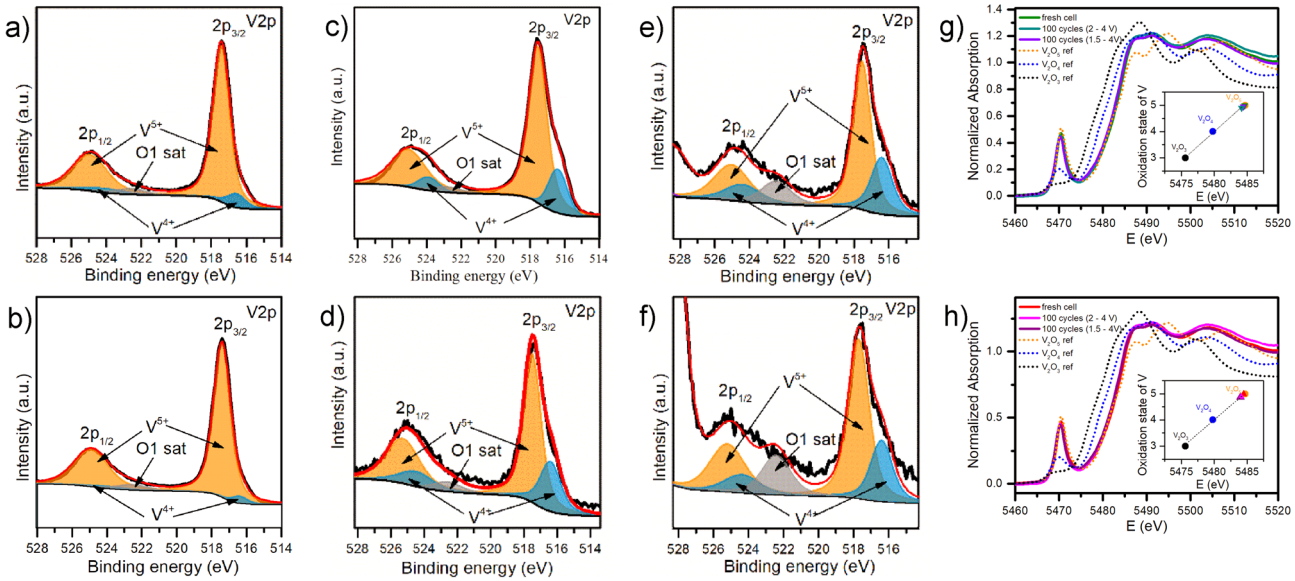

Figure 6. (**a–f**) *Ex-situ* high resolution XPS spectra of the V2p regions in pristine (**a**) KVO-20, and (**b**) KVO-40 electrode, and a fully discharged state of the KVO-20 and KVO-40 electrode after 100 charges/discharge test at j = 1 A g^{-1} in two potential ranges: 2.0-4 V (**c, d**) for KVO-20 and KVO-40 respectively), and 1.5–4 V (**e,f**) for KVO-20 and KVO-40 respectively); (**g,h**) Ex-situ V K-edge XANES spectra of the pristine electrodes and a fully discharged state after 100 charges/discharges test at j = A g^{-1} in two potential ranges: 2.0–4.0 and 1.5–4.0 for (**g**) KVO-20 and (**h**) KVO-40, respectively.

diffraction peaks are visible (Fig. S13), which confirms the preservation of the crystalline structure of the samples after charge/discharge cycles. After 100 cycles in the 2.0–4.0 V range, the (002) peak was shifted from 11.15° to 12.10° for sample KVO-20 and 10.90° for sample KVO-40. The shift of the (002) peak position to lower angle values for KVO-40 electrode indicated that during uptake/removal of Li^+ from KVO-40 lattice, a small amount of Li^+ might have remained trapped in the crystal structure[54]. For the broader potential range, the (002) Bragg peak was shifted from 11.15° to higher angles for both samples. For the sample KVO-20 the peak is located at 12.54° after 100 cycles. Whereas, for the sample KVO-40, the (002) Bragg peak is shifted to 12.46° after 100 cycles.

The ex-situ XPS analysis (Fig. 6) showed that the ratio of $V^{4+}/V^{5+}$is increasing after cycling in comparison to the initial samples (Table S2). The significant change of V^{4+} concentration, over 20 times greater, is observed for KVO-40 material after 100 cycles in 2.0–4.0 V potential range, whereas for KVO-20 material, the V^{4+}/V^{5+} ratio is doubled. After charge/discharge cycles in broader potential range, the V^{4+}/V^{5+} ratio is the same for both samples, and equal to 40 after 100 cycles. The ex-situ V K-edge XANES analysis (Fig. 6) showed that the vanadium oxidation state of pristine electrodes is the same as for the powdered sample and is equal to 5+. After 100 charged/discharged cycles in both potential ranges, the average oxidation state of V is lower than for V_2O_5. Based on the maximum of the first derivative of the XANES spectrum, the mixed valence state of vanadium for electrodes after cycling was estimated. After 100 cycles in the 2.0–4.0 V potential range, the valence state of vanadium in the KVO-20 material (Fig. 6g) is 4.95, where after cycling in wider potential range equal to 4.90. Thus, the V^{4+} concentration equals 5% and 10%, respectively. Whereas, for the KVO-40 material (Fig. 6h) after 100 cycles in both potential ranges, the vanadium oxidation state is around 4.9, it suggests that about 10% of V^{4+} ions are

in the bulk KVO-40 material. The shift of the (002) Bragg peak evidenced that stoichiometry of fresh material undergoes structural changes due to this replacement. To confirm this phenomenon, the MP-AES measurements (microwave plasma-atomic emission spectroscopy) were performed. The MP-AES analysis confirmed that the relative atomic ratio of V/K in both samples is increasing after galvanostatic cycles, and depends on the potential range and number of cycles (Table S2). Moreover, the presence of the lithium was detected, for all samples. The relative atomic ratio of V/Li is close to one after cycles in broader potential range, whereas for narrower potential range is almost 5-times greater The XRD pattern of KVO-20 after CD cycles in narrower potential range agrees with two phases: $K_{0.25}V_2O_5$ (JCPDS no. 00-039-0889) and $Li_{0.30}V_2O_5$ (JCPDS no. 00-018-0755). This indicated that potassium was gradually removed from the crystal structure in the subsequent cycles and replaced with lithium, and probably intermediated phase ($Li_xK_yV_6O_{16}$) is created. In $K_{0.25}V_2O_5$ the potassium is known to act as a "pillar" connecting the adjacent V–O layers and leading to more stable interlayer structure as well as preventing the relative slippage of two adjacent V–O layers[12,22,23].

We believe that this flexibility of the KVO-20 structure was caused by the higher contribution of V^{4+} ions on the sample surface, which could facilitate the potassium removal from the lattice. This phenomenon was probably related to the observation of increasing specific capacity with cycles, see Fig. 4a,b. The MP-AES analysis (Table S3, ESM) confirmed that the relative atomic ratio of V/K changed from 3.9 (pristine electrode) to 6.89 (potential range 1.5–4 V, Fig. 4a) and to 5.38 (potential range 1.5–4 V, Fig. 4b). Moreover, the atomic ratio of V/Li equals 1.40 and 4.70 for sample KVO-20 after 100 cycling in the 1.5–4.0 V and 2.0–4.0 V potentials range, respectively. These results suggest that structural changes of the KVO-20 sample occur faster in the 1.5–4.0 V potential range, and the phase with higher capacity formed at the beginning of the cycling. Therefore, we do not observe a gradual increase of specific capacity (Fig. 4a). In the case of the narrower potential range, the structural changes occurred gradually ($Li_xK_yV_6O_{16}$, with continuous increase of x and decrease of y, cycle per cycle). Interestingly, the positions of indexed reflections on the XRD pattern suggested that after cycling, the KVO-40 material in 2.0–4.0 V potential range preserved the pristine structure, but the relative amount of potassium was smaller in comparison with no cycled material, and the presence of lithium in the structure was detected. Additionally, based on the XPS and XAS data, the contribution of V^{4+} was more dominant in the KVO-40 material after cycling. It was likely related to the fact that the higher capacity fading was observed for KVO-40 material in comparison with KVO-20. The lithium concentration significantly increased when KVO-40 material cycled in both potential ranges were compared. The XRD patterns of KVO-40 after galvanostatic cycles in broader potential range corresponded to the $Li_{0.30}V_2O_5$ (JCPDS no. 00-018-0755). This suggests that in the 1.5–4.0 V potential range, the $K_2V_6O_{16}{\cdot}nH_2O$ structure is more flexible. However, the MP-AES results showed that the K to Li exchange occurs faster for KVO-20 material than for KVO-40 material. Therefore, after reaching ~ 100 cycle in wider potential range, KVO-20 material exhibits more gradual capacity drop than KVO-40 material (Fig. 4c), because the irreversible structural changes occur faster. We assumed that the initial V^{4+}/V^{5+} ratio has an impact on these processes. The KVO-20 sample has a 5-times greater concentration of V^{4+} on the surface than for sample KVO-40. We believe that this initial V^{4+} concentration is crucial to structural changes during cycling. Moreover, the structural changes in the sample KVO-40 lead to a faster increase of V^{4+} vacancies, both on the surface and in the bulk, which relates to constant structure damages, and the capacity is constantly declining. In the case of sample KVO-20, the concentration of V^{4+} is changing gradually. Moreover, the greater quantity of fringe-free domains in the KVO-20 sample prevents the structure from collapsing during replacing potassium with lithium within subsequent charges/discharges cycles. The comparison of electrochemical performance of the KVO-20 and KVO-40 electrode material with potassium vanadium compounds for LiBs is given in Table S4.

Conclusions

In summary, the single-phase $K_2V_6O_{16}{\cdot}nH_2O$ nanostructures were successfully synthesized by the novel LPE-IonEx method. Obtained samples have the same structure, comparable water content, similar shape, and size but they vary with V^{4+} contribution. For the first time, the Li-ion storage performance of layered hydrated potassium hexavanadate nanobelts cathode was reported, which delivered a remarkable capacity of 260 mAh g^{-1} at 100 mA g^{-1} and good cycling performance with a high capacity retention of 99.98% after 100 cycles at 1 A g^{-1}. The electrochemical performance, as well as the structural flexibility of $K_2V_6O_{16}{\cdot}nH_2O$, strongly depends on the vanadium valence state. The charge on hydrated potassium vanadate is stored via redox reaction mainly at the surface. Thus, via the presence of the V^{4+} on the surface, the electronic transfer is facilitated, and higher capacity is achievement. Moreover, the higher V^{4+} surface concertation leads to faster structural changes during subsequent charge/discharge cycles. The ex-situ characterization by XRD and MP-AES shows that during the subsequent charge/discharge cycle, the potassium ions in the $K_2V_6O_{16}{\cdot}nH_2O$ structure are replacing by lithium. However, the higher initial concentration of V^{4+} leads to increased vacancies gradually during cycling, both on the surface and in the bulk as confirmed by the ex-situ XPS and XANES analysis. Therefore, the structural damage occur slowly. The unusual construction of the nanobelts, composed of crystalline and amorphous domains arranged alternately, probably also prevents the crystal structure from collapsing during this exchange. The obtained $K_2V_6O_{16}{\cdot}nH_2O$ cathode materials with unique morphology and structure might open a new approach for rechargeable multivalent metal ions in lithium-ion batteries.

Data availability

The datasets used and/or analysed during the current study available from the corresponding author on reasonable request.

Received: 25 July 2022; Accepted: 1 November 2022
Published online: 05 November 2022

References

1. Chen, Y., Chen, C., Chen, W., Liu, H. & Zhu, J. Influence of thermal-decomposition temperatures on structures and properties of V2O5 as cathode materials for lithium ion battery. *Prog. Nat. Sci. Mater. Int.* **25**, 42–46 (2015).
2. Reddy, C. V. S. *et al.* Cathodic performance of (V2O5+PEG) nanobelts for Li ion rechargeable battery. *J. Power Sources* **166**, 244–249 (2007).
3. Rahman, M. M. *et al.* Self-assembled V2O5 interconnected microspheres produced in a fish-water electrolyte medium as a high-performance lithium-ion-battery cathode. *Nano Res.* **8**, 3591–3603 (2015).
4. Ng, S. H. *et al.* Synthesis and electrochemical properties of V2O5 nanostructures prepared via a precipitation process for lithium-ion battery cathodes. *J. Power Sources* **174**, 1032–1035 (2007).
5. Song, H. *et al.* Facile synthesis of mesoporous V2O5 nanosheets with superior rate capability and excellent cycling stability for lithium ion batteries. *J. Power Sources* **294**, 1–7 (2015).
6. Prześniak-Welenc, M. *et al.* The influence of nanostructure size on V2O5 electrochemical properties as cathode materials for lithium ion batteries. *RSC Adv.* **6**, 55689–55697 (2016).
7. An, H. *et al.* Highly flexible self-assembled V2O5 cathodes enabled by conducting diblock copolymers. *Sci. Rep.* **5**, 1–10 (2015).
8. Liu, Q. *et al.* Graphene-modified nanostructured vanadium pentoxide hybrids with extraordinary electrochemical performance for Li-ion batteries. *Nat. Commun.* **6**, 1–10 (2015).
9. Liu, Y. *et al.* Facile synthesis of mesoporous NH4V4O10 nanoflowers with high performance as cathode material for lithium battery. *J. Mater. Sci.* **53**, 2045–2053 (2018).
10. Ma, Y. *et al.* Synthesis of novel ammonium vanadium bronze Synthesis of novel ammonium vanadium bronze (NH4)0.6V2O5 and its application in Li-ion battery. *RSC Adv.* **5**, 90888–90894 (2015).
11. Prześniak-Welenc, M., Nadolska, M., Nowak, A. P. & Sadowska, K. Pressure in charge. Neglected parameter in hydrothermal synthesis turns out to be crucial for electrochemical properties of ammonium vanadates. *Electrochim. Acta* **339**, 8 (2020).
12. Li, S. *et al.* Synthesis of polycrystalline K0.25V2O5 nanoparticles as cathode for aqueous zinc-ion battery. *J. Alloys Compd.* **801**, 82–89 (2019).
13. Tong, Z. *et al.* Defect-engineered vanadium trioxide nanofiber bundle@graphene hybrids for high-performance all-vanadate Na-ion and K-ion full batteries. *J. Mater. Chem. A* **7**, 19581–19588 (2019).
14. Xie, Z., Lai, J., Zhu, X. & Wang, Y. Green synthesis of vanadate nanobelts at room temperature for superior aqueous rechargeable zinc-ion batteries. *ACS Appl. Energy Mater.* **1**, 6401–6408 (2018).
15. Prześniak-Welenc, M. *et al.* The influence of nanostructure size on V_2O_5 electrochemical properties as cathode materials for lithium ion batteries. *RSC Adv.* **6**, 55689–55697 (2016).
16. Raistrick, I. D. & Huggins, R. A. An electrochemical study of the mixed beta-vanadium bronzes LiyNaxV2O5 and LiyKxV2O5. *Mater. Res. Bull.* **18**, 337–346 (1983).
17. Raistrick, I. D. & Huggins, R. A. Electrochemical studies of lithium insertion reactions of vanadium oxide bronzes. *Proc. Electrochem. Soc.* **84–91**, 374–384 (1984).
18. Manev, V., Momchilov, A., Nassalevska, A., Pistoia, G. & Pasquali, M. A new approach to the improvement of Lil+xV308 performance in rechargeable lithium batteries. *J. Power Sources* **54**, 501–507 (1995).
19. Baddour-Hadjean, R., Boudaoud, A., Bach, S., Emery, N. & Pereira-Ramos, J. P. A comparative insight of potassium vanadates as positive electrode materials for li batteries: Influence of the long-range and local structure. *Inorg. Chem.* **53**, 1764–1772 (2014).
20. Chen, R. *et al.* Synthesis of K0.25V2O5 hierarchical microspheres as a high-rate and long-cycle cathode for lithium metal batteries. *J. Alloys Compd.* **772**, 852–860 (2019).
21. Fang, G. *et al.* General synthesis of three-dimensional alkali metal vanadate aerogels with superior lithium storage properties. *J. Mater. Chem. A* **4**, 14408–14415 (2016).
22. Fang, G. *et al.* Effect of crystalline structure on the electrochemical properties of K0.25V2O5 nanobelt for fast Li insertion. *Electrochim. Acta* **218**, 199–207 (2016).
23. Fang, G. *et al.* Facile synthesis of potassium vanadate cathode material with superior cycling stability for lithium ion batteries. *J. Power Sources* **275**, 694–701 (2015).
24. Fan, Y. *et al.* Understanding the effect of interplanar space and preintercalated cations of vanadate cathode materials on potassium-ion battery performance. *ACS Appl. Mater. Interfaces* **13**, 7377–7388 (2021).
25. Deng, L. *et al.* Layered potassium vanadate K0.5V2O5 as a cathode material for nonaqueous potassium ion batteries. *Adv. Funct. Mater.* **28**, 1800670 (2018).
26. Baddour-Hadjean, R., Thanh Nguyen Huynh, L., Batyrbekuly, D., Bach, S. & Pereira-Ramos, J.-P. Bilayered potassium vanadate K0.5V2O5 as superior cathode material for Na-ion batteries. *ChemSusChem* **12**, 5192–5198 (2019).
27. Dong, L. W. *et al.* Layered potassium vanadate K2V6O16 nanowires: A stable and high capacity cathode material for calcium-ion batteries. *J. Power Sources* **479**, 228793 (2020).
28. Sambandam, B. *et al.* K2V6O16·2.7H2O nanorod cathode: An advanced intercalation system for high energy aqueous rechargeable Zn-ion batteries. *J. Mater. Chem. A* **6**, 15530–15539 (2018).
29. Kong, X. *et al.* Controllable synthesis and morphology evolution from two-dimensions to one-dimension of layered K2V6O16·nH2O. *CrystEngComm* **17**, 3777–3782 (2015).
30. Bai, L., Xue, Y., Zhang, J., Pan, B. & Wu, C. Synthetic potassium vanadium oxide K2V6O 16·1.5H2O superlong nanobelts: A 1D room-temperature ferromagnetic semiconductor. *Eur. J. Inorg. Chem.* **2013**, 3497. https://doi.org/10.1002/ejic.201201536 (2013).
31. Islam, S. *et al.* K+ intercalated V2O5 nanorods with exposed facets as advanced cathodes for high energy and high rate zinc-ion batteries. *J. Mater. Chem. A* **7**, 20335–20347 (2019).
32. Tang, B. *et al.* Potassium vanadates with stable structure and fast ion diffusion channel as cathode for rechargeable aqueous zinc-ion batteries. *Nano Energy* **51**, 579–587 (2018).
33. Prześniak-Welenc, M., Nadolska, M., Kościelska, B. & Sadowska, K. Tailoring the size and shape—New path for ammonium metavanadate synthesis. *Materials (Basel)* **12**, 3446 (2019).
34. Miller, D. J., Biesinger, M. C. & McIntyre, N. S. Interactions of CO2 and CO at fractional atmosphere pressures with iron and iron oxide surfaces: One possible mechanism for surface contamination?. *Surf. Interface Anal.* **33**, 299–305 (2002).
35. Wang, C. *et al.* Flexible potassium vanadate nanowires on Ti fabric as a binder-free cathode for high-performance advanced lithium-ion battery. *Chem. Eng. J.* **307**, 382–388 (2017).
36. Nakamoto, K. *Infrared and Raman Spectra of Inorganic and Coordination Compounds* (Wiley, 2008).
37. Muhler, M., Schlögl, R. & Ertl, G. The nature of the iron oxide-based catalyst for dehydrogenation of ethylbenzene to styrene 2. Surface chemistry of the active phase. *J. Catal.* **138**, 413–444 (1992).
38. Ambade, R. B., Ambade, S. B., Mane, R. S. & Lee, S. H. Interfacial engineering importance of bilayered ZnO cathode buffer on the photovoltaic performance of inverted organic solar cells. *ACS Appl. Mater. Interfaces* **7**, 7951–7960 (2015).
39. Prześniak-Welenc, M. *et al.* Electrical conductivity and relaxation processes in V2O5 nanorods prepared by sol-gel method. *Phys. Status Solidi Basic Res.* **252**, 2111 (2015).
40. Silversmit, G., Depla, D., Poelman, H., Marin, G. B. & De Gryse, R. Determination of the V2p XPS binding energies for different vanadium oxidation states (V5+ to V0+). *J. Electron Spectros. Relat. Phenomena* **135**, 167–175 (2004).

41. Gupta, S. S. & Van Huis, M. A. Adsorption study of a water molecule on vacancy-defected nonpolar CdS surfaces. *J. Phys. Chem. C* **121**, 9815–9824 (2017).
42. Niu, X. *et al.* High-performance layered potassium vanadium oxide for K-ion batteries enabled by reduced long-range structural order. *J. Mater. Chem. A* **9**, 13125–13134 (2021).
43. Haskel, D. *et al.* Local structural order in the disordered vanadium tetracyanoethylene room-temperature molecule-based magnet. *Phys. Rev. B Condens. Matter Mater. Phys.* **70**, 54422 (2004).
44. Zimmermann, P. *et al.* Modern X-ray spectroscopy: XAS and XES in the laboratory. *Coord. Chem. Rev.* **423**, 213466 (2020).
45. Soundharrajan, V. *et al.* Na2V6O16·3H2O barnesite nanorod: An open door to display a stable and high energy for aqueous rechargeable Zn-ion batteries as cathodes. *Nano Lett.* **18**, 2402–2410 (2018).
46. Steunou, N. & Livage, J. Rational design of one-dimensional vanadium(v) oxide nanocrystals: An insight into the physico-chemical parameters controlling the crystal structure, morphology and size of particles. *CrystEngComm* **17**, 6780–6795 (2015).
47. Liu, T.-C., Pell, W. G., Conway, B. E. & Roberson, S. L. Behavior of molybdenum nitrides as materials for electrochemical capacitors: Comparison with ruthenium oxide. *J. Electrochem. Soc.* **145**, 1882–1888 (1998).
48. Szkoda, M., Zarach, Z., Trzciński, K. & Nowak, A. P. An aqueous exfoliation of wo3 as a route for counterions fabrication—Improved photocatalyticand capacitive properties of polyaniline/WO3 composite. *Materials (Basel)* **13**, 1–16 (2020).
49. Wang, H., Wang, W., Ren, Y., Huang, K. & Liu, S. A new cathode material Na2V6O16· xH2O nanowire for lithium ion battery. *J. Power Sources* **199**, 263–269 (2012).
50. Zhang, W., Xu, G., Yang, L. & Ding, J. Ultra-long Na2V6O16·xH2O nanowires: Large-scale synthesis and application in binder-free flexible cathodes for lithium ion batteries. *RSC Adv.* **6**, 5161–5168 (2016).
51. Zhang, X. *et al.* Ultralong metahewettite CaV6O16·3H2O nanoribbons as novel host materials for lithium storage: Towards high-rate and excellent long-term cyclability. *Nano Energy* **22**, 38–47 (2016).
52. Le Bacq, O., Jakse, N. & Pasturel, A. Striking impact of Na insertion on structural and electronic properties of the electrode material Na2+xV6O16. *J. Phys. Condens. Matter* **28**, 485501 (2016).
53. Wang, P., Cheng, Z., Lv, G., Qu, L. & Zhao, Y. Coupling interconnected MoO3/WO3 nanosheets with a graphene framework as a highly efficient anode for lithium-ion batteries. *Nanoscale* **10**, 396–402 (2018).
54. Xia, C. *et al.* Rechargeable aqueous zinc-ion battery based on porous framework zinc pyrovanadate intercalation cathode. *Adv. Mater.* **30**, 1–7 (2018).
55. Christensen, C. K., Sørensen, D. R., Hvam, J. & Ravnsbæk, D. B. Structural evolution of disordered LixV2O5 bronzes in V2O5 cathodes for Li-ion batteries. *Chem. Mater.* **31**, 512–520 (2019).
56. Malik, R., Burch, D., Bazant, M. & Ceder, G. Particle size dependence of the ionic diffusivity. *Nano Lett.* **10**, 4123–4127 (2010).
57. Feng, B., Sun, D., Wang, H., Tan, S. & Zhang, H. A simple method for the synthesis of KV3O8 0.42H2O nanorod and its lithium insertion/deinsertion properties. *Int. J. Electrochem. Sci.* **8**, 1095–1102 (2013).
58. Meng, J. *et al.* A synergistic effect between layer surface configurations and K ions of potassium vanadate nanowires for enhanced energy storage performance. *J. Mater. Chem. A* **4**, 4893–4899 (2016).

Acknowledgements

This research was funded by National Science Centre, Poland, [Grant Number 2020/37/N/ST5/03697]. The XANES experiments were performed on beamline ASTRA at SOLARIS National Synchrotron Radiation Centre, Cracow, Poland. We are grateful to Alexey Maximenko at SOLARIS for aiding the measurements at beamline ASTRA.

Author contributions

M.P.W.: Conceptualization, Supervision, Writing—Original Draft, Visualization, Investigation. M.N.: Writing—Original Draft, Investigation, Visualization, Funding acquisition. K.J.: Writing—review & editing, Investigation. J.L.: Investigation. K.G.: Investigation. A.M.G.: Writing—review & editing, Investigation. G.R.: Investigation. A.N: Writing—Original Draft, Investigation, Visualization.

Competing interests

The authors declare no competing interests.

Additional information

Supplementary Information The online version contains supplementary material available at https://doi.org/10.1038/s41598-022-23509-x.

Correspondence and requests for materials should be addressed to M.P.-W.

Reprints and permissions information is available at www.nature.com/reprints.

Publisher's note Springer Nature remains neutral with regard to jurisdictional claims in published maps and institutional affiliations.

Supporting Information

The valance state of vanadium- key factor in the flexibility of potassium vanadates structure as cathode materials in li-ion batteries

Marta Prześniak-Welenc, Małgorzata Nadolska, Kacper Jurak ,Jinjin Li, Karolina Górnicka, Aleksandra Mielewczyk-Gryń, Małgorzata Rutkowska, Aandrzej Paweł Nowak*

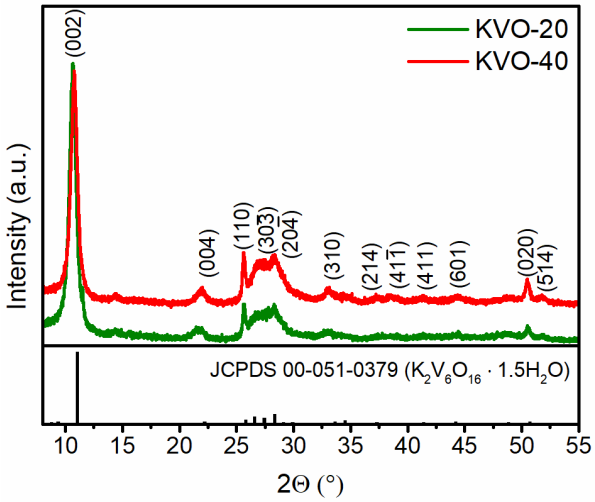

Figure S1. XRD pattern of KVO-20 and KVO-40.

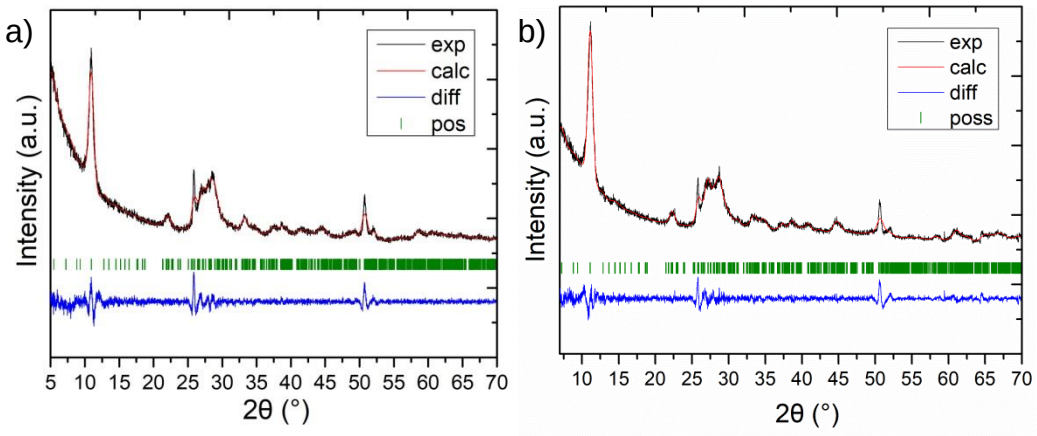

Figure S2. Le Bail refinement of $K_2V_6O_{16}$·1.5H_2O for KVO-20 (a) and KVO-40 (b). The experimentally obtained data are shown with a black line, calculated pattern is shown with a red line and the green vertical marks indicate expected Bragg reflections for $K_2V_6O_{16}$·1.5H_2O. The blue line at the bottom shows the difference between the observed and calculated data.

Table S1. The lattice parameters obtained from Le Bail refinement

	a	b	c	α	β	γ
KVO-20	12,23	3,58	16,21	90	93,33	90
KVO-40	12,25	3,60	15,95	90	93,74	90

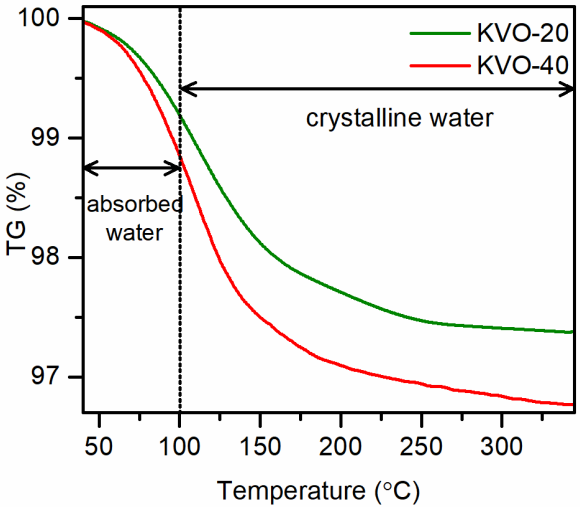

Figure S3. TG curves of KVO-20 and KVO-40

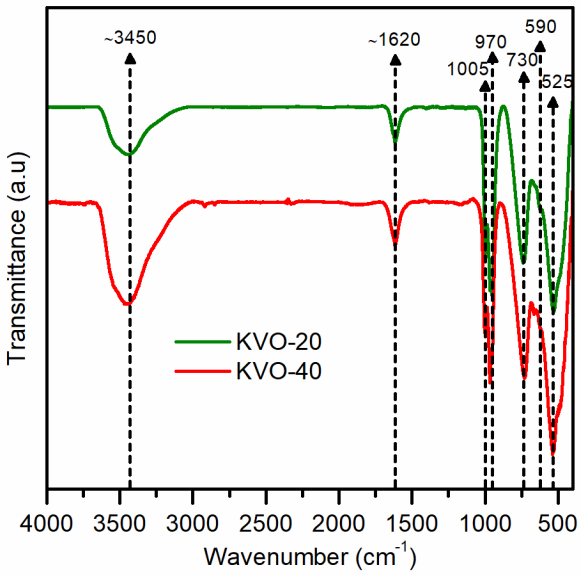

Figure S4. FTIR spectra of sample KVO-20 and KVO-40.

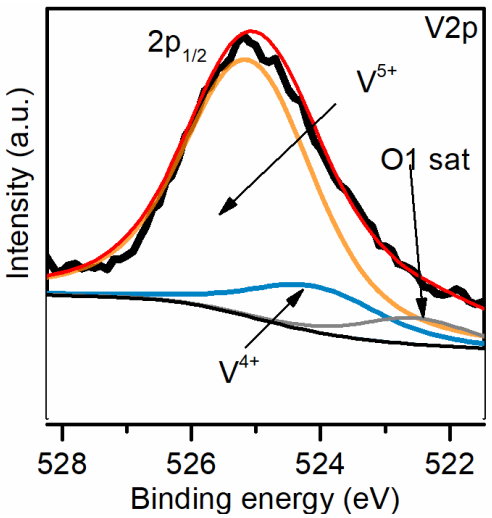

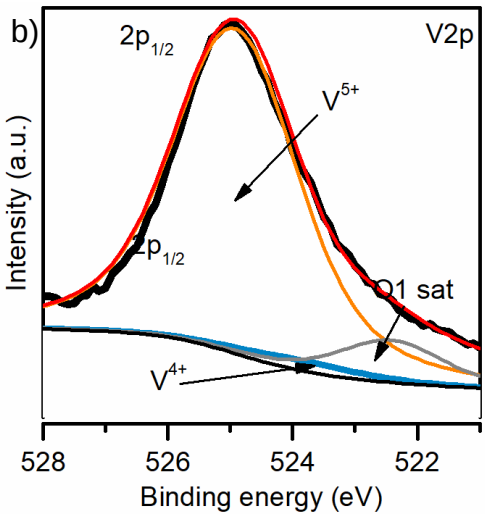

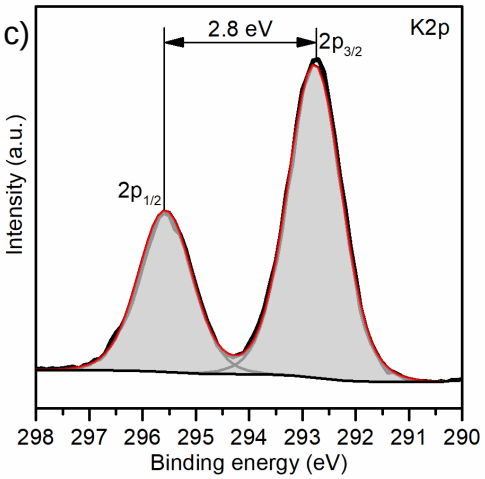

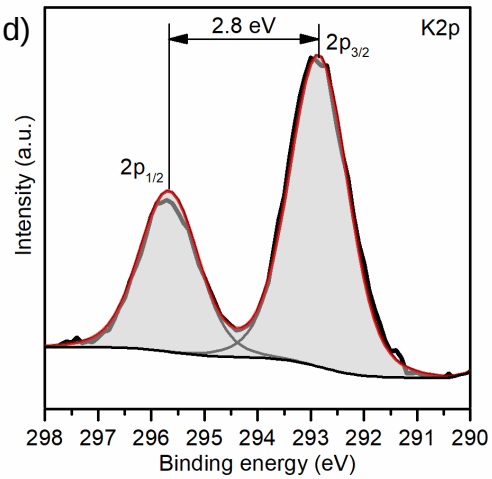

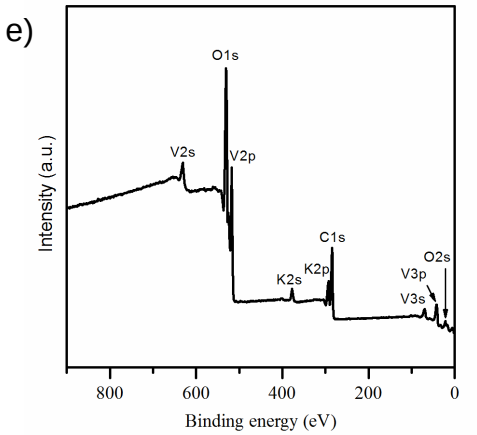

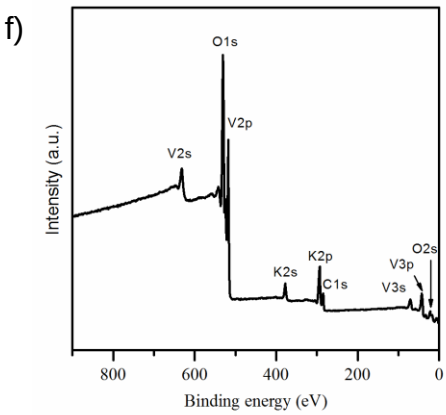

Figure S5. The XPS spectra of samples, (a) and (b) the $2p_{1/2}$ V2p region of KVO-20 and KVO-40 respectively, (c) and (d) K 2p spectrum of KVO-20 and KVO-40 respectively, (e) and (f) Survey spectrum of KVO-20 and KVO-40 respectively.

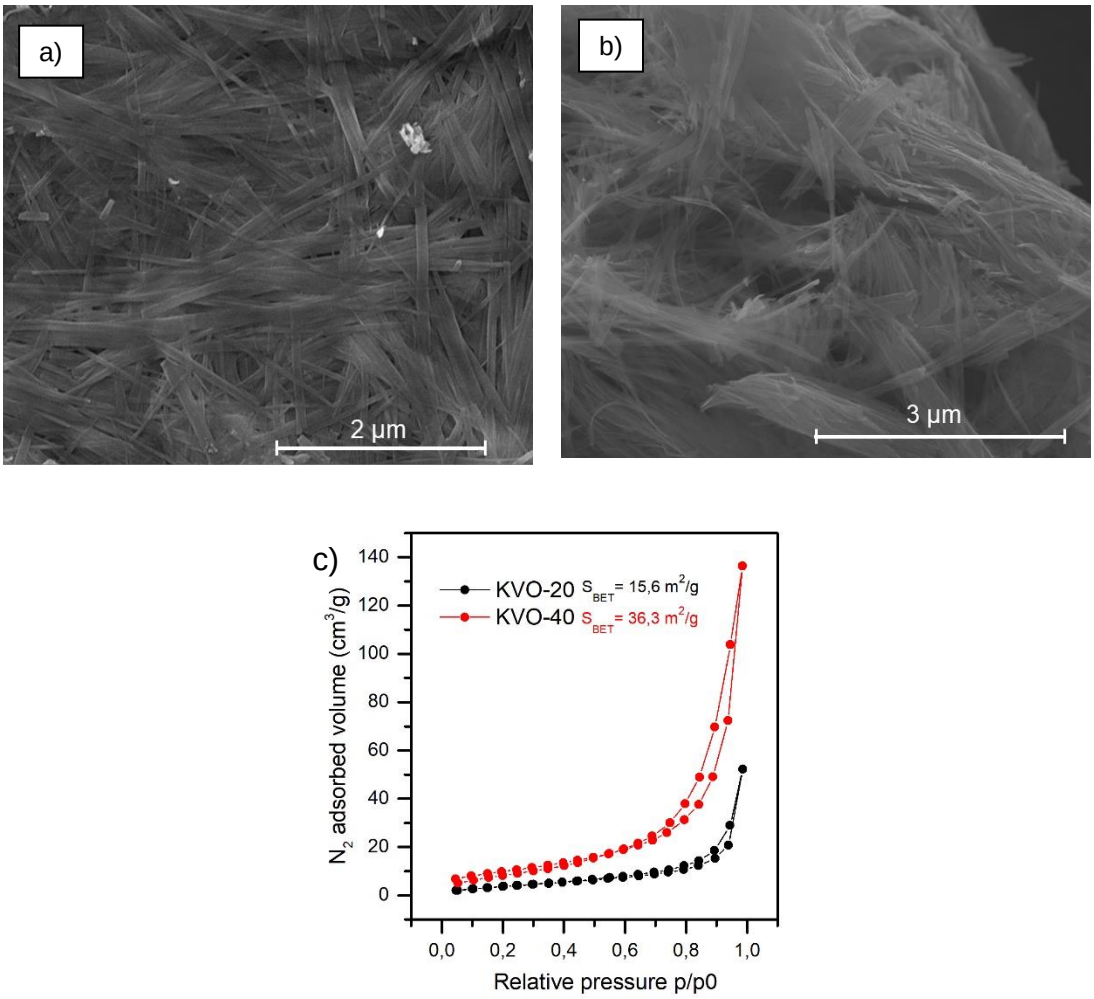

Figure S6. a-b SEM images of KVO-20 (a) and KVO-40 (b), c N_2 adsorption-desorption isotherm of KVO-20 (black) and KVO-40 (red) with calculated specific surface areas.

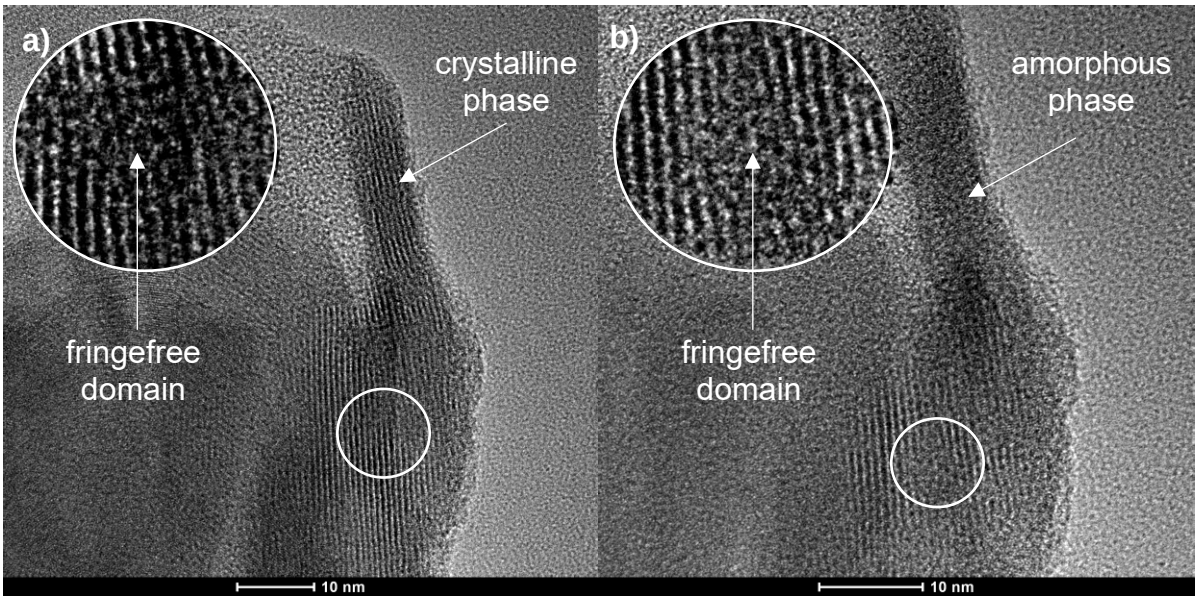

Figure S7. The HRTEM image of KVO-40 (a) of the same position as (b) after irradiating with the electron beam for 30 seconds

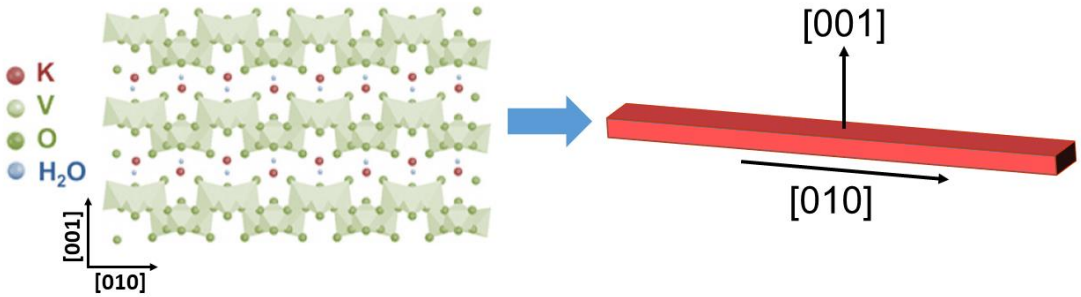

Figure S8. (a) Projection of the structure of $K_2V_6O_{16}\cdot 1.5H_2O$ along [010], (b) The schematic image of $K_2V_6O_{16}\cdot nH_2O$ nanobelt.

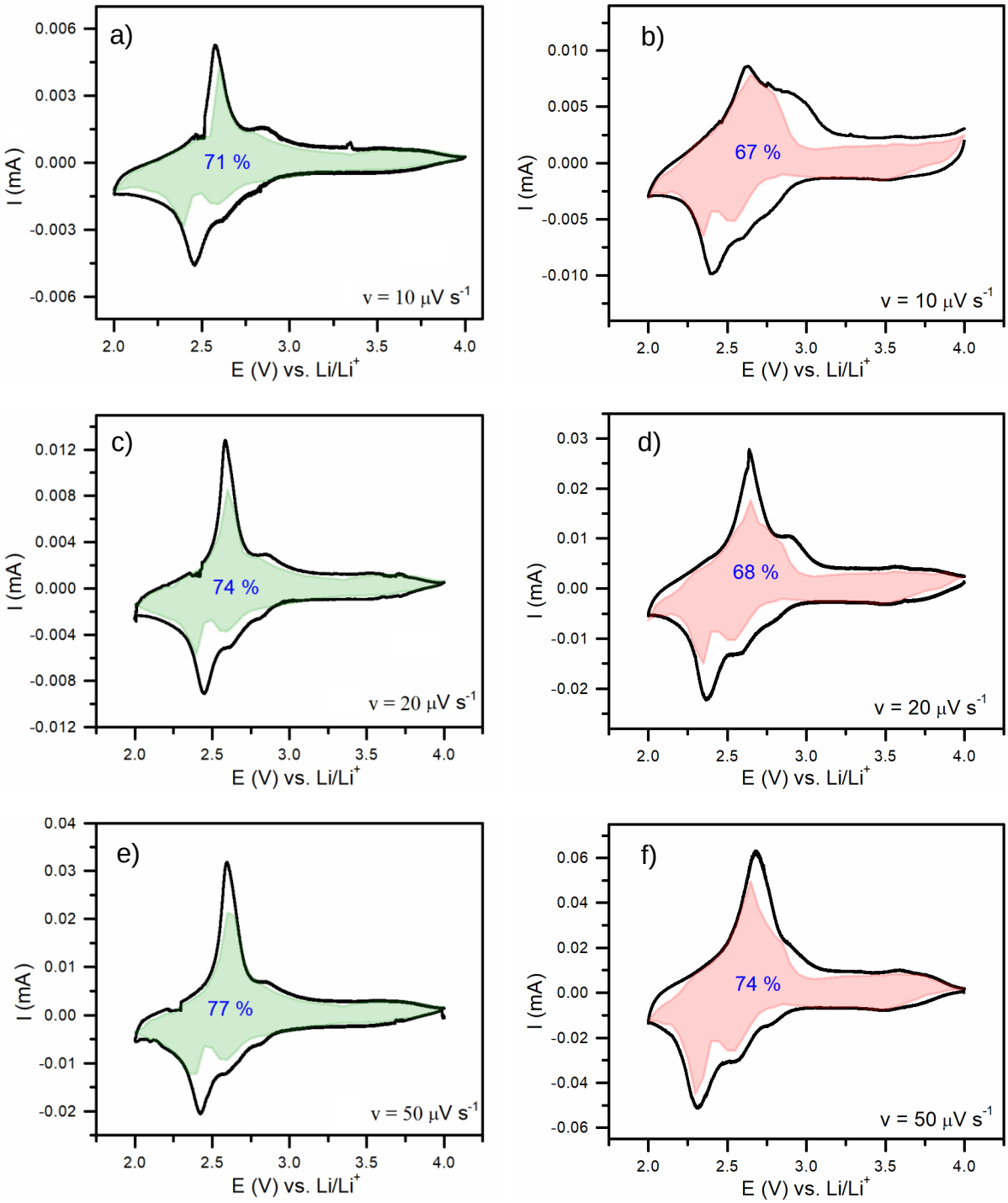

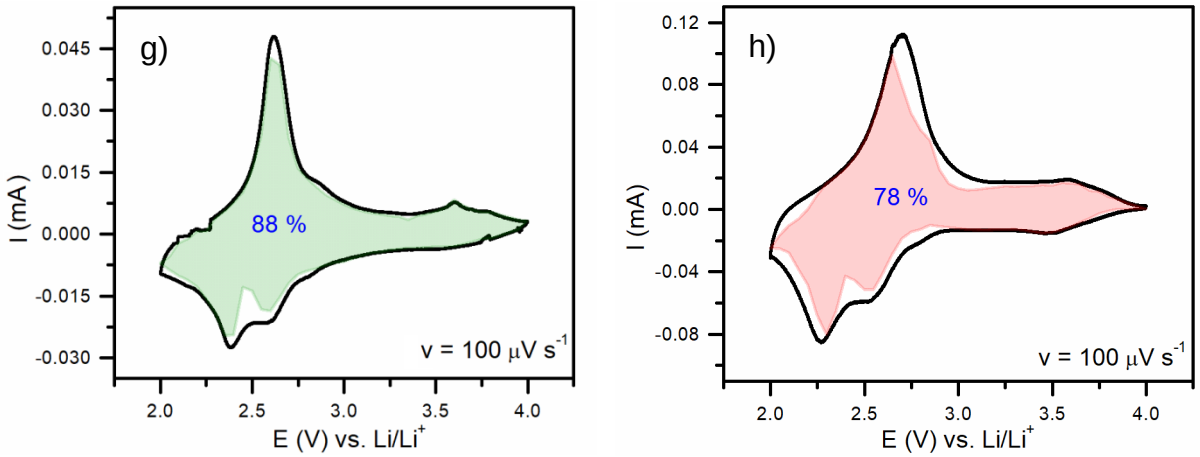

Figure S9. Charge storage contributions at (a) 10 μV s^{-1}, (c) 20 μV s^{-1}, (e) 50 μV s^{-1} and (g) 100 μV s^{-1} of KVO-20 electrode material and at (b) 10 μV s^{-1}, (d) 20 μV s^{-1}, (f) 50 μV s^{-1} and (h) 100 μV s^{-1} of KVO-40 electrode material. Shaded regions presents the capacitive currents with their percentage contribution in the total charge storage.

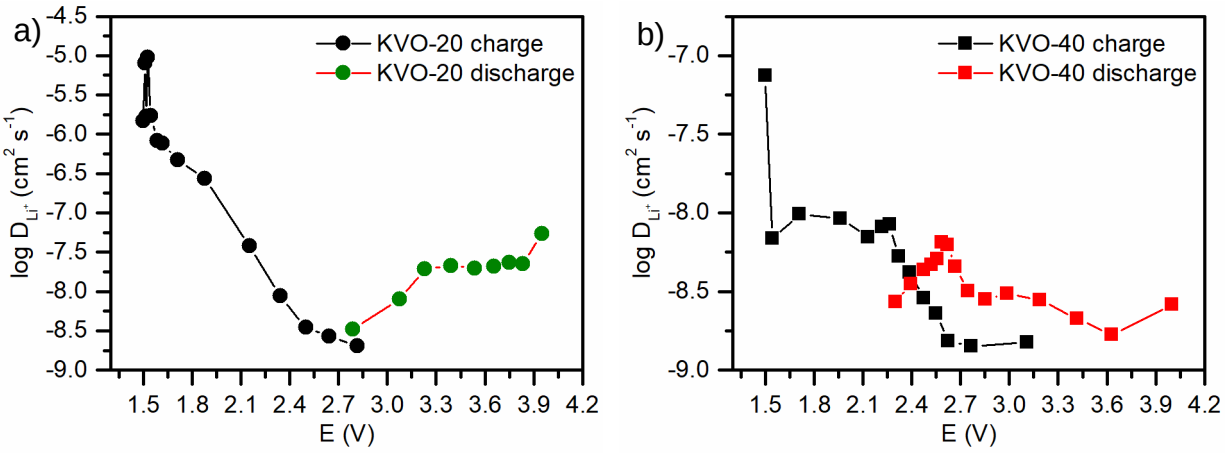

Figure S10. The calculated diffusion coefficient of KVO-20 (a) and KVO-40 (b) electrode material at the first cycle.

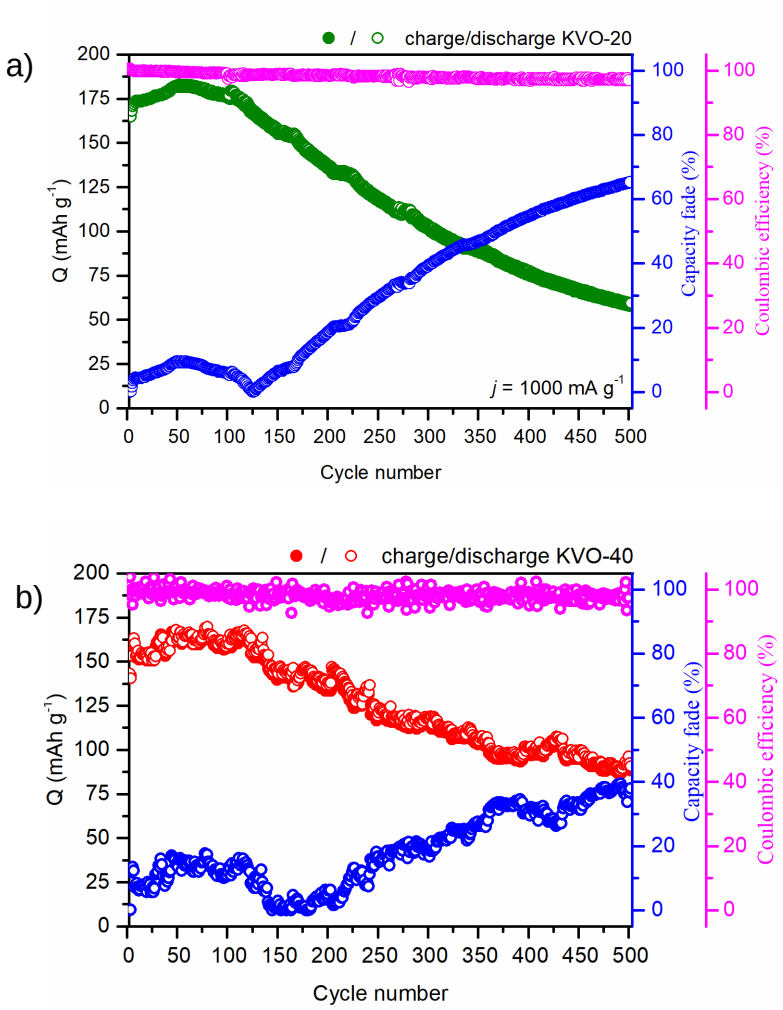

Figure S11. The coulombic efficiency and capacity fade for a) KVO-20 and b) KVO-40 electrode material during 500 subsequent charge/discharge test at j = 1 A g^{-1} in 1.5-4V.

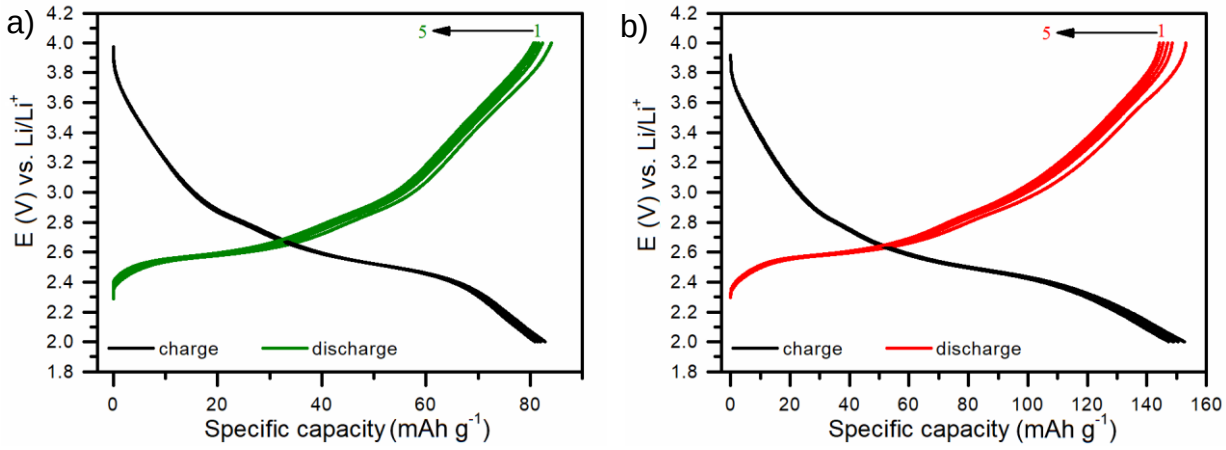

Figure S12. Galvanostatic charge/discharge profiles of electrode materials after extended cycling at 1 A g^{-1}in the 2.0 – 4.0 potential range (a) KVO-20 and (b) 1 KVO-40. The applied current density j = 100 mA g^{-1}.

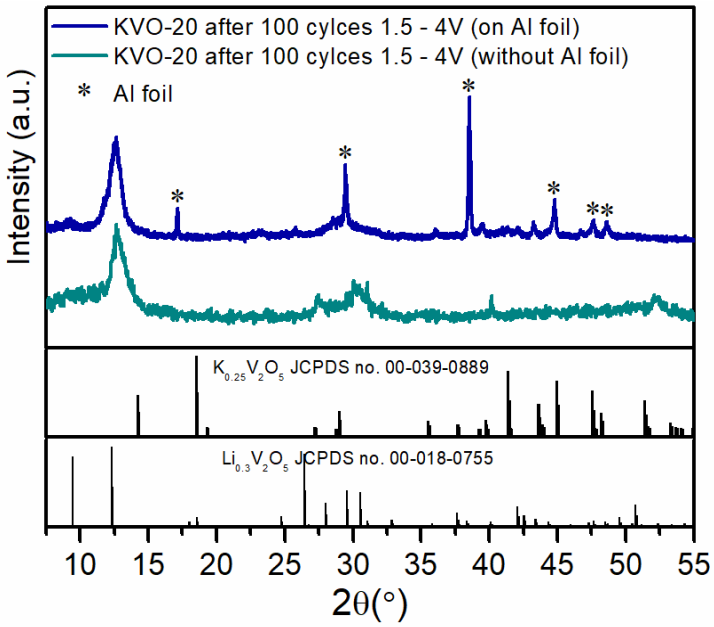

Figure S13. The representative XRD patterns after 100 cycles. KVO-20 electrode material on Al foil (blue line) and KVO-20 electrode material collected from Al foil (cyan line).

Table S2. The element ratio from the XPS analysis.

Sample	KVO-20			KVO-40		
	Pristine	2 – 4 V	1.5 – 4 V	Pristine	2 – 4 V	1.5 – 4 V
Cycles / Atomic ratio	-	100	100	-	100	100
V^{4+}/V^{5+}	0.10	0.20	0.40	0.02	0.40	0.40

Table S3. The element ratio from the MP-AES analysis.

Voltage range	Cycles	KVO-20		KVO-40	
		Atomic ratio			
		V/K	V/Li	V/K	V/Li
2 – 4 V	100	5.33	4.70	4.22	5.50
1.5 – 4 V	100	6.89	1.40	5.29	1.62

Table S4. The electrochemical performance of cathode materials based on potassium vanadium oxides for LiBs

Material	Voltage range (V)	Capacity ($mAhg^{-1}$)	Current density ($mA\ g^{-1}$)	Cycles	Ref.
$K_{0.25}V_2O_5$ nanobelts	1.5 – 4.0	120	1000	800	[59]
$K_{0.5}V_2O_5$ nanorods	2.0 – 4.0	200	100	70	[63]
$K_{0.25}V_2O_5$ nanowires	1.5 – 4.0	172 292	1000 100	500 100	[61]
KV_3O_8 nanowires		178 301	1000 100	500 100	
KV_3O_8 nanorods	1.5 – 4.0	130	15	20	[60]
$K_{0.25}V_2O_5$ microspheres	1.5 – 4.0	249 215 190	100 300 500	30 100 500	[60]
$K_{0.66}V_3O_8$ nanobelts	1.5 – 4.0	197	75	25	[64]
KVO-20 ($K_2V_6O_{16}\cdot 0.65H_2O$ nanobelts)	2.0 – 4.0	164 224	1000 100	100 5	This work
	1.5 – 4.0	142 260	1000 100	100 5	This work
KVO-40 ($K_2V_6O_{16}\cdot 0.76H_2O$ nanobelts)	2.0 – 4.0	164 170	1000 100	100 5	This work
	1.5 – 4.0	179 260	1000 100	100 5	This work

3.4. [A4] Insight into Potassium Vanadates as Visible-Light-Driven Photocatalysts: Synthesis of V(IV)-Rich Nano/Microstructures for the Photodegradation of Methylene Blue

3.4.1. Research background and objectives

Photocatalysis has received much attention as a promising tool for water purification. Pioneering works devoted to the photocatalytic removal of pollutants in water date back to the 1970s and present photooxidation of organic solvents in the presence of ZnO or TiO_2 [158]. Since then, a large number of new materials have been investigated and proposed as efficient photocatalysts for the degradation of various water contaminants [159,160]. Examples include metal oxides (e.g., Cu_2O, $SrTiO_3$, WO_3, and $BiVO_4$), nitrides [161,162], sulfides (CdS, ZnS, and MoS_2) [163,164], metal nanoparticles [165], MXenes [166] and metal-organic frameworks [167]. Among them, TiO_2 is still the most commonly used due to its commercial availability, low cost, good photocatalytic activity and photochemical stability. However, due to the large band gap (3-3.2 eV), TiO_2 can only be activated under UV light irradiation. While UV radiation accounts for only 4% of the entire incoming solar energy, the visible range represents approximately 45%.

Therefore, to efficiently utilize the energy from the sun, much effort has been devoted to the design of visible light-driven photocatalysts [159,168]. In addition to reducing the band gap by various approaches (e.g., doping, coupling with other materials, dye sensitization [169,170]), researchers are focused on the investigation of new visible-active materials. Recent studies have demonstrated that vanadium compounds exhibit promising photocatalytic activity in the decomposition of water pollutants under solar irradiation. Conducted research is mostly focused on $BiVO_4$, however, other vanadates, such as Ag_3VO_4 [171], $Cu_3V_2O_8$ [172–174], $Cd_2V_2O_7$ [175], $Co_2V_2O_7$ [176], $GdVO_4$ [177], $InVO_4$ [7] or $Zn_2V_2O_7$ [178], have also been proposed. On the other hand, there is a lack of literature dedicated to the application of alkali metal vanadates in photocatalysis. For instance, there is only one report devoted to potassium vanadate compounds that use hydrated $K_2V_6O_{16}$ for the photodegradation of methyl orange in aqueous solution. Utilization of potassium vanadates, instead of other metal vanadates, seems promising due to the low cost and high abundance of potassium resources. However, the reported photocatalytic performance in the abovementioned example is low, and after 90 min of visible light irradiation, only 40% of the dye was degraded. On the other hand, it is well known that photocatalytic activity can be influenced by multiple factors, such as chemical composition, structure, morphology, or surface defects.

All the above was motivation to undertake more detailed research on the photocatalytic properties of potassium vanadates, which are presented in [A4]. It was proposed to examine $K_2V_6O_{16}{\cdot}nH_2O$ nanobelts and KV_3O_8 microplatelets for the photocatalytic degradation of Methylene Blue under simulated solar light illumination. As shown in [A3], potassium vanadates synthesized by us via the LPE-IonEX method are characterized by the presence of V^{4+} on the surface. Thus, it was expected that the investigated potassium vanadates should exhibit better photocatalytic performance than potassium vanadates previously reported in the literature.

The aim of the study was to synthesize potassium vanadates and investigate their photoactivity. The obtained samples were fully characterized using XRD, FTIR, XPS, Physical Property Measurement System (PPMS), TGA-MS, SEM and N_2 adsorption. The optical properties were investigated with UV–vis DRS and PL. In addition, electrochemical characterization (Mott-Schottky analysis) allowed to estimate the energy band gap position. The photocatalytic activity of potassium vanadates towards the oxidation of MB was evaluated. The mechanism of MB photodegradation was studied through active species capture experiments and analysis of the degradation products by ultra-performance liquid chromatography quadrupole time-of-flight mass spectrometry (UPLC–QTOF-MS/MS).

3.4.2. Summary of main results

Potassium vanadates were prepared via the LPE-IonEX method, according to the protocol described in [A3]. The synthesis reaction was carried out at four different temperatures: 20°C, 40°C, 60°C and 80°C.

Varied synthesis temperatures resulted in different phase compositions and morphologies of the obtained potassium vanadates. The synthesis at the lowest temperature (20°C) led to the formation of hydrated phase $K_2V_6O_{16}{\cdot}nH_2O$, while at the highest temperature (80°C), it led to nonhydrated KV_3O_8. When the synthesis temperature was equal to 40°C or 60°C, a mixture of these structures was obtained. $K_2V_6O_{16}{\cdot}nH_2O$ consisted of nanobelts (width: 50-200 nm, length: a few μm, thickness: 10-40 nm), while KV_3O_8 consisted of microplatelets (width and length: 1-10 μm, thickness: 150 nm). Consequently, a decrease in the specific surface area (from 30.9 m^2g^{-1} to 4.6 m^2g^{-1}) was observed with increasing synthesis temperature. The synthesis of hydrated and non-hydrated potassium vanadates was also confirmed with TG and FTIR analysis. The sample obtained at 80°C was thermally stable up to 350°C, while for samples obtained at lower temperatures, weight loss attributed to the evaporation of adsorbed and crystalline water was observed. Other evidence for crystalline water was revealed in FTIR analysis. Additional bands associated with the OH bridge between two vanadium atoms can be observed in the spectra of samples obtained at 20°C, 40°C, and 60°C. Additionally, the stretching and bending modes of water shifted to lower wavenumbers with decreasing synthesis temperature, which indicates the existence of strongly bonded water. In addition, in all spectra, splitting of the V=O band was observed, which is characteristic of VO_3 and VO_6 polyhedra and typical for hexavanadates and mixed-valence vanadium compounds. To further investigate the oxidation state of V, XPS and static magnetic susceptibility were measured, which confirmed the coexistence of V^{5+} and V^{4+} in the materials. The relative share of vanadium V^{4+}, estimated from XPS analysis, was similar (9-16%) for the samples obtained at 20°C, 40°C, and 60°C. In contrast, for the sample obtained at the highest temperature, the vanadium V^{4+} valence state is dominant and equals 62%. On the other hand, the value of effective magnetic moments calculated from static magnetic susceptibility was much smaller than the expected value for the free V^{4+} ion. Thus,

the obtained potassium vanadates were characterized by a high content of V^{4+} on the surface, not in the bulk, which was further important in view of catalytic action.

The photocatalytic activity of the samples was evaluated by the degradation of MB under simulated solar light illumination. Before irradiation, all samples showed considerable adsorption of dye, which reached 30% after 30 min. The sample obtained at 80°C exhibited the highest photocatalytic activity, resulting in more than 90% degradation of dye within the first 30 min of illumination. In the case of the rest of the samples (obtained at 20, 40, and 60°C), the observed photoactivity was similar, and the time needed for MB degradation was longer (approximately 90% degradation after 90 min). The kinetics of the photodegradation process were similar for all samples, and the most likely is pseudo-first-order kinetic according to the Langmuir-Hinshelwood model. Next, more detailed studies of photocatalytic and optical properties were carried out for single-phase samples of $K_2V_6O_{16}\cdot nH_2O$ nanobelts (obtained at 20°C) and KV_3O_8 microplatelets (obtained at 80°C). Both samples showed efficient absorption in the visible wavelength region with narrow band gap energies of 1.80 eV and 1.91 eV, respectively. The Mott–Schottky analysis, carried out for KV_3O_8, revealed that the obtained nonhydrated potassium vanadate is an n-type semiconductor with a flat band potential of approximately 0.765 V vs NHE. The scavenger tests indicated that OH radicals and holes are the main active species in the process of photocatalytic degradation of MB. It was observed that the role of direct oxidation (holes) in the case of KV_3O_8 is smaller than that for $K_2V_6O_{16}\cdot nH_2O$ but still significant. Further analysis by means of UPLC-QTOF-MS/MS confirmed effective photodegradation of the dye. After using KV_3O_8 microplatelets as catalysts, only small amounts (<1%) of two simple degradation compounds, aniline and phenol, were identified. The photodegradation process catalysed by $K_2V_6O_{16}\cdot nH_2O$ nanobelts was less efficient, and a significant amount of benzenesulfonic acid was generated as well as trace amounts of amino-5-(methylamino)-hydroxybenzenesulfonic acid, 4-nitroaniline, and phenol.

In summary, the obtained results demonstrate that potassium vanadates can be used as efficient photocatalysts for the decomposition of organic dyes. In comparison to the previously reported potassium vanadate photocatalysts (only one work [136], devoted to hydrated $K_2V_6O_{16}\cdot nH_2O$), the samples described in the publication [A4] exhibit much better photocatalytic activity. It is known that the activity of photocatalysts is related to many factors. Usually, photocatalysts in the form of nanostructures show improved photocatalytic properties compared to their bulk counterparts. Numerous examples can be found in the literature, which prove that nanometric dimensions are favourable for the excitation, separation, and migration of photocatalytic electron-hole pairs. Additionally, reducing the particle size to the nanoscale leads to the growth of the specific surface area and an increase in the number of reactive sites. Nonetheless, for the investigated potassium vanadates, the reverse tendency was observed. The $K_2V_6O_{16}\cdot nH_2O$ nanobelts with the highest surface area exhibit the worst photocatalytic performance, while KV_3O_8 microplatelets (the lowest surface area) are the best. It is suggested that the observed excellent photocatalytic performance is attributed to the high content of V^{4+} surface species. The existence of surface defects in vanadium-based photocatalysts has been

reported to be crucial in enhancing performance in water splitting and degradation of pollutants [179,180]. V^{4+} defects trap electrons and facilitate charge separation of photogenerated electrons and holes [181,182]. It has also been shown that V^{4+} -doped samples possess enhanced photocurrent density and smaller charge transfer resistance [183]. The formation of defects has also been claimed to reduce the bandgap by introducing additional sublevels inside the electronic bandgap, allowing for extended light absorption [82]. Likewise, in the case of the sample reported by us, the calculated band gap for $K_2V_6O_{16}{\cdot}nH_2O$ is narrower than that previously published. Surface defects are also beneficial for the adsorption of positively charged compounds, such as Methylene Blue. Thus, the good adsorptive capacity observed for the obtained samples can be explained by the high content of V^{4+} surface species. Adsorption is an essential process in photocatalysis, which enriches the pollutants around the catalyst surface and improves photocatalytic performance [184–186].

Publication [A4] extends the current knowledge on the utilization of potassium vanadates as photocatalysts. In addition to more detailed studies on $K_2V_6O_{16}{\cdot}nH_2O$ (kinetics and mechanism of the photocatalysis process), nonhydrated KV_3O_8 was presented as a new photoactive material for the first time. Moreover, the conducted studies confirm the importance of V^{4+} species in photocatalysis. Importantly, reported potassium vanadates are activated under solar light and are obtained via facile synthesis (reaction temperature below 100°C, easy operation, no need for complicated equipment, good repeatability) from low-cost simple potassium salt. Therefore, they can be considered promising alternatives for the efficient degradation of dyes and have great potential in wastewater treatment.

3.4.3. Full content of the article

Title: Insight into Potassium Vanadates as Visible-Light-Driven Photocatalysts: Synthesis of V(IV)-Rich Nano/Microstructures for the Photodegradation of Methylene Blue

Authors: M. Nadolska, M. Szkoda, K. Trzciński, P. Niedziałkowski, J. Ryl, A. Mielewczyk-Gryń, K. Górnicka, M. Prześniak-Welenc

Journal: Inorganic Chemistry, 2022, 61, 25, 9433–9444

Impact factor: 5.165 (2022)

Ministerial Points: 140 pts

DOI: https://doi.org/10.1021/acs.inorgchem.2c00136

I contributed to this work by conceptualizing experiments under the supervision of dr. Marta Prześniak-Welenc. In particular, I proposed to study potassium vanadates as photocatalysts for Methylene Blue degradation. I participated in samples synthesis and their characterization (XRD, FTIR, TG, N_2 adsorption). I also discussed the relationship between the physicochemical properties and photocatalytic performance of studied samples. I prepared the first version of the manuscript and answers for the reviewers. I was responsible for the submission of the manuscript and funding acquisition.

Inorganic Chemistry

pubs.acs.org/IC

Article

Insight into Potassium Vanadates as Visible-Light-Driven Photocatalysts: Synthesis of V(IV)-Rich Nano/Microstructures for the Photodegradation of Methylene Blue

Małgorzata Nadolska, Mariusz Szkoda, Konrad Trzciński, Paweł Niedziałkowski, Jacek Ryl, Aleksandra Mielewczyk-Gryń, Karolina Górnicka, and Marta Prześniak-Welenc*

Cite This: *Inorg. Chem.* 2022, 61, 9433−9444

Read Online

ACCESS | Metrics & More | Article Recommendations | Supporting Information

ABSTRACT: Photocatalysis is regarded as a promising tool for wastewater remediation. In recent years, many studies have focused on investigating novel photocatalysts driven by visible light. In this study, $K_2V_6O_{16}{\cdot}nH_2O$ nanobelts and KV_3O_8 microplatelets were synthesized and investigated as photocatalysts. Samples were obtained via the facile method based on liquid-phase exfoliation with ion exchange. By changing the synthesis temperature (20−80 °C), different compositions, morphologies, and V^{4+}/V^{5+} ratios were obtained and investigated as photocatalysts for organic dye degradation. Potassium vanadates' structural, morphological, and optical properties were characterized using X-ray diffraction(XRD), Fourier transform infrared spectroscopy (FTIR), X-ray photoelectron spectroscopy (XPS), Physical Property Measurement System (PPMS), thermogravimetric analysis (TGA) with mass spectrometry (MS), N_2 adsorption, scanning electron microscopy (SEM), photoluminescence (PL), and UV−vis diffuse reflectance spectroscopy (DRS). Synthesized $K_2V_6O_{16}{\cdot}nH_2O$ and KV_3O_8 showed an efficient absorption in the visible wavelength region with a narrow band gap energy of 1.80 and 1.91 eV, respectively. Their photocatalytic activity was evaluated by the degradation of methylene blue (MB) under simulated solar light illumination. The KV_3O_8 microplatelets exhibited the greatest photocatalytic activity, resulting in more than 90% degradation of the dye within the first 30 min. It is suggested that the observed excellent photocatalytic performance is attributed to the high content of V^{4+} species. Furthermore, the influence of active species was investigated, and the mechanism responsible for the photodegradation of the MB dye was discussed for the first time for potassium vanadates.

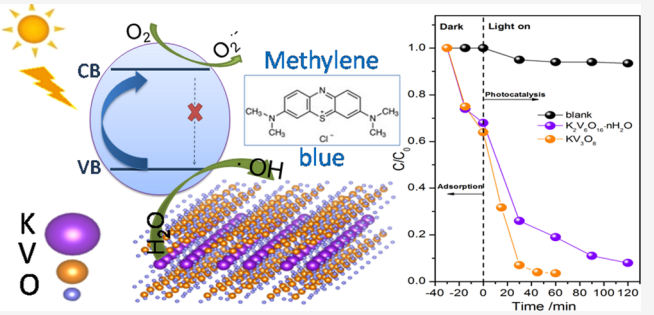

INTRODUCTION

The search for new, efficient, and low-cost photocatalysts has attracted increasing attention due to their perfect utilization of clean and renewable solar energy for treating wastewaters. In the past years, various materials have been investigated and tested for water purification.[1−4] Examples include metal[5,6] and metal oxide nanoparticles,[7] sulfides,[8,9] nitrides,[10] metal−organic frameworks,[11,12] or carbon-based nanostructures.[13] Recent studies demonstrate that metal vanadates exhibit promising visible-light photocatalytic reactivity in decomposing pollutants and water splitting.[14−17] A series of compounds can be mentioned here, such as Ag_3VO_4,[18] AgV_7O_{18},[19] CuV_2O_6,[20] $FeVO_4$,[21] $Cd_2V_2O_7$,[22] $InVO_4$,[23] $GdVO_4$,[24] and $BiVO_4$[25,26] as the most known representatives from the vanadate family. The conducted research is mainly devoted to the nanostructured vanadates, which can appear in various forms such as nanoparticles,[27,28] nanobelts,[29,30] or nanotubes.[31] It is well known that the shape and size play a significant role, as broadly described in the literature.[32−35] The photocatalytic properties are also strongly dependent on the crystalline structure. Generally, the monoclinic scheelite $BiVO_4$ (m-$BiVO_4$) is considered to be more active than the other two tetragonal phases.[36−38] In addition, the face-dependent photocatalytic behavior was also shown with the beneficial effect of (040) facets on contaminant degradation.[39−42] Another critical factor in the photocatalytic reaction is crystal defects, for example, oxygen vacancies, which trap photogenerated pairs and reduce their recombination rate.[43] The presence of oxygen vacancies can also broaden the activity range of a semiconductor oxide from UV to NIR light.[44] As a result, new pathways to synthesize photocatalysts with controllable properties are sought.

Received: January 14, 2022
Published: June 10, 2022

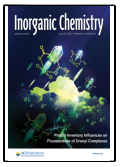

In this study, we present a new synthesis method of potassium vanadates as efficient photocatalysts for methylene blue (MB) degradation. Potassium vanadates were prepared by the facile LPE-IonEx method (liquid-phase exfoliation with ion exchange), which was recently proposed by our group.[63] LPE-IonEx is a straightforward, low-temperature, one-pot approach for the synthesis for transition metal oxide bronzes with controlled structural and morphological properties. Notably, the proposed method uses water as a solvent, making it eco-friendly. We demonstrated that, depending on the synthesis temperature (20−80 °C), the hydrated single-phase $K_2V_6O_{16}\cdot nH_2O$ to nonhydrated KV_3O_8 can be obtained through their mixture. In addition, an increase in temperature leads to increased V^{4+} concentration. The photocatalytic activity of prepared materials was evaluated by the degradation of an organic dye—methylene blue—in water under simulated solar light illumination. So far, KV_3O_8 has been considered as a precursor for V_3O_7 nanobelt synthesis for photocatalytic water splitting applications.[45] To the best of our knowledge, the photocatalytic properties of nonhydrated phase KV_3O_8 have never been investigated. Furthermore, the mechanism and kinetics of photocatalytic degradation were studied for the first time.

EXPERIMENTAL SECTION

Synthesis. Potassium formate (99%, Sigma Aldrich) and V_2O_5 (99.2%, Alfa Aesar) without further purification were used as reagents. Milli-Q deionized water was used (resistivity >19 MΩ·cm). The samples were prepared via the LPE-IonEx method, where the procedure was as follows: 500 mg of V_2O_5 was added to 50 mL of a 1 M solution of potassium formate in deionized water. The mixture was vigorously stirred for 72 h, and the synthesis was conducted in four temperatures: 20, 40, 60, and 80 °C. The samples were labeled according to the reaction temperature as KVO-20, KVO-40, KVO-60, and KVO-80, respectively. From the obtained solution, rusty red to burnt orange to orange precipitations were collected by centrifugation. After washing several times with deionized water, products were dried overnight at 40 °C under reduced pressure (0.01 bar).

Physicochemical Characterization. The X-ray diffractograms (XRD) were collected on a BrukerD2 Phaser diffractometer with Cu Kα radiation (λ = 1.5404 Å) in the range 2θ of 5−70° at room temperature. The samples' morphology was studied at room temperature by an FEI Quanta FEG 250 scanning electron microscope (SEM) in secondary electron mode using an Everhart-Thornley detector (ETD). Fourier transform infrared (FTIR) spectra were measured on a Perkin Elmer Frontier spectrophotometer. The KBr pellet method was used, and transmittance spectra were recorded from 4000 to 500 cm^{-1} with a resolution of 4 cm^{-1}. The high-resolution X-ray photoelectron spectroscopy (XPS) analysis was performed using an Escalab 250Xi device (ThermoFisher Scientific, USA) equipped with a monochromatic Al Kα source. Measurements were carried out at 25 eV pass energy with 0.05 eV energy step size. The X-ray spot size was 250 μm. The calibration of the XPS spectrum was done using the characteristic peak of adventitious carbon C 1s at 284.6 eV.[46] Thermogravimetric analysis (TGA) was carried out under an argon atmosphere with a flow rate 60 mL min^{-1} in the temperature range of 40−400 °C (with a heating rate of 5 °C min^{-1}) using Netzsch STA449 F1. A constant sample mass (20 ± 0.5 mg) was used. The thermal behavior has also been studied by EGA−MS (evolved gas analysis−MS). The gases that come out from the sample during heating were monitored by the quadruple mass spectrometer Netzsch QMS 403 Aëolos. The differential scanning calorimetry (DSC) measurement was performed under an argon atmosphere with a flow rate 60 mL min^{-1} in the temperature range of 35−450 °C (with a heating rate of 15 °C min^{-1}) using a NETZSCH DSC 204 F1 Phoenix calorimeter.

Nitrogen adsorption−desorption isotherms were measured on a surface area analyzer (NOVAtouch 2, Quantachrome Instruments) at 77 K. Before the measurements, samples were degassed under a dynamic vacuum at 40 °C for 12 h. The specific surface area was calculated using the Brunauer−Emmett−Teller (BET) linear equation in the relative pressure range (p/p_0) from 0.1 to 0.3. The correlation coefficient of the linear regression was not less than 0.99.

The UV−vis reflectance spectra of the selected materials were measured with a UV−vis spectrophotometer (Lambda 35, Perkin-Elmer) equipped with a diffuse reflectance accessory. The spectra were registered in a range of 300−900 nm with a scanning speed of 120 nm min^{-1}. Band gap energy values were determined as the intercept of the tangent of the plot of transformation of the Kubelka−Munk function. To determine the energy band gap (E_{bg}) of the chosen powders, the Kubelka−Munk function (eq 1) was applied:

$$f(\mathrm{KM}) = \frac{(1-R)^2}{2R} \tag{1}$$

where R is the reflectance.

The band gap was estimated by extrapolation of the linear region of $(f(\mathrm{KM})\ h\nu)^n$ vs $h\nu$ to $y = 0$, where the power "n" depends on the electron transition (n = 1/3, indirect forbidden (i.f.); n = 0.5, indirect allowed (i.a.); n = 2/3, direct forbidden (d.f.); and n = 2, direct allowed (d.a.)).[47] The photoluminescence spectra were recorded using 0.3 m Czerny−Turner spectrograph (SR303i, Andor) equipped with an ICCD camera (DH740, Andor). Powders were excited with UV LED (365 nm, 9 nm FWHM, 350 mW).

Magnetic Properties. Quantum Design Physical Property Measurement System (PPMS) with a vibrating sample magnetometer function was used to measure the temperature-dependent magnetic susceptibility (defined as $\chi = M/H$, where M is the magnetization and H is the applied field). The temperature dependence of the zero-field cooled (ZFC) magnetization was measured in the applied field of 3 T. Magnetic measurements were performed on a sample of arbitrary shape with a mass of about 10 mg.

Photocatalytic Activity. To evaluate the powders' photocatalytic activity, the degradation rate of methylene blue (MB) dye was monitored. Twenty milligrams of catalysts and 50 mL of an aqueous solution of MB ($C_0 = 10^{-5}$ M) were transferred to the beaker. Before irradiation, the suspension was magnetically stirred in the dark for 30 min to achieve adsorption/desorption equilibrium. Then, the suspension was irradiated with sunlight irradiation (a high-pressure 150 W xenon lamp, LOT−Quantum Design GmbH equipped with an AM1.5G filter) with constant magnetic stirring (150 rpm). The intensity of the light that reached the solution's surface was equal to 100 mW cm^{-2}. The changes of the concentration of MB (C) during decomposition were monitored using a UV−vis spectrophotometer at a wavelength of 665 nm. The quantitative evaluation of the role of the chemical individuals responsible for dye decomposition was performed using appropriate scavengers (1 mM of *tert*-butyl alcohol, benzoquinone, and ammonium oxalate).

The MB products after photocatalytic degradation using KVO-20 and KVO-80 samples were analyzed by ultra-performance liquid chromatography quadrupole time-of-flight mass spectrometry (UPLC−QTOF-MS/MS). The analysis of solutions obtained after photocatalytic degradation was performed on an Agilent 1290 Infinity liquid chromatograph and Agilent 6550 iFunnel Q-TOF LC/MS System. The mobile phase consisted of phase A: 0. 1% aqueous formic acid with 0.3% acetonitrile and phase B: 0.1% formic acid in acetonitrile. The analysis was recorded with a gradient elution from 0 to 100% B during 10 min with an injection volume of 5 μL. The Agilent ZORBAX RRHD Eclipse Plus C18 column (95 Å, 2.1 × 50 mm, 1.8 μm) was used for the separation and detection of resulting products with a column temperature of 24 °C and flow rate 0.3 mL/min. The mass spectra were obtained in positive modes using the following operating parameters: capillary voltage 3.5 kV, nozzle voltage 2 kV, and fragmentor voltage 175 V. The gas temperature was 250 °C with a flow rate of 12 L/min and nebulizer pressure of 40 psi; the sheath gas temperature was 300 °C with a flow rate 11 L/min.

https://doi.org/10.1021/acs.inorgchem.2c00136
Inorg. Chem. 2022, 61, 9433−9444

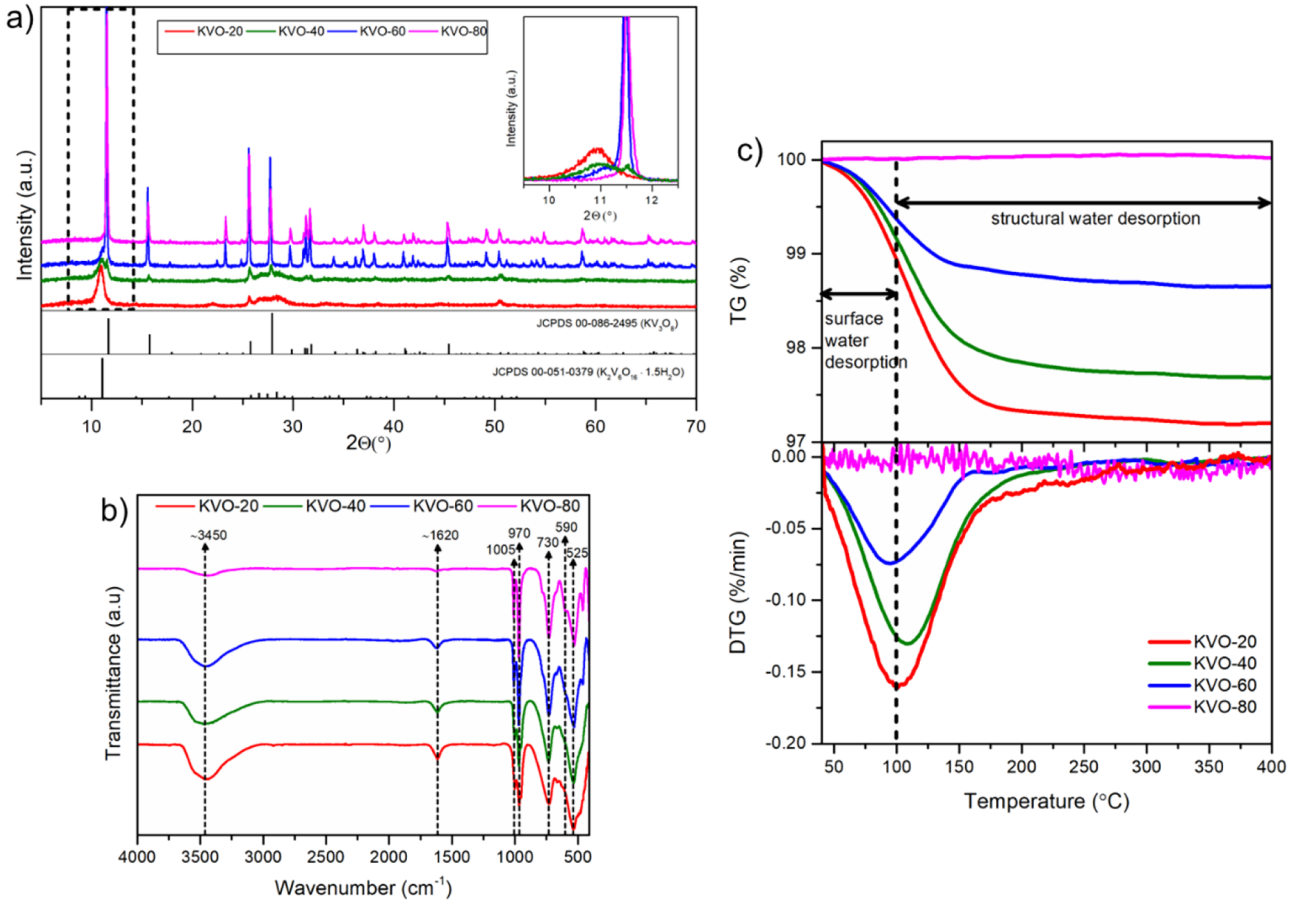

Figure 1. (a) XRD patterns, (b) FTIR spectra, and (c) TG and DTG curves of the samples obtained under different reaction temperatures. The inset shows the zoomed view of the XRD's most intense peaks ascribed to KV_3O_8 (JCPDS card no. 00-086-24-95) and $K_2V_6O_{16}\cdot 1.5H_2O$ (JCPDS card no. 00-051-0379).

The mass spectra were monitored in the range from 50 to 1000 m/z with a scan range of one spectrum per second. The obtained UPLC−QTOF-MS/MS data were analyzed using the Mass Hunter Qualitative Analysis software.

Electrochemical Characterization. The electrochemical measurements were performed using an Ivium Vertex potentiostat/galvanostat in a three-electrode cell using Pt mesh as the counter electrode and Ag/AgCl (3 M KCl) as the reference electrode. The tested powder was deposited onto degreased FTO (fluorine-doped tin oxide) using a dip-coating method according to the procedure described previously.[48] Measurements were performed in deaerated aqueous 0.2 M K_2SO_4. The Mott−Schottky analysis was performed to determine the flat band potential. The impedance spectra were recorded at a potential range from 0.4 to 0.9 V vs Ag/AgCl (3 M KCl). The potential was held before each spectrum registration to achieve a steady-state condition. The potential range for analysis was determined on the basis of a cyclic voltammetry (CV) curve. The space charge capacitance was determined from 1000 Hz frequency according to the formula $C_{sc} = 1/\omega Z''$.

RESULTS AND DISCUSSION

Structural Analysis. The X-ray diffractograms were recorded to confirm the phase purity and crystallinity of obtained samples (see Figure1a). For the diffractogram for the sample synthesized at 20 °C (KVO-20), all indices can be indexed within hydrated potassium vanadate phase $K_2V_6O_{16}\cdot 1.5H_2O$, JCPDS card no. 00-051-0379, which corresponds to a monoclinic structure with lattice parameter values of a = 12.29 Å, b = 3.59 Å, and c = 16.01 Å. The main diffraction peak, located at approximately 11°, corresponds to the diffraction from the (002) crystallographic plane of this phase. Moreover, no signals of other phases were detected, indicating the high purity of the sample. For the samples synthesized at higher temperatures, additional peaks can be observed, indicating the presence of the secondary phase KV_3O_8, JCPDS card no. 00-086-24-95, which corresponds to a monoclinic structure with lattice parameter values of a = 4.97 Å, b = 8.38 Å, and c = 7.64 Å. The presence of KV_3O_8 is revealed by its characteristic diffraction peak located at approximately 11.5°, which corresponds to the (001) crystallographic plane (see inset in Figure 1a). With increasing synthesis temperature, the intensity of the diffraction peaks ascribed to the KV_3O_8 phase increases, and the first peak of KVO-40 and KVO-60 is split. This suggests the existence of two phases in these samples. The XRD pattern of sample KVO-80 shows indexed reflection only for the KV_3O_8 phase. The characteristic peak for the hydrated potassium vanadate phase is no more visible. FTIR spectra of the samples are shown in Figure 1b and summarized in Table S1. The bands at ∼1005 and ∼970 cm^{-1} can be assigned to V═O vibrations, while those at 525 and 590 cm^{-1} can be assigned to the symmetric and asymmetric stretching of V−O−V.[49] The band at 730 cm^{-1} corresponds to bridging V−O···K stretching.[50] In all spectra, the splitting of the V═O bands can be observed. Such phenomenon implies the distortions in the vanadium oxide layers and the existence of VO_5 and VO_6 polyhedra, which are typical for hexavanadates and mixed-valence vanadium compounds.[51,52] Significant changes were

https://doi.org/10.1021/acs.inorgchem.2c00136
Inorg. Chem. 2022, 61, 9433−9444

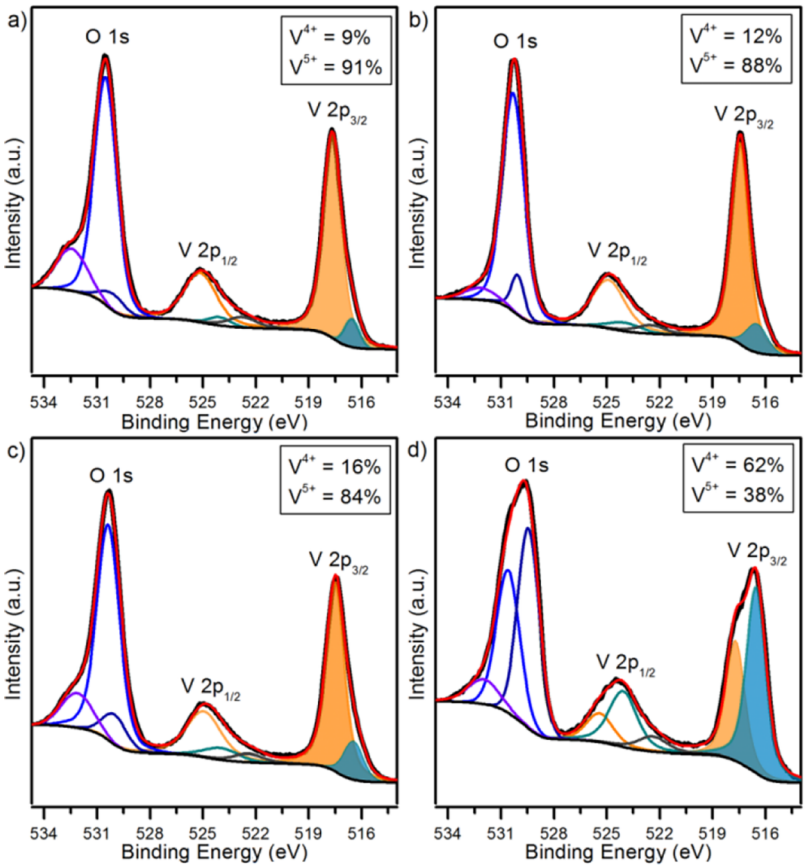

Figure 2. The XPS spectra of the O 1s and V 2p region of (a) KVO-20, (b) KVO-40, (c) KVO-60, and (d) KVO-80, respectively.

also observed in the position of the absorption band located ca. 1005 cm^{-1}. In comparison to KVO-20, the maximum for KVO-80 is shifted from 1000 to 1010 cm^{-1}. This is linked to the shortening of the bond length and reducing the distance between vanadium oxide layers. The distance between layers for the hydrated potassium vanadate ($K_2V_6O_{16}{\cdot}1.5H_2O$) is almost doubled than for the nonhydrated phase (KV_3O_8).[49,53,54] Also, in all spectra, there are two extra bands at ∼3450 and ∼1620 cm^{-1} that can be associated with water molecules' stretching and bending vibrations.[45] Their positions vary within the samples, and peaks shift to the low wavenumber from 1633 and 3475 cm^{-1} for KVO-80 to 1615 and 3435 cm^{-1} for KVO-20. According to the literature, a decrease in wavenumber is evidence of the binding of water with other atoms.[55] In case of anhydrous KV_3O_8 (KVO-80), physisorbed water molecules are only weakly bonded to the samples' surface, while for hydrated $K_2V_6O_{16}{\cdot}nH_2O$ (KVO-20), water molecules are trapped in the crystalline lattice by either interactions with potassium ion or vanadium-oxide layers. Moreover, in the KVO-20, KVO-40, and KVO-60 spectra, an additional band at 950 cm^{-1} can be observed. The position of this band suggests the existence of the OH bridge between two metals, probably between V.[56] Thermogravimetric measurements were performed to further investigate the weight percentage of crystalline water in samples (Figure 1c). According to the TG and DTG curves, the decomposition of the material occurred stepwise. Especially for single-phase, KVO-20 is seen on the DTG curve that a broad peak between 40 and 180 is asymmetric (which indicates two different decomposition kinetics) and overlaps with another broad one. Simultaneously, the molecular weight channels 17 (corresponding to OH) and 18 (H_2O) on the EGA−MS curves showed a broad peak ion current corresponding to the shape of the peak on the DTG curve (Supporting Information Figure S1a). The ratio of the integrated ionic current of m/z = 17 and 18 is around 0.2 in the whole temperature range, which corresponds to a well-known signature of water molecules.[57] Thus, the weight loss between 40 and 100 °C is attributed to the evaporation of physisorbed water and that between 100 and 400 °C to crystalline water.[58] The weight loss of crystalline water for a single-phase hydrated sample (KVO-20) is 1.75 wt %, which corresponds to 0.65 molecule of water per $K_2V_6O_{16}$ formula unit. The weight loss for KVO-40 and KVO-60 samples is smaller and equal to 1.48 and 0.72%, respectively. According to the XRD and FTIR results, these samples are composed of two phases: the hydrated and nonhydrated one. Therefore, upon comparison, the weight loss of the crystalline water in these samples will be smaller. The KVO-80 sample is thermally stable up to 350 °C, which is confirmed by DSC results where no thermal effects are visible (Supporting Information Figure S1b). The structural and thermal measurements confirmed that this sample consists of only a nonhydrated KV_3O_8 phase.

X-ray photoelectron spectroscopy (XPS) was used to assess the chemical composition and the charge state of vanadium ions in the studied samples. The high-resolution XPS spectra recorded in O 1s and V 2p binding energy regions (Figure 2a−d) show a complex shape of not less than three peaks located around 530 eV attributed to O 1s, as well as 517 and 524 eV attributed to the V $2p_{3/2}$ and V $2p_{1/2}$ peak doublet.[59] The V 2p peaks for all samples show an asymmetric shape with a very weak shoulder line shifted toward negative binding energies

https://doi.org/10.1021/acs.inorgchem.2c00136
Inorg. Chem. 2022, 61, 9433−9444

versus the primary component. Based on these findings, two different V components should be used for spectral deconvolution. The V $2p_{3/2}$ peaks at 516.5 and 517.5 eV correspond to V^{4+} and V^{5+}, respectively.[59] Finally, the O 1s satellite at 522 eV was also considered in the deconvolution model based on previous findings.[60] The XPS analysis allows one to estimate the relative share of vanadium V^{4+} to be on a similar level (9−16%) for the samples KVO-20, KVO-40, and KVO-60, whereas for the sample KVO-80, the vanadium V^{4+} valence state is dominant and equals 62%. The revealed significant difference in V^{4+} affects photocatalytic properties, originating from a narrow band gap of V^{4+} species facilitating charge carrier separation. The O 1s core-level spectra could be fitted by three components. The two most notable peaks at 530.1 and 530.5 eV are attributed to the O 1s orbitals of the O−V^{4+} and O−V^{5+} bonds, respectively, whose ratios are in good agreement with the V^{5+}/V^{4+} ratios estimated from the deconvolution of V $2p_{3/2}$. The third peak centered at 532.5 eV, observable for all samples, is ascribed to adsorbed OH^- ions on the surface.[61]

The above XPS analysis confirms the mixed-valence character of the obtained samples and the existence of V(IV) and V(V) in their structure. However, it should be borne in mind that XPS is a surface-sensitive technique and that the obtained results indicate a high content of V^{4+} on the surface (which is important in the view of catalytic action) and not in the bulk. Thus, to further investigate the valence of vanadium in the materials, static magnetic susceptibility was measured for samples obtained at the lowest (KVO-20) and highest temperature (KVO-80).

The temperature dependence of the magnetic susceptibility for KVO-20 and KVO-80 measured in an applied field of 3 T is shown in Figure 3. It can be clearly seen that for both samples

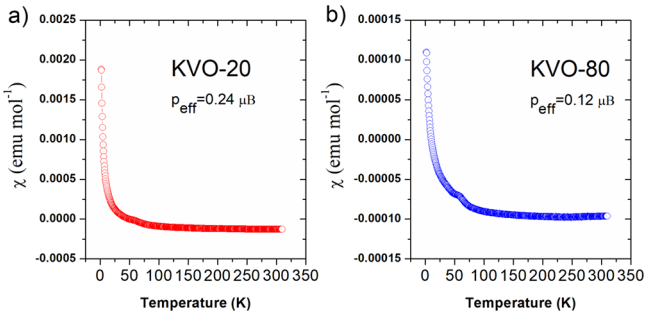

Figure 3. The temperature dependence of the magnetic susceptibility for (a) KVO-20 and (b) KVO-80 samples.

above about 50 K, $\chi(T)$ is weakly temperature-dependent and its magnitude is small. At low temperatures, the pronounced tail is observed, which can be attributed to the presence of a small amount of uncompensated V^{4+} ions.[62] To determine the effective magnetic moment (p_{eff}), the experimental data were fitted by the modified Curie−Weiss law, $\chi = \chi_0 + C/(T - \theta_P)$, where χ_0, C, and θ_P are the temperature-independent susceptibility, the Curie constant, and the paramagnetic Curie temperature, respectively. The fit gave C = 0.00712(3) emuK for KVO-20 and C = 0.00178(2) emuK for KVO-80. Assuming that the magnetic moment originates from V^{4+} only, the effective magnetic moment per V can be obtained using the relation $p_{eff} = (3Ck_B/\mu_B^2 N_A)^{1/2}$, where k_B is the Boltzmann constant, μ_B is the Bohr magneton, and N_A is Avogadro's number. The resulting effective magnetic moment p_{eff} is 0.24 and 0.12 μ_B/V for KVO-20 and KVO-80, respectively. The calculated effective magnetic moments are much smaller than the expected value of p_{eff} = 1.73 μ_B for the free V^{4+} ion. Thus, obtained results suggest that the samples consist of a vast majority of nonmagnetic V(V) species and only a small fraction of V(IV) located on the sample surface or between crystalline grains, and in case of bulk samples, the V^{4+}/V^{5+} ratio is smaller than that on the surface.

The morphologies of the samples undergo significant temperature evolution. The sample KVO-20 (single-phase $K_2V_6O_{16}\cdot 0.65H_2O$ according to XRD, FTIR, and TG results) consists of belt-like structures with a width between 50 and 200 nm, a thickness of 10−40 nm, and a length of a few micrometers (Figure 4a,b). With the increase of the synthesis temperature, the $K_2V_6O_{16}\cdot 0.65H_2O$ nanobelts become thinner, and their cross-sections decrease. For samples KVO-40 and KVO-60, the width of $K_2V_6O_{16}\cdot 0.65H_2O$ nanostructures is between 30 and 50, 20 and 40, and 10 and 20 nm, respectively, while the thickness of nanobelts is below 10 nm. Moreover, the $K_2V_6O_{16}\cdot 0.65H_2O$ nanobelts' length decreases from a few micrometers (sample KVO-40) to 100−250 nm (sample KVO-60). The crystals of the secondary phase (KV_3O_8) exhibit a plate-like morphology, and for sample KVO-40 (Figure 4c,d), the width of plates is between 0.5 and 2.5 μm, the length is between 0.5 and 4 μm, and the thickness is about 50 nm. With increasing synthesis temperature (sample KVO-60 and KVO-80), the length of KV_3O_8 crystal rises up to 0.5−7 and 1−10 μm, respectively, and the width of crystals equals ca. 150 nm. The thickness of KV_3O_8 crystals in the single-phase sample KVO-80 (Figure 4g,h) is more uniform and equals 150 nm, whereas for the multiphase sample KVO-60 (Figure 4e,f), it is in the range between 50 and 350 nm. Moreover, the

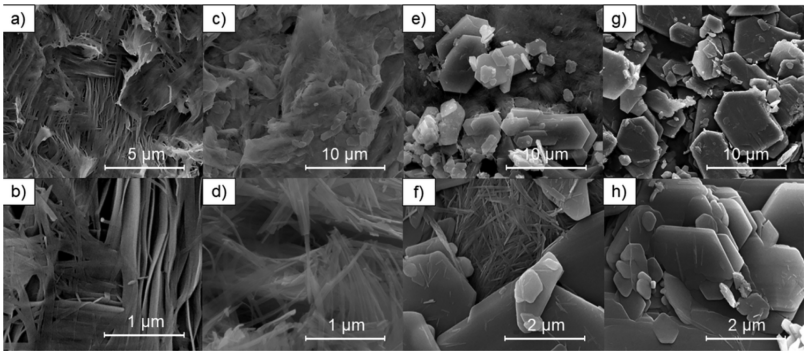

Figure 4. SEM images of samples (a, b) KVO-20, (c, d) KVO-40, (e, f) KVO-60, and (g, h) KVO-80.

https://doi.org/10.1021/acs.inorgchem.2c00136
Inorg. Chem. 2022, 61, 9433−9444

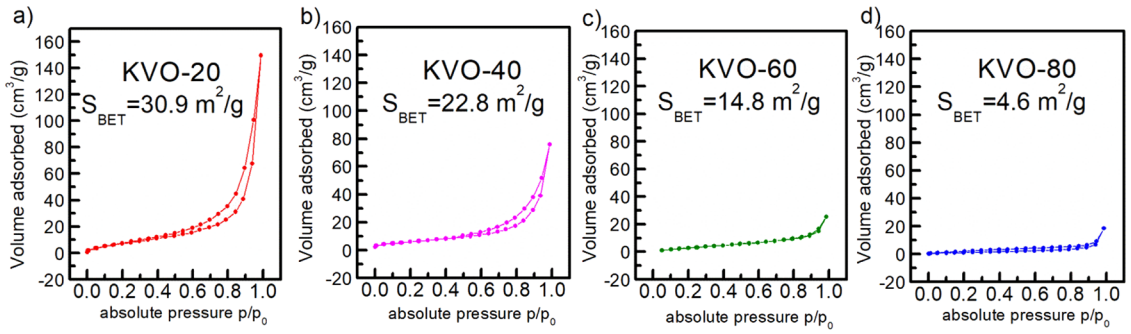

Figure 5. N_2 adsorption−desorption isotherm and calculated surface area for (a) KVO-20, (b) KVO-40, (c) KVO-60, and (d) KVO-80.

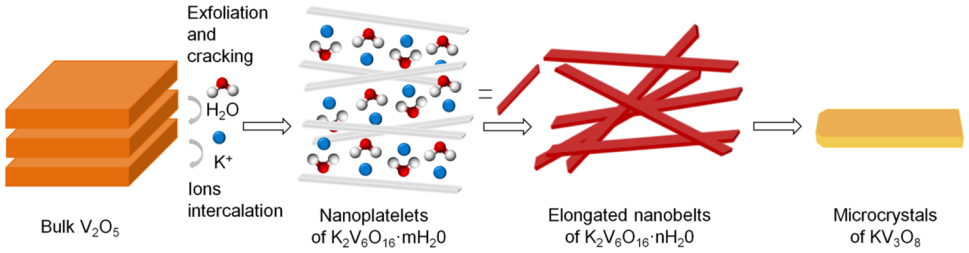

Figure 6. Schematic illustration of the evolution of potassium vanadate morphology.

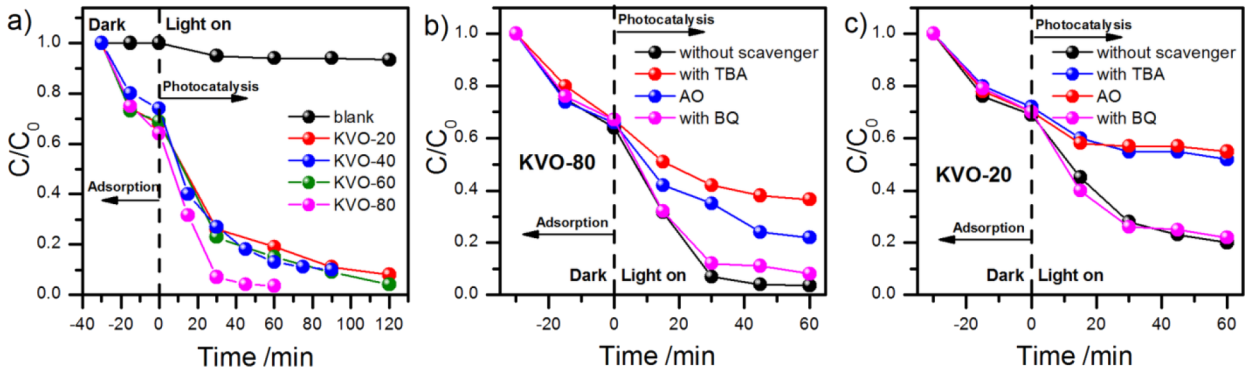

Figure 7. (a) The C/C_0 vs t plot representing the photocatalytic degradation of MB for all tested samples. (b, c) The effect of scavengers on the MB degradation rate for single-phase samples KVO-80 (KV_3O_8) and KVO-20 ($K_2V_6O_{16}{\cdot}0.65H_2O$), respectively.

surface areas of samples were determined through N_2 adsorption and BET analysis (Figure 5). As expected, the highest surface area (30.9 m^2/g) has been noted for KVO-20 with a nanostructural morphology and the lowest (4.6 m^2/g) for KVO-80 with microplatelets.

The schematic illustration of the evolution of potassium vanadate morphology is presented in Figure 6. The synthesis reaction is based on the intercalation of the solvent molecule into layer spacing and its further exchange with alkali metal ions. The reaction scheme of KVO by the LPE-IonEx synthesis method is similar to the ammonium metavanadate synthesis reported previously.[63] The solid vanadium oxide underwent delamination by the insertion of water molecules into the interlayer space. The H_2O molecules are partially trapped during potassium ion intercalation, and hydrated potassium vanadate ($K_2V_6O_{16}{\cdot}mH_2O$) is formed. During the synthesis at room temperature, the water stoichiometry is stabilized and elongated nanobelts ($K_2V_6O_{16}{\cdot}nH_2O$) are obtained. The KV_3O_8 microcrystals are formed via the dehydration and recrystallization of $K_2V_6O_{16}{\cdot}mH_2O$ at higher synthesis temperatures because the exchange between solvent molecule and potassium ion is more efficient, and a nonhydrated phase is obtained: KV_3O_8. Throughout the dehydration process, the c axis of the crystal unit cell is decreased by almost half. During this process, the creation of V^{4+} species is probable. Therefore, the obtained KV_3O_8 phase possesses a rich vanadium-defective structure.

Photocatalytic Properties. The photocatalytic performance of investigated powders is presented as a C to C_0 ratio in Figure 7a. Additionally, the effect of the photolysis of MB is added for comparison (blank). Before the irradiation, methylene blue was adsorbed on the surface of the tested powders at a similar, considerable level of 30%. Adsorption is an essential process in photocatalysis, which enriches the pollutants around the catalyst surface, and often, strong adsorption results in increased photocatalytic performance.[64] All samples acted as efficient photocatalysts for dye decomposition; however, the sample obtained at 80 °C exhibited the highest photoactivity. After about 30 min of exposure, over 90% of MB was degraded. In the case of the rest of the samples (obtained at 20, 40, and 60 °C), the observed photoactivity was similar and the time required for MB degradation was longer (approximately 90% of degradation after 90 min). To the best of our knowledge, there is only one

https://doi.org/10.1021/acs.inorgchem.2c00136
Inorg. Chem. 2022, 61, 9433−9444

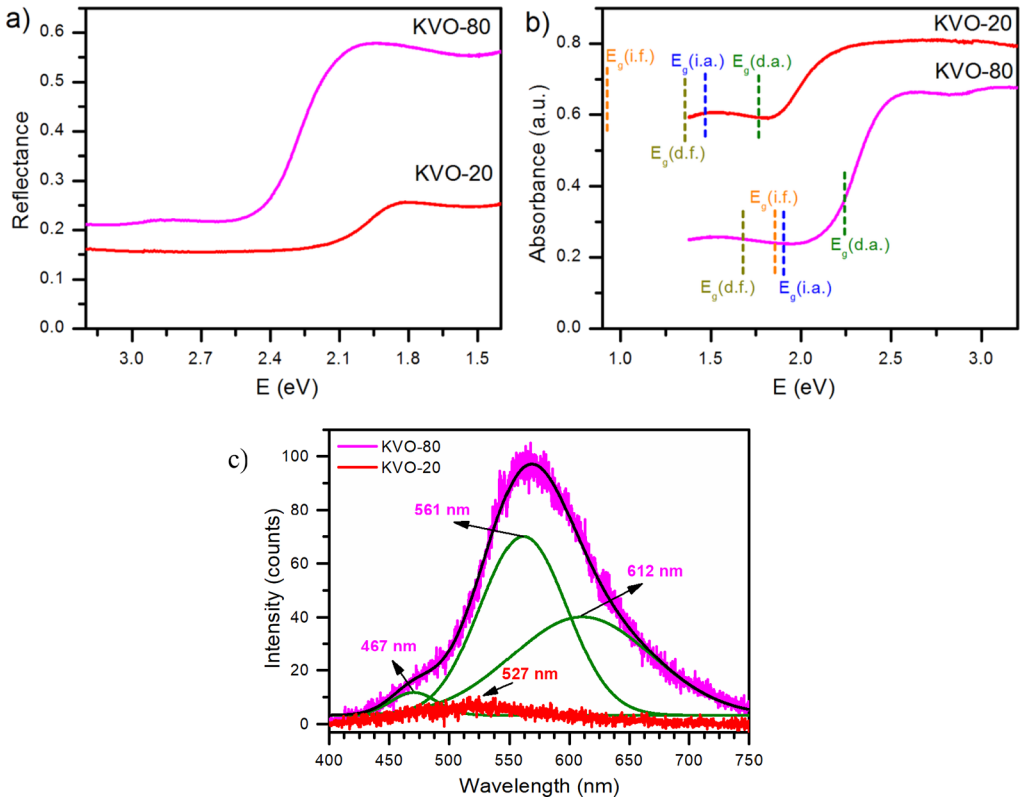

Figure 8. (a) Reflectance (measured) and (b) absorbance (calculated) spectra of KV_3O_8 microplatelet (KVO-80) and $K_2V_6O_{16}{\cdot}0.65H_2O$ nanobelt (KVO-20) samples. (c) Photoluminescence spectra of KV_3O_8 (KVO-80) and $K_2V_6O_{16}{\cdot}0.65H_2O$ (KVO-20).

report[65] devoted to the potassium vanadate compounds that presents using of hydrated vanadates ($K_2V_6O_{16}{\cdot}1.5H_2O$/$2.7H_2O$) for the photodegradation of methyl orange. In comparison to the mentioned work, samples obtained by our method exhibit better photocatalytic activity. Furthermore, the calculated band gap for $K_2V_6O_{16}{\cdot}nH_2O$ is narrower in the case of the sample reported by us. Moreover, herein, for the first time, we present nonhydrated KV_3O_8 as a new efficient photocatalyst. This implies that the photocatalytic efficiency of our samples results from the specific structural properties, which were provided by the proposed innovative LPE-IonEx method. Often, the developed surface also has a beneficial effect for photocatalytic efficiency. It is reported that a high surface area inhibits the electron−hole recombination and allows the adsorption of more MB molecules.[66−68] Nonetheless, for investigated samples, the reverse tendency was observed. The sample with the lowest surface area (according to the BET method) exhibited the best photocatalytic performance, while for the sample with the highest surface area, the degradation process was the least effective. This confirms that, in the case of the synthesized samples, their photocatalytic activity is not dependent on the surface area. It is supposed that the presence of V^{4+} species plays a pivotal role here. Surface defect engineering has gained a lot of attention in the development of efficient photocatalysts. The existence of defect sites in vanadates has been reported to be crucial in enhancing photocatalytic performance in water splitting and degradation of pollutants.[69−71] Zhang et al. have shown enhanced photoelectrochemical performance of V^{4+} self-doped m-$BiVO_4$. Compared to the pure $BiVO_4$, V^{4+} doped samples possess enhanced photocurrent density, smaller charge transfer resistance, longer electron lifetime, and improved separation of photogenerated electrons and holes.[72] Yu and co-workers presented CaV_2O_6 nanorods that exhibited improved photocatalytic activity in MB degradation due to the coexistence of V^{4+}/V^{5+} in the lattice. CaV_2O_6 shows an indirect allowed electronic transition with a band gap energy of 2.56 eV and hydroxyl radicals as the major active species.[73] Saputera et al. obtained $BiVO_4$ with a different vanadium vacancy content by changing the calcination temperature after sol−gel synthesis. Obtained samples were then evaluated by the degradation of palm oil mill effluent waste under UV−visible light. Results revealed that the higher the V^{4+} content was, the better were the degradation rates and reaction rate constant. It was also observed that the increase in V^{4+} content resulted in a slight increase of band gap energy (2.44 to 2.50 eV).[74]

To investigate the kinetics of the process, the $\ln(C/C_0)$ vs t plot was prepared (see Supporting Information Figure S2). The most probable is the pseudo-first-order kinetics according to the Langmuir−Hinshelwood model;[75] however, the mechanism of the photocatalytic degradation can be more complex. Thus, the additional measurements for single-phase samples $K_2V_6O_{16}{\cdot}0.65H_2O$ (KVO-20) and KV_3O_8 (KVO-80) in the presence of appropriate scavengers were performed (see Figure 7b,c). *tert*-Butyl alcohol (TBA), benzoquinone (BQ), and ammonium oxalate (AO) act as a hydroxyl radical, superoxide radical, and hole scavenger, respectively.[76] The decrease of the decomposition efficiency in a solution containing a scavenger suggests the role of the relevant species in the mechanism of the degradation mechanism. Thus, in both cases, the role of superoxide radicals is negligible. On the other hand, degradation efficiency in the presence of a hydroxyl radical scavenger is significantly diminished in comparison with the control measurement. It is indirect

https://doi.org/10.1021/acs.inorgchem.2c00136
Inorg. Chem. 2022, 61, 9433−9444

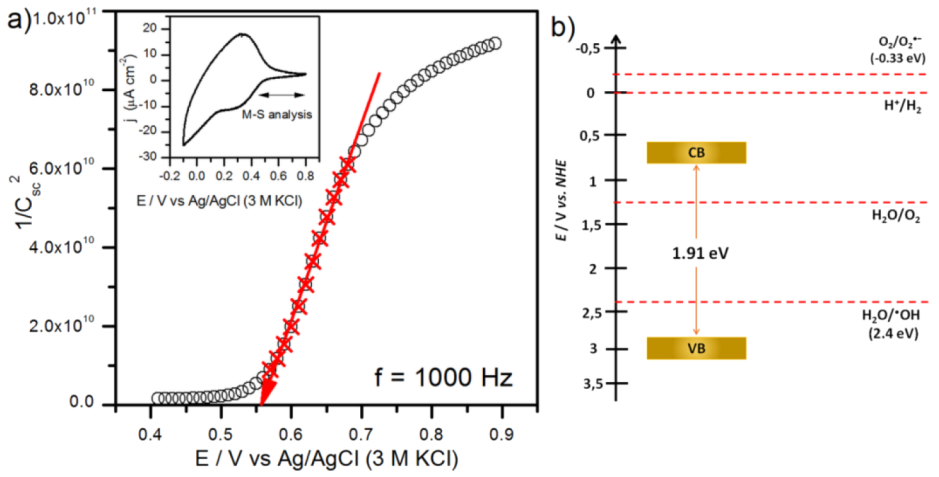

Figure 9. (a) The Mott−Schottky analysis performed for KV_3O_8 (KVO-80). Inset: cyclic voltammetry curve recorded with 50 mV/s. (b) The energy band position diagram of the sample KV_3O_8 (KVO-80).

proof that OH· is formed during the illumination of the $K_2V_6O_{16}·0.65H_2O$ (KVO-20) and KV_3O_8 (KVO-80) aqueous suspensions. Noteworthily, the direct oxidation of MB by photoexcited holes from the valence band of the photocatalyst also takes part in the degradation process. According to the results presented in Figure 7b, it can be concluded that approximately equal amounts of MB are decomposed by OH radicals and holes in the case of $K_2V_6O_{16}·0.65H_2O$. The role of direct oxidation in the case of KV_3O_8 is smaller but still significant (Figure 7c).

Optical Properties of $K_2V_6O_{16}·0.65H_2O$ Nanobelts and KV_3O_8 Microplatelets. The optical behavior of single-phase samples KV_3O_8 microplatelets and $K_2V_6O_{16}·0.65H_2O$ nanobelts, which were, respectively, the most and the least photoactive material, was further examined using UV−vis spectroscopy in the reflectance mode. The spectra of both samples are presented in Figure 8a. As can be seen, synthesized materials absorb a significant part of the light in the visible range. This feature is beneficial for the materials used in photocatalysis. Reflectance edges seen on both spectra are related to the energy band gap transition, so the obtained results allowed the energy band gap to be estimated. There is no information about the type of electron transition; thus, all possibilities were taken into account, as presented in Figure S3. The absorbance spectra of both powders with marked band gaps estimated from $(f(\mathrm{KM})·h\nu)^n$ vs $h\nu$ plots are presented in Figure 8b. Since the energy band gap corresponds to the absorbed photons with the lowest energy, the direct energy band gap (d.a.) in the case of $K_2V_6O_{16}·0.65H_2O$ nanobelts is the most probable. On the other hand, the estimated value of the direct band gap for KV_3O_8 microplatelets corresponds to a wavelength that is already within the absorption edge. Thus, it is very likely that the optical band gap of the KV_3O_8 material is related to the allowed indirect transition (i.d.); nevertheless, the direct band gap can be taken into account as well. Thus, the determined direct energy band gaps for $K_2V_6O_{16}·0.65H_2O$ and KV_3O_8 are 1.80 and 2.23 eV (and the indirect energy band gap for KV_3O_8 is equal to 1.91 eV), respectively. These values are in accordance with the observed colors: dark red for the hydrated phase and orange for the nonhydrated phase. The differences in estimated energy band gaps suggest that KVO-20 could be a better photocatalyst due to the wider range of electromagnetic radiation that can be absorbed and converted. As shown in Figure 7, it is not the case. In the case of KV_3O_8 and $K_2V_6O_{16}·0.65H_2O$, direct comparison is misleading because they are two different compounds with different crystal structure and stoichiometry (Figure 1), surface composition (Figure 2), morphology (Figure 4), and surface area (Figure 5). It can be concluded that all the above-mentioned parameters have a greater impact on photoactivity than UV−vis absorption ability.

Additionally, the photoluminescence spectra have been recorded using UV excitation. Results are presented in Figure 8c. Generally, the emission spectrum of KVO-80 is characterized by a much higher intensity of photoluminescence in comparison with KVO-20. It could be simply related to the better crystallinity of the sample prepared at a higher temperature;[77] however, the shape of the emission bands is also different. Often, photocatalysts are examined with PL to compare emission intensity. In the case of photoactive materials, a higher PL intensity means a higher rate of recombination processes and therefore poorer photocatalytic performance. Thus, here PL spectra suggest that better photocatalytic activity should be observed for the KVO-20 sample (which is not true). However, such direct comparison can be done for samples with similar characteristics (composition, morphology, surface area, etc.) because PL intensity is affected by many parameters.[78]

The PL intensity of the KVO-20 spectrum is very low, which makes the analysis very difficult to perform. The maximum can be found at about 527 nm (2.35 eV). Taking into account the absorbance spectrum, the recorded emission is not related with conduction to valence band extinction. In the case of the KVO-80 sample, the spectrum can be deconvoluted to 3 Gaussian peaks with the maximum at 467 nm (2.66 eV), 561 nm (2.21 eV), and 612 nm (2.03 eV). The PL emission at energies lower than the band gap (2.03 eV) is related to the presence of states within the energy band gap. Here, it can be associated with the presence of oxygen vacancies and V(IV) centers seen on XPS. A similar phenomenon was observed for partially reduced metal oxides (TiO_2, SnO_2, and In_2O_3), while for fully oxidized materials, visible light photoluminescence was diminished.[79] The PL bands at energies lower than the energy band gap were also reported for V_2O_5 and were described as an effect of the oxygen vacancies' presence.[80] The second band at the PL spectrum of KVO-80 has an energy (2.21 eV, 561 nm) close to

https://doi.org/10.1021/acs.inorgchem.2c00136
Inorg. Chem. 2022, 61, 9433−9444

the band gap; thus, it probably originates from the direct band edge transition. The low-intensity band at 467 nm that can be seen in Figure 8c and a similar one were already reported for V_2O_5 nanostructures. It was described as the recombination of UV excited electrons from a higher level in the V 3d orbital (in the conduction band) to the ground level.[81]

Energy Band Position of KV_3O_8 (KVO-80). Electrochemical characterization of the sample allowed the estimation of the energy band position for the stable nonhydrated KV_3O_8 phase. The procedure of sample thin film preparation did not affect its crystal structure and the charge state of vanadium (see Supporting Information Figures S4 and S5). The flat band potential (E_{fb}) was determined using the Mott−Schottky (MS) analysis. To estimate the space charge region capacitance (C_{sc}), the impedance spectra were measured at dark conditions as a function of applied potential. The range of potential for MS analysis was chosen on the basis of the cyclic voltammetry (CV) study presented in the Figure 9a inset. The peaks observed at the CV curve are probably related to the V center oxidation/reduction with the simultaneous K^+ intercalation/deintercalation process. The impedance spectra were measured between 0.4 and 0.9 V vs Ag/AgCl (3 M KCl), but the linear behavior of $1/C_{sc}^2$ vs E was found between 0.58 and 0.69 V (see Figure 8a). The positive slope of the Mott−Schottky plot confirmed that the obtained nonhydrated KV_3O_8 phase is an n-type semiconductor and E_{fb} equals to about 0.56 V vs Ag/AgCl (3 M KCl) (0.765 V vs NHE). The energy band diagram was prepared assuming that E_{fb} lies just below the conduction band and the UV−vis determined indirect energy band gap of KV_3O_8 is 1.91 eV. As presented in Figure 8b, the valence band (VB) location allows photoexcited holes to react with adsorbed water and form hydroxyl radicals. On the other hand, the potential of the photoexcited electrons from the conduction band (CB) is not enough to form superoxide radicals. These conclusions are consistent with the efficiency of the photocatalysts.

According to the above-described results, the possible mechanism of photocatalytic performance of KV_3O_8 has been proposed. The major reaction steps responsible for the photocatalytic activity could be expressed as follows:

(1) $KV_3O_8 + h\nu \rightarrow e^-(CB, KV_3O_8) + h^+(CB, KV_3O_8)$

(2) $e^- + O_2 \rightarrow O_2^{\cdot -}$

(3) $h^+ + H_2O/OH^- \rightarrow OH\cdot$

(4) $OH\cdot + MB \rightarrow$ other product $\rightarrow CO_2 + H_2O$

(5) $h^+(CB, KV_3O_8) + MB$

$\rightarrow$ other product

$\rightarrow CO_2 + H_2O$

The UPLC−QTOF-MS/MS was further applied to identify the main MB degradation products for samples obtained after photocatalytic degradation by KVO-80 (KV_3O_8) and KVO-20 ($K_2V_6O_{16}\cdot 0.65H_2O$) used as a catalyst. The total ion current chromatograms (TICs, Supporting Information) are presented in Figure S6. On the basis of the received data after using KVO-80 as a catalyst, besides the nondecomposed MB, two additional degradation compounds were identified. The observed peaks on the chromatogram at 2.576 and 8.122 min correspond probably to 4-nitroaniline $[C_6H_6N_2O_2 + H]^+$ and m/z 139.0512, and phenol $[C_6H_6O + H]^+$ and m/z 95.0494, respectively (see Figure S7, Supporting Information), while the peak observed at 4.591 min is attributed to MB. The above photodegradation process generates about 8.34% of nondecomposed MB, 0.12% of aniline, and 0.45% of phenol. The possible degradation pathway where the aniline occurred as a product was described elsewhere.[82]

In the case of analysis of MB degradation products using KVO-20 as the photocatalyst, the obtained results allowed for the identification of at least four additional compounds besides MB residues (4.586 min, see Figure S8). The observed peaks on the chromatogram at 2.604 and 8.116 min in the resulting products, as in the case of KVO-80 catalyst, can be assigned to 4-nitroaniline $[C_6H_6N_2O_2 + H]^+$ and m/z 139.0508, and phenol $[C_6H_6O + H]^+$ and m/z 95.0494, respectively. Analysis of the sample after the use of KVO-20 as a catalyst also identifies two additional compounds. On the chromatogram at 3.12 min, the $[C_7H_{10}N_2O_4S + H]^+$ and m/z 219.0444 was identified, corresponding to 2-amino-5-(methylamino)-hydroxybenzenesulfonic acid, which was previously described in the photocatalytic MB degradation pathway,[83] which leads to H_2O and CO_2. In addition, it is worth mentioning that on the chromatogram peak presence at 5.219 min reveal to benzenesulfonic acid $[C_6H_6O_3S + H]^+$ and m/z 159.0063, which also occur in the photocatalytic MB degradation pathway as previously described.[84] Comparing the efficiency of MB degradation through the use of the KVO-20 catalyst with the KVO-80 catalyst, the efficiency of the KVO-20 catalyst is significantly lower. The photodegradation process catalyzed by KVO-20 generates about 16.78% of nondecomposed MB, 36.27% of benzenesulfonic acid, and comparable amounts (0.40%) of phenol and the amino-5-(methylamino)-hydroxybenzenesulfonic acid, which is formed in approximately 0.46%. On the other hand, a negligible 0.07% amount of 4-nitroaniline is formed when the KVO-20 catalyst was applied, which indicates the efficiency and difference of the photodegradation mechanisms of MB using the described catalysts.

CONCLUSIONS

In this study, $K_2V_6O_{16}\cdot 0.65H_2O$ nanobelts and KV_3O_8 microplatelets were synthesized using the facile LPE-IonEx method and investigated as catalysts for organic dye degradation. The obtained samples were characterized using XRD, FTIR, XPS,PPMS, UV−vis DRS, PL, TGA with MS, SEM, and N_2 adsorption isotherms. Controlling the reaction temperature (20−80 °C) resulted in various phase compositions, morphologies, and surface areas. Moreover, different synthesis temperatures provided varied concentrations of V^{4+} (from 9% up to such a high content as 62%). The photocatalytic degradation of methylene blue, under simulated solar light illumination, was examined to evaluate the photocatalytic performance of prepared samples. All samples acted as efficient photocatalysts, resulting in approximately 90% degradation of the dye within the first 30−90 min. The highest activity was observed for the sample obtained at 80 °C. According to the scavenger test, OH radicals and holes are the main active species in the case of $K_2V_6O_{16}\cdot 0.65H_2O$. The role of direct oxidation in the case of KV_3O_8 is smaller but still significant. The results indicate that potassium vanadates are potential candidates for light-driven photocatalysts. The observed excellent photocatalytic performances result from the specific structural properties, which were provided by the proposed innovative LPE-IonEx method. We suggest that it can be attributed to the high content of V^{4+} species in the samples, which traps electrons and facilitates charge separation.

https://doi.org/10.1021/acs.inorgchem.2c00136
Inorg. Chem. 2022, 61, 9433−9444

■ ASSOCIATED CONTENT

Supporting Information

The Supporting Information is available free of charge at https://pubs.acs.org/doi/10.1021/acs.inorgchem.2c00136.

TG and DTG curves with ion current curves of the KVO-20 sample; DSC curves of the KVO-20 and KVO-80 sample; FTIR, XRD, and SEM image of sample KVO-20 after heat treatment; XRD of as-prepared sample KVO-80 and XRD and XPS of KVO-80 deposited onto degreased FTO (KVO-80/FTO); results of MB photodegradation presented as the $\ln(C/C_0)$ vs time plots; and UPLC−QTOF-MS/MS (chromatograms and mass spectra) of MB degradation products for samples obtained after photocatalytic degradation by KVO-80 and KVO-20 (PDF)

■ AUTHOR INFORMATION

Corresponding Author

Marta Prześniak-Welenc − *Faculty of Applied Physics and Mathematics, Institute of Nanotechnology and Materials Engineering, Gdansk University of Technology, Gdansk 80-233, Poland;* orcid.org/0000-0002-7640-2677; Email: marwelen@pg.edu.pl

Authors

Małgorzata Nadolska − *Faculty of Applied Physics and Mathematics, Institute of Nanotechnology and Materials Engineering, Gdansk University of Technology, Gdansk 80-233, Poland;* orcid.org/0000-0001-5998-2975

Mariusz Szkoda − *Faculty of Chemistry, Gdansk University of Technology, Gdansk 80-233, Poland*

Konrad Trzciński − *Faculty of Chemistry, Gdansk University of Technology, Gdansk 80-233, Poland*

Paweł Niedziałkowski − *Faculty of Chemistry, University of Gdansk, Gdansk 80-308, Poland*

Jacek Ryl − *Faculty of Applied Physics and Mathematics, Institute of Nanotechnology and Materials Engineering, Gdansk University of Technology, Gdansk 80-233, Poland;* orcid.org/0000-0002-0247-3851

Aleksandra Mielewczyk-Gryń − *Faculty of Applied Physics and Mathematics, Institute of Nanotechnology and Materials Engineering, Gdansk University of Technology, Gdansk 80-233, Poland;* orcid.org/0000-0001-6795-3840

Karolina Górnicka − *Faculty of Applied Physics and Mathematics, Institute of Nanotechnology and Materials Engineering, Gdansk University of Technology, Gdansk 80-233, Poland*

Complete contact information is available at: https://pubs.acs.org/10.1021/acs.inorgchem.2c00136

Author Contributions

The manuscript was written through contributions of all authors. All authors have given approval to the final version of the manuscript.

Notes

The authors declare no competing financial interest.

■ ACKNOWLEDGMENTS

The authors would like to acknowledge Professor M. Sawczak from The Szewalski Institute of Fluid-Flow Machinery Polish Academy of Sciences for PL and UV−VIS enabling measurements. This work is supported by the National Science Center of Poland (Grant 2020/37/N/ST5/03697). The authors also acknowledge the financial support from Gdańsk University of Technology by the DEC-3/2020/IDUB/I.3.3 grant under the Argentum-"Excellence Initiative-Research University" and the National Centre for Research and Development via Grant LIDER/15/0088/L-10/18/NCBR/2019 (Integrated prototype of a photo-supercapacitor for energy storage obtained as a result of solar radiation conversion).

■ REFERENCES

(1) Melchionna, M.; Fornasiero, P. Updates on the Roadmap for Photocatalysis. *ACS Catal.* **2020**, *10*, 5493−5501.

(2) Anwer, H.; Mahmood, A.; Lee, J.; Kim, K. H.; Park, J. W.; Yip, A. C. K. Photocatalysts for Degradation of Dyes in Industrial Effluents: Opportunities and Challenges. *Nano Res.* **2019**, *12*, 955−972.

(3) Di Paola, A.; García-López, E.; Marcì, G.; Palmisano, L. A Survey of Photocatalytic Materials for Environmental Remediation. *J. Hazard. Mater.* **2012**, *211-212*, 3−29.

(4) Nazri, M. K. H. M.; Sapawe, N. A Short Review on Photocatalytic toward Dye Degradation. *Mater. Today: Proc.* **2020**, *31*, A42−A47.

(5) Nagajyothi, P. C.; Prabhakar Vattikuti, S. V.; Devarayapalli, K. C.; Yoo, K.; Shim, J.; Sreekanth, T. V. M. Green Synthesis: Photocatalytic Degradation of Textile Dyes Using Metal and Metal Oxide Nanoparticles-Latest Trends and Advancements. *Crit. Rev. Environ. Sci. Technol.* **2020**, *50*, 2617−2723.

(6) Marimuthu, S.; Antonisamy, A. J.; Malayandi, S.; Rajendran, K.; Tsai, P. C.; Pugazhendhi, A.; Ponnusamy, V. K. Silver Nanoparticles in Dye Effluent Treatment: A Review on Synthesis, Treatment Methods, Mechanisms, Photocatalytic Degradation, Toxic Effects and Mitigation of Toxicity. *J. Photochem. Photobiol. B Biol.* **2020**, *205*, No. 111823.

(7) Koe, W. S.; Lee, J. W.; Chong, W. C.; Pang, Y. L.; Sim, L. C. An Overview of Photocatalytic Degradation: Photocatalysts, Mechanisms, and Development of Photocatalytic Membrane. *Environ. Sci. Pollut. Res.* **2020**, *27*, 2522−2565.

(8) Chandrasekaran, S.; Yao, L.; Deng, L.; Bowen, C.; Zhang, Y.; Chen, S.; Lin, Z.; Peng, F.; Zhang, P. Recent Advances in Metal Sulfides: From Controlled Fabrication to Electrocatalytic, Photocatalytic and Photoelectrochemical Water Splitting and Beyond. *Chem. Soc. Rev.* **2019**, *48*, 4178−4280.

(9) Ayodhya, D.; Veerabhadram, G. A Review on Recent Advances in Photodegradation of Dyes Using Doped and Heterojunction Based Semiconductor Metal Sulfide Nanostructures for Environmental Protection. *Mater. Today Energy* **2018**, *9*, 83−113.

(10) Hasija, V.; Raizada, P.; Sudhaik, A.; Sharma, K.; Kumar, A.; Singh, P.; Jonnalagadda, S. B.; Thakur, V. K. Recent Advances in Noble Metal Free Doped Graphitic Carbon Nitride Based Nanohybrids for Photocatalysis of Organic Contaminants in Water: A Review. *Appl. Mater. Today* **2019**, *15*, 494−524.

(11) Dong, J. P.; Shi, Z. Z.; Li, B.; Wang, L. Y. Synthesis of a Novel 2D Zinc(Ii) Metal-Organic Framework for Photocatalytic Degradation of Organic Dyes in Water. *Dalt. Trans.* **2019**, *48*, 17626−17632.

(12) Wu, Y.; Luo, H.; Wang, H. Synthesis of Iron(Iii)-Based Metal-Organic Framework/Graphene Oxide Composites with Increased Photocatalytic Performance for Dye Degradation. *RSC Adv.* **2014**, *4*, 40435−40438.

(13) Hasanpour, M.; Hatami, M. Photocatalytic Performance of Aerogels for Organic Dyes Removal from Wastewaters: Review Study. *J. Mol. Liq.* **2020**, *309*, No. 113094.

(14) Ghiyasiyan-Arani, M.; Masjedi-Arani, M.; Salavati-Niasari, M. Facile Synthesis, Characterization and Optical Properties of Copper Vanadate Nanostructures for Enhanced Photocatalytic Activity. *J. Mater. Sci.: Mater. Electron.* **2016**, *27*, 4871−4878.

(15) Huang, Z. F.; Pan, L.; Zou, J. J.; Zhang, X.; Wang, L. Nanostructured Bismuth Vanadate-Based Materials for Solar-Energy-Driven Water Oxidation: A Review on Recent Progress. *Nanoscale* **2014**, *6*, 14044−14063.

(16) Xiang, L.; Fan, J.; Zhong, W.; Mao, L.; You, K.; Yin, D. Heteroatom-Induced Band-Reconstruction of Metal Vanadates for Photocatalytic Cyclohexane Oxidation towards KA-Oil Selectivity. *Appl. Catal., A* **2019**, *575*, 120−131.
(17) Guo, J.; Liang, J.; Yuan, X.; Jiang, L.; Zeng, G.; Yu, H.; Zhang, J. Efficient Visible-Light Driven Photocatalyst, Silver (Meta)Vanadate: Synthesis, Morphology and Modification. *Chem. Eng. J.* **2018**, *352*, 782−802.
(18) Zhao, X.; Huang, J.; Feng, L.; Cao, L.; Li, J.; Zhou, L. Facile Synthesis of α-Ag3VO4 Hollow Nanospheres with Improved Photocatalytic Activities. *J. Alloys Compd.* **2017**, *718*, 7−14.
(19) Wang, F.; Zhang, H.; Liu, L.; Shin, B.; Shan, F. AgV7O18: A New Silver Vanadate Semiconductor with Photodegradation Ability on Dyes under Visible-Light Irradiation. *Mater. Lett.* **2016**, *169*, 82−85.
(20) Khan, I.; Qurashi, A. Shape Controlled Synthesis of Copper Vanadate Platelet Nanostructures, Their Optical Band Edges, and Solar-Driven Water Splitting Properties. *Sci. Rep.* **2017**, *7*, 1−11.
(21) Sajid, M. M.; Zhai, H.; Shad, N. A.; Shafique, M.; Afzal, A. M.; Javed, Y.; Khan, S. B.; Ikram, M.; Amin, N.; Zhang, Z. Photocatalytic Performance of Ferric Vanadate (FeVO4) Nanoparticles Synthesized by Hydrothermal Method. *Mater. Sci. Semicond. Process.* **2021**, *129*, No. 105785.
(22) Li, D.; Bai, X.; Pan, C.; Zhu, Y. Investigations on the Phase Transition between CdV2O6 and Cd2V2O7 and Their Photocatalytic Performances. *Eur. J. Inorg. Chem.* **2013**, 3070−3075.
(23) Yang, R.; Zhang, Y.; Fan, Y.; Wang, R.; Zhu, R.; Tang, Y.; Yin, Z.; Zeng, Z. InVO4-Based Photocatalysts for Energy and Environmental Applications. *Chem. Eng. J.* **2022**, *428*, No. 131145.
(24) Mazierski, P.; Sowik, J.; Miodyńska, M.; Trykowski, G.; Mikołajczyk, A.; Klimczuk, T.; Lisowski, W.; Nadolna, J.; Zaleska-Medynska, A. Shape-Controllable Synthesis of GdVO 4 Photocatalysts and Their Tunable Properties in Photocatalytic Hydrogen Generation. *Dalt. Trans.* **2019**, *48*, 1662−1671.
(25) Wang, L.; Shi, X.; Jia, Y.; Cheng, H.; Wang, L.; Wang, Q. Recent Advances in Bismuth Vanadate-Based Photocatalysts for Photoelectrochemical Water Splitting. *Chin. Chem. Lett.* **2021**, *32*, 1869−1878.
(26) Sajid, M. M.; Amin, N.; Shad, N. A.; khan, S. B.; Javed, Y.; Zhang, Z. Hydrothermal Fabrication of Monoclinic Bismuth Vanadate (m-BiVO 4) Nanoparticles for Photocatalytic Degradation of Toxic Organic Dyes. *Mater. Sci. Eng., B* **2019**, *242*, 83−89.
(27) Monsef, R.; Ghiyasiyan-Arani, M.; Salavati-Niasari, M. Application of Ultrasound-Aided Method for the Synthesis of NdVO4 Nano-Photocatalyst and Investigation of Eliminate Dye in Contaminant Water. *Ultrason. Sonochem.* **2018**, *42*, 201−211.
(28) Sivakumar, V.; Suresh, R.; Giribabu, K.; Narayanan, V. BiVO 4 Nanoparticles: Preparation, Characterization and Photocatalytic Activity. *Cogent Chem.* **2015**, *1*, 1074647.
(29) Roy, J. S.; Dugas, G.; Morency, S.; Ribeiro, S. J. L.; Messaddeq, Y. Enhanced Photocatalytic Activity of Silver Vanadate Nanobelts in Concentrated Sunlight Delivered through Optical Fiber Bundle Coupled with Solar Concentrator. *SN Appl. Sci.* **2020**, *2*, 1−11.
(30) Pei, L. Z.; Lin, N.; Wei, T.; Yu, H. Y. Synthesis of Manganese Vanadate Nanobelts and Their Visible Light Photocatalytic Activity for Methylene Blue. *J. Exp. Nanosci.* **2016**, *11*, 197−214.
(31) Wang, W.; Yu, Y.; An, T.; Li, G.; Yip, H. Y.; Yu, J. C.; Wong, P. K. Visible-Light-Driven Photocatalytic Inactivation of E. Coli K-12 by Bismuth Vanadate Nanotubes: Bactericidal Performance and Mechanism. *Environ. Sci. Technol.* **2012**, *46*, 4599−4606.
(32) Kása, Z.; Almási, E. E.; Hernádi, K.; Gyulavári, T.; Baia, L.; Veréb, G.; László, Z.; Pap, Z. New Insights into the Photoactivity of Shape-Tailored BiVO4 Semiconductors via Photocatalytic Degradation Reactions and Classical Reduction Processes. *Molecules* **2020**, *25*, 1−14.
(33) Chen, L.; Wang, J.; Meng, D.; Wu, X.; Wang, Y.; Zhong, E. The PH-Controlled {040} Facets Orientation of BiVO4 Photocatalysts with Different Morphologies for Enhanced Visible Light Photocatalytic Performance. *Mater. Lett.* **2016**, *162*, 150−153.
(34) Zhang, K.; Deng, J.; Liu, Y.; Xie, S.; Dai, H. Photocatalytic Removal of Organics over BiVO4-Based Photocatalysts. In *Materials, Mechanisms and Applications, Wenbin Cao, IntechOpen*.
(35) Wu, M.; Jing, Q.; Feng, X.; Chen, L. BiVO 4 Microstructures with Various Morphologies: Synthesis and Characterization. *Appl. Surf. Sci.* **2018**, *427*, 525−532.
(36) Zhao, Y.; Li, R.; Mu, L.; Li, C. Significance of Crystal Morphology Controlling in Semiconductor-Based Photocatalysis: A Case Study on BiVO4 Photocatalyst. *Cryst. Growth Des.* **2017**, *17*, 2923−2928.
(37) Tokunaga, S.; Kato, H.; Kudo, A. Selective Preparation of Monoclinic and Tetragonal BiVO4 with Scheelite Structure and Their Photocatalytic Properties. *Chem. Mater.* **2001**, *13*, 4624−4628.
(38) Li, W.; Wang, X.; Wang, Z.; Meng, Y.; Sun, X.; Yan, T.; You, J.; Kong, D. Relationship between Crystalline Phases and Photocatalytic Activities of BiVO4. *Mater. Res. Bull.* **2016**, *83*, 259−267.
(39) Thalluri, S. M.; Hussain, M.; Saracco, G.; Barber, J.; Russo, N. Green-Synthesized BiVO4 Oriented along {040} Facets for Visible-Light-Driven Ethylene Degradation. *Ind. Eng. Chem. Res.* **2014**, *53*, 2640−2646.
(40) Kamble, G. S.; Ling, Y. C. Solvothermal Synthesis of Facet-Dependent BiVO4 Photocatalyst with Enhanced Visible-Light-Driven Photocatalytic Degradation of Organic Pollutant: Assessment of Toxicity by Zebrafish Embryo. *Sci. Rep.* **2020**, *10*, 1−11.
(41) Bakhtiarnia, S.; Sheibani, S.; Billard, A.; Sun, H.; Aubry, E.; Yazdi, M. A. P. Enhanced Photocatalytic Activity of Sputter-Deposited Nanoporous BiVO4 Thin Films by Controlling Film Thickness. *J. Alloys Compd.* **2021**, *879*, No. 160463.
(42) Pham, M. Q.; Ngo, T. M.; Nguyen, V. H.; Nong, L. X.; Vo, D. V. N.; Van Tran, T.; Nguyen, T. D.; Bui, X. T.; Nguyen, T. D. Facile Solvothermal Synthesis of Highly Active Monoclinic Scheelite BiVO4 for Photocatalytic Degradation of Methylene Blue under White LED Light Irradiation. *Arab. J. Chem.* **2020**, *13*, 8388−8394.
(43) Pantò, F.; Dahrouch, Z.; Saha, A.; Patanè, S.; Santangelo, S.; Triolo, C. Photocatalytic Degradation of Methylene Blue Dye by Porous Zinc Oxide Nanofibers Prepared via Electrospinning: When Defects Become Merits. *Appl. Surf. Sci.* **2021**, *557*, No. 149830.
(44) Shi, C.; Dong, X.; Wang, J.; Wang, X.; Ma, H.; Zhang, X. Interfacial Defect Engineering over Fusiform Bismuth Vanadate Photocatalyst Enables to Excellent Solar-to-Chemical Energy Coupling. *RSC Adv.* **2017**, *7*, 26717−26721.
(45) Wen, P.; Liu, T.; Wei, F.; Ai, L.; Yao, F. Soft Chemical Topotactic Synthesis and Crystal Structure Evolution from Two-Dimensional KV3O8 Plates to One-Dimensional V3O7 Nanobelts. *CrystEngComm* **2016**, *18*, 8880−8886.
(46) Miller, D. J.; Biesinger, M. C.; McIntyre, N. S. Interactions of CO2 and CO at Fractional Atmosphere Pressures with Iron and Iron Oxide Surfaces: One Possible Mechanism for Surface Contamination? *Surf. Interface Anal.* **2002**, *33*, 299−305.
(47) López, R.; Gómez, R. Band-Gap Energy Estimation from Diffuse Reflectance Measurements on Sol−Gel and Commercial TiO2: A Comparative Study. *J. Sol-Gel Sci. Technol.* **2012**, *61*, 1−7.
(48) Trzciński, K.; Szkoda, M.; Herman, A.; Borowska-Centkowska, A.; Lisowska-Oleksiak, A. Does the Low Optical Band Gap of Yellow Bi3YO6 Guarantee the Photocatalytical Activity under Visible Light Illumination? *J. Solid State Electrochem.* **2018**, *22*, 2095−2105.
(49) Bai, L.; Xue, Y.; Zhang, J.; Pan, B.; Wu, C. Synthetic Potassium Vanadium Oxide K2V6O 16·1.5H2O Superlong Nanobelts: A 1D Room-Temperature Ferromagnetic Semiconductor. *Eur. J. Inorg. Chem.* **2013**, *20*, 3497−3505.
(50) Wang, C.; Cao, Y.; Luo, Z.; Li, G.; Xu, W.; Xiong, C.; He, G.; Wang, Y.; Li, S.; Liu, H.; Fang, D. Flexible Potassium Vanadate Nanowires on Ti Fabric as a Binder-Free Cathode for High-Performance Advanced Lithium-Ion Battery. *Chem. Eng. J.* **2017**, *307*, 382−388.
(51) Zavalij, P. Y.; Whittingham, M. S. Structural Chemistry of Vanadium Oxides with Open Frameworks. *Acta Crystallogr. Sect. B Struct. Sci.* **1999**, *55*, 627−663.

https://doi.org/10.1021/acs.inorgchem.2c00136
Inorg. Chem. 2022, 61, 9433−9444

(52) Frederickson, L. D.; Hausen, D. M. Infrared Spectra-Structure Correlation Study of Vanadium-Oxygen Compounds. *Anal. Chem.* **1963**, *35*, 818−827.
(53) Baddour-Hadjean, R.; Boudaoud, A.; Bach, S.; Emery, N.; Pereira-Ramos, J. P. A Comparative Insight of Potassium Vanadates as Positive Electrode Materials for Li Batteries: Influence of the Long-Range and Local Structure. *Inorg. Chem.* **2014**, *53*, 1764−1772.
(54) Wang, J.; Gao, G.; Zhou, X.; Wu, J.; Yang, H.; Li, Q.; Wu, G. A Facile Method to Prepare Bi-Phase Lithium Vanadate as Cathode Materials for Li-Ion Batteries. *J. Solid State Electrochem.* **2014**, *18*, 2459−2467.
(55) Li, L.; Liu, S.; Liu, W.; Ba, D.; Liu, W.; Gui, Q.; Chen, Y.; Hu, Z.; Li, Y.; Liu, J. Electrolyte Concentration Regulation Boosting Zinc Storage Stability of High-Capacity K0.486V2O5 Cathode for Bendable Quasi-Solid-State Zinc Ion Batteries. *Nano-Micro Lett.* **2021**, *13*, 1−14.
(56) Nakamoto, K. *Infrared and Raman Spectra of Inorganic and Coordination Compounds*; John Wiley & Sons, Ltd., 2008, DOI: 10.1002/9780470405888.fmatter.
(57) Linstrom, P. J.; Mallard, W. G. Mass Spectra. *In NIST Chemistry WebBook*; National Institute of Standards and Technology: Gaithersburg.
(58) Xie, Z.; Lai, J.; Zhu, X.; Wang, Y. Green Synthesis of Vanadate Nanobelts at Room Temperature for Superior Aqueous Rechargeable Zinc-Ion Batteries. *ACS Appl. Energy Mater.* **2018**, *1*, 6401−6408.
(59) Prześniak-Welenc, M.; Szreder, N. A.; Winiarski, A.; Łapiński, M.; Kościelska, B.; Barczyński, R. J.; Gazda, M.; Sadowski, W. Electrical Conductivity and Relaxation Processes in V2O5 Nanorods Prepared by Sol-Gel Method. *Phys. Status Solidi Basic Res.* **2015**, *252*, 2111.
(60) Silversmit, G.; Depla, D.; Poelman, H.; Marin, G. B.; De Gryse, R. Determination of the V2p XPS Binding Energies for Different Vanadium Oxidation States (V5+ to V0+). *J. Electron Spectros. Relat. Phenomena* **2004**, *135*, 167−175.
(61) Ambade, R. B.; Ambade, S. B.; Mane, R. S.; Lee, S. H. Interfacial Engineering Importance of Bilayered ZnO Cathode Buffer on the Photovoltaic Performance of Inverted Organic Solar Cells. *ACS Appl. Mater. Interfaces* **2015**, *7*, 7951−7960.
(62) Zakharova, G. S.; Täschner, C.; Kolb, T.; Jähne, C.; Leonhardt, A.; Büchner, B.; Klingeler, R. Morphology Controlled NH4V3O8 Microcrystals by Hydrothermal Synthesis. *Dalt. Trans.* **2013**, *42*, 4897−4902.
(63) Prześniak-Welenc, M.; Nadolska, M.; Kościelska, B.; Sadowska, K. Tailoring the Size and Shape — New Path for Ammonium Metavanadate Synthesis. *Materials* **2019**, *12*, 3446.
(64) Li, H.; Chen, Y.; Zhou, W.; Gao, H.; Tian, G. Tuning in BiVO 4 /Bi 4 V 2 O 10 Porous Heterophase Nanospheres for Synergistic Photocatalytic Degradation of Organic Pollutants. *Appl. Surf. Sci.* **2019**, *470*, 631−638.
(65) Kong, X.; Guo, Z.; Wen, P.; Huang, J.; Cao, L.; Yin, L.; Li, J.; Feng, Q. Controllable Synthesis and Morphology Evolution from Two-Dimensions to One-Dimension of Layered K2V6O16·nH2O. *CrystEngComm* **2015**, *17*, 3777−3782.
(66) Phanichphant, S.; Nakaruk, A.; Chansaenpak, K.; Channei, D. Evaluating the Photocatalytic Efficiency of the BiVO4/RGO Photocatalyst. *Sci. Rep.* **2019**, *9*, 1−9.
(67) Wang, Z.; Wang, J.; Pan, Y.; Liu, F.; Lai, Y.; Li, J.; Jiang, L. Preparation and Characterization of a Novel and Recyclable InVO4/ZnFe2O4 Composite for Methylene Blue Removal by Adsorption and Visible-Light Photocatalytic Degradation. *Appl. Surf. Sci.* **2020**, *501*, No. 144006.
(68) Wang, X.; Zhou, J.; Zhao, S.; Chen, X.; Yu, Y. Synergistic Effect of Adsorption and Visible-Light Photocatalysis for Organic Pollutant Removal over BiVO 4 /Carbon Sphere Nanocomposites. *Appl. Surf. Sci.* **2018**, *453*, 394−404.
(69) Wu, J. M.; Chen, Y.; Pan, L.; Wang, P.; Cui, Y.; Kong, D. C.; Wang, L.; Zhang, X.; Zou, J. J. Multi-Layer Monoclinic BiVO4 with Oxygen Vacancies and V4+ Species for Highly Efficient Visible-Light Photoelectrochemical Applications. *Appl. Catal. B Environ.* **2018**, *221*, 187−195.
(70) Cheng, C.; Fang, Q.; Fernandez-Alberti, S.; Long, R. Controlling Charge Carrier Trapping and Recombination in BiVO4-with the Oxygen Vacancy Oxidation State. *J. Phys. Chem. Lett.* **2021**, *12*, 3514−3521.
(71) Zhang, Y.; Guo, Y.; Duan, H.; Li, H.; Sun, C.; Liu, H. Facile Synthesis of V4+ Self-Doped, [010] Oriented BiVO4 Nanorods with Highly Efficient Visible Light-Induced Photocatalytic Activity. *Phys. Chem. Chem. Phys.* **2014**, *16*, 24519−24526.
(72) Guo, L.; Li, J.; Lei, N.; Song, Q.; Liang, Z. Morphological Evolution and Enhanced Photoelectrochemical Performance of V4+ Self-Doped, [010] Oriented BiVO4 for Water Splitting. *J. Alloys Compd.* **2019**, *771*, 914−923.
(73) Yu, R.; Xue, N.; Huo, S.; Li, J.; Wang, J. Structure Characteristics and Photoactivity of Simultaneous Luminescence and Photocatalysis in CaV2O6 Nanorods Synthesized by the Sol-Gel Pechini Method. *RSC Adv.* **2015**, *5*, 63502−63512.
(74) Saputera, W. H.; Amri, A. F.; Mukti, R. R.; Suendo, V.; Devianto, H.; Sasongko, D. Photocatalytic Degradation of Palm Oil Mill Effluent (Pome) Waste Using Bivo4 Based Catalysts. *Molecules* **2021**, *26*, 6225.
(75) Kumar, K. V.; Porkodi, K.; Rocha, F. Langmuir-Hinshelwood Kinetics - A Theoretical Study. *Catal. Commun.* **2008**, *9*, 82−84.
(76) Yang, M. Q.; Han, C.; Zhang, N.; Xu, Y. J. Precursor Chemistry Matters in Boosting Photoredox Activity of Graphene/Semiconductor Composites. *Nanoscale* **2015**, *7*, 18062−18070.
(77) Wu, J.; Lü, X.; Zhang, L.; Xia, Y.; Huang, F.; Xu, F. Crystallinity Control on Photocatalysis and Photoluminescence of TiO2-Based Nanoparticles. *J. Alloys Compd.* **2010**, *496*, 234−240.
(78) Liqiang, J.; Yichun, Q.; Baiqi, W.; Shudan, L.; Baojiang, J.; Libin, Y.; Wei, F.; Honggang, F.; Jiazhong, S. Review of Photoluminescence Performance of Nano-Sized Semiconductor Materials and Its Relationships with Photocatalytic Activity. *Sol. Energy Mater. Sol. Cells* **2006**, *90*, 1773−1787.
(79) Wu, P.; Li, Q.; Zou, X.; Cheng, W.; Zhang, D.; Zhao, C.; Chi, L.; Xiao, T. Correlation between Photoluminescence and Oxygen Vacancies in In 2O3, SnO2 and ZnO Metal Oxide Nanostructures. *J. Phys. Conf. Ser.* **2009**, 188.
(80) Kang, M.; Chu, M.; Kim, S. W.; Ryu, J. W. Optical and Electrical Properties of V2O5 Nanorod Films Grown Using an Electron Beam. *Thin Solid Films* **2013**, *547*, 198−201.
(81) Le, T. K.; Kang, M.; Kim, S. W. Morphology Engineering, Room-Temperature Photoluminescence Behavior, and Sunlight Photocatalytic Activity of V2O5 Nanostructures. *Mater. Charact.* **2019**, *153*, 52−59.
(82) Jia, P.; Tan, H.; Liu, K.; Gao, W. Synthesis, Characterization and Photocatalytic Property of Novel ZnO/Bone Char Composite. *Mater. Res. Bull.* **2018**, *102*, 45−50.
(83) Xia, S.; Zhang, L.; Pan, G.; Qian, P.; Ni, Z. Photocatalytic Degradation of Methylene Blue with a Nanocomposite System: Synthesis, Photocatalysis and Degradation Pathways. *Phys. Chem. Chem. Phys.* **2015**, *17*, 5345−5351.
(84) Houas, A.; Lachheb, H.; Ksibi, M.; Elaloui, E.; Guillard, C.; Herrmann, J. M. Photocatalytic Degradation Pathway of Methylene Blue in Water. *Appl. Catal. B Environ.* **2001**, *31*, 145−157.

https://doi.org/10.1021/acs.inorgchem.2c00136
Inorg. Chem. 2022, 61, 9433−9444

Insight into potassium vanadates as visible-light-driven photocatalysts: synthesis of V(IV)-rich nano/microstructures for photodegradation of methylene blue

Małgorzata Nadolska[a], Mariusz Szkoda[b], Konrad Trzciński[b], Paweł Niedziałkowski[c], Jacek Ryl[a], Aleksandra Mielewczyk-Gryń[a], Karolina Górnicka[a], Marta Prześniak-Welenc[a*]

[a]*Faculty of Applied Physics and Mathematics, Institute of Nanotechnology and Materials Engineering, Gdansk University of Technology, Narutowicza 11/12, 80-233 Gdansk, Poland*

[b]*Faculty of Chemistry, Gdansk University of Technology, Narutowicza11/12, 80-233 Gdansk, Poland*

[c]*Faculty of Chemistry, University of Gdansk, Wita Stwosza 63, Gdansk, 80-308, Poland*

*Corresponding author; e-mail: marta.welenc@pg.edu.pl, tell: +48 583486606,

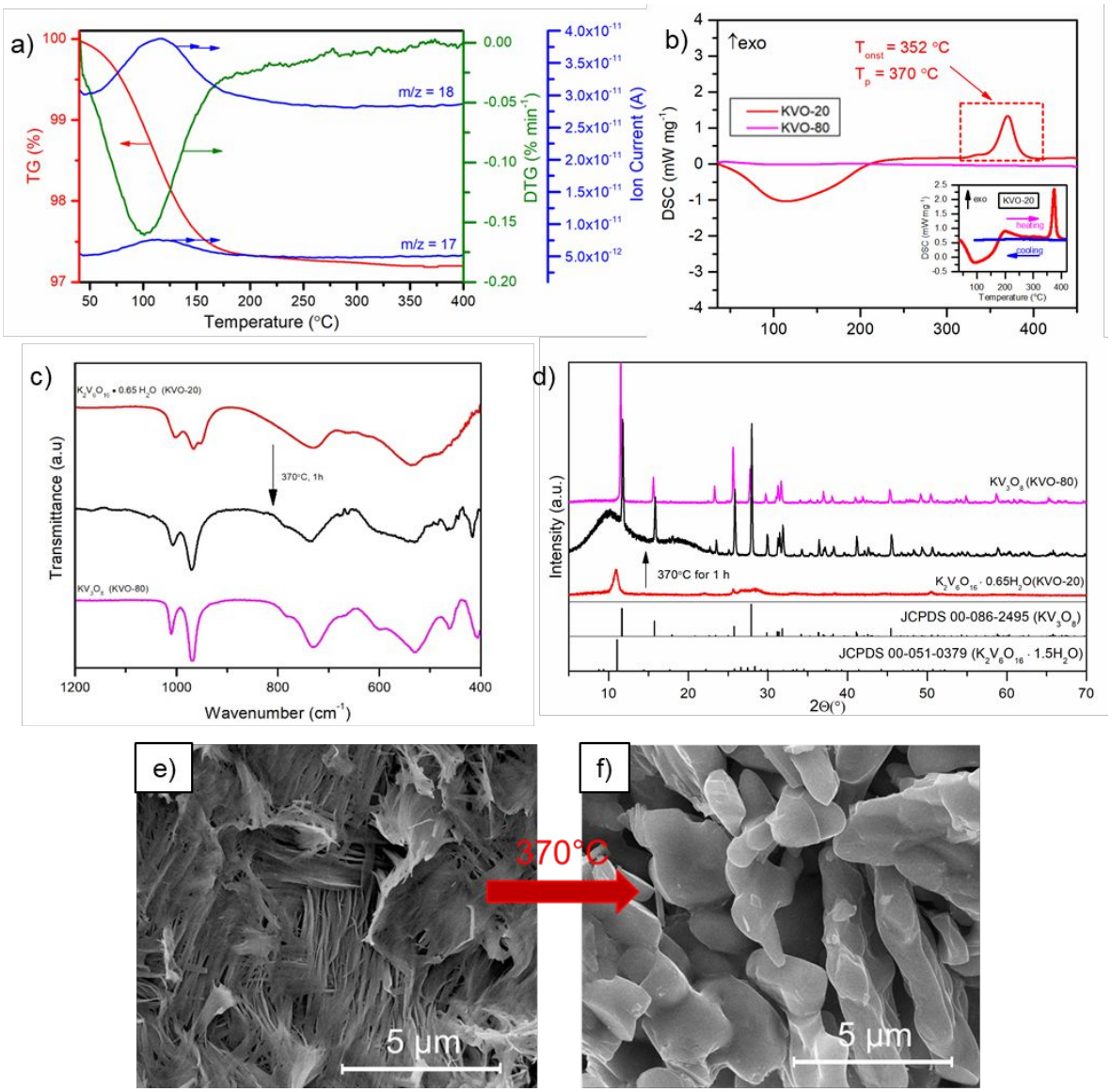

Figure S1.a) TG and DTG curves of the KVO-20 with Ion Current curves for m/z =18 and m/z = 17 b) DSC curves of the KVO-20 and KVO-80 sample, inset: DSC curves of the KVO-20 during heating and cooling rate, c) XRD patterns, d) FTIR spectra the KVO-20 after heat treatment at 370°C for 1h,e) and f) SEM images of sample KVO-20 before and after heat treatment at 370°C for 1h, respectively.

The asymmetric bell-shaped peak located between 35-250°C on DSC curve of KVO-20 (Fig. S1a) is caused by decomposition of $K_2V_6O_{16}{\cdot}0.65H_2O$ with the elimination of the physisorbed water and water of the crystallization. The asymmetric peak with a shoulder between 100-250°C on DTG curve (Fig. S1c) indicates stepwise water elimination. The peak located at 352°C (T_{onst}) is attributed to recrystallization of $K_2V_6O_{16}{\cdot}0.65H_2O$ to non-hydrated form KV_3O_8. To further confirm this assumption the KVO-20 (single phase, $K_2V_6O_{16}{\cdot}0.65H_2O$) sample was heated at 370 °C for one h and the SEM, FTIR and XRD analysis were performed. Both, XRD and FTIR confirm that after heating KVO-20 recrystallize to KV_3O_8 and FTIR spectrum and diffractogram are similar to that registered for KVO-80 (KV_3O_8).

Table S1. Summary of the IR bands position

		Band position (cm^{-1})	
	Vibrational mode	KVO-20	KVO-80
vandate	V=O streching vibrations	1001	1010
	V=O streching vibrations	966 952	968
	bridging V-O···K stretching	727	730
	V-O-V stretching	535	530/600
water	H-O-H bending	1615	1633
	O-H streching	3435	3475

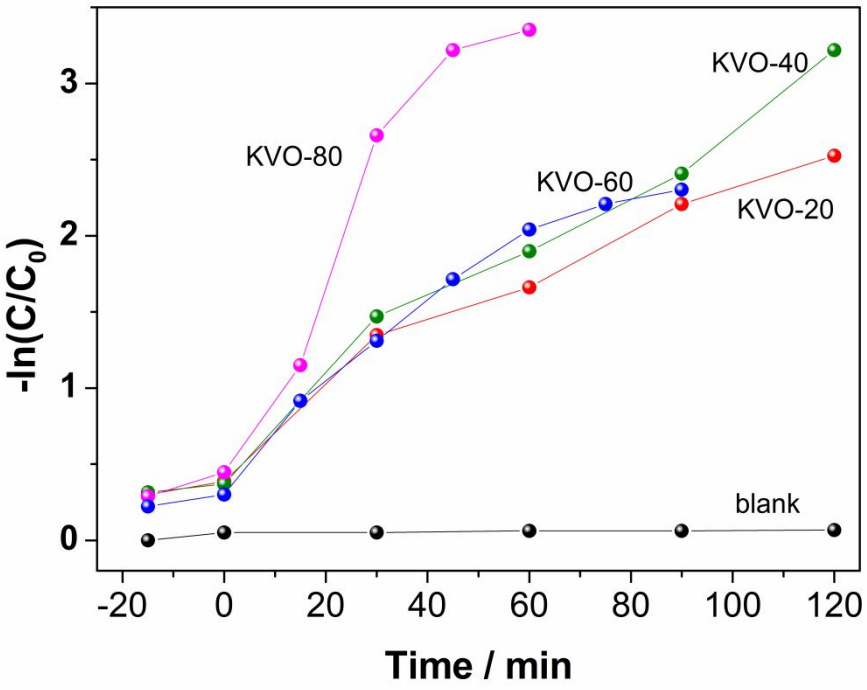

Figure S2.The results of MB photodegradation presented as the $\ln(c/c_0)$ vs time plots.

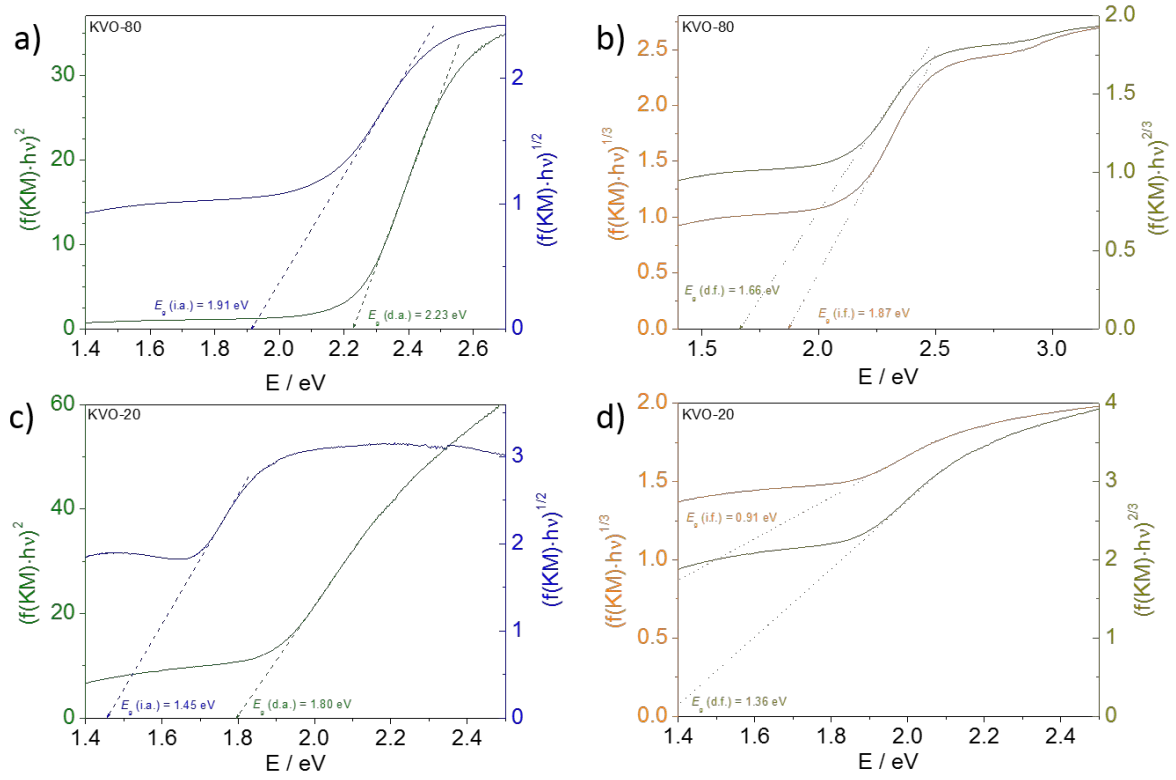

Figure S3. The $(f(KM)\cdot h\nu)^n$ vs. $h\nu$ plots (n = 1/2 (a); 2 (b); 1/3 (c); and 2/3 (d)) resulting from the UV-Vis reflectance spectra of KVO-20 and KVO-80 powders.

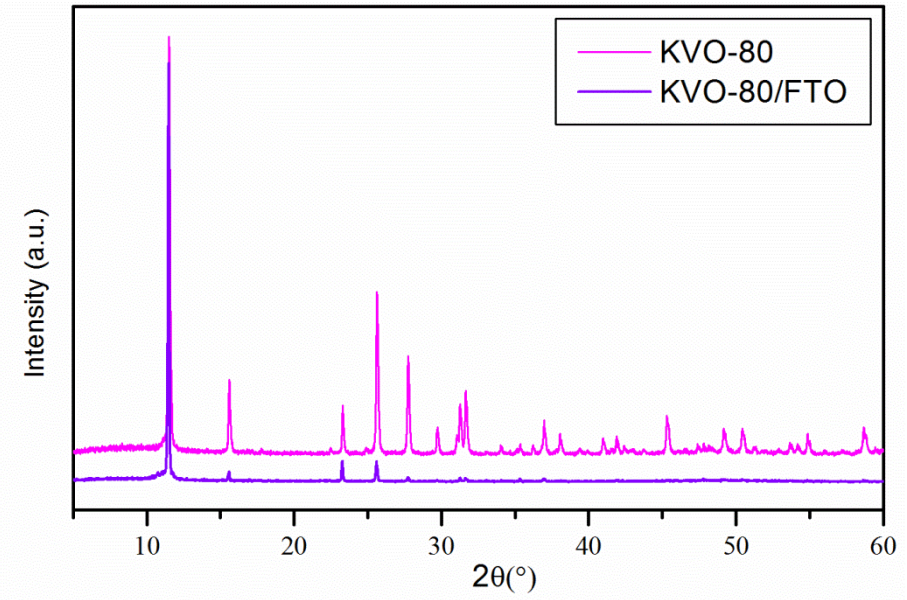

Figure S4.The X-ray diffractograms of as-prepared sample KVO-80 and KVO-80 deposited onto degreased FTO (KVO-80/FTO).

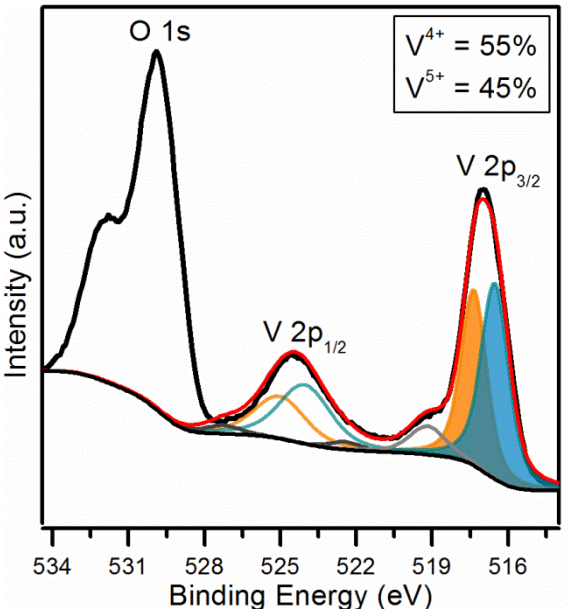

Figure S5.The XPS spectra of O1s and V2p region of KVO-80 sample deposited onto degreased FTO.

The two different components of V $2p_{3/2}$ are located around 516.5 eV and the 517.5 eV, and correspond to the V^{4+} and V^{5+}respectively [64]. These components are also present for V $2p_{1/2}$ peak, the two peaks centered at 525 eV (V^{5+})and 524 eV (V^{4+}). The peaks located around 522 and 519 eV were attributed to the O1s satellite [65]. Based on the area of the fitted curves, the relative atomic percentage of vanadium V^{+4} was estimated to 55%.

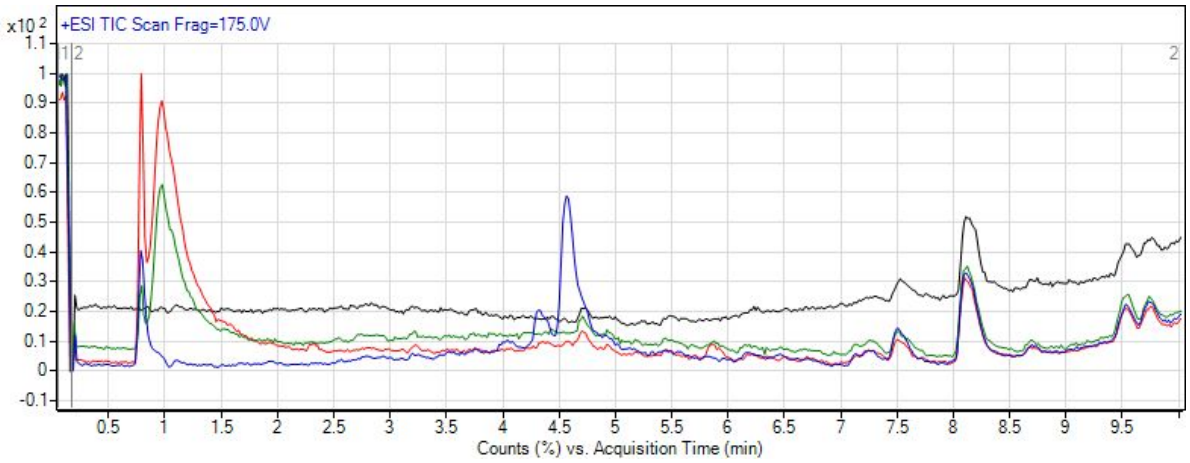

Figure S6.The total ion current chromatogram (TIC, ESI^+) for MB (blue line) and of samples obtained after photocatalytic degradation using KVO-20 (red line) and KVO-80 (green line) as a catalyst. The ion current chromatogram (TIC) for water was added as black line.

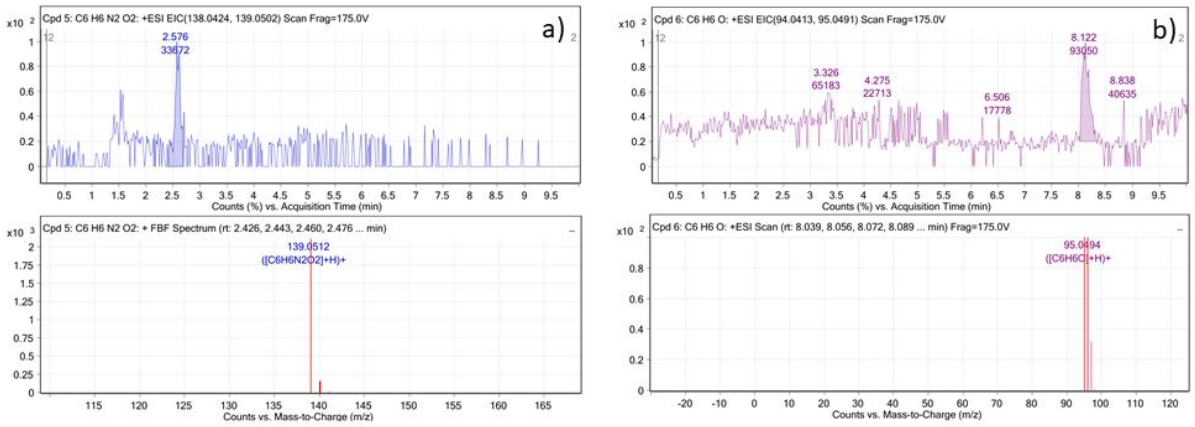

Figure S7.The chromatograms, and mass spectra for products identified after photocatalytic degradation of MB applying KVO-80 as catalyst.

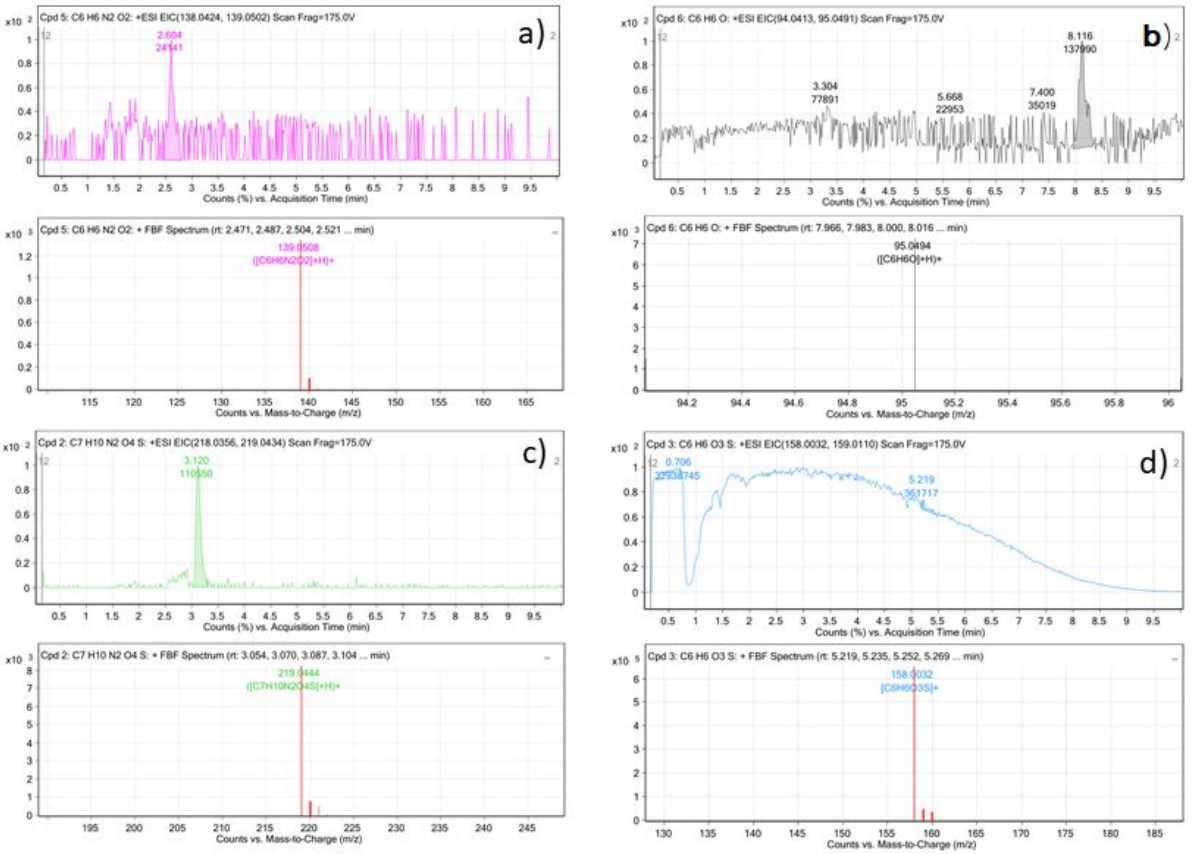

Figure S8.The chromatograms, and mass spectra for products identified after photocatalytic degradation of MB applying KVO-20 as catalyst.

3.5. [A5] New light on the photocatalytic performance of $NH_4V_4O_{10}$ and its composite with rGO

3.5.1. Research background and objectives

Solar-light-driven photocatalysis is one of the most promising approaches for wastewater treatment due to the utilization of clean energy as well as the direct degradation of pollutants. Accordingly, intense research effort has been dedicated to the development of efficient and low-cost photoactive materials. In recent years, the application of metal vanadates for the visible-light-driven photodegradation of water pollutants has been frequently addressed by many original works. In addition to the most well-known $BiVO_4$, a series of other compounds can be mentioned here, such as Ag_3VO_4 [54,171,187], $InVO_4$ [7], and $FeVO_4$ [56]. Unfortunately, in many cases, vanadates still suffer from long photodegradation times and fast photocorrosion. Thus, tremendous work has been made to enhance the material's photocatalytic performance and improve surface reactivity, light absorption, charge separation, or stability during cycles. Various approaches can be listed here, for example, designing heterojunction structures, coupling with carbon materials [183,188,189], doping [190], or dye sensitization. Considerable attention has also been paid to photocatalysts in the form of nanostructures. In addition to the development of previously reported photocatalysts, new photoactive materials are sought, especially those that can be obtained via facile, low-cost synthesis.

In [A4], it was proposed to use a facile water-based reaction and simple potassium salt as a promising alternative for the synthesis of visible-light-driven photocatalysts, potassium vanadates. In the described publication [A5], we make a further step and report an efficient $NH_4V_4O_{10}$ photocatalyst that is composed of NH_4^+ instead of metallic cations and can be synthesized from an easily accessible NH_4VO_3 precursor.

As already described in the previous chapter, only three publications devoted to the usage of ammonium vanadates in photocatalytic applications can be found in the literature. All of the examples are dedicated to the $NH_4V_4O_{10}$ phase. The first work was published 10 years ago [82]. In fact, the results revealed low photocatalytic activity of ammonium vanadates, and the investigated cross-like $NH_4V_4O_{10}$ nanobelt arrays did not show any catalytic action for the degradation of Rhodamine B after 210 min under visible light. However, it was shown that photoactivity can be induced by calcination (400°C for 40 min) of the as-obtained structures. Such post-processing led to the formation of a mixed-phase product consisting of V_2O_5 and a small amount of VO_2 and a 4-fold increase in surface area (from 10 m^2g^{-1} before calcination to 44 m^2g^{-1} after calcination). Most importantly, the calcinated product demonstrated 64% removal efficiency of dye after 210 min of illumination. The improved photodegradation activity was attributed not only to the increased surface area but also to the existence of V^{4+} species in the sample, which resulted in a narrower band gap. Recently, $NH_4V_4O_{10}$ has attracted scientists' attention again and has been proposed for the construction of heterojunction photocatalysts. Examples include the combination of $NH_4V_4O_{10}$ nanobelts with quantum dots, CdS [101] or C-dots [102] and their utilization for the removal of antibiotics from an aqueous environment. Such composites

presented high photocatalytic efficiency, resulting in more than 90% degradation of dye after 120 min under simulated solar light. It should be noted that photocatalytic activity was also observed for pure $NH_4V_4O_{10}$; however, the efficiency was lower and equal to ca. 20% for sulfamethoxazole, aureomycin hydrochloride, and ciprofloxacin and ca. 50% for amoxicillin.

Such limited literature as well as previously mentioned advantages of ammonium vanadates (facile synthesis, easily accessible NH_4VO_3 precursor) were motivation to carry on studies included in [A5]. On the basis of previous experience and published work, it is proposed to add oxalic acid in the hydrothermal synthesis of $NH_4V_4O_{10}$. As shown in the literature and confirmed in [A2], oxalic acid serves as a reductant and induces the formation of V^{4+} on the surface of $NH_4V_4O_{10}$ during the hydrothermal process. It is also worth noting that oxalic acid can act as a forming agent and promote the assembly of organized, three-dimensional ammonium vanadate structures. It is known that V^{4+} surface species (the importance of which has also been underlined in [A4]) and specific surface area play a pivotal role in the photocatalytic process. Therefore, it is suggested that the obtained $NH_4V_4O_{10}$ should exhibit high photocatalytic performance. Moreover, it is proposed to combine $NH_4V_4O_{10}$ with reduced graphene oxide and investigate for the first time the use of such composites in photocatalytic applications. The positive effect of rGO on the enhancement of the photocatalytic properties of other vanadates (mainly $BiVO_4$) has already been shown in the literature. Based on the available study, the carbon material is expected to decrease the energy band gap and inhibit the adverse recombination process. Importantly, the proposed $NH_4V_4O_{10}$/rGO composite can be obtained with a one-pot hydrothermal synthesis. This is an enormous advantage in contrast to multistep reactions, which are needed in the synthesis of the abovementioned heterojunctions or composites based on other vanadates and carbon materials. Additionally, the simultaneous reduction of graphene oxide and formation of ammonium vanadate structures in the hydrothermal synthesis of $NH_4V_4O_{10}$/rGO should lead to a hierarchical, porous composite structure with a well-developed surface. Consequently, such a structure should ensure cyclic stability and prevent photocorrosion.

The aim of the study was to synthesize $NH_4V_4O_{10}$ and its composite with rGO and investigate their photoactivity. The obtained samples were thoroughly characterized using XRD, FTIR, Raman, XPS, XAS, TG-MS, SEM, N_2 adsorption, PL, and UV–Vis DRS. The photocatalytic activity of synthesized $NH_4V_4O_{10}$ and $NH_4V_4O_{10}$/rGO was evaluated by the oxidation of MB and reduction of Cr(VI) under simulated solar light illumination. Moreover, the reusability of photocatalysts was tested in four consecutive cycles. Finally, the main radicals participating in the photocatalytic process were determined, and the photodegradation mechanism was discussed.

3.5.2. Summary of main results

$NH_4V_4O_{10}$ (NVO) and its composite with rGO (NVO/rGO) were prepared via a hydrothermal method in an autoclave. The synthesis parameters were selected based on the literature review and preliminary studies. Similar to [A2], the reaction was carried out for 8 h at 180°C, and NH_4VO_3 and oxalic acid were used as precursors for the synthesis of ammonium

vanadate structures. In the case of NVO/rGO, a proper amount of GO water dispersion was added to the precursor solution, and the analogous procedure as for the bare $NH_4V_4O_{10}$ was repeated. In the publication [A5], the representative composite sample was presented, in which the NH_4VO_3:GO ratio was equal to 10:1. The proposed synthesis temperature and time are also sufficient for the reduction of GO to rGO and are often used in the hydrothermal reduction of GO [191,192].

The phase purity of ammonium vanadate structures in the samples was verified by XRD analysis, which revealed that all diffraction reflexes correspond well with the monoclinic $NH_4V_4O_{10}$ phase. The characteristic diffraction reflexes of rGO were not observed in the NVO/rGO pattern due to the intrinsic weak diffraction intensities of the graphene phase as well as good dispersion of the carbon material within the composite. The presence of rGO in the composite was confirmed by Raman and FTIR spectroscopy. In the case of the first method, the evidence was two distinct modes, namely, the G and D bands, which are characteristic for graphene-based materials and are associated with the hexagonal carbon lattice and its defects/disorders. However, in the FTIR spectrum, bands associated with C=C and C-O bonds were observed, indicating that after the hydrothermal reaction, some oxygen functionalities were still present on the surface of the graphene sheets. Such residual groups are a typical feature of rGO and are beneficial for attracting dye molecules and metal ions. The FTIR and Raman analysis also provided valuable information regarding the chemical structure and bonds of $NH_4V_4O_{10}$, such as the existence of V^{5+} and V^{4+} in the structure (typical for $NH_4V_4O_{10}$, which belongs to the mixed-valence vanadium compound). The mixed-valence nature of the samples was further confirmed by XAS and XPS analysis. Considering the stoichiometry of $NH_4V_4O_{10}$, the mean valence of vanadium is equal to 4.75, which was also confirmed for the obtained samples by XAS analysis. Thus, the theoretical content of V^{5+} is 75%, while that of V^{4+} is 25%. However, the XPS results revealed a high content of V^{4+} species on the surface of the samples, and for both NVO and NVO/rGO, the relative share of V^{4+} surface species was equal to 39%. The content of rGO in the NVO/rGO composite was determined from TGA (air atmosphere) and was equal to 18.9%. Moreover, TGA served as further evidence of the chemical composition of synthesized ammonium vanadate structures, and the obtained results were in good agreement with the non-hydrated $NH_4V_4O_{10}$ phase. The morphology of NVO and NVO/rGO was investigated using SEM, which revealed clear differences between samples. NVO exhibited a flower-like microstructure composed of nanobelts. The average diameter size of the microflower was equal to 10 μm, while the nanobelts had a length of 2-7 μm, width of approximately 500 nm, and thickness of approximately 40 nm. In contrast, NVO/rGO was characterized by a spatial network structure formed by connected nanobelts wrapped with rGO sheets. Such a well-developed structure of both samples resulted in a relatively high specific surface area, which was equal to 28 m^2g^{-1} for NVO and 33 m^2g^{-1} for NVO/rGO. The optical properties of samples were further examined using UV–Vis DRS and PL. The energy band gap for NVO was found to be 2.28 eV, which is consistent with previous findings for $NH_4V_4O_{10}$ phase [101,193], while the band gap for NVO/rGO was determined to be 1.5 eV. The PL spectra of both samples displayed low emission intensity, suggesting slow recombination

of photogenerated charges within the materials. Furthermore, the observed intensity was markedly lower for the NVO/rGO composite. The Mott–Schottky analysis revealed that $NH_4V_4O_{10}$ is an n-type semiconductor, and its flat band potential was estimated to be around 0.52 V vs NHE.

The photocatalytic activity of the samples was evaluated under simulated solar light. Initially, the degradation of MB was studied. Before irradiation, both samples showed considerable adsorption of dye, which reached ca. 20% after 30 min. After 60 min of illumination, a significant decrease in the concentration of MB was observed for both samples: NVO degraded 82% of the dye, while NVO/rGO degraded 92%. The results also revealed that at the beginning of illumination, the process was much faster for NVO/rGO, for which the photocatalytic efficiency reached approximately 80% within the first 15 minutes, whereas NVO alone achieved approximately 40% degradation within the same timeframe. Further kinetics studies revealed that the most likely kinetics are pseudo-first-order kinetics according to the Langmuir-Hinshelwood model. However, for NVO/rGO, the mechanism of MB photodegradation can be more complex, as indicated by a relatively low linear regression coefficient. The scavenger tests indicated that OH radicals and holes are the main active species in the process of photocatalytic degradation of MB by NVO. In the case of NVO/rGO, h^+ and $\cdot OH$ also contribute to the degradation of MB; however, the most dominant were O2- radicals. The reusability of the prepared photocatalysts was investigated by carrying out 4 consecutive photodegradation cycles. The results revealed that the activity of NVO gradually decreases, and in the 4th cycle, the efficiency drops to 56%. Better stability was observed in the case of the NVO/rGO composite, for which the efficiency was ca. 80% in the 4th cycle. The obtained photocatalysts were also used in the Cr(VI) photoreduction process at pH 3. The efficiency of Cr(VI) photoreduction for NVO equalled only 20% after 60 min of illumination, while for NVO/rGO, it reached 71%. Similarly, for the dye, the photocatalytic process for NVO/rGO was much faster at the beginning of the illumination, and the concentration of Cr(VI) decreased to ca. 42% after 15 min. Additionally, the degradation efficiency of Cr(VI) for NVO/rGO was maintained at a good level during each reaction cycle, and only a slight drop (ca. 5%) was observed after 4 cycles.

In summary, the above results demonstrate that ammonium vanadates can be successfully used as photocatalysts for the degradation of water pollutants. In contrast to the previous study, pristine $NH_4V_4O_{10}$ described in [A5] reveals notable efficiency in decomposing organic dye. Moreover, coupling of $NH_4V_4O_{10}$ with rGO results in enhanced light absorption, accelerated photocatalytic reaction, and improved cyclic stability. Studies show that the proposed composite can be used not only for the photooxidation of organic pollution but also for the photoreduction of inorganic pollutants, with toxic Cr(VI) as an example. Compared to other vanadium-based photocatalysts described in the literature, the obtained samples present improved or similar efficiency in the photodegradation of MB and Cr(VI). It is also worth emphasizing that the proposed photocatalysts can be activated by solar light, and the degradation of pollutants occurs within the first 60 minutes of illumination.

Publication [A5] extends the current knowledge on the utilization of ammonium vanadates as photocatalysts. In addition to new insights into $NH_4V_4O_{10}$ photocatalyst usage, its composite with rGO is introduced for the first time as a novel photocatalytic material. The presented samples exhibit excellent performance in the photodegradation of MB and Cr(VI) under solar irradiation. This is attributed to the high content of V^{4+} surface species (which promotes charge carrier separation, reducing the recombination rate) and the developed surface area (which provides more active sites for the adsorption and photocatalytic reactions). Such features were obtained through the use of hydrothermal synthesis with the addition of oxalic acid. Furthermore, the conducted studies emphasize the positive impact of rGO on the activity and stability of vanadate photocatalysts. The efficient photocatalytic process, utilization of renewable energy, and facile synthesis (one-pot reaction, low-cost precursors, water as a reaction medium) make the reported ammonium vanadates promising materials for solar-driven water purification.

3.5.3. Full content of the article

Title: New light on the photocatalytic performance of $NH_4V_4O_{10}$ and its composite with rGO

Authors: M. Nadolska, M. Szkoda, K. Trzciński, J. Ryl, A. Lewkowicz, K. Sadowska, J. Smalc-Koziorowska, M. Prześniak-Welenc

Journal: Scientific Reports, 2023, 13, 3946.

Impact factor: 4.996 (2023)

Ministerial Points: 140 pts

DOI: https://doi.org/10.1038/s41598-023-31130-9

My contribution included conceptualizing and the idea to study ammonium vanadates and their composites as photocatalysts in the degradation of water pollutants. I planned and carried out the syntheses as well as physicochemical characterization of the obtained samples (XRD, FTIR, TG, SEM, N_2 adsorption). I also assisted in XAS measurements. I discussed the relationship between the physicochemical properties and photocatalytic performance of studied samples. I prepared figures, the first version of the manuscript, the submission of the manuscript and answers for the reviewers. Furthermore, research was carried out within the Project for which I was the PI (Grant no. 2020/37/N/ST5/03697, Preludium, National Science Center).

scientific reports

Check for updates

OPEN

New light on the photocatalytic performance of $NH_4V_4O_{10}$ and its composite with rGO

M. Nadolska[1], M. Szkoda[2], K. Trzciński[2], J. Ryl[1], A. Lewkowicz[3], K. Sadowska[4], J. Smalc-Koziorowska[5] & M. Prześniak-Welenc[1]✉

Solar-driven photocatalysis has shown great potential as a sustainable wastewater treatment technology that utilizes clean solar energy for pollutant degradation. Consequently, much attention is being paid to the development of new, efficient and low-cost photocatalyst materials. In this study, we report the photocatalytic activity of $NH_4V_4O_{10}$ (NVO) and its composite with rGO (NVO/rGO). Samples were synthesized via a facile one-pot hydrothermal method and successfully characterized using XRD, FTIR, Raman, XPS, XAS, TG-MS, SEM, TEM, N_2 adsorption, PL and UV−vis DRS. The results indicate that the obtained NVO and NVO/rGO photocatalysts exhibited efficient absorption in the visible wavelength region, a high content of V^{4+} surface species and a well-developed surface area. Such features resulted in excellent performance in methylene blue photodegradation under simulated solar light illumination. In addition, the composite of $NH_4V_4O_{10}$ with rGO accelerates the photooxidation of the dye and is beneficial for photocatalyst reusability. Moreover, it was shown that the NVO/rGO composite can be successfully used not only for the photooxidation of organic pollution but also for the photoreduction of inorganic pollutants such as Cr(VI). Finally, an active species trapping experiment was conducted, and the photodegradation mechanism was discussed.

Population growth and rapid urbanization adversely affect the aqueous environment. Every day, industries, agriculture and households generate copious amounts of wastewater that can pollute rivers, lakes and seas. One of the major concerns is organic contaminations such as dyes or antibiotics, which are usually toxic and nonbiodegradable[1]. Even low concentrations of dyes in water systems can be very dangerous for aquatic life due to the blocking of sunlight required for photosynthesis[2,3]. Another hazardous group of pollutants is heavy metal ions, which are highly soluble in aquatic environments and nonbiodegradable and therefore tend to accumulate in living organisms either directly or through the food chain[4]. The toxic effect of many heavy metals is indisputable, and in many cases, exposure to trace amounts of these metals can cause serious damage to human health and the ecosystem[5]. For example, Cr(VI) is highly carcinogenic. U.S. Environmental Protection Agency listed it in the top 20 on the Hazardous Substance Priority List[6], while the recommended WHO safe limit of Cr(VI) in drinking water equals 0.1 ppm[7]. Unfortunately, industrial wastewater coming from the manufacturing of paints, papers, preservatives or metal surface treatment (electroplating) can still be listed as the main source of Cr(VI). Hence, it is very important to remove the abovementioned pollutants from wastewater and protect the environment. Many methods of treating wastewater have been proposed, such as adsorption, filtration, coagulation, or photocatalytic degradation[8]. In particular, the latter is highly promising since it not only removes contaminations but also leads to their decomposition. Thus, compared to other popular methods in which contaminants are transferred from one phase to another, photocatalysis wins because of the absence of secondary pollution. Moreover, the process is usually fast, often uses a natural source of light and can be carried out under ambient conditions. Due to the above advantages, searching and developing new photocatalytic materials is an important ongoing research topic[9,10]. Among the various materials, metal oxides have been extensively investigated for the photodegradation of water pollutants[11,12]. Vanadium-based oxides are particularly promising because of their efficient visible light-harvesting ability (owing to their narrow band gap, E_g~2eV), high chemical stability and

[1]Institute of Nanotechnology and Materials Engineering, and Advanced Materials Centre, Gdansk University of Technology, Narutowicza 11/12, 80-233 Gdansk, Poland. [2]Faculty of Chemistry, Gdansk University of Technology, Narutowicza St. 11/12, 80-233 Gdansk, Poland. [3]Institute of Experimental Physics, Faculty of Mathematics, Physics and Informatics, University of Gdańsk, Wita Stwosza 57, 80-308 Gdańsk, Poland. [4]Nalecz Institute of Biocybernetics and Biomedical Engineering, Polish Academy of Sciences, Ks Trojdena 4, 02-109 Warsaw, Poland. [5]Institute of High Pressure Physics, Polish Academy of Sciences, Sokołowska 29/37, 01-142 Warsaw, Poland. ✉email: marta.welenc@pg.edu.pl

significant catalytic activity[13,14]. Many metal vanadates have been proposed as promising solar-driven photocatalysts. Examples include $Cu_3V_2O_8$[15], $Ag_3VO_4/AgVO_3$[16], $InVO_4$[17] or $BiVO_4$[18], which are the most well-known catalysts in this field. Recently, we proposed using a simple potassium salt (potassium formate) as a promising alternative for the synthesis of visible-light-driven photocatalysts. The obtained potassium vanadates (KV_3O_8, $K_2V_6O_{16}•nH_2O$) exhibited excellent photocatalytic activity, resulting in more than 90% degradation of methylene blue (MB) within the first 30 min[19].

In this study, we present an efficient $NH_4V_4O_{10}$ photocatalyst that is composed of NH_4^+ instead of metallic cations and can be synthesized via a facile hydrothermal method from an easily accessible NH_4VO_3 precursor. Moreover, we propose to combine it with rGO and investigate for the first time the use of such a composite for the photodegradation of water pollutants. The idea of the combination of vanadates with rGO to enhance the photocatalytic properties is known from the literature. It was already shown that the transfer of excited electrons from vanadate to rGO is possible in such composites[20]. This phenomenon can positively affect e-/h + separation and inhibit the adverse recombination process. Usually, the preparation of vanadate/rGO composites requires two steps: separate synthesis of vanadates and their further reaction with carbonaceous materials. A huge advantage of the proposed $NH_4V_4O_{10}$/rGO composite is its one-pot synthesis, involving simultaneous hydrothermal reduction of NH_4VO_3 and GO. Notably, the $NH_4V_4O_{10}$/rGO composite was already reported and proposed as an efficient electrode material for capacitive deionization[21] and aqueous zinc-ion batteries[22,23]. However, it has never been tested in photocatalytic applications.

The photocatalytic activity of synthesized $NH_4V_4O_{10}$ and $NH_4V_4O_{10}$/rGO was evaluated towards the oxidation of methylene blue and the reduction of Cr(VI) under simulated solar light illumination. The excellent performance in MB photodegradation is attributed to the high content of V^{4+} surface species (which promotes charge carrier separation) as well as the developed surface area (which ensures more active sites for the adsorption and photocatalysis process). Moreover, we show that the combination of $NH_4V_4O_{10}$ with rGO widens its application, and the proposed composite can be used not only for photooxidation of organic pollution but also for photoreduction of inorganic pollutants with Cr(VI) as an example. The addition of rGO also enhances light absorption in the visible region, accelerates the photooxidation reaction, and ensures cyclic stability.

Results and discussion

Structure characterization. The XRD patterns of NVO and NVO/rGO are presented in Fig. 1a. All diffraction reflexes correspond well with the ammonium vanadate phase $NH_4V_4O_{10}$, PDF no. 230493 (ICSD), which corresponds to a monoclinic structure with lattice parameter values of a = 11.57 Å, b = 3.65 Å, and c = 9.81 Å)[24,25], which is characterized by a layered structure built from corner-shared VO_6 layers and NH_4^+ cations between them. The strongest line corresponds to the 001 plane, which indicates preferential growth along the c-axis. The absence of any other reflexes indicates that a pure phase was obtained for both samples. In addition, characteristic diffraction reflexes of rGO were not observed for the NVO/rGO composite due to the intrinsic weak diffraction intensities of the graphene phase. Moreover, it has also been reported that no rGO reflexes are observed when carbon material is homogeneously dispersed in the composite[21,26]. Broad reflexes for both samples indicate a small size of ammonium vanadate crystals, which is in agreement with further SEM observations. Raman spectroscopy analysis was performed to identify the characteristic bonds of $NH_4V_4O_{10}$ as well as to confirm the presence of rGO in the composite (Fig. 1b). The bands observed in the low wavenumber region (< 1000 cm^{-1}) are associated with V–O bonds and are similar to those reported for $NH_4V_4O_{10}$[27]. The band at 147 cm^{-1} is due to the layered structure of $NH_4V_4O_{10}$ and bending vibration of $(V_2O_2)_n$ chains[28]. The band at 285 cm^{-1} originates from the bending vibration of O-V = O[28]. The symmetric and antisymmetric stretching modes of V–O-V appear at 540 cm^{-1} and 720 cm^{-1}, respectively, while the bending mode appears at 450 cm^{-1}[29]. In the NVO/rGO spectrum, two new distinct modes located at 1351 cm^{-1} and 1616 cm^{-1} are the D and G bands, which are characteristic of graphene-based materials and prove the presence of rGO. The G band arises from the in-planar stretching of symmetric sp^2 C–C bonds in graphite-derived carbon materials. The D band is attributed to the presence of interruptions that occurred in the symmetric hexagonal graphitic lattice, such as heptagon and pentagon rings, edge defects, and functional groups. Such disruptions are typical for rGO and are beneficial for composite preparation, as the folding of the defective graphene sheets facilitates the homogeneous distribution of the material in the final structure. The characteristic bonds of $NH_4V_4O_{10}$ and rGO were further confirmed by FTIR analysis (Fig. S1). The spectrum of pristine NVO contains a few pronounced bands associated with the vibrations of V–O bonds: symmetric and asymmetric stretching of V–O-V (535 cm^{-1} and 740 cm^{-1}) and symmetric stretching of V = O (980 cm^{-1})[30]. The observed splitting of the V = O band indicates the existence of V^{5+} and V^{4+} in the structure and is typical for $NH_4V_4O_{10}$, which belongs to the mixed-valence vanadium compounds[28]. Absorption bands at 1405 cm^{-1} and 3180 cm^{-1} correspond to the bending and stretching modes of N–H in NH_4^+, respectively[31]. Bands located at 1630 cm^{-1} and 3450 cm^{-1} can be assigned to the O–H bending and stretching vibrations of adsorbed water. In the NVO/rGO spectrum, a new band located at 1560 cm^{-1} can be clearly observed, which corresponds to the C = C skeleton vibration of the graphene sheet [32]. In addition, weak bands associated with carbon−oxygen bonds can also be observed for NVO/rGO. This implies that after the hydrothermal reaction, some oxygen functionalities are still present on the surface of the graphene sheets. Such residual groups are a typical feature of rGO and are beneficial for attracting dye molecules[33] and metal ions.

The content of various components within the vanadate/rGO composites can be estimated by TGA under an air atmosphere. Calculations are based on the difference in mass loss between pure ammonium vanadate and its composites with rGO[22,34]. As shown in Fig. 1c, the total mass loss for pure NVO up to 600 °C is 5.5%, and two main regions can be distinguished, which correspond to the removal of adsorbed water (before 110 °C) and ammonium groups (110–370 °C) by the release of ammonia and water. The 4.9% loss in the second region indicates the absence of crystal water, and its value agreed well with the molar mass of the ammonium group in

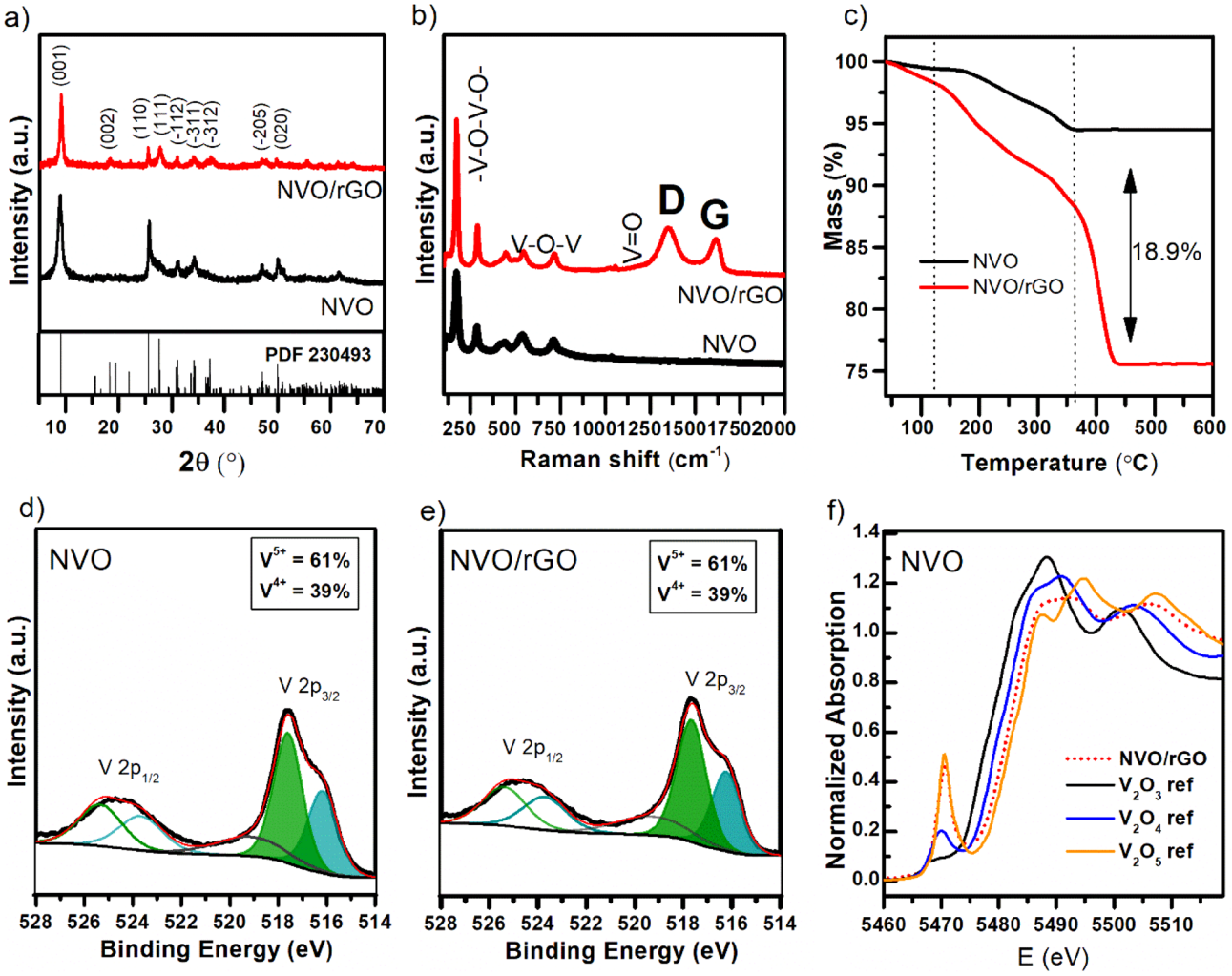

Figure 1. Structural analysis of NVO and NVO/rGO: (**a**) XRD, (**b**) Raman, (**c**) TG (air, 10 °C/min), (**d**,**e**) V 2p XPS spectra and (**f**) V K-edge XANES spectra (the inset shows the relation between the vanadium oxidation state and the edge position).

the nonhydrated $NH_4V_4O_{10}$ phase. Compared to NVO, NVO/rGO reveals an additional sharp mass loss (12.9%) with a maximum ca. 410 °C, which is attributed to the combustion of rGO sheets in the composite [22]. Moreover, the mass loss in the range of 110–370 °C is doubled. This is caused by the decomposition of residual oxygen-containing groups of rGO. Considering the differences in the total mass loss between both samples, the content of rGO in the NVO/rGO composite was calculated to be equal to 18.9%. To investigate the surface oxidation state of V in the studied samples, XPS analysis was carried out. The high-resolution XPS spectra of the V 2p region (Fig. 1d,e) reveal two peaks located at 524.5 eV and 517.3 eV assigned to the V $2p_{1/2}$ and V $2p_{3/2}$ doublets. The observed asymmetry of the peaks indicates the coexistence of V^{5+} and V^{4+} and confirms the mixed-valence nature of the obtained samples. Thus, for further analysis, V $2p_{3/2}$ was deconvoluted for two peaks at 517.6 eV and 516.2 eV corresponding to V^{5+} and V^{4+}, respectively. According to the fitted peak areas, the ratio of V^{5+}/V^{4+} in both samples is similar and equal to 1.6, which is almost two times lower than the theoretical value for $NH_4V_4O_{10}$. Taking into account the stoichiometry of $NH_4V_4O_{10}$, the theoretical content of V^{5+} is 75%, while that of V^{4+} is 25%. At the same time, it should be kept in mind that XPS is a surface-sensitive method, and the obtained results indicate a high content of V^{4+} (39%) on the surface, which may be different in the bulk. Furthermore, the valence state of vanadium in the bulk determined from XAS analysis was 4.75. As shown in Fig. 1f, the edge position for NVO/rGO lies between the energies of the V_2O_5 and V_2O references. It should be noted that transmission mode XAS analysis refers to the bulk oxidation state, while XPS is a surface-sensitive method. It is known from the literature that V^{4+} species can be generated on the surface of vanadates during their synthesis[35,36]. It was also proven that the presence of surface V^{4+} species is also beneficial for the photocatalytic process and will be discussed later.

The morphology of the prepared samples was investigated using SEM. As shown in Fig. 2a,c), NVO exhibits a flower-like microstructure with an average diameter size equal to 10 μm. The observed structures are built of nanobelts with a length of 2–7 μm and a width of 500 nm. The thickness of the nanobelt is approximately 40 nm. By comparison, the NVO/rGO sample possesses a very different morphology. As seen in Fig. 2b,d), the composite is characterized by a porous structure made of connected nanobelts, which are wrapped with rGO sheets. The

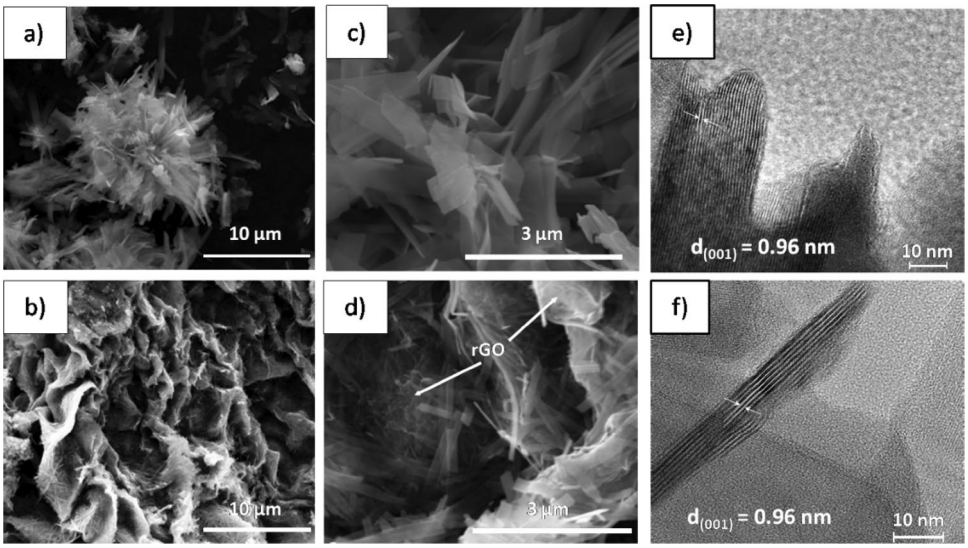

Figure 2. SEM images of NVO (**a**,**c**) and NVO/rGO (**b**,**d**) and (**e**,**f**) high-resolution TEM images of NVO and NVO/rGO, respectively.

width of the nanobelts is smaller than that for NVO and equal to 200 nm, which can be attributed to the slower growth rate limited by rGO. Such a unique structure should facilitate the migration of aqueous solution, ensuring better contact of pollutants with active sites when used as a photocatalyst material for water treatment. It is also expected that the hierarchically organized structure of the NVO/rGO composite ensures its stability, which will improve the reusability of photocatalysts. Figure S2 shows the N_2 adsorption–desorption isotherms of NVO and NVO/rGO. Both samples exhibit a type-IV isotherm with a hysteresis loop typical for mesoporous materials. It is known that the existence of mesopores in the photocatalyst facilitates the accessibility of pollutant molecules, enhancing its effectiveness[37]. The pore size distribution, calculated with the BJH model, reveals that for both samples, the pore radius is in the range of 2–40 nm. NVO possesses mostly small pores with a mean radius size equal to 2 nm, while NVO/rGO is characterized by a bimodal size distribution with pore radii centered at 2 nm and 8 nm. The cumulative pore volume of NVO/rGO (0.19 cm^3/g) was more than two times larger than that of NVO (0.08 cm^3/g). In addition, the specific surface area was determined to be 28 m^2/g and 33 m^2/g for NVO and NVO/rGO, respectively. As expected, the composite shows a larger surface area, owing to the high intrinsic surface area of rGO and the self-organized porous structure of NVO/rGO. The high-resolution TEM images of NVO (Fig. 2e) and NVO/rGO (Fig. 2f) show that the lattice plane is 0.96 nm and corresponds to the characteristic (001) plane of $NH_4V_4O_{10}$, as observed from the XRD pattern (shown in Fig. 1a).

Diffuse reflectance UV−Vis spectroscopy was applied to study the optical properties of both materials. The band gap energies were calculated using the Kubelka–Munk method based on the diffuse reflectance spectra presented in Fig. 3a. The Kubelka–Munk model is the basis for determining the band gap of thick, optically rough

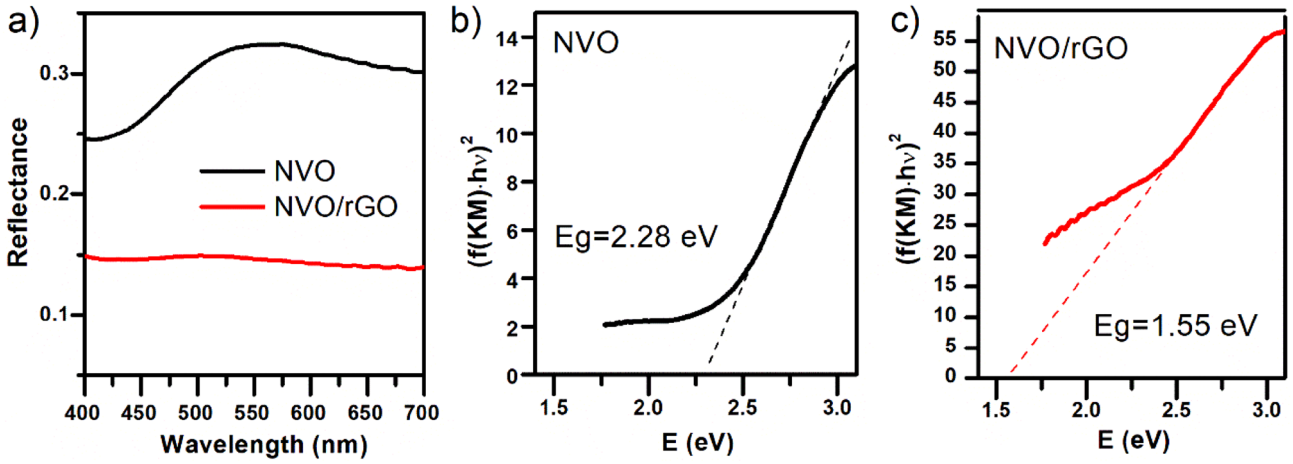

Figure 3. Optical properties of NVO and NVO/rGO: Reflectance spectra (**a**) and the $(f(KM)\cdot h\nu)^2$ vs hν plots resulting from the UV−Vis reflectance spectra with corresponding energy band gaps for NVO (**b**) and NVO/rGO (**c**).

powder samples. Following[38], $(f(KM)\cdot hv)^{1/n}$ (for n = 1/2 assuming a direct bandgap) was plotted as a function of the incident photon energy (hv), and the results are depicted in Fig. 3b,c for NVO and NVO/rGO, respectively. The band gap of both materials was determined by extrapolation of the linear region of $(f(KM)\cdot hv)^2$ vs hv to y = 0. The intersection point of the extrapolated line with the abscissa gives the value of E_g. As shown in Fig. 3b, the obtained energy band gap for NVO is 2.28 eV, which is in good agreement with the previously published value[39,40]. The optical band gap of NVO/rGO was determined to be 1.5 eV. The reported values for rGO cover a wide range between 0.02 and ca. 2 eV[41–43], but the E_g of rGO is generally lower than that of NVO; thus, the bandgap narrowing in a synthesized composite is not surprising. The band gap decrease upon adding rGO to known photocatalysts, such as ZnO or TiO_2, was also reported in the literature[44,45]. The positive influence of rGO on photocatalytic activity has been recently reviewed by Mondal et al.[46]. The results obtained by us are in line with the worldwide trends summarized in this review.

The photoemission spectra of the samples were measured using UV radiation as the excitation source. The results are shown in Figure S3. The intensity of emission is very low for both NVO and NVO/rGO. Nevertheless, a band at approximately 460 nm was registered. Similar behaviour was already observed for K-containing vanadate—$K_2V_6O_{16}\cdot 0.65H_2O$[19]. Taking into account that the energy band gap estimated from the UV−vis spectrum equals approximately 2.28 eV (~ 543 nm), the observed emission band is not related to the conduction to valence band transition. The emission band with a maximum at 460 nm was reported for V_2O_5 nanostructures and was associated with recombination of electrons photoexcited to higher than conduction band edge levels[47]. Here, despite the very low intensity of emission, it can be seen that the presence of rGO in the composite quenches the photoluminescence significantly. It is often an indication that recombination is hindered due to the transfer of photoexcited electrons to rGO, and the separation of charge carriers that can participate in photocatalytic processes is improved. The comparison of EIS spectra recorded at rest potential is shown in Fig. 4a. As expected, the presence of highly conductive rGO affects the electrical properties of the material. The resistance of charge transfer, seen as the diameter of the semicircle on the spectra, is evidently diminished, suggesting that the conductivity of the sample is enhanced due to the presence of rGO. To compare the electrochemical activity of both materials using the cyclic voltammetry technique, see Figure S4. In the case of bare NVO, reversible redox activity, probably associated with the electrochemical activity of surface V-containing groups, was registered. Additionally, the cathodic current can be seen at a potential lower than approximately 0 V vs Ag/AgCl (3 M KCl), which can be related to the conduction band level. Such a shape is characteristic of n-type semiconductors because n-type semiconductors can act as cathodes for both illuminated and dark conditions[48]. The CV curve of NVO/rGO is much more complex and contains 4 electrochemical activities in the measured potential range. Additionally, the measured current is much higher than that for NVO. Despite the fact that both materials differ from each other by the presence of rGO, the additional electroactivities do not originate from the rGO[49]. Their presence is related to the better electrical properties of the investigated electrode material and facilitated electrochemical activity of NVO. Mott-Schottky analysis was performed to estimate the flat-band potential of NVO (see Fig. 4b). The slope of the $1/C_{sc}^2$ is positive, confirming that NVO is n-type semiconductor. Some frequency dispersion was observed; however, it can be concluded that the flat-band potential is approximately -0.1 V vs Ag/AgCl (3 M KCl) (0.52 V vs NHE). Notably, the estimated value is close to the maximum of the cathodic peak seen on the CV curve, which is consistent and characteristic with the n-type conductivity (the conduction band edge and flat-band potential are close to each other).

Photocatalysis of organic pollutants. The photocatalytic activity of the prepared samples was first evaluated by the degradation of the organic dye methylene blue (MB) under simulated sunlight. Before the photocatalysis experiments, the adsorption of MB on the surface of the tested powders was evaluated under dark conditions (Figure S5a). Adsorption–desorption equilibrium was achieved after ca. 30 min for both samples, and approximately 20% of the dye was adsorbed. The observed good adsorption ability comes from the high specific surface area of the tested materials (confirmed by BET) and is essential for the photocatalysis process,

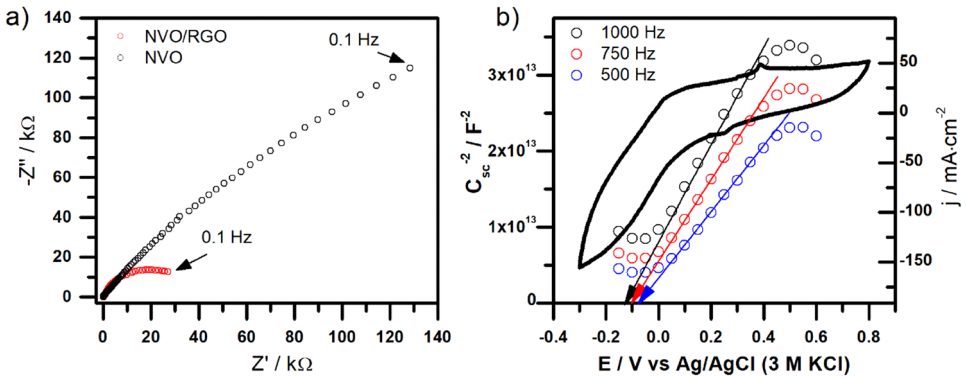

Figure 4. (**a**) Typical Nyquist plots recorded for NVO/RGO and NVO at rest potential equals to about 0.3 V and (**b**) the cyclic voltammetry curve of NVO, recorded in 0.2 M K_2SO_4, scan rate: 50 mV/s and Mott–Schottky plot of NVO electrode at different frequencies.

ensuring improved contact between the pollutant molecules and reaction active sites[50,51]. Figure 5 presents the results of the photocatalytic performance of NVO and NVO/rGO toward MB degradation. An illuminated MB solution without the addition of photocatalysts (blank) was also added for comparison and revealed a negligible photolysis effect. Similarly, the photocatalytic performance of pure rGO was measured as a control experiment and is presented in Figure S5b. After 60 min of illumination, NVO degraded 82% of MB. To the best of our knowledge, only three publications devoted to the usage of $NH_4V_4O_{10}$ in photocatalytic applications have been reported. For example, the experiments conducted by Aboood et al. reveal that the cross-like $NH_4V_4O_{10}$ nanobelt arrays do not show any catalytic action for the degradation of rhodamine B after 210 min under visible light[52]. However, scientists have shown that photoactivity can be induced by calcination (above 400 °C) of the as-obtained structures and their transformation to V_2O_5. Two other works are devoted to the heterojunction of $NH_4V_4O_{10}$ with quantum dots (CdS and C-dots). Y. Zhang et al. designed an efficient ternary C-dots/$SrTiO_3$/$NH_4V_4O_{10}$ catalyst for the removal of sulfamethoxazole, aureomycin hydrochloride, and ciprofloxacin residues in aqueous samples[26]. The reported photocatalytic degradation efficiency of the antibiotics for pure $NH_4V_4O_{10}$ was lower than 20%, which was 4–5 times lower than that for the heterojunction. S. Le prepared an intercalated CdS/$NH_4V_4O_{10}$ composite that degraded 90% of amoxicillin within 120 min under simulated sunlight, while pure $NH_4V_4O_{10}$ can degrade 50%. Taking into consideration the above examples, the photocatalytic efficiency obtained in this work for pure $NH_4V_4O_{10}$ is unexpectedly high. It is suggested that the excellent photoactivity of NVO results from the high content of V^{4+} on the surface and well-developed surface area. It has been demonstrated that V^{4+} can trap photogenerated electrons and promote efficient charge separation, enhancing photocatalytic performance in water splitting and degradation of pollutants[35,53,54]. It has also been reported that the existence of V^{4+} can lead to the formation of intermediate defect energy states and the widening of the optical absorption range[55]. V^{4+} species can be introduced into the structure of various vanadates in several different ways, such as doping with other elements[54], post-treatment (e.g., calcination[56], plasma modification[53]) or hydrothermal reduction with reducing additives[35]. The last approach was also used in this study, and oxalic acid was added during the synthesis. As confirmed by physicochemical characterization, oxalic acid serves as a reductant and induces the formation of V^{4+} on the surface of $NH_4V_4O_{10}$ during the hydrothermal process. It should also be noted that oxalic acid can act as a forming agent during the hydrothermal synthesis of ammonium vanadates[22]. Thus, it is suggested that its addition led to the formation of 3D flower-like microstructures, as observed here for bare $NH_4V_4O_{10}$.

Moreover, herein, we propose to combine $NH_4V_4O_{10}$ with rGO. This can be done during a hydrothermal reaction, which in contrast to the synthesis of previously mentioned heterojunctions is a one-step process. Another advantage of such synthesis is a hierarchal porous structure that is formed during the hydrothermal reaction. In contrast to the NVO sample, in the case of the NVO/rGO composite, the morphology is probably affected by both oxalic acid and graphene oxide. As shown in Fig. 5, the coupling of $NH_4V_4O_{10}$ with rGO resulted in improved photocatalytic performance, which reached 92% within 60 min.

The kinetics of MB photodegradation were further studied by plotting -ln(C/C_0) as a function of irradiation time (Figure S6). In the case of NVO, the is most likely pseudo-first-order kinetics according to the Langmuir–Hinshelwood model, and the calculated rate constant k was equal to 0.0251 min^{-1}. For NVO/rGO, the mechanism of MB photodegradation can be more complex (as indicated by the low linear regression coefficient); however, it can be clearly seen that at the beginning of illumination, the process is much faster. To identify the main reactive species involved in the photodegradation process, further tests were performed in the presence of different scavengers. Benzoquinone (BQ), ammonium oxalate (AO), and tert-butyl alcohol (TBA) were used as scavengers for ·O2- radicals, holes h+, and hydroxyl radicals ·OH, respectively. As depicted in Fig. 5b-c), compared with the photocatalytic process without scavengers, the removal rate of MB by NVO decreased by 47% and 29% in the presence of TBA and AO, while no change was observed with the addition of BQ. This indicates that ·OH and h+ play a critical role in MB photodegradation. In contrast, the degradation of MB with the composite is highly suppressed by BQ, indicating the main role of ·O2- radicals in the process. The addition of

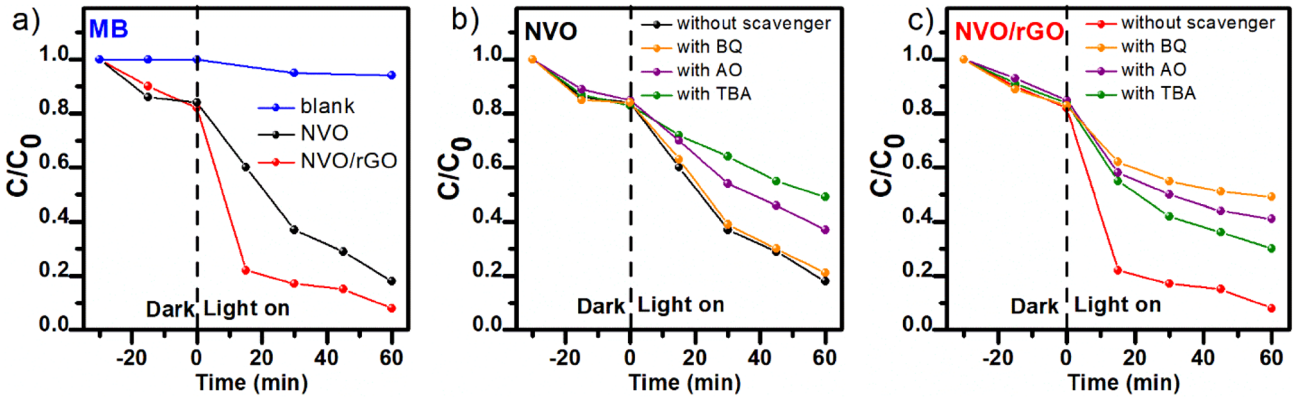

Figure 5. Photocatalytic degradation of MB under simulated solar light: (**a**) C/C_0 vs t plot and (**b**,**c**) active species trapping experiments with the addition of BQ, AO, and TBA as scavengers for O2- radicals, holes h+, and hydroxyl radicals ·OH, respectively.

AO and TBA also shows a significant inhibitory effect, which indicates that h + and ·OH also contribute to the degradation of MB. The reusability of NVO and NVO/rGO was further investigated by performing 4 consecutive photodegradation cycles for MB (Fig. 6). The results revealed that the activity of NVO gradually decreases, and in the 4th cycle, the efficiency drops to 56%. Better stability was observed in the case of the composite. The results obtained for NVO/rGO show that the degradation efficiency was maintained at a good level during each reaction cycle during irradiation, and consequently, the photocatalyst could be reused.

Photoreduction of inorganic pollutants. The obtained photocatalysts were also used in the Cr(VI) photoreduction process at pH 3. It is well known that under acidic conditions, Cr(VI) is mainly present in the form of $HCrO_4^-$ or $Cr_2O_7^{2-}$, which eventually promotes the reduction of Cr(VI) to Cr(III)[57]. As in the case of the photodegradation of MB, the composite was characterized by a better reduction efficiency of the chromium compound. The adsorption–desorption equilibrium was attained for 30 min in the dark. The results are presented in Fig. 7a.

The decrease in Cr(VI) concentration due to dark adsorption as well as during illumination was higher for the composite. The greatest decrease in Cr(VI) concentration in the case of NVO/rGO was observed in the first 15 min of illumination, and then the performance of the catalyst slowly stopped. As a result, after one hour of exposure, the photoreduction amounted to approximately 70% (in the case of NVO, only 20%). The modified material, namely, NVO/rGO, showed a greater ability to degrade the hazardous chromium form, which was due to the presence of rGO, which was responsible for more efficient separation and prolonged recombination time of electron–hole pairs. Moreover, as shown in Fig. 7b, the NVO/rGO composite displays good reusability and after four consecutive cycles, the degradation efficiency of Cr(VI) slightly decreases to 65%. The above experimental results demonstrate the great potential of the obtained NVO and NVO/rGO in the photodegradation of water pollutants. In contrast to the previous study[52], it was shown that pristine $NH_4V_4O_{10}$ can be efficiently used for the degradation of organic dyes. Moreover, the proposed combination of $NH_4V_4O_{10}$ with rGO not only increases the photocatalytic degradation reaction rate and improves the cyclic stability of photocatalyst but also widens its application, allowing for the efficient photoreduction of toxic Cr(VI). In comparison to other vanadium-based photocatalysts reported in the literature[19,58–65] (Tables S1 and S2), NVO and NVO/rGO present better or similar efficiency towards the photodegradation of MB and Cr(VI). Importantly, proposed photocatalysts can be

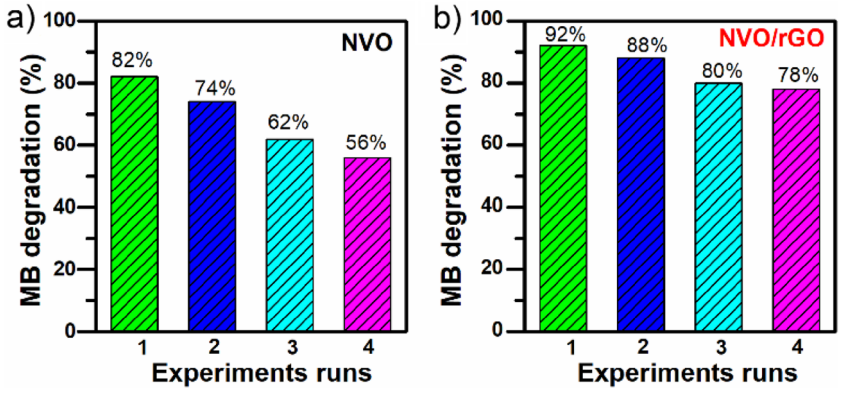

Figure 6. Reusability of the NVO (**a**) and NVO/rGO (**b**) photocatalysts for the degradation of MB.

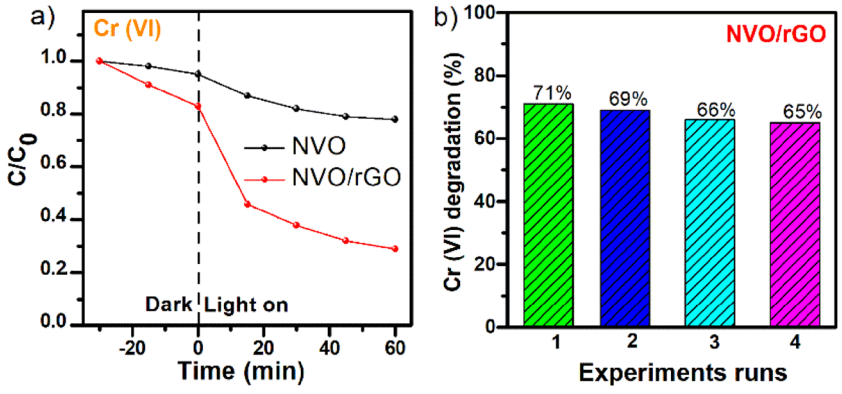

Figure 7. The photocatalytic reduction of Cr(VI) to Cr(III) under simulated solar light: (**a**) C/C0 vs t plot and (**b**) reusability of NVO/rGO.

activated under solar light and exhibit significant photocatalytic degradation of pollutants within the first 60 min of illumination. Such an efficient and fast process, together with facile synthesis (one-step reaction, low-cost precursors) and good cyclic stability of NVO and NVO/rGO make them promising materials for solar-driven water purification.

Therefore, E_{cb} and E_{vb} were calculated to be 0.75 eV and 3.03 eV, respectively. On the basis of the obtained results, a possible mechanism for the photocatalytic performance of NVO and NVO/rGO has been proposed and is schematically presented in Fig. 8.

When NVO or NVO/rGO is exposed to solar illumination, $NH_4V_4O_{10}$ becomes excited, and electron–hole pairs are generated. The photogenerated holes in the VB of $NH_4V_4O_{10}$ can oxidize MB directly or react with water to produce (·OH), which are also able to indirectly oxidize organic species. At the same time, the E_{cb} of $NH_4V_4O_{10}$ is lower than the reduction potential of O_2 to ·O2- (-0.33 eV)[66]. However, in the case of the NVO/rGO composite, the photogenerated electrons can migrate from $NH_4V_4O_{10}$ to rGO [67,68]. It is known that the electrons at the reduced graphene oxide surface react readily with oxygen molecules and generate superoxide radical anions (·O2-) [67], which subsequently degrade the MB dye molecules. According to the results obtained from the active species trapping experiment, this process was the most dominant in NVO/rGO. On the other hand, the potential of the conduction band is more negative than the redox potential of the $Cr_2O_7^{2-}/Cr^{3+}$ couple (1.33 eV vs NHE), which indicates that $NH_4V_4O_{10}$ can reduce Cr(VI) ions using their photoexcited electrons. The efficiency of Cr(VI) photoreduction for NVO equals only 20% after 60 min of illumination, while for NVO/rGO, it reaches 70%. The improved photocatalytic performance originates from the unique structure of the NVO/rGO composite, in particular the existence of rGO, which acts as an electron acceptor and inhibits the recombination of electrons and holes. In addition, the NVO/rGO composite is characterized by a narrower band gap and higher adsorption capacity of Cr(VI) than NVO.

Conclusions

A one-pot hydrothermal method was successfully used to obtain $NH_4V_4O_{10}$ (NVO) and its composite with rGO (NVO/rGO). The photocatalytic activity of synthesized NVO and NVO/rGO was evaluated towards methylene blue (MB) degradation and Cr(VI) to Cr(III) reduction under simulated solar light illumination. Excellent performance in MB photodegradation was obtained for both studied materials, which was attributed to the high content of V^{4+} surface species revealed by XPS studies, as well as the developed surface area of the photocatalysts. The positive impact of rGO in terms of the activity and stability of the photocatalyst was especially pronounced. Reactions carried out in the presence of specific scavengers revealed differences in the mechanism of photocatalyst action. In the case of NVO, ·OH and h + play a critical role in MB photodegradation, while for NVO/rGO, ·O2- radicals are the dominant active species responsible for dye degradation. Moreover, the proposed composite showed activity in the photoreduction of highly toxic Cr(VI) ions in an acidic environment and is therefore a promising photocatalyst for wastewater treatment containing both organic and inorganic contaminants. The hydrothermal synthesis parameters of NVO/rGO can cause different morphologies, particle sizes and crystallizations, resulting in different photocatalytic activities; therefore, such studies are planned to be carried out in our laboratory.

Materials and methods

Chemicals. Ammonium metavanadate (NH_4VO_3, 99.0%), oxalic acid dihydrate ($C_2H_2O_4 \times 2H_2O$, 97.0%), and methylene blue (MB > 98%) were obtained from Sigma−Aldrich and used without further purification. Deionized water was used in all experiments (conductivity < 0,06 µS/cm). Graphene oxide (GO) employed in the composite synthesis was prepared using the modified Hummers method [69]. Potassium dichromate ($K_2Cr_2O_7$, ≥ 99.0%) and ammonium oxalate (AO, ≥ 99%) were purchased from Merck. Benzoquinone (BQ, > 98%) and *tert*-butyl alcohol (TBA, > 99.5%) were received from CheMondis.

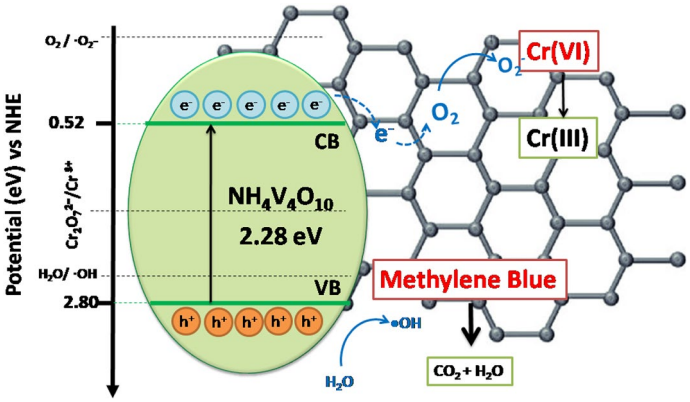

Figure 8. Schematic diagram of the band-energy levels of NVO/rGO with the possible photocatalytic mechanism.

Synthesis of photocatalysts. The $NH_4V_4O_{10}$/rGO (NVO/rGO) photocatalyst was prepared via a facile one-pot hydrothermal method. NH_4VO_3 and GO were used as precursors and mixed with a weight ratio of 10:1. In brief, 0.6 g of NH_4VO_3 and 0.6 g of oxalic acid were dissolved in 90 ml of deionized water. In the meantime, 60 mg of GO was dispersed in 30 ml of deionized water with ultrasonication (20 W, 30 min). Next, the prepared reagents were mixed together and sonicated for 15 min. Then, the as-obtained reaction mixture was transferred to a Teflon-lined stainless-steel autoclave (volume 1.8 L) for 8 h and 180 °C. Finally, the obtained product was washed with deionized water and dried at 40 °C under reduced pressure (0.01 bar). For comparison, bare $NH_4V_4O_{10}$ (NVO) without GO was synthesized in an analogous procedure.

Physicochemical characterization. The crystal structure and phase composition of the samples were examined using powder X-ray diffraction (XRD, BrukerD2 Phaser diffractometer) with Cu Kα radiation (λ = 1.5404 Å). Raman spectra were acquired using a confocal micro-Raman system (Horiba Jobin Yvon) with a 632.8 nm laser excitation wavelength. Fourier transform infrared (FTIR) analysis was carried out on a Perkin Elmer Frontier spectrophotometer in the range of 500–4000 cm^{-1}. Measurements were made in transmittance mode, and the potassium bromide pellet method was used. The valence state of vanadium was analysed using X-ray photoelectron spectroscopy (XPS) and X-ray absorption spectroscopy (XPS). The high-resolution V 2p XPS spectra were collected on an Escalab 250Xi device (Thermo Fisher Scientific) equipped with a monochromatic AlKα source. Measurements were carried out at a 25 eV pass energy with a 0.1 eV energy step. The X-ray spot size was 250 µm. The calibration of the XPS spectrum was performed using the characteristic C1s peak at 284.6 eV. XAS analysis was performed at the ASTRA beamline at SOLARIS National Synchrotron Radiation Centre, Cracow, Poland. The V K-edge XANES of powder samples was obtained in transmission mode in the range of 5265 to 5550 eV. V_2O_3, VO_2, and V_2O_5 were used as reference materials for the V(III), V(IV) and V(V) oxidation states. Thermogravimetric analysis (TGA) was conducted under air using a Netzsch STA 449 F1 at 10 °C/min from 40 °C to 600 °C. The morphology of the samples was investigated using scanning electron microscopy (SEM, ESEM Quanta Feg 250) and transition electron microscopy (TEM, FEI TECNAI G2 F20). N_2 adsorption–desorption isotherms were measured on a NOVAtouch™ 2 surface analyser, and the Brunauer—Emmett—Teller (BET) method was used to calculate the specific surface area (relative pressure range p/p_0: 0.1 to 0.3). The correlation coefficient of the linear regression was not less than 0.999. The pore size distribution and cumulative pore volume were evaluated using the BJH (Barrett, Joyner and Halenda) method from the desorption branch. The UV—vis reflectance spectra of the selected materials were measured with a UV—vis spectrophotometer (Lambda 35, Perkin-Elmer) equipped with a diffuse reflectance accessory. The spectra were registered in the range of 300–900 nm, with a scanning speed of 120 nm min^{-1}. Band gap energy values were determined as the intercept of the x-axis of the plot of transformation of the Kubelka–Munk function. To determine the energy band gap (E_{bg}) of the chosen powders, the Kubelka–Munk function was applied:

$$f(KM) = \frac{2R}{(1-R)^2}$$

where R –reflectance. The bandgap was estimated by extrapolation of the linear region of $(f(KM)\ h\nu)^n$ vs hν to y = 0. The power of n equals 2, assuming a direct band gap.

The PL spectra were measured using SCINCO FluoroMate FS-2 fluorescence spectrometer (excitation wavelength: 375 nm). Electrochemical measurements were accomplished using an Ivium Vertex potentiostat/galvanostat and a three-electrode cell with Pt mesh as the counter electrode and Ag/AgCl (3 M KCl) as the reference electrode. To perform these measurements, aqueous suspensions of NVO and NVO/rGO were drop-cast on glassy carbon disc electrodes. After drying with a hot stream of air, electrodes were tested in aqueous 0.2 M Na_2SO_4 solution. The EIS response was measured for 3 frequencies (500, 750, and 1000 Hz). The capacitance was estimated from the single points using the $C_{sc} = -1/\omega Z''$ formula (ω – angular frequency, Z" – imagine part of impedance).

Evaluation of photocatalytic activity. The photocatalytic behaviour was investigated by the oxidation of methylene blue and reduction of Cr(VI). The photocatalytic performance was evaluated under simulated solar light using a 300 W Xe lamp (a high-pressure 150 W xenon lamp, LOT – QuantumDesign GmbH equipped with the AM1.5G filter). The intensity of the incident light that reaches the surface of the investigated solution was equal to 100 $mWcm^{-2}$ (measured using a Coherentâ FieldMate Laser Power Meter). In a typical test, 20 mg of catalyst was placed in a 50 mL aqueous pollutant solution. The concentration of MB and Cr(VI) was $1{\cdot}10^{-5}$ M. Before irradiation, the suspension was vigorously stirred in the dark for 30 min to reach desorption-adsorption equilibrium. The change in MB and Cr(VI) concentration was monitored by its absorption at 665 nm and 351 nm, respectively, from the UV–Vis (Spektrofotometr UV5100) spectra of the solution, using distilled water as a reference. A total of 0.75 ml of suspension was collected and centrifuged before UV—Vis measurement. In the case of Cr(VI) photoreduction, the process was conducted in acidified (pH = 3) solutions.

To study the reusability of the prepared photocatalysts, the cycle experiment was repeated 4 times for the photodegradation of methylene blue. After each photodegradation test, the catalyst was collected by centrifugation, dried under natural conditions and used for the next degradation experiment. Moreover, to indicate the role of hydroxyl radicals (·OH), (h +) holes and superoxide radicals (·O2-) in the process of MB degradation, experiments were performed in the presence of appropriate scavengers: t-butanol (TBA), ammonium oxalate (AO) and benzoquinone (BQ). The concentration of each scavenger was equal to 1 mM.

Data availability

All data generated or analysed during this study are included in this published article (and its Supplementary Information files).

Received: 21 December 2022; Accepted: 7 March 2023
Published online: 09 March 2023

References

1. Thirunavukkarasu, A., Nithya, R. & Sivashankar, R. A review on the role of nanomaterials in the removal of organic pollutants from wastewater. *Rev. Environ. Sci. Biotechnol.* **19**, 751–778 (2020).
2. Saini, R. D. Textile organic dyes: Polluting effects and elimination methods from textile waste water. *Int. J. Chem. Eng. Res.* **9**, 975–6442 (2017).
3. Fernández, C., Larrechi, M. S. & Callao, M. P. An analytical overview of processes for removing organic dyes from wastewater effluents. *TrAC–Trends Analyt. Chem.* **29**, 1202–1211 (2010).
4. Zamora-Ledezma, C. *et al.* Heavy metal water pollution: A fresh look about hazards, novel and conventional remediation methods. *Environ. Technol. Innov.* **22**, 101504 (2021).
5. Fato, F. P., Li, D. W., Zhao, L. J., Qiu, K. & Long, Y. T. Simultaneous removal of multiple heavy metal ions from river water using ultrafine mesoporous magnetite nanoparticles. *ACS Omega* **4**, 7543–7549 (2019).
6. Xu, B., Dong, J., Wang, X. & Yao, Y. Monitoring Cr(VI) photoreduction at different depths by operando low-field NMR relaxometry. *Magnet. Resonance Lett.* **2**, 170–176 (2022).
7. Kinuthia, G. K. *et al.* Levels of heavy metals in wastewater and soil samples from open drainage channels in Nairobi, Kenya: Community health implication. *Sci. Rep.* **10**, 1–13 (2020).
8. Kamble, G. S. & Ling, Y. C. Solvothermal synthesis of facet-dependent BiVO4 photocatalyst with enhanced visible-light-driven photocatalytic degradation of organic pollutant: Assessment of toxicity by zebrafish embryo. *Sci. Rep.* **10**, 1–11 (2020).
9. Rajaitha, P. M. *et al.* Unraveling highly efficient nanomaterial photocatalyst for pollutant removal: A comprehensive review and future progress. *Mater. Today Chem.* **23**, 100692 (2022).
10. Singh, V. *et al.* Highly functionalized photo-activated metal–organic frameworks for dye degradation: Recent advancements. *Materialstoday Commun.* **34**, 105180 (2023).
11. Gautam, S. *et al.* Metal oxides and metal organic frameworks for the photocatalytic degradation: A review. *J Environ Chem Eng* **8**, 103723 (2020).
12. He, H., Luo, Z., Tang, Z. Y. & Yu, C. Controllable construction of ZnWO4 nanostructure with enhanced performance for photosensitized Cr(VI) reduction. *Appl. Surf. Sci.* **490**, 460 (2019).
13. Samsudin, M. F. R., Sufian, S. & Hameed, B. H. Epigrammatic progress and perspective on the photocatalytic properties of BiVO4-based photocatalyst in photocatalytic water treatment technology: A review. *J. Mol. Liq.* **268**, 438–459 (2018).
14. Lotfi, S., Ouardi, M. E., Ahsaine, H. A. & Assani, A. Recent progress on the synthesis, morphology and photocatalytic dye degradation of BiVO4 photocatalysts: A review. *Catal. Rev. Sci. Eng.* **00**, 1–45 (2022).
15. Hassan, A., Iqbal, T., Tahir, M. B. & Afsheen, S. A review on copper vanadate-based nanostructures for photocatalysis energy production. *Int. J. Energy Res.* **43**, 9–28 (2019).
16. Guo, J. *et al.* Efficient visible-light driven photocatalyst, silver (meta)vanadate: Synthesis, morphology and modification. *Chem. Eng. J.* **352**, 782–802 (2018).
17. Yanga, R. *et al.* InVO4-based photocatalysts for energy and environmental applications. *Chem. Eng. J.* **428**, 131145 (2022).
18. Trzciński, K., Szkoda, M., Sawczak, M., Karczewski, J. & Lisowska-Oleksiak, A. Visible light activity of pulsed layer deposited BiVO 4 /MnO 2 films decorated with gold nanoparticles: The evidence for hydroxyl radicals formation. *Appl. Surf. Sci.* **385**, 199–208 (2016).
19. Nadolska, M. *et al.* Insight into potassium vanadates as visible-light-driven photocatalysts: Synthesis of V(IV)-rich nano/microstructures for the photodegradation of methylene blue. *Inorg. Chem.* **61**, 9433–9444 (2022).
20. Le, T. K., Kang, M., Tran, V. T. & Kim, S. W. Relation of photoluminescence and sunlight photocatalytic activities of pure V2O5 nanohollows and V2O5/RGO nanocomposites. *Mater. Sci. Semicond. Process.* **100**, 159–166 (2019).
21. Li, C. *et al.* NH4V4O10/rGO Composite as a high-performance electrode material for hybrid capacitive deionization. *Environ. Sci. (Camb)* **6**, 303–311 (2020).
22. Cui, F. *et al.* Deficiency and surface engineering boosting electronic and ionic kinetics in NH4V4O10 for high-performance aqueous zinc-ion battery. *Energy Storage Mater* **44**, 197–205 (2022).
23. Wang, H. *et al.* Mo-doped NH4V4O10 with enhanced electrochemical performance in aqueous Zn-ion batteries. *J. Alloys Compd.* **858**, 15830 (2021).
24. Chen, Q., Xia, Q., Xu, Y., Wang, P. & Tan, Q. NH 4 V 4 O 10 micro-flowers as cathode material for high performance hybrid magnesium-lithium-ion batteries. *Mater. Lett.* **247**, 178–181 (2019).
25. Esparcia, E. A., Chae, M. S., Ocon, J. D. & Hong, S. T. Ammonium vanadium bronze (NH4V4O10) as a high-capacity cathode material for nonaqueous magnesium-ion batteries. *Chem. Mater.* **30**, 3690–3696 (2018).
26. Zhang, Y., Li, Y., Yuan, Y. & Lin, K. C-dots decorated SrTiO3/NH4V4O10 Z-scheme heterojunction for sustainable antibiotics removal: Reaction kinetics, DFT calculation and mechanism insight. *Sep. Purif. Technol.* **295**, 121268 (2022).
27. Fang, D. *et al.* Novel hierarchical three-dimensional ammonium vanadate nanowires electrodes for lithium ion battery. *Appl. Surf. Sci.* **360**, 658–665 (2016).
28. Zhang, H. *et al.* Layered ammonium vanadate nanobelt as efficient adsorbents for removal of Sr2+ and Cs+ from contaminated water. *J. Colloid. Interface Sci.* **615**, 110–123 (2022).
29. Frost, R. L., Erickson, K. L., Weier, M. L. & Carmody, O. Raman and infrared spectroscopy of selected vanadates. *Spectrochim. Acta A Mol. Biomol. Spectrosc.* **61**, 829–834 (2005).
30. Sarkar, S., Veluri, P. S. & Mitra, S. Morphology controlled synthesis of layered NH4V 4O10 and the impact of binder on stable high rate electrochemical performance. *Electrochim. Acta* **132**, 448–456 (2014).
31. Prześniak-Welenc, M., Nadolska, M., Nowak, A. P. & Sadowska, K. Pressure in charge. Neglected parameter in hydrothermal synthesis turns out to be crucial for electrochemical properties of ammonium vanadates. *Electrochim Acta*, **339**, 0–8 (2020).
32. Ţucureanu, V., Matei, A. & Avram, A. M. FTIR spectroscopy for carbon family study. *Crit. Rev. Anal. Chem.* **46**, 502–520 (2016).
33. Jahan, N. *et al.* A comparative study on sorption behavior of graphene oxide and reduced graphene oxide towards methylene blue. *Case Stud. Chem. Environ. Eng.* **6**, 100239 (2022).
34. Kou, L., Wang, Y. & Song, J. Reduced graphene oxide nanosheets decorated carbon-coated NH4V3O8 as cathode materials with superior cycle stabilities for lithium-ion batteries. *Appl. Phys. A Mater. Sci. Process* **128**, 1–8 (2022).
35. Zhang, Y. *et al.* Facile synthesis of V4+ self-doped, [010] oriented BiVO4 nanorods with highly efficient visible light-induced photocatalytic activity. *Phys. Chem. Chem. Phys.* **16**, 24519–24526 (2014).
36. Song, H., Luo, M. & Wang, A. High rate and stable li-ion insertion in oxygen-deficient LiV3O8 nanosheets as a cathode material for lithium-ion battery. *ACS Appl. Mater. Interfaces* **9**, 2875–2882 (2017).

37. Appavu, B., Thiripuranthagan, S., Ranganathan, S., Erusappan, E. & Kannan, K. BiVO4 /N-rGO nano composites as highly efficient visible active photocatalyst for the degradation of dyes and antibiotics in eco system. *Ecotoxicol. Environ. Saf.* **151**, 118–126 (2018).
38. Landi, S. *et al.* Use and misuse of the Kubelka-Munk function to obtain the band gap energy from diffuse reflectance measurements. *Solid State Commun.* **341**, 114573 (2022).
39. Le, S., Ma, Y., He, D., Wang, X. & Guo, Y. CdS/NH4V4O10 S-scheme photocatalyst for sustainable photo-decomposition of amoxicillin. *Chem. Eng. J.* **426**, 130354 (2021).
40. Wang, H. *et al.* Mo-doped NH4V4O10 with enhanced electrochemical performance in aqueous Zn-ion batteries. *J. Alloys Compd.* **858**, 158380 (2021).
41. Shen, Y. *et al.* Evolution of the band-gap and optical properties of graphene oxide with controllable reduction level. *Carbon N. Y.* **62**, 157–164 (2013).
42. Zelechowska, K., Prześniak-Welenc, M., Łapiński, M., Kondratowicz, I. & Miruszewski, T. Fully scalable one-pot method for the production of phosphonic graphene derivatives. *Beilstein J. Nanotechnol.* **8**, 1094–1103 (2017).
43. Jin, Y., Zheng, Y., Podkolzin, S. G. & Lee, W. Band gap of reduced graphene oxide tuned by controlling functional groups. *J. Mater. Chem. C Mater.* **8**, 4885–4894 (2020).
44. Merazga, A. *et al.* Optical band-gap of reduced graphene oxide/TiO2 composite and performance of associated dye-sensitized solar cells. *Mater. Sci. Eng. B Solid State Mater. Adv. Technol.* **259**, 145581 (2020).
45. Mangavati, S. *et al.* Defects and band gap shrinkage in ZnO/rGO composite nano-pebbles prepared by solid–state reaction. *Diam. Relat. Mater.* **123**, 108886 (2022).
46. Mondal, A., Prabhakaran, A., Gupta, S. & Subramanian, V. R. Boosting photocatalytic activity using reduced graphene oxide (RGO)/semiconductor nanocomposites: Issues and future scope. *ACS Omega* **6**, 8734–8743. https://doi.org/10.1021/acsomega.0c06045 (2021).
47. Le, T. K., Kang, M. & Kim, S. W. Morphology engineering, room-temperature photoluminescence behavior, and sunlight photocatalytic activity of V2O5 nanostructures. *Mater. Charact.* **153**, 52 (2019).
48. Bott, A. W. Electrochemistry of semiconductors. *Curr. Sep.* **17**, 87–91 (1998).
49. Chen, Y., Zhang, X., Zhang, D., Yu, P. & Ma, Y. High performance supercapacitors based on reduced graphene oxide in aqueous and ionic liquid electrolytes. *Carbon N. Y.* **49**, 573 (2011).
50. Chen, J. *et al.* Insight into the synergistic effect of adsorption-photocatalysis for the removal of organic dye pollutants by Cr-doped ZnO. *Langmuir* **44**, 520–533 (2020).
51. Chang, L. *et al.* Excellent adsorption-photocatalysis synergistic activity of 3D–3D flower-like BiOBr/graphene hydrogel composite and the removal of potassium butyl xanthate. *New J. Chem.* **44**, 2479–2488 (2020).
52. Abbood, H. A., Peng, H., Gao, X., Tan, B. & Huang, K. Fabrication of cross-like NH4V4O10 nanobelt array controlled by CMC as soft template and photocatalytic activity of its calcinated product. *Chem. Eng. J.* **209**, 245–254 (2012).
53. Che, G. *et al.* Solution plasma boosts facet-dependent photoactivity of decahedral BiVO4. *Chem. Eng. J.* **397**, 125381 (2020).
54. Kong, D. *et al.* Ni-Doped BiVO4 with V4+ Species and Oxygen Vacancies for Efficient Photoelectrochemical Water Splitting. *Transact. Tianjin Univ.* **25**, 340–347 (2019).
55. Chen, L. *et al.* In situ synthesis of V4+ and Ce3+ self-doped BiVO4/CeO2 heterostructured nanocomposites with high surface areas and enhanced visible-light photocatalytic activity. *J. Phys. Chem. C* **120**, 18548–18559 (2016).
56. Saputera, W. H. *et al.* Photocatalytic degradation of palm oil mill effluent (Pome) waste using bivo4 based catalysts. *Molecules* **26**, 6225 (2021).
57. Szkoda, M., Zarach, Z., Nadolska, M., Trykowski, G. & Trzciński, K. SnO2 nanoparticles embedded onto MoS2 nanoflakes–an efficient catalyst for photodegradation of methylene blue and photoreduction of hexavalent chromium. *Electrochim. Acta* **414**, 140173 (2022).
58. Phanichphant, S., Nakaruk, A., Chansaenpak, K. & Channei, D. Evaluating the photocatalytic efficiency of the BiVO4/rGO photocatalyst. *Sci. Rep.* **9**, 16091 (2019).
59. Bhardwaj, D., Sangwan, S., Shivashankar, S. A. & Umarji, A. M. Microwave-assisted synthesis of reduced graphene oxide/V2O5 nano-composite as an efficient photocatalyst for dye degradation. *Bull. Mater. Sci.* **45**, 135 (2022).
60. Muhammad Salim Mansha, T. I. Experimental and theoretical study of novel rGO/AgVO3 nano-hetrostructures for their application as efficient photocatalyst. *Opt. Mater. Amst.* **131**, 112591 (2022).
61. Sajid, M. M. *et al.* Photocatalytic performance of ferric vanadate (FeVO4) nanoparticles synthesized by hydrothermal method. *Mater. Sci. Semicond. Process* **129**, 105785 (2021).
62. Hu, J. *et al.* In situ preparation of Bi2S3nanoribbon-anchored BiVO4nanoscroll heterostructures for the catalysis of Cr(vi) photoreduction. *Catal. Sci. Technol.* **10**, 3843 (2020).
63. Jia, J. *et al.* La3+, Gd3+-codoped BiVO4 nanorods with superior visible-light-driven photocatalytic performance for simultaneous removing aqueous Cr(VI) and azo dye. *J. Nanopart. Res.* **22**, 1 (2020).
64. Dadigala, R. *et al.* Fabrication of novel 1D/2D V2O5/g-C3N4 composites as Z-scheme photocatalysts for CR degradation and Cr (VI) reduction under sunlight irradiation. *J. Environ. Chem. Eng.* **7**, 102822 (2019).
65. Li, C., Che, H., Yan, Y., Liu, C. & Dong, H. Z-scheme AgVO3/ZnIn2S4 photocatalysts: "One Stone and Two Birds" strategy to solve photocorrosion and improve the photocatalytic activity and stability. *Chem. Eng. J.* **398**, 125523 (2020).
66. Santos, R. K. *et al.* Ag3PO4/NiO composites with enhanced photocatalytic activity under visible light. *ACS Omega* **5**, 21651–21661 (2020).
67. Sajid, M. M. *et al.* Study of the interfacial charge transfer in bismuth vanadate/reduce graphene oxide (BiVO4/rGO) composite and evaluation of its photocatalytic activity. *Res. Chem. Intermed.* **46**, 1201 (2020).
68. Zhang, L. *et al.* Synthesis of butterfly-like BiVO4/RGO nanocomposites and their photocatalytic activities. *Chin. J. Chem. Eng.* **26**, 667 (2018).
69. Kondratowicz, I., Żelechowska, K., Nadolska, M., Jażdżewska, A. & Gazda, M. Comprehensive study on graphene hydrogels and aerogels synthesis and their ability of gold nanoparticles adsorption. *Colloids Surf. A Physicochem. Eng. Asp.* **528**, 65–73 (2017).

Acknowledgements

This work is supported by the National Science Center of Poland (Grant No. 2020/37/N/ST5/03697). The authors also acknowledge the financial support from Gdańsk University of Technology by the DEC- 39/2021/IDUB/I.3.3 grant under the Argentum—'Excellence Initiative—Research University program. The authors would like to acknowledge Michał Maciejewski from Gdańsk University of Technology, Faculty of Applied Physics and Mathematics, for enabling the PL measurements.

Author contributions

Conceptualization: M.N., Investigation: M.N., M.S., K.T., J.R., A.L., M.P.W., Formal Analysis: M.N., M.S., J.R., A.L., Writing – Original Draft: M.N., M.S., K. T, K.S., Review & Editing: M.N., J.R., K.S., M.P.W. Visualization: M.N., Supervision: M.P.W., Project administration: M.N., Funding acquisition: M.N. and M.P.W.

Competing interests
The authors declare no competing interests.

Additional information
Supplementary Information The online version contains supplementary material available at https://doi.org/10.1038/s41598-023-31130-9.

Correspondence and requests for materials should be addressed to M.P.-W.

Reprints and permissions information is available at www.nature.com/reprints.

Publisher's note Springer Nature remains neutral with regard to jurisdictional claims in published maps and institutional affiliations.

Supporting Information

New light on the photocatalytic performance of $NH_4V_4O_{10}$ and its composite with rGO

M. Nadolska[a], M. Szkoda[b], K. Trzciński[b], J. Ryl[a], A. Lewkowicz[c], K. Sadowska[d], , J. Smalc-Koziorowska[e], M. Prześniak-Welenc[a*]

[a]Institute of Nanotechnology and Materials Engineering, and Advanced Materials Centre, Gdansk University of Technology, Narutowicza 11/12, 80-233 Gdansk, Poland,

[b]Faculty of Chemistry, Gdansk University of Technology, Narutowicza St. 11/12, 80-233 Gdansk, Poland

[c] Insitute of Experimental Physics, Faculty of Mathematics, Physics and Informatics, University of Gdańsk, Wita Stwosza 57, 80-308 Gdańsk, Poland

[d] Nalecz Institute of Biocybernetics and Biomedical Engineering, Polish Academy of Sciences, Ks. Trojdena 4, Warsaw, 02-109, Poland

[e] Institute of High Pressure Physics, Polish Academy of Sciences, Sokołowska 29/37, 01-142 Warsaw, Poland

[*] marwelen@pg.edu.pl

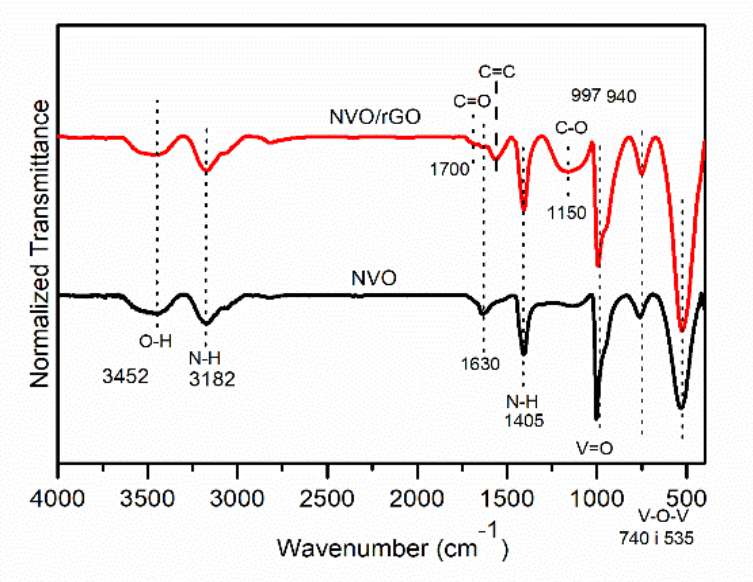

Figure S1. FTIR analysis of NVO and NVO/rGO

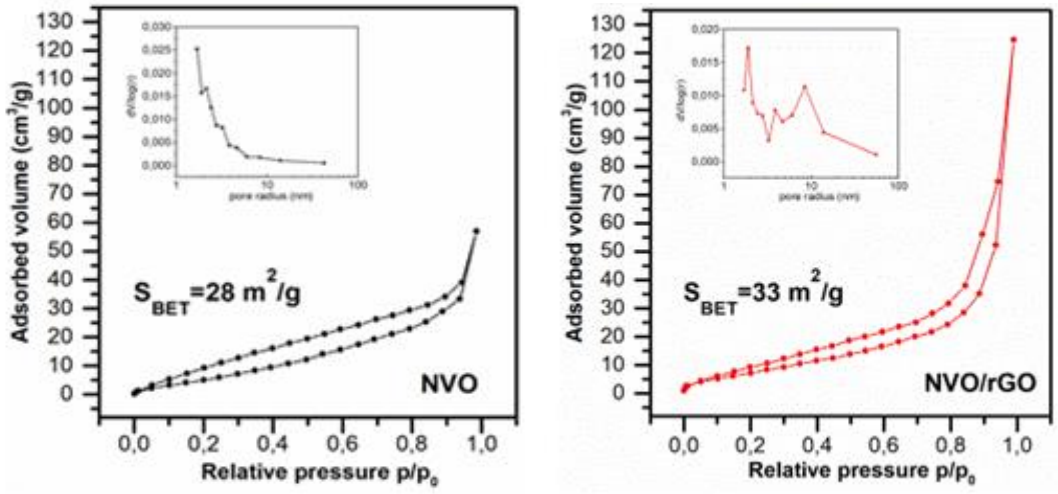

Figure S2. N_2 adsorption-desorption isotherms with pore size distribution (inset) of NVO (left) and NVO/rGO (right).

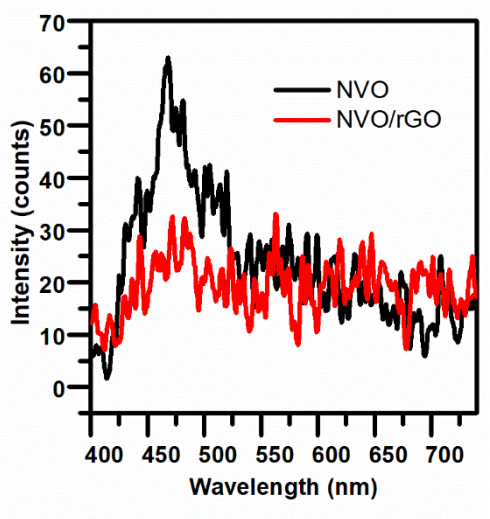

Figure S3. Photoluminescence spectra of NVO and NVO/rGO

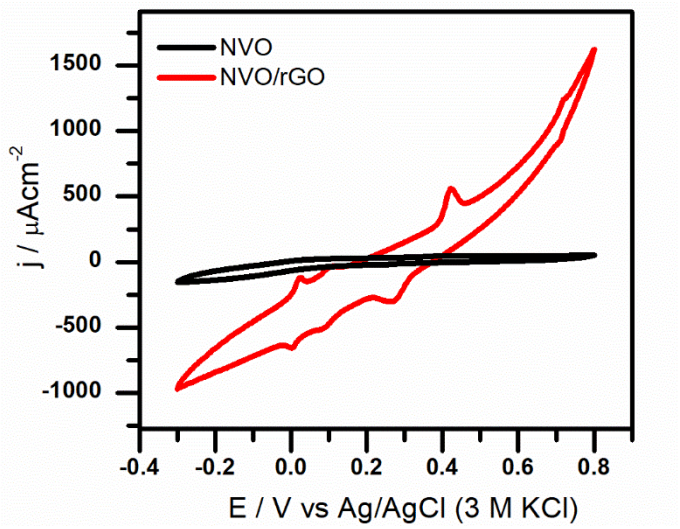

Figure S4. The cyclic voltammetry curves of NVO (a) and NVO/rGO (b), recorded in 0.2 M K_2SO_4, scan rate: 50 mV/s

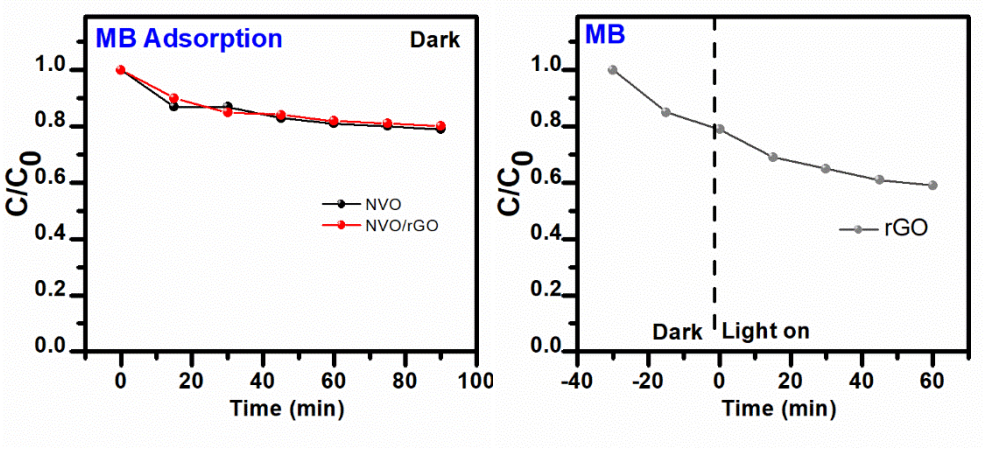

Figure S5. Control tests for the photocatalytic degradation of MB: a) The adsorption of MB on the surface of NVO and NVO/rGO under dark conditions and b) photocatalytic removal of MB by rGO

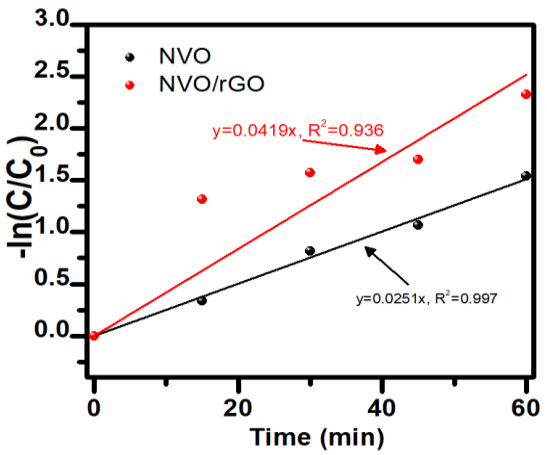

Figure S6. Photocatalytic degradation of MB under simulated solar light-ln(C/C_0) as a function of irradiation time representing the kinetics of the process.

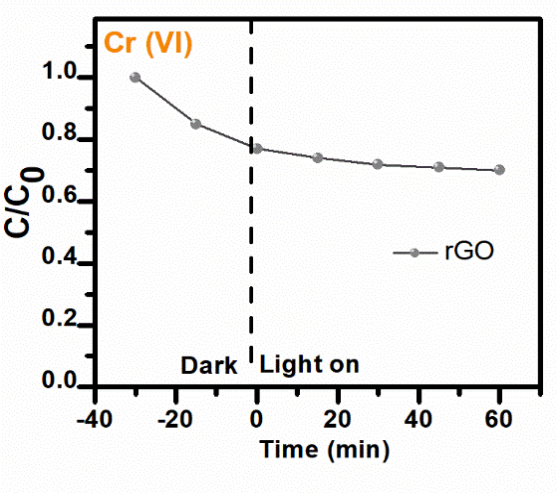

Figure S7. Photocatalytic removal of Cr(VI) by rGO

Table 1 Comparison of MB degradation efficiency for different vanadium-based photocatalysts

Photocatalyst	Efficiency (%)	Time (min)	Ref
$BiVO_4$	60	120	58
$BiVO_4$/rGO	90	120	58
V_2O_5	34	90	59
V_2O_5/rGO	80	90	59
$AgVO_3$	42	150	60
$AgVO_3$/rGO	91	150	60

$FeVO_4$	81	180	61
KV_3O_8	92	60	19
$NH_4V_4O_{10}$	82	60	Present work
$NH_4V_4O_{10}$/rGO	92	60	Present work

Table 1 Comparison of Cr(VI) photoreduction efficiency for different vanadium-based photocatalysts

Photocatalyst	Efficiency (%)	Time (min)	Ref
$BiVO_4$	61	330	62
$BiVO_4/Bi_2S_3$	100	150	62
$BiVO_4$	9	100	63
La,Gd-$BiVO_4$	47	100	63
V_2O_5	3	90	64
V_2O_5 /g-C_3N_4	71	90	64
$AgVO_3$	10	25	65
$AgVO_3/ZnIn_2S_4$	90	25	65
$NH_4V_4O_{10}$	20	60	Present work
$NH_4V_4O_{10}$/rGO	71	60	Present work

4. CONCLUSIONS

The subject of this thesis was manufacturing and structural characterization of ammonium/potassium vanadates. Special attention was paid to possibility of using ammonium/potassium vanadates in electrochemical devices (as cathode materials for LIBs) and photocatalysis (for the degradation of water contaminants). The search for new materials tailored to specific applications is intricately linked to the development of their synthesis methods and their comprehensive characterization, which was the initial stage of conducted research. Samples were synthesized using two different methods: ammonium vanadates were obtained by hydrothermal synthesis, while potassium vanadates were obtained via a novel method based on liquid-phase exfoliation with ion exchange. Both methods are characterized by mild conditions, such as relatively low temperatures (typically below 200°C) and use water as a reaction medium. They are also one-pot processes, which, combined with the use of low-cost chemicals (easily accessible ammonium and potassium sources), not only make them highly attractive for large-scale applications but also align with the principles of sustainability and environmental responsibility. Most importantly, synthesis procedures established within the doctoral research allow for the repeatable synthesis of uniform nanostructures of ammonium/potassium vanadates. Furthermore, the presented research highlights the importance of precursor morphology and initial pressure in the hydrothermal synthesis of vanadates, which is the most commonly used method for synthesizing various vanadates. These two parameters have not been previously discussed, despite their significant influence on the phase and morphology of the final product. The conducted research has demonstrated that utilizing a nanostructured precursor and applying initial hydrothermal pressure results in the formation of thinner nanostructures of ammonium vanadates and facilitates their self-organization into porous, hierarchical structures. These factors also promote the reduction of V^{5+} to V^{4+} and the synthesis of mixed-valence ammonium vanadates.

Another important research aspect involved the comprehensive physicochemical characterization of the obtained materials. Various analytical techniques were applied, including spectroscopy (FTIR, Raman, XPS, XAS, PL, and UV–vis DRS), microscopy (SEM and TEM), thermal analysis (TG-MS and DSC), XRD, and N_2 adsorption. The results and their analysis enabled the determination of structural, morphological, and optical properties of the obtained ammonium/potassium vanadate structures; the assessment of the relationship between synthesis conditions and final product characteristics; and the selection of samples for further investigation in a specific application.

Finally, the obtained ammonium/potassium vanadates were tested as cathode materials for LIBs and as photocatalysts for the degradation of organic dye in aqueous solution (MB was used as a model water pollutant). In the case of the first application, the electrochemical properties of $(NH_4)_2V_{10}O_{25}{\cdot}nH_2O$ and $K_2V_6O_{16}{\cdot}nH_2O$ as cathode materials for LIBs were investigated for the first time. In the literature, there are only single studies regarding the use of such compounds as cathodes for aqueous ZIBs, while they have never been considered for LIBs. The obtained results

confirm the stability of both compounds in nonaqueous systems and their ability for the reversible intercalation and deintercalation of lithium ions. The presented ammonium/potassium vanadates delivered good specific capacity (197/260 $mAhg^{-1}$ at 100 mAg^{-1}) and satisfactory capacity retention (83/100% after 50 cycles). These values are competitive with those of recently reported metal vanadates. Potassium vanadates demonstrated better electrochemical performance and, notably, high rate capability (181 $mAhg^{-1}$ at 1 Ag^{-1} with 99.98% capacity retention after 100 cycles).

In the case of photocatalytic applications, two new materials were introduced (KV_3O_8 and the $NH_4V_4O_{10}$/rGO composite). It is essential to emphasize that the literature is notably limited in this field. Only one single report can be found on potassium vanadates (i.e., $K_2V_6O_{16}{\cdot}nH_2O$), and three about ammonium vanadates (i.e., $NH_4V_4O_{10}$). The results from these previous studies suggest that unmodified vanadates have demonstrated low efficiency in the photodegradation of pollutants, leading researchers to seek ways to enhance photoactivity, such as post-treatment (calcination to produce V_2O_5) or heterojunction creation ($CdS/NH_4V_4O_{10}$ and C-dot/$SrTiO_3$/$NH_4V_4O_{10}$). Therefore, within this thesis, it was also decided to undertake more detailed studies on $K_2V_6O_{16}{\cdot}nH_2O$ and $NH_4V_4O_{10}$. All presented samples acted as efficient photocatalysts, resulting in 82-92% degradation of the dye within the first 30–90 min. Significantly, the obtained ammonium/potassium vanadates exhibited efficient absorption in the visible wavelength region and were activated under simulated solar light illumination. The outstanding photocatalytic performance, rapid degradation, and utilization of clean energy sources display the potential of ammonium and potassium vanadates as promising photocatalysts and place them at a high position among other known photocatalysts. The best efficiency was noted for KV_3O_8 and the $NH_4V_4O_{10}$/rGO composite. Moreover, it was shown that the combination of $NH_4V_4O_{10}$ with rGO provides the possibility of effective reuse of photocatalyst and widens its application. It was shown, that the proposed composite can be used not only for photooxidation of organic pollutants but also for photoreduction of inorganic pollutants with Cr(VI) as an example.

The excellent electrochemical and photocatalytic properties of the studied ammonium/potassium vanadates are attributed to the combination of several factors, including their unique layered structure, the presence of V^{4+} surface species, well-developed surface areas, and the homogeneity of the samples (in terms of phase and morphology). The obtained results confirm the formulated hypotheses and demonstrate that the nanostructures of ammonium/potassium vanadates exhibit properties suitable for use as efficient cathode materials in LIBs and as solar light-driven photocatalysts for decomposing water pollutants.

In conclusion, the research conducted within this thesis paves the way for a deeper understanding of ammonium and potassium vanadates, from their synthesis and structure control to their diverse applications in energy conversion and environmental remediation. Despite their potential, these compounds are relatively underexplored, with available reports still mainly focusing on lithium, zinc, or bismuth vanadate. The undoubted advantage of using ammonium and potassium vanadates, compared to other well-recognized metal vanadates, is their facile synthesis, low cost, and abundance of ammonium/potassium sources.

5. REFERENCES

[1] Yang B, He J, Zhang G, Guo J. Vanadium Extraction, Manufacturing and Applications. 1st ed. Elsevier; 2020, Chapter 2, pp. 9-32.

[2] Xu X, Xiong F, Meng J, Wang X, Niu C, An Q, et al. Vanadium-Based Nanomaterials: A Promising Family for Emerging Metal-Ion Batteries. Adv Funct Mater 2020;30:1–36. https://doi.org/10.1002/adfm.201904398.

[3] Yao G, Zhang N, Zhang Y, Zhou T. Nanostructured transition metal vanadates as electrodes for pseudo-supercapacitors: a review. Journal of Nanoparticle Research 2021;23. https://doi.org/10.1007/s11051-021-05158-9.

[4] Xia D, Gao H, Li M, Gong F, Li M. Transition metal vanadates electrodes in lithium-ion batteries: A holistic review. Energy Storage Mater 2021;35:169–91. https://doi.org/10.1016/j.ensm.2020.10.023.

[5] Yao B, Wu K, Zhang C, Zhang H, Wang Z, Wang J, et al. Crystal growth and laser performance of neodymium-doped scandium orthovanadate. J Cryst Growth 2010;312:720–3. https://doi.org/10.1016/j.jcrysgro.2009.12.012.

[6] Cole ER. Yttrium and Rare Earth Vanadates. Nature 1963;198:1084. https://doi.org/https://doi.org/10.1038/1981084a0.

[7] Yang R, Zhang Y, Fan Y, Wang R, Zhu R, Tang Y, et al. InVO4-based photocatalysts for energy and environmental applications. Chemical Engineering Journal 2022;428. https://doi.org/10.1016/j.cej.2021.131145.

[8] Varma KBR, Subbanna GN, Row TNG, Raoa CNR. Synthesis and characterization of layered bismuth vanadates. Journal of Materials Research 1990, 5. https://doi.org/10.1557/JMR.1990.2718.

[9] Zheng W, Hu X, Wu M, Zhan F, He Q, Chen L, et al. Advanced ammonium salt materials for electrochemical energy storage: Recent progress and future perspectives. Chemical Engineering Journal 2023;454. https://doi.org/10.1016/j.cej.2022.140194.

[10] Brough C, Bowell RJ, Larkin J. An introduction to vanadium chemistry, occurrence and applications. Nova Science Publishers, Inc.; 2019.

[11] Yang B, He J, Zhang G, Guo J. Vanadium: Extraction, manufacturing and applications. 1st ed. Elsevier; 2021, Chapter 3, pp. 33-55.

[12] Range KJ, Zintl R, Heyns AM. The Thermal Decomposition of Ammonium Metavanadate(V) in Open and Closed Systems. Zeitschrift Fur Naturforschung - Section B Journal of Chemical Sciences 1988;43:309–17. https://doi.org/10.1515/znb-1988-0313.

[13] Brock LR, Keister JW, France M, Fierro N, DeVore TC. The Thermal Decomposition of Ammonium Meta-Vanadate under Restricted Flow Conditions. Am J Analyt Chem 2017;08:35–50. https://doi.org/10.4236/ajac.2017.81003.

[14] Dell'agli G, Grippo SM, Mascolo G. Thermal behaviour of (NH4)2V6016 prepared by hydrothermal crystallization. Thermochimica Acta, 1993, 227. https://doi.org/10.1016/0040-6031(93)80262-9

[15] Ulicka L, Zorkova L. THERMAL REACTIVITY OF DECAVANADATES. Journal of Thermal Analysis, 1981, 20. https://doi.org/10.1007/BF01913006

[16] Mocała K, Ziółkowski J. Polymorphism of the Bivalent Metal Vanadates MeV2O6 (Me = Mg. Journal of Solid State Chemistry 1987, 69, 2. https://doi.org/10.1016/0022-4596(87)90087-9

[17] Gonzalez-Platas J, Lopez-Moreno S, Bandiello E, Bettinelli M, Errandonea D. Precise Characterization of the Rich Structural Landscape Induced by Pressure in Multifunctional FeVO4. Inorg Chem 2020;59:6623–30. https://doi.org/10.1021/acs.inorgchem.0c00772.

[18] Cheng X, Guan J, Jiang L, Zhang H, Wang P, Adeniyi AO, et al. Pressure-induced structural transformations and new polymorphs in BiVO4. Physical Chemistry Chemical Physics 2020;22:10238–46. https://doi.org/10.1039/d0cp01274b.

[19] Zavalij PY, Whittingham MS. Structural chemistry of vanadium oxides with open frameworks. Acta Crystallogr B 1999;55:627–63. https://doi.org/10.1107/S0108768199004000.

[20] Song M, Tan H, Chao D, Fan HJ. Recent Advances in Zn-Ion Batteries. Adv Funct Mater 2018;28. https://doi.org/10.1002/adfm.201802564.

[21] Xu X, Xiong F, Meng J, Wang X, Niu C, An Q, et al. Vanadium-Based Nanomaterials: A Promising Family for Emerging Metal-Ion Batteries. Adv Funct Mater 2020;30. https://doi.org/10.1002/adfm.201904398.

[22] Zhang Y, Ang EH, Yang Y, Ye M, Du W, Li CC. Interlayer Chemistry of Layered Electrode Materials in Energy Storage Devices. Adv Funct Mater 2021;31. https://doi.org/10.1002/adfm.202007358.

[23] Wu C, Tan H, Huang W, Liu C, Wei W, Chen L, et al. The strategies to improve the layered-structure cathodes for aqueous multivalent metal-ion batteries. Mater Today Energy 2021;19. https://doi.org/10.1016/j.mtener.2020.100595.

[24] Chen S, Zhao D, Chen L, Liu G, Ding Y, Cao Y, et al. Emerging Intercalation Cathode Materials for Multivalent Metal-Ion Batteries: Status and Challenges. Small Struct 2021;2. https://doi.org/10.1002/sstr.202100082.

[25] Liu Z, Sun H, Qin L, Cao X, Zhou J, Pan A, et al. Interlayer Doping in Layered Vanadium Oxides for Low-cost Energy Storage: Sodium-ion Batteries and Aqueous Zinc-ion Batteries. ChemNanoMat 2020;6:1553–66. https://doi.org/10.1002/cnma.202000384.

[26] Gu Y, Han Y, Qin Z, Li D, Wang L. A strategy to control crystal water content in hydrated vanadium oxide cathode for promoting aqueous rechargeable zinc-ion batteries. J Alloys Compd 2022;911. https://doi.org/10.1016/j.jallcom.2022.165102.

[27] Tian M, Liu C, Zheng J, Jia X, Jahrman EP, Seidler GT, et al. Structural engineering of hydrated vanadium oxide cathode by K+ incorporation for high-capacity and long-cycling aqueous zinc ion batteries. Energy Storage Mater 2020;29:9–16. https://doi.org/10.1016/j.ensm.2020.03.024.

[28] Li Y, Zhang D, Huang S, Yang HY. Guest-species-incorporation in manganese/vanadium-based oxides: Towards high performance aqueous zinc-ion batteries. Nano Energy 2021;85. https://doi.org/10.1016/j.nanoen.2021.105969.

[29] Dong Y, Deng S, Ma Z, Yin G, Li C, Yuan X, et al. Sodium vanadium oxides: From nanostructured design to high-performance energy storage materials. J Mater Sci Technol 2022;121. https://doi.org/10.1016/j.jmst.2021.12.017.

[30] Chen H, Cheng S, Chen D, Jiang Y, Ang EH, Liu W, et al. Vanadate-based electrodes for rechargeable batteries. Mater Chem Front 2021;5:1585–609. https://doi.org/10.1039/d0qm00656d.

[31] Tang H, Peng Z, Wu L, Xiong F, Pei C, An Q, et al. Vanadium-Based Cathode Materials for Rechargeable Multivalent Batteries: Challenges and Opportunities. Electrochemical Energy Reviews 2018;1:169–99. https://doi.org/10.1007/s41918-018-0007-y.

[32] Lanlan F, Zhenhuan L, Nanping D. Recent advances in vanadium-based materials for aqueous metal ion batteries: Design of morphology and crystal structure, evolution of mechanisms and electrochemical performance. Energy Storage Mater 2021;41:152–82. https://doi.org/10.1016/j.ensm.2021.05.004.

[33] Liu PC, Zhu KJ, Gao YF, Luo HG, Lu L. Recent progress in the applications of vanadium-based oxides on energy storage: From low-dimensional nanomaterials synthesis to 3D micro/nano-structures and free-standing electrodes fabrication. Adv Energy Mater 2017;7. https://doi.org/10.1002/aenm.201700547.

[34] Zhang S, Tan H, Rui X, Yu Y. Vanadium-based materials: Next generation electrodes powering the battery revolution? Acc Chem Res 2020;53:1660–71. https://doi.org/10.1021/acs.accounts.0c00362.

[35] Pistoia G, Panero S, Tocci M, Moshtev R V., Manev V. Solid solutions Li1+xV3O8 as cathodes for high rate secondary Li batteries. Solid State Ion 1984;13. https://doi.org/10.1016/0167-2738(84)90073-0.

[36] Wang Q, Xu J, Zhang W, Mao M, Wei Z, Wang L, et al. Research progress on vanadium-based cathode materials for sodium ion batteries. J Mater Chem A Mater 2018;6:8815–38. https://doi.org/10.1039/c8ta01627e.

[37] Wu Y, Chen G, Wu X, Li L, Yue J, Guan Y, et al. Research progress on vanadium oxides for potassium-ion batteries. Journal of Semiconductors 2023;44. https://doi.org/10.1088/1674-4926/44/4/041701.

[38] Liu Y, Feng Z, Jiang H, Dong X, Meng C, Zhang Y. Tailoring NH4+ storage by regulating oxygen defect in ammonium vanadate. Green Energy and Environment 2023. https://doi.org/10.1016/j.gee.2023.02.001.

[39] Zhang X, Li D, Ruan Q, Liu L, Wang B, Xiong F, et al. Vanadium-based cathode materials for rechargeable magnesium batteries. Mater Today Energy 2023;32. https://doi.org/10.1016/j.mtener.2022.101232.

[40] Zhang X, Xu X, Song B, Duan M, Meng J, Wang X, et al. Towards a Stable Layered Vanadium Oxide Cathode for High-Capacity Calcium Batteries. Small 2022;18. https://doi.org/10.1002/smll.202107174.

[41] Zhou T, Xie L, Han Q, Qiu X, Xiao Y, Yang X, et al. Progress and prospect of vanadates as aqueous zn-ion batteries cathodes. Coord Chem Rev 2024;498. https://doi.org/10.1016/j.ccr.2023.215461.

[42] Kumar S, Satish R, Verma V, Ren H, Kidkhunthod P, Manalastas W, et al. Investigating FeVO4 as a cathode material for aqueous aluminum-ion battery. J Power Sources 2019;426. https://doi.org/10.1016/j.jpowsour.2019.03.119.

[43] Wang Y, Zhang Y, You J, Hu F, Zhang H. NH4V4O10 nanobelts as a novel cathode material for aqueous nickel ion batteries. Mater Lett 2023;341. https://doi.org/10.1016/j.matlet.2023.134280.

[44] Zhang Z, Mo F, Ling W, Cui M, Wei J, Yu M, et al. Aqueous Nickel-Ion Batteries with Long Lifetime, High Capacity, and High Rate Capability Based on K2V6O16·1.64H2O Cathodes. Energy and Fuels 2022;36. https://doi.org/10.1021/acs.energyfuels.2c00941.

[45] Zuo S, Xu X, Ji S, Wang Z, Liu Z, Liu J. Cathodes for Aqueous Zn-Ion Batteries: Materials, Mechanisms, and Kinetics. Chemistry - A European Journal 2021;27:830–60. https://doi.org/10.1002/chem.202002202.

[46] Zhou T, Zhu L, Xie L, Han Q, Yang X, Chen L, et al. Cathode materials for aqueous zinc-ion batteries: A mini review. J Colloid Interface Sci 2022;605:828–50. https://doi.org/10.1016/j.jcis.2021.07.138.

[47] Jia X, Liu C, Neale ZG, Yang J, Cao G. Active Materials for Aqueous Zinc Ion Batteries: Synthesis, Crystal Structure, Morphology, and Electrochemistry. Chem Rev 2020;120:7795–866. https://doi.org/10.1021/acs.chemrev.9b00628.

[48] Ni S, Liu J, Chao D, Mai L. Vanadate-Based Materials for Li-Ion Batteries: The Search for Anodes for Practical Applications. Adv Energy Mater 2019;9. https://doi.org/10.1002/aenm.201803324.

[49] Yao G, Zhang N, Zhang Y, Zhou T. Nanostructured transition metal vanadates as electrodes for pseudo-supercapacitors: a review. Journal of Nanoparticle Research 2021;23. https://doi.org/10.1007/s11051-021-05158-9.

[50] Wang Y, Cao G. Developments in nanostructured cathode materials for high-performance lithium-ion batteries. Advanced Materials 2008;20:2251–69. https://doi.org/10.1002/adma.200702242.

[51] Monfort O, Petrisková P. Binary and ternary vanadium oxides: General overview, physical properties, and photochemical processes for environmental applications. Processes 2021;9:1–57. https://doi.org/10.3390/pr9020214.

[52] Oladipo AA, Mustafa FS. Bismuth-based nanostructured photocatalysts for the remediation of antibiotics and organic dyes. Beilstein Journal of Nanotechnology 2023;14:291–321. https://doi.org/10.3762/BJNANO.14.26.

[53] Samsudin MFR, Sufian S, Hameed BH. Epigrammatic progress and perspective on the photocatalytic properties of BiVO4-based photocatalyst in photocatalytic water treatment technology: A review. J Mol Liq 2018;268:438–59. https://doi.org/10.1016/j.molliq.2018.07.051.

[54] Guo J, Liang J, Yuan X, Jiang L, Zeng G, Yu H, et al. Efficient visible-light driven photocatalyst, silver (meta)vanadate: Synthesis, morphology and modification. Chemical Engineering Journal 2018;352:782–802. https://doi.org/10.1016/j.cej.2018.07.071.

[55] Hassan A, Iqbal T, Tahir MB, Afsheen S. A review on copper vanadate-based nanostructures for photocatalysis energy production. Int J Energy Res 2019;43:9–28. https://doi.org/10.1002/er.4195.

[56] Yang M, Ma G, Yang H, Xiaoqiang Z, Yang W, Hou H. Advanced strategies for promoting the photocatalytic performance of FeVO4 based photocatalysts: A review of recent progress. J Alloys Compd 2023;941. https://doi.org/10.1016/j.jallcom.2023.168995.

[57] Samsudin MFR, Sufian S, Hameed BH. Epigrammatic progress and perspective on the photocatalytic properties of BiVO4-based photocatalyst in photocatalytic water treatment technology: A review. J Mol Liq 2018;268:438–59. https://doi.org/10.1016/j.molliq.2018.07.051.

[58] Li F, Kang Y, Chen M, Liu G, Lv W, Yao K, et al. Photocatalytic degradation and removal mechanism of ibuprofen via monoclinic BiVO4 under simulated solar light. Chemosphere 2016;150. https://doi.org/10.1016/j.chemosphere.2016.02.045.

[59] Qin K, Zhao Q, Yu H, Xia X, Li J, He S, et al. A review of bismuth-based photocatalysts for antibiotic degradation: Insight into the photocatalytic degradation performance, pathways and relevant mechanisms. Environ Res 2021;199. https://doi.org/10.1016/j.envres.2021.111360.

[60] Monfort O, Plesch G. Bismuth vanadate-based semiconductor photocatalysts: a short critical review on the efficiency and the mechanism of photodegradation of organic pollutants. Environmental Science and Pollution Research 2018;25:19362–79. https://doi.org/10.1007/s11356-018-2437-9.

[61] Malathi A, Madhavan J, Ashokkumar M, Arunachalam P. A review on BiVO4 photocatalyst: Activity enhancement methods for solar photocatalytic applications. Appl Catal A Gen 2018;555:47–74. https://doi.org/10.1016/j.apcata.2018.02.010.

[62] Xu C, Ravi Anusuyadevi P, Aymonier C, Luque R, Marre S. Nanostructured materials for photocatalysis. Chem Soc Rev 2019;48:3868–902. https://doi.org/10.1039/c9cs00102f.

[63] Xiao M, Wang Z, Lyu M, Luo B, Wang S, Liu G, et al. Hollow Nanostructures for Photocatalysis: Advantages and Challenges. Advanced Materials 2019;31. https://doi.org/10.1002/adma.201801369.

[64] Jiang L, Chen D, Qin L, Liang J, Sun X, Huang Y. Enhanced photocatalytic activity of hydrogenated BiVO4 with rich surface-oxygen-vacancies for remarkable degradation of tetracycline hydrochloride. J Alloys Compd 2019;783:10–8. https://doi.org/10.1016/j.jallcom.2018.12.290.

[65] Tayyebi A, Soltani T, Hong H, Lee BK. Improved photocatalytic and photoelectrochemical performance of monoclinic bismuth vanadate by surface defect states (Bi1-xVO4). J Colloid Interface Sci 2018;514:565–75. https://doi.org/10.1016/j.jcis.2017.12.067.

[66] Xiong J, Di J, Xia J, Zhu W, Li H. Surface Defect Engineering in 2D Nanomaterials for Photocatalysis. Adv Funct Mater 2018;28. https://doi.org/10.1002/adfm.201801983.

[67] Wiberg E, Wiberg N, Holleman A. Inorganic chemistry. Academic Press; 1st English ed., 2001.

[68] Nightingale ER. Phenomenological Theory of Ion Solvation. Effective Radii of Hydrated Ions. J Phys Chem 1959, 63, 9. https://doi.org/10.1021/j150579a011

[69] Evans HT. Crystal structure refinement and vanadium bonding in the metavanadates KV03, NH4V03 and KV03-H20. Zeitschrift für Kristallographie - Crystalline Materials 1960, 114. https://doi.org/10.1524/zkri.1960.114.16.257

[70] Dubois P, Breton P. Mineral chemistry - A study of ammonium vanadates. C R Hebd Seances Acad Sci 1938;206:1969–72.

[71] Ahuja K, Bayas S. Ammonium Metavanadate Market Size By Form (Powder, Granule), By Purity (98% - 99%, Minimum 99%), By Application (Chemical Reagent, Catalyst, Paints, Inks & Dyes, Ceramics), Industry Outlook Report, Regional Analysis, Application Potential, Price Trends, Competitive Market Share & Forecast, 2019 – 2025 2019. https://www.gminsights.com/toc/detail/ammonium-metavanadate-market (accessed November 7, 2023).

[72] National Center for Biotechnology Information. PubChem Compound Summary for CID 516859, Ammonium metavanadate. National Center for Biotechnology Information 2004. https://pubchem.ncbi.nlm.nih.gov/compound/Ammonium-metavanadate (accessed November 7, 2023).

[73] Baker RH, Zimmermann H, Maxson RN. Ammonium Metavanadate. Inorg Syntheses 1950;3:117. https://doi.org/10.1002/9780470132340.ch30.

[74] Vezina JA, Gow WA. The preparation of high-purity ammonium metavanadate from impure vanadium pentoxide by precipitation with ammonium chloride. Mines Branch Technical Bulletin 1965;64. https://doi.org/10.4095/299951.

[75] Sinitia G. Patent No. US3063795, Preparation of ammonium metavanadate, 1962, United States Patent Office.

[76] Qianwen L, Haijun H, Zhaoqian Y, Caixia L, Xiaoping Z. Patent No. CN103420416A, Ammonium metavanadate preparation method, 2015, China.

[77] Nadolska M, Prześniak-Welenc M, Żelechowska K. Wpływ parametrów syntezy hydrotermalnej na strukturę i morfologię wanadanów amonu. Zagadnienia aktualnie poruszane przez młodych naukowców, vol. 14, Kraków: Creativetime; 2019, p. 43–9.

[78] Zakharova GS, Täschner C, Kolb T, Jähne C, Leonhardt A, Büchner B, et al. Morphology controlled NH4V3O8 microcrystals by hydrothermal synthesis. Dalton Transactions 2013;42:4897–902. https://doi.org/10.1039/c3dt32550d.

[79] Chandrappa GT, Chithaiah P, Ashoka S, Livage J. Morphological evolution of (NH4)0.5V 2O5• m H2O fibers into belts, triangles, and rings. Inorg Chem 2011;50:7421–8. https://doi.org/10.1021/ic2005858.

[80] Chithaiah P, Vijaya Kumar G, Nagabhushana GP, Nagaraju G, Chandrappa GT. Synthesis of single crystalline (NH4)2V 6O16·1.5H2O nest-like structures. Physica E Low Dimens Syst Nanostruct 2014;59:218–22. https://doi.org/10.1016/j.physe.2013.12.022.

[81] Liu Y, Xu M, Shen B, Xia Z, Li Y, Wu Y, et al. Facile synthesis of mesoporous NH4V4O10nanoflowers with high performance as cathode material for lithium battery. J Mater Sci 2018;53:2045–53. https://doi.org/10.1007/s10853-017-1619-z.

[82] Abbood HA, Peng H, Gao X, Tan B, Huang K. Fabrication of cross-like NH4V4O10 nanobelt array controlled by CMC as soft template and photocatalytic activity of its calcinated product. Chemical Engineering Journal 2012;209:245–54. https://doi.org/10.1016/j.cej.2012.08.027.

[83] Wang H, Ren Y, Wang W, Huang X, Huang K, Wang Y, et al. NH4V3O8 nanorod as a high performance cathode material for rechargeable Li-ion batteries. J Power Sources 2012;199:315–21. https://doi.org/10.1016/j.jpowsour.2011.10.069.

[84] Fang D, Cao Y, Liu R, Xu W, Liu S, Luo Z, et al. Novel hierarchical three-dimensional ammonium vanadate nanowires electrodes for lithium ion battery. Appl Surf Sci 2016;360:658–65. https://doi.org/10.1016/j.apsusc.2015.11.038.

[85] Jiang Y, Jiang L, Wu Z, Yang P, Zhang H, Pan Z, et al. In situ growth of (NH4)2V10O25·8H2O urchin-like hierarchical arrays as superior electrodes for all-solid-state supercapacitors. J Mater Chem A Mater 2018;6:16308–15. https://doi.org/10.1039/c8ta05706k.

[86] Shanshan C, Jianfeng H, Zhanwei X, Jiayin L, Haibo O, Liyun C, et al. Influence of microwave heating on the structure and electrochemical property of NH4V3O8cathode material for lithium ion batteries. Ceram Int 2015;41:6747–52. https://doi.org/10.1016/j.ceramint.2015.01.119.

[87] Jiang Y, Jiang L, Wu Z, Yang P, Zhang H, Pan Z, et al. In situ growth of (NH4)2V10O25·8H2O urchin-like hierarchical arrays as superior electrodes for all-solid-

state supercapacitors. J Mater Chem A Mater 2018;6:16308–15. https://doi.org/10.1039/c8ta05706k.

[88] Wang X, Xi B, Feng Z, Chen W, Li H, Jia Y, et al. Layered (NH4)2V6O16·1.5H2O nanobelts as a high-performance cathode for aqueous zinc-ion batteries. J Mater Chem A Mater 2019;7:19130–9. https://doi.org/10.1039/c9ta05922a.

[89] Theobald FR, Theobald JG, Vedrine JC, Clad R, Renard J. Crystal growth, structure, electron paramagnetic resonance and magnetic properties of (NH4)2V3O8. Journal of Physics and Chemistry of Solids 1984;45. https://doi.org/10.1016/0022-3697(84)90050-7.

[90] Heo JW, Bu H, Hyoung J, Hong ST. Ammonium Vanadium Bronze, (NH4)2V7O16, as a New Lithium Intercalation Host Material. Inorg Chem 2020;59. https://doi.org/10.1021/acs.inorgchem.9b03160.

[91] Ottmann A, Zakharova GS, Ehrstein B, Klingeler R. Electrochemical performance of single crystal belt-like NH4V3O8 as cathode material for lithium-ion batteries. Electrochim Acta 2015;174:682–7. https://doi.org/10.1016/j.electacta.2015.06.027.

[92] Cheng Y, Huang J, Li J, Cao L, Xu Z, Wu J, et al. Structure-controlled synthesis and electrochemical properties of NH4V3O8 as cathode material for Lithium ion batteries. Electrochim Acta 2016;212:217–24. https://doi.org/10.1016/j.electacta.2016.07.008.

[93] Esparcia EA, Chae MS, Ocon JD, Hong ST. Ammonium Vanadium Bronze (NH4V4O10) as a High-Capacity Cathode Material for Nonaqueous Magnesium-Ion Batteries. Chemistry of Materials 2018;30:3690–6. https://doi.org/10.1021/acs.chemmater.8b00462.

[94] Cui F, Wang D, Hu F, Yu X, Guan C, Song G, et al. Deficiency and surface engineering boosting electronic and ionic kinetics in NH4V4O10 for high-performance aqueous zinc-ion battery. Energy Storage Mater 2022;44:197–205. https://doi.org/10.1016/j.ensm.2021.10.001.

[95] Torardi CC, Miao CR. New battery cathode materials: Synthesis, characterization, and electrochemical performance of M1-xV3 O8-yFz·nH2O (M = NH4, K). Chemistry of Materials 2002;14. https://doi.org/10.1021/cm020620u.

[96] Fei H, Liu X, Lin Y, Wei M. Facile synthesis of ammonium vanadium oxide nanorods for Na-ion battery cathodes. J Colloid Interface Sci 2014;428. https://doi.org/10.1016/j.jcis.2014.04.029.

[97] Vo TN, Kim H, Hur J, Choi W, Kim IT. Surfactant-assisted ammonium vanadium oxide as a superior cathode for calcium-ion batteries. J Mater Chem A Mater 2018;6:22645–54. https://doi.org/10.1039/c8ta07831a.

[98] Esparcia EA, Chae MS, Ocon JD, Hong ST. Ammonium Vanadium Bronze (NH4V4O10) as a High-Capacity Cathode Material for Nonaqueous Magnesium-Ion Batteries. Chemistry of Materials 2018;30:3690–6. https://doi.org/10.1021/acs.chemmater.8b00462.

[99] Kou L, Cao L, Huang J, Yang J. Facile synthesis of reduced graphene oxide/NH4V3O8 with high capacity as a cathode material for lithium ion batteries. Micro Nano Lett 2017;12:940–3. https://doi.org/10.1049/mnl.2017.0107.

[100] Li C, Wang S, Wang G, Wang S, Che X, Li D, et al. NH4V4O10/rGO Composite as a high-performance electrode material for hybrid capacitive deionization. Environ Sci (Camb) 2020;6:303–11. https://doi.org/10.1039/c9ew00499h.

[101] Le S, Ma Y, He D, Wang X, Guo Y. CdS/NH4V4O10 S-scheme photocatalyst for sustainable photo-decomposition of amoxicillin. Chemical Engineering Journal 2021;426:130354. https://doi.org/10.1016/j.cej.2021.130354.

[102] Zhang Y, Li Y, Yuan Y, Lin K. C-dots decorated SrTiO3/NH4V4O10 Z-scheme heterojunction for sustainable antibiotics removal: Reaction kinetics, DFT calculation and mechanism insight. Sep Purif Technol 2022;295:121268. https://doi.org/10.1016/j.seppur.2022.121268.

[103] National Center for Biotechnology Information. PubChem Compound Summary for CID 4571336, Potassium metavanadate. 2023. https://pubchem.ncbi.nlm.nih.gov/compound/Potassium-metavanadate. (accessed November 9, 2023).

[104] Wen P, Liu T, Wei F, Ai L, Yao F. Soft chemical topotactic synthesis and crystal structure evolution from two-dimensional KV3O8 plates to one-dimensional V3O7 nanobelts. CrystEngComm 2016;18:8880–6. https://doi.org/10.1039/c6ce01696k.

[105] Hao P, Zhu T, Su Q, Lin J, Cui R, Cao X, et al. Electrospun Single Crystalline Fork-Like K2V8O21 as High-Performance Cathode Materials for Lithium-Ion Batteries. Front Chem 2018;6:195. https://doi.org/10.3389/fchem.2018.00195.

[106] Li G, Su G, Zhuang X, Li Z, He Y. Characterization and properties of a new IR nonlinear optical crystal: K3V5O14. Opt Mater (Amst) 2004;27:539–42. https://doi.org/10.1016/j.optmat.2004.07.003.

[107] Chernaya V V., Shpanchenko R V., Velikodnyi YA, Kovba ML, Antipov E V. Crystal structure of the pyrovanadate K4V2O 7. Russian Journal of Inorganic Chemistry 2006;51:779–84. https://doi.org/10.1134/S0036023606050159.

[108] Kato K, Takayama-Muromachi E. Pentapotassium trivanadate, K5V3O10. Acta Crystallogr C 1985;41. https://doi.org/10.1107/s0108270185004966.

[109] Bach S, Boudaoud A, Emery N, Baddour-Hadjean R, Pereira-Ramos JP. K0.5V2O5: A novel Li intercalation compound as positive electrode material for rechargeable lithium batteries. Electrochim Acta 2014;119:38–42. https://doi.org/10.1016/j.electacta.2013.12.039.

[110] Chen R, Wang Z, Chen Z, Wang P, Fang G, Zhou J, et al. Synthesis of K0.25V2O5 hierarchical microspheres as a high-rate and long-cycle cathode for lithium metal batteries. J Alloys Compd 2019;772:852–60. https://doi.org/10.1016/j.jallcom.2018.09.076.

[111] Niu X, Qu J, Hong Y, Deng L, Wang R, Feng M, et al. High-performance layered potassium vanadium oxide for K-ion batteries enabled by reduced long-range structural order. J Mater Chem A Mater 2021;9. https://doi.org/10.1039/d1ta01807h.

[112] Sambandam B, Soundharrajan V, Kim S, Alfaruqi MH, Jo J, Kim S, et al. K2V6O16·2.7H2O nanorod cathode: An advanced intercalation system for high energy aqueous rechargeable Zn-ion batteries. J Mater Chem A Mater 2018;6:15530–9. https://doi.org/10.1039/c8ta02018c.

[113] Aleksandrova A, Uzunov I, Banov B, Momchilov A. Potassium bronzes as active material for Li-Ion batteries. Functional Properties of Nanostructured Materials 2006:479–84.

[114] Maingot S, Baffler N, Pereira-Ramos JP, Wiumann P. A potassium vanadium pentoxide bronze prepared via a sol-gel process as lithium intercalation compound. Solid State Ion 1993;67:29–34.

[115] Fang G, Zhou J, Hu Y, Cao XX, Tang Y, Liang S. Facile synthesis of potassium vanadate cathode material with superior cycling stability for lithium ion batteries. J Power Sources 2015;275:694–701. https://doi.org/10.1016/j.jpowsour.2014.11.052.

[116] Li YQ, Shi H, Wang SB, Zhou YT, Wen Z, Lang XY, et al. Dual-phase nanostructuring of layered metal oxides for high-performance aqueous rechargeable potassium ion microbatteries. Nat Commun 2019;10. https://doi.org/10.1038/s41467-019-12274-7.

[117] Purbarani ME, Hyoung J, Hong ST. Crystal-Water-Free Potassium Vanadium Bronze (K0.5V2O5) as a Cathode Material for Ca-Ion Batteries. ACS Appl Energy Mater 2021;4:7487–91. https://doi.org/10.1021/acsaem.1c01158.

[118] Jo JH, Hwang JY, Choi JU, Kim HJ, Sun YK, Myung ST. Potassium vanadate as a new cathode material for potassium-ion batteries. J Power Sources 2019;432:24–9. https://doi.org/10.1016/j.jpowsour.2019.05.064.

[119] Fang G, Zhou J, Liang C, Cai Y, Pan A, Tan X, et al. General synthesis of three-dimensional alkali metal vanadate aerogels with superior lithium storage properties. J Mater Chem A Mater 2016;4:14408–15. https://doi.org/10.1039/c6ta05568k.

[120] Hawthorne FC, Calvo C. The Crystal Chemistry of the M+VO3 Pyroxenes. Journal of Solid State Chemistry 1977, 22, 2. https://doi.org/10.1016/0022-4596(77)90033-0.

[121] Evans HT, Block S. The Crystal Structures of Potassium and Cesium Trivanadates. Inorganic Chemistry 1966, 10,5. https://doi.org/10.1021/ic50044a037.

[122] Baddour-Hadjean R, Boudaoud A, Bach S, Emery N, Pereira-Ramos JP. A comparative insight of potassium vanadates as positive electrode materials for li batteries: Influence of the long-range and local structure. Inorg Chem 2014;53:1764–72. https://doi.org/10.1021/ic402897d.

[123] Zhang G, Xiong T, Xia L, Yao X, Zhao Y, Zheng L, et al. Operando Observation of Coupled Discontinuous-Continuous Transitions in Ion-Stabilized Intercalation Cathodes. Batteries 2022;8:252. https://doi.org/10.3390/batteries8120252.

[124] Fan Y, Qu Z, Zhong W, Hu Z, Younus HA, Yang C, et al. Understanding the Effect of Interplanar Space and Preintercalated Cations of Vanadate Cathode Materials on Potassium-Ion Battery Performance. ACS Appl Mater Interfaces 2021;13:7377–88. https://doi.org/10.1021/acsami.0c23152.

[125] Tian M, Liu C, Zheng J, Jia X, Jahrman EP, Seidler GT, et al. Structural Engineering of Hydrated Vanadate Cathode by K + Introduction for High-Capacity and Long-Cycling Aqueous Zinc Ion Batteries Structural Engineering of Hydrated Vanadium Oxide Cathode by K + Incorporation for High-Capacity and Long-Cycling Aqueous Zinc Ion Batteries. Energy Storage Materials 2020,29. https://doi.org/10.1016/j.ensm.2020.03.024.

[126] Raistrick ID, Huggins RA. Electrochemical studies of lithium insertion reactions of vanadium oxide bronzes. Proc Electrochem Soc 1984;84:374–84.

[127] Baddour-Hadjean R, Thanh Nguyen Huynh L, Batyrbekuly D, Bach S, Pereira-Ramos J-P. Bilayered Potassium Vanadate K0.5V2O5 as Superior Cathode Material for Na-Ion Batteries. ChemSusChem 2019;12:5192–8. https://doi.org/10.1002/cssc.201902093.

[128] Deng L, Niu X, Ma G, Yang Z, Zeng L, Zhu Y, et al. Layered Potassium Vanadate K0.5V2O5 as a Cathode Material for Nonaqueous Potassium Ion Batteries. Adv Funct Mater 2018;28. https://doi.org/10.1002/adfm.201800670.

[129] Hao Y, Zhang S, Tao P, Shen T, Huang Z, Yan J, et al. Pillaring Effect of K Ion Anchoring for Stable V2O5-Based Zinc-Ion Battery Cathodes. ChemNanoMat 2020;6:797–805. https://doi.org/10.1002/cnma.202000105.

[130] Fang G, Liang C, Zhou J, Cai G, Liang S, Liu J. Effect of crystalline structure on the electrochemical properties of K0.25V2O5 nanobelt for fast Li insertion. Electrochim Acta 2016;218:199–207. https://doi.org/10.1016/j.electacta.2016.09.103.

[131] Meng J, Liu Z, Niu C, Xu X, Liu X, Zhang G, et al. A synergistic effect between layer surface configurations and K ions of potassium vanadate nanowires for enhanced energy storage performance. J Mater Chem A Mater 2016;4:4893–9. https://doi.org/10.1039/c6ta00556j.

[132] Li S, Chen M, Fang G, Shan L, Cao X, Huang J, et al. Synthesis of polycrystalline K0.25V2O5 nanoparticles as cathode for aqueous zinc-ion battery. J Alloys Compd 2019;801:82–9. https://doi.org/10.1016/j.jallcom.2019.06.084.

[133] Su G, Chen S, Dong H, Cheng Y, Liu Q, Wei H, et al. Tuning the electronic structure of layered vanadium pentoxide by pre-intercalation of potassium ions for superior room/low-temperature aqueous zinc-ion batteries. Nanoscale 2021;13:2399–407. https://doi.org/10.1039/d0nr07358j.

[134] Liu C, Luo S, Huang H, Wang Z, Wang Q, Zhang Y, et al. Potassium vanadate K0.23V2O5 as anode materials for lithium-ion and potassium-ion batteries. J Power Sources 2018;389:77–83. https://doi.org/10.1016/j.jpowsour.2018.04.014.

[135] Xu M, Han J, Li G, Niu Y, Liu S, Hou J, et al. Synthesis of novel book-like K0.23V2O5 crystals and their electrochemical behavior in lithium batteries. Chemical Communications 2015;51:15290–3. https://doi.org/10.1039/c5cc05425g.

[136] Kong X, Guo Z, Wen P, Huang J, Cao L, Yin L, et al. Controllable synthesis and morphology evolution from two-dimensions to one-dimension of layered K2V6O16·nH2O. CrystEngComm 2015;17:3777–82. https://doi.org/10.1039/c5ce00256g.

[137] Chen P, He K, Yuan B, Liu S, He J, Wu P, et al. Preparation of ultra-pure ammonium metavanadate via heterogeneous self-assembly crystallization. Colloids Surf A Physicochem Eng Asp 2023;668. https://doi.org/10.1016/j.colsurfa.2023.131461.

[138] Supothina S, Rattanakam R, Suwan M. Effect of precursor morphology on the hydrothermal synthesis of nanostructured potassium tungsten oxide. Microelectron Eng 2013;108. https://doi.org/10.1016/j.mee.2013.01.045.

[139] Zheng J, Zhang Y, Hu T, Lv T, Meng C. New Strategy for the Morphology-Controlled Synthesis of V2O5 Microcrystals with Enhanced Capacitance as Battery-type Supercapacitor Electrodes. Cryst Growth Des 2018;18. https://doi.org/10.1021/acs.cgd.8b00776.

[140] Darr JA, Zhang J, Makwana NM, Weng X. Continuous Hydrothermal Synthesis of Inorganic Nanoparticles: Applications and Future Directions. Chem Rev 2017;117. https://doi.org/10.1021/acs.chemrev.6b00417.

[141] Nandagudi A, Nagarajarao SH, Santosh MS, Basavaraja BM, Malode SJ, Mascarenhas RJ, et al. Hydrothermal synthesis of transition metal oxides, transition metal oxide/carbonaceous material nanocomposites for supercapacitor applications. Materials Today Sustainability 2022;19. https://doi.org/10.1016/j.mtsust.2022.100214.

[142] Zhang Y, Guo Y, Duan H, Li H, Sun C, Liu H. Facile synthesis of V4+ self-doped, [010] oriented BiVO4 nanorods with highly efficient visible light-induced photocatalytic activity.

Physical Chemistry Chemical Physics 2014;16:24519–26. https://doi.org/10.1039/c4cp03795b.

[143] Qin DD, Wang T, Song YM, Tao CL. Reduced monoclinic BiVO4 for improved photoelectrochemical oxidation of water under visible light. Dalton Transactions 2014;43. https://doi.org/10.1039/c3dt53575d.

[144] Lamers M, Fiechter S, Friedrich D, Abdi FF, Van De Krol R. Formation and suppression of defects during heat treatment of BiVO4 photoanodes for solar water splitting. J Mater Chem A Mater 2018;6. https://doi.org/10.1039/c8ta06269b.

[145] Wang G, Ling Y, Lu X, Qian F, Tong Y, Zhang JZ, et al. Computational and photoelectrochemical study of hydrogenated bismuth vanadate. Journal of Physical Chemistry C 2013;117. https://doi.org/10.1021/jp401972h.

[146] Che G, Wang D, Wang C, Yu F, Li D, Suzuki N, et al. Solution plasma boosts facet-dependent photoactivity of decahedral BiVO4. Chemical Engineering Journal 2020;397:125381. https://doi.org/10.1016/j.cej.2020.125381.

[147] Wu C, Xie Y. Promising vanadium oxide and hydroxide nanostructures: From energy storage to energy saving. Energy Environ Sci 2010;3. https://doi.org/10.1039/c0ee00026d.

[148] McNulty D, Buckley DN, O'Dwyer C. Synthesis and electrochemical properties of vanadium oxide materials and structures as Li-ion battery positive electrodes. J Power Sources 2014;267. https://doi.org/10.1016/j.jpowsour.2014.05.115.

[149] Tan HT, Rui X, Sun W, Yan Q, Lim TM. Vanadium-based nanostructure materials for secondary lithium battery applications. Nanoscale 2015;7. https://doi.org/10.1039/c5nr04126k.

[150] Armer CF, Yeoh JS, Li X, Lowe A. Electrospun vanadium-based oxides as electrode materials. J Power Sources 2018;395. https://doi.org/10.1016/j.jpowsour.2018.05.076.

[151] Yao X, Zhao Y, Castro FA, Mai L. Rational Design of Preintercalated Electrodes for Rechargeable Batteries. ACS Energy Lett 2019;4. https://doi.org/10.1021/acsenergylett.8b02555.

[152] Guo J, Ma W, Zheng Y, Chen H, Sang Z, Yang D. Cation pre-intercalation and oxygen vacancies in vanadium oxide for synergistically enhanced high-rate and stability for zinc-ion batteries. Appl Surf Sci 2023;612. https://doi.org/10.1016/j.apsusc.2022.155876.

[153] Tang H, Xiong F, Jiang Y, Pei C, Tan S, Yang W, et al. Alkali ions pre-intercalated layered vanadium oxide nanowires for stable magnesium ions storage. Nano Energy 2019;58. https://doi.org/10.1016/j.nanoen.2019.01.053.

[154] Chen R, Wang Z, Chen Z, Wang P, Fang G, Zhou J, et al. Synthesis of K0.25V2O5 hierarchical microspheres as a high-rate and long-cycle cathode for lithium metal batteries. J Alloys Compd 2019;772:852–60. https://doi.org/10.1016/j.jallcom.2018.09.076.

[155] Manev V, Momchilov A, Nassalevska A, Pistoia G, Pasquali M. Potassium vanadates - promising materials for secondary lithium batteries. J Power Sources 1993;44. https://doi.org/10.1016/0378-7753(93)80203-2.

[156] Zhang W, Xu G, Yang L, Ding J. Ultra-long Na2V6O16·xH2O nanowires: Large-scale synthesis and application in binder-free flexible cathodes for lithium ion batteries. RSC Adv 2016;6:5161–8. https://doi.org/10.1039/c5ra22711a.

[157] Zhang X, Yang W, Liu J, Zhou Y, Feng S, Yan S, et al. Ultralong metahewettite CaV6O16·3H2O nanoribbons as novel host materials for lithium storage: Towards high-rate and excellent long-term cyclability. Nano Energy 2016;22:38–47. https://doi.org/10.1016/j.nanoen.2016.02.006.

[158] Long Z, Li Q, Wei T, Zhang G, Ren Z. Historical development and prospects of photocatalysts for pollutant removal in water. J Hazard Mater 2020;395. https://doi.org/10.1016/j.jhazmat.2020.122599.

[159] Dong S, Feng J, Fan M, Pi Y, Hu L, Han X, et al. Recent developments in heterogeneous photocatalytic water treatment using visible light-responsive photocatalysts: A review. RSC Adv 2015;5. https://doi.org/10.1039/c4ra13734e.

[160] Bahnemann D. Photocatalytic water treatment: Solar energy applications. Solar Energy 2004;77. https://doi.org/10.1016/j.solener.2004.03.031.

[161] Hasija V, Raizada P, Sudhaik A, Sharma K, Kumar A, Singh P, et al. Recent advances in noble metal free doped graphitic carbon nitride based nanohybrids for photocatalysis of organic contaminants in water: A review. Appl Mater Today 2019;15:494–524. https://doi.org/10.1016/j.apmt.2019.04.003.

[162] Liu T-C, Pell WG, Conway BE, Roberson SL. Behavior of Molybdenum Nitrides as Materials for Electrochemical Capacitors: Comparison with Ruthenium Oxide. J Electrochem Soc 1998;145:1882–8. https://doi.org/10.1149/1.1838571.

[163] Chandrasekaran S, Yao L, Deng L, Bowen C, Zhang Y, Chen S, et al. Recent advances in metal sulfides: From controlled fabrication to electrocatalytic, photocatalytic and photoelectrochemical water splitting and beyond. Chem Soc Rev 2019;48:4178–280. https://doi.org/10.1039/c8cs00664d.

[164] Ayodhya D, Veerabhadram G. A review on recent advances in photodegradation of dyes using doped and heterojunction based semiconductor metal sulfide nanostructures for environmental protection. Mater Today Energy 2018;9:83–113. https://doi.org/10.1016/j.mtener.2018.05.007.

[165] Marimuthu S, Antonisamy AJ, Malayandi S, Rajendran K, Tsai PC, Pugazhendhi A, et al. Silver nanoparticles in dye effluent treatment: A review on synthesis, treatment methods, mechanisms, photocatalytic degradation, toxic effects and mitigation of toxicity. J Photochem Photobiol B 2020;205:111823. https://doi.org/10.1016/j.jphotobiol.2020.111823.

[166] Kuang P, Low J, Cheng B, Yu J, Fan J. MXene-based photocatalysts. J Mater Sci Technol 2020;56. https://doi.org/10.1016/j.jmst.2020.02.037.

[167] Vishavjeet S, Sanjeev G, Simranpreet K, Navdeep K, Mandeep K, Gupta R. Highly functionalized photo-activated metal–organic frameworks for dye degradation: Recent advancements. Materials today Communications 2023;34:105180. https://www.sciencedirect.com/science/article/pii/S2352492822020219

[168] Yuhua W, Xinlong Ma, Hao Li, Bin Liu, Huihui Li SY and TS. Recent Advances in Visible-Light Driven Photocatalysis, InTech 2016. doi: 10.5772/61864

[169] Arora I, Chawla H, Chandra A, Sagadevan S, Garg S. Advances in the strategies for enhancing the photocatalytic activity of TiO2: Conversion from UV-light active to visible-light active photocatalyst. Inorg Chem Commun 2022;143. https://doi.org/10.1016/j.inoche.2022.109700.

[170] Fajrina N, Tahir M. A critical review in strategies to improve photocatalytic water splitting towards hydrogen production. Int J Hydrogen Energy 2019;44. https://doi.org/10.1016/j.ijhydene.2018.10.200.

[171] Zhao X, Huang J, Feng L, Cao L, Li J, Zhou L. Facile synthesis of α-Ag3VO4 hollow nanospheres with improved photocatalytic activities. J Alloys Compd 2017;718:7–14. https://doi.org/10.1016/j.jallcom.2017.05.107.

[172] Ghiyasiyan-Arani M, Masjedi-Arani M, Salavati-Niasari M. Novel Schiff base ligand-assisted in-situ synthesis of Cu3V2O8 nanoparticles via a simple precipitation approach. J Mol Liq 2016;216. https://doi.org/10.1016/j.molliq.2015.12.100.

[173] Zhang S, Sun Y, Li C, Ci L. Cu3V2O8 hollow spheres in photocatalysis and primary lithium batteries. Solid State Sci 2013;25. https://doi.org/10.1016/j.solidstatesciences.2013.08.003.

[174] Yaghoobi Rahni S, Mohammadzadeh Kakhki R. Facile and green synthesis of Cu3V2O8 nanostructures via Moringa peregrina natural extract as a high performance photo catalyst. Appl Organomet Chem 2020;34. https://doi.org/10.1002/aoc.5392.

[175] Li D, Bai X, Pan C, Zhu Y. Investigations on the phase transition between CdV2O6 and Cd2V2O7 and their photocatalytic performances. Eur J Inorg Chem 2013:3070–5. https://doi.org/10.1002/ejic.201300020.

[176] Ghiyasiyan-Arani M, Masjedi-Arani M, salavati-Niasari M. Size controllable synthesis of cobalt vanadate nanostructures with enhanced photocatalytic activity for the degradation of organic dyes. J Mol Catal A Chem 2016;425. https://doi.org/10.1016/j.molcata.2016.09.023.

[177] Mazierski P, Sowik J, Miodyńska M, Trykowski G, Mikołajczyk A, Klimczuk T, et al. Shape-controllable synthesis of GdVO 4 photocatalysts and their tunable properties in photocatalytic hydrogen generation. Dalton Transactions 2019;48:1662–71. https://doi.org/10.1039/c8dt04225j.

[178] Pei LZ, Lin N, Wei T, Liu HD, Yu HY. Zinc vanadate nanorods and their visible light photocatalytic activity. J Alloys Compd 2015;631. https://doi.org/10.1016/j.jallcom.2015.01.115.

[179] Wu JM, Chen Y, Pan L, Wang P, Cui Y, Kong DC, et al. Multi-layer monoclinic BiVO4 with oxygen vacancies and V4+ species for highly efficient visible-light photoelectrochemical applications. Appl Catal B 2018;221:187–95. https://doi.org/10.1016/j.apcatb.2017.09.031.

[180] Cheng C, Fang Q, Fernandez-Alberti S, Long R. Controlling Charge Carrier Trapping and Recombination in BiVO4with the Oxygen Vacancy Oxidation State. Journal of Physical Chemistry Letters 2021;12:3514–21. https://doi.org/10.1021/acs.jpclett.1c00713.

[181] Guo L, Li J, Lei N, Song Q, Liang Z. Morphological evolution and enhanced photoelectrochemical performance of V4+ self-doped, [010] oriented BiVO4 for water splitting. J Alloys Compd 2019;771:914–23. https://doi.org/10.1016/j.jallcom.2018.09.037.

[182] Yalavarthi R, Zbořil R, Schmuki P, Naldoni A, Kment Š. Elucidating the role of surface states of BiVO4 with Mo doping and a CoOOH co-catalyst for photoelectrochemical water splitting. J Power Sources 2021;483. https://doi.org/10.1016/j.jpowsour.2020.229080.

[183] Kong D, Qi J, Liu D, Zhang X, Pan L, Zou J. Ni-Doped BiVO4 with V4+ Species and Oxygen Vacancies for Efficient Photoelectrochemical Water Splitting. Transactions of Tianjin University 2019;25:340–7. https://doi.org/10.1007/s12209-019-00202-1.

[184] Wang X, Zhou J, Zhao S, Chen X, Yu Y. Synergistic effect of adsorption and visible-light photocatalysis for organic pollutant removal over BiVO 4 /carbon sphere

nanocomposites. Appl Surf Sci 2018;453:394–404. https://doi.org/10.1016/j.apsusc.2018.05.073.

[185] Chen J, Xiong Y, Duan M, Li X, Li J, Fang S, et al. Insight into the Synergistic Effect of Adsorption-Photocatalysis for the Removal of Organic Dye Pollutants by Cr-Doped ZnO. Langmuir 2020;36:520–33. https://doi.org/10.1021/acs.langmuir.9b02879.

[186] Chang L, Pu Y, Shen G, Cui Y, Wei X, Cao B, et al. Excellent adsorption-photocatalysis synergistic activity of 3D-3D flower-like BiOBr/graphene hydrogel composite and the removal of potassium butyl xanthate. New Journal of Chemistry 2020;44:2479–88. https://doi.org/10.1039/c9nj06060j.

[187] Roy JS, Dugas G, Morency S, Ribeiro SJL, Messaddeq Y. Enhanced photocatalytic activity of silver vanadate nanobelts in concentrated sunlight delivered through optical fiber bundle coupled with solar concentrator. SN Appl Sci 2020;2:1–11. https://doi.org/10.1007/s42452-020-1969-z.

[188] Phanichphant S, Nakaruk A, Chansaenpak K, Channei D. Evaluating the photocatalytic efficiency of the BiVO4/rGO photocatalyst. Sci Rep 2019;9. https://doi.org/10.1038/s41598-019-52589-5.

[189] Balakumar V, Chuaicham C, Sasaki K, Sekar K. Fabrication of BiVO4/ reduced graphene oxide photocatlyst for hexavalent chromium reduction under visible region. Mater Today Proc, vol. 50, 2021. https://doi.org/10.1016/j.matpr.2021.11.381.

[190] Jia J, Zhang M, Liu Z, Yu C, Zhou W, Li Z. La3+,Gd3+-codoped BiVO4 nanorods with superior visible-light-driven photocatalytic performance for simultaneous removing aqueous Cr(VI) and azo dye. Journal of Nanoparticle Research 2020;22. https://doi.org/10.1007/s11051-020-05012-4.

[191] Kondratowicz I, Żelechowska K, Nadolska M, Jażdżewska A, Gazda M. Comprehensive study on graphene hydrogels and aerogels synthesis and their ability of gold nanoparticles adsorption. Colloids Surf A Physicochem Eng Asp 2017;528:65–73. https://doi.org/10.1016/j.colsurfa.2017.05.063.

[192] Kondratowicz I, Nadolska M, Şahin S, Łapiński M, Prześniak-Welenc M, Sawczak M, et al. Tailoring properties of reduced graphene oxide by oxygen plasma treatment. Appl Surf Sci 2018;440:651–9. https://doi.org/10.1016/j.apsusc.2018.01.168.

[193] Wang H, Jing R, Shi J, Zhang M, Jin S, Xiong Z, et al. Mo-doped NH4V4O10 with enhanced electrochemical performance in aqueous Zn-ion batteries. J Alloys Compd 2021;858. https://doi.org/10.1016/j.jallcom.2020.158380.

6. LIST OF FIGURES

Figure 1. Representative examples of chain, layered and 3D-tunnel structure of vanadates (a). Types of the V-O polyhedra, horizontal axis represents the oxidation state of vanadium (b). Figure was drawn using VESTA software. 10

Figure 2. SEM images of: $NH_4V_3O_8$ obtained at pH = 2.5 (a), 3 (b), 4.5 ÷ 5.5 (c), 6 (d) [78]; $NH_4V_4O_{10}{\cdot}nH_2O$ obtained after 24 h (e) and 48h (f) [79]; $(NH_4)_2V_6O_{16}{\cdot}nH_2O$ obtained at 130°C (g) and 160°C (h) [80] 18

Figure 3. SEM images of $NH_4V_4O_{10}$ (a-f) and $(NH_4)_2V_{10}O_{25}{\cdot}8H_2O$ (g-h) obtained without and with the utilization of the following templates: β-cyclodextrin (a-b) [81], carboxymethyl cellulose (c-d) [82], Ti foil (e-f) [84] or Ni foam (g-h) [85]. 18

Figure 4. Representative crystal structures of ammonium vanadates on the example of NH_4VO_3 (Crystal system, space group: orthorhombic, Pbcm) and $NH_4V_4O_{10}$ (Crystal system, space group: monoclinic, C12/m1). Figure was drawn using VESTA software. 19

Figure 5. Representative crystal structures of ammonium vanadates on the example of KVO_3 (Crystal system, space group: orthorhombic, Pbcm) and KV_3O_8. (Crystal system, space group: monoclinic, P21/m). Figure was drawn using VESTA software. 22

Figure 6. Comparison of KV_3O_8, $K_{0.5}V_2O_5$, and $K_{0.25}V_2O_5$: a) crystal structure b) electrochemical performance as cathode materials for LIBs (at C/10 rate in the 4−2 V potential range) [122]. .. 23

Figure 7. Stability measurements of V_2O_5 and $K_{0.5}V_2O_5$. a) Control of the 3 M $ZnSO_4$ electrolyte (over an 8-day period with soaked electrodes. b) Comparison of pristine electrodes and electrodes after one month in $ZnSO_4$ electrolyte (3 M). c) The electrochemical performance of $K_{0.5}V_2O_5$ and V_2O_5 as cathode materials in ZIBs [129]. 25

Figure 8. High-resolution XPS spectra of the V2p regions for samples obtained without applying initial pressure (p0) and with the application of 5, 25, and 50 bar (p5, p25, p50, respectively. XPS measurements were performed with Omicron NanoTechnology spectrometer with Mg Kα as an excitation source. The binding energies were corrected using the background C1s (285.0 eV) line as a reference. XPS spectra were analysed with Casa-XPS software using Shirley background subtraction and Gaussian-Lorentzian curve as a fitting algorithm.
…….252

7. LIST OF SCIENTIFIC ACHIEVEMENTS

List of publications related to the thesis:

1. **M. Nadolska**, M. Szkoda, K. Trzciński, J. Ryl, A. Lewkowicz, K. Sadowska, J. Smalc-Koziorowska, M. Prześniak-Welenc, New light on the photocatalytic performance of NH4V4O10 and its composite with rGO. Scientific Reports, 2023, 13, 3946. https://doi.org/10.1038/s41598-023-31130-9

2. **M. Nadolska**, M. Szkoda, K. Trzciński, P. Niedziałkowski, J. Ryl, A. Mielewczyk-Gryń, K. Górnicka, M. Prześniak-Welenc. Insight into Potassium Vanadates as Visible-Light-Driven Photocatalysts: Synthesis of V(IV)-Rich Nano/Microstructures for the Photodegradation of Methylene Blue, Inorganic Chemistry, 2022, 61, 25, 9433–9444. https://doi.org/10.1021/acs.inorgchem.2c00136

3. M. Prześniak-Welenc, **M. Nadolska**, K. Jurak, J. Li, K. Górnicka, A. Mielewczyk-Gryń, M. Rutkowska, A. P. Nowak. The valance state of vanadium-key factor in the flexibility of potassium vanadates structure as cathode materials in LIBs, Scientific Reports, 2022, 12, 18751. https://doi.org/10.1038/s41598-022-23509-x

4. M. Prześniak-Welenc, **M. Nadolska**, A. Nowak, K. Sadowska. Pressure in charge. Neglected parameter in hydrothermal synthesis turns out to be crucial for electrochemical properties of ammonium vanadates. Electrochimica Acta, 2020, 339, 135919. https://doi.org/10.1016/j.electacta.2020.135919

5. M. Prześniak-Welenc, **M. Nadolska**, B. Kościelska, K.Sadowska. Tailoring the size and shape –new path for ammonium metavanadate synthesis, Materials, 2019, 12(20), 3446. https://doi.org/10.3390/ma12203446

List of other publications:

from JCR list

6. Chmayssem, **M. Nadolska**, E. Tubbs, K. Sadowska, P. Vadgma, I. Shitanda, S. Tsujimura, Y. Lattach, M. Peacock, S. Tingry, S. Marinesco, P. Mailley, S. Lablanche, P. Y. Benhamou, A. Zebda. Insight into continuous glucose monitoring: from medical basics to commercialized devices. Microchimica Acta, 2023, 190, 177. https://doi.org/10.1007/s00604-023-05743-w
7. G. Menassol, L. Dubois, **M. Nadolska**, P. Vadgama, D.K. Martin, A. Zebda. A biocompatible iron doped graphene based cathode for an implantable glucose biofuel cell, Electrochimica Acta, 2023, 439, 141627, https://doi.org/10.1016/j.electacta.2022.141627
8. Kondratowicz, I. Shalayel, **M. Nadolska**, S. Tsujimura, Y. Yamagata, I. Shitanda, A. Zebda. Impact of Lactic Acid and Genipin Concentration on Physicochemical and Mechanical Properties of Chitosan Membranes. Journal of Polymers and the Environment, 2023, 31, 1221–1231. https://doi.org/10.1007/s10924-022-02691-z
9. M. Bartmański, M. Rościszewska, M. Wekwejt, A. Ronowska, **M. Nadolska**-Dawidowska, A. Mielewczyk-Gryń. Properties of New Composite Materials Based on Hydroxyapatite Ceramic and Cross-Linked Gelatin for Biomedical Applications. International Journal of Molecular Sciences, 2022, 23(16), 9083. https://doi.org/10.3390/ijms23169083
10. M. Pierpaoli, A. Lewkowicz, B. Dec, **M. Nadolska**, R. Bogdanowicz. Impedimetric sensing of α-amino acids driven by micro-patterned 1,8-Diazafluoren-9-one into titania- boron- doped maze-like nanocarbons. Sensors and Actuators B: Chemical, 2022, 371, 132459. https://doi.org/10.1016/j.snb.2022.132459
11. P. Jakóbczyk, G. Skowierzak, I.Kaczmarczyk, **M. Nadolska**, A. Wcisło, K. Lota, R. Bogdanowicz, T. Ossowski, P. Rostkowski, G.Lota, J. Ryl. Electrocatalytic performance of oxygen-activated carbon fibre felt anodes mediating degradation mechanism of

acetaminophen in aqueous environments. Chemosphere, 2022, 304, 135381. https://doi.org/10.1016/j.chemosphere.2022.135381
12. M. Szkoda, Z. Zarach, M.Nadolska, G. Tyrkowski, K. Trzciński. SnO2 nanoparticles embedded onto MoS2 nanoflakes - An efficient catalyst for photodegradation of methylene blue and photoreduction of hexavalent chromium, Electrochimica Acta, 2022, 414, 140173. https://doi.org/10.1016/j.electacta.2022.140173
13. D. Gierszewska, I. Szpunar, F.Oseko , J. Pośpiech , **M. Nadolska** ,M. Pieragowska, K. Reniecka, K. Waniek, K. Leszczyński, A. Mielewczyk-Gryń, M. Gazda, S. Wachowski. Microstructural design of ba0.5 la0.5 co0.5 fe0.5 o3 perovskite ceramics. Materials, 2021, 14(16), 4656. https://doi.org/10.3390/ma14164656
14. M. Wekwejt, S. Chen, B. Kaczmarek-Szczepańska, **M. Nadolska**, K. Łukowicz, A. Pałubicka, A. Michno, A. M. Osyczka, M. Michálek, A. Zieliński. Nanosilver-loaded PMMA bone cement doped with different bioactive glasses–evaluation of cytocompatibility, antibacterial activity, and mechanical properties. Biomaterials science, 2021, 9(8), 3112-3126. https://doi.org/10.1039/D1BM00079A
15. **M. Nadolska**, M. Prześniak-Welenc, M. Łapiński, K. Sadowska. Synthesis of phosphonated carbon nanotubes: New insight into carbon nanotubes functionalization. Materials, 2021, 14(11), 2726. https://doi.org/10.3390/ma14112726
16. M. Wekwejt, M. Michalska-Sionkowska, M. Bartmański, **M. Nadolska**, K. Łukowicz, A.Pałubicka, A.M. Osyczka, A. Zieliński. Influence of several biodegradable components added to pure and nanosilver-doped PMMA bone cements on its biological and mechanical properties. Materials Science and Engineering: C, 2020, 111286. https://doi.org/10.1016/j.msec.2020.111286
17. R. Olszewski*, **M. Nadolska***, M. Łapiński, M., B. Cieślik, K. Żelechowska: Solvent-Free Synthesis of Phosphonic Graphene Derivative and Its Application in Mercury Ions Adsorption, Nanomaterials, 2019, 9(4), 485. https://doi.org/10.3390/nano9040485
18. Kondratowicz*, **M. Nadolska***, S. Şahin, M. Łapiński, M. Prześniak-Welenc, M. Sawczak, E.H.Yu, W. Sadowski, K. Żelechowska. Tailoring properties of reduced graphene oxide by oxygen plasma treatment. Applied Surface Science, 2018, 440, 651-659. https://doi.org/10.1016/j.apsusc.2018.01.168
19. Kondratowicz, **M. Nadolska**, K. Żelechowska. Reduced Graphene Oxide Joins Graphene Oxide To Teach Undergraduate Students Core Chemistry and Nanotechnology Concepts. Journal of Chemical Education, 2018, 95 (6), 1012–1017. https://doi.org/10.1021/acs.jchemed.7b00568
20. Kondratowicz, K. Żelechowska, **M. Nadolska**, A. Jażdżewska, M. Gazda, Comprehensive study on graphene hydrogels and aerogels synthesis and their ability of gold nanoparticles adsorption, Colloids and Surfaces A. 2017, 528, 65-73. https://doi.org/10.1016/j.colsurfa.2017.05.063

** Both authors contributed equally to this work*

Others:

1. **M. Nadolska**, K. Żelechowska, M. Prześniak-Welenc, Wpływ parametrów syntezy hydrotermalnej na strukturę i morfologię wanadanów amonu, Zagadnienia aktualnie poruszane przez młodych naukowców, Creativetime, Kraków 2019, ISBN:97 88363058876- Chapter in a monograph.
2. **M. Nadolska**, K. Żelechowska, Funkcjonalizowane adsorbenty węglowe do efektywnego usuwania jonów metali z wody, Zagadnienia aktualnie poruszane przez młodych naukowców, Creativetime, Kraków 2019, ISBN:9788363058876- Chapter in a monograph.
3. **M. Nadolska**, Funkcjonalizowane nanomateriały węglowe – w trosce o zdrowie i środowisko, Laborant, no.14/ 2020- Article.

List of conference presentations

Oral presentations:

1. M. Nadolska, M. Szkoda, K. Trzciński, A. Nowak, J. Ryl, M. Prześniak-Welenc, Ammonium Vanadate/Reduced Graphene Oxide Composites: From Fabrication to Application, oral presentation, IEEE 12th International Conference “Nanomaterials: Applications &Properties”, Polska, Kraków, 11-1 6.09.22.
2. M. Nadolska, M. Prześniak-Welenc, A. Nowak, K. Sadowska, Ammonium vanadate/rGO composites: synthesis and applications, oral presentation, International Workshop on Functional Nanostructured Materials – FuNaM-3, Kraków, 06-08.10.21- *1st prize for the best Young Scientist oral presentation.*
3. M. Nadolska, M. Prześniak-Welenc, K. Sadowska, Wykorzystanie termograwimetrii w ocenie procesu funkcjonalizacji materiałów węglowych, oral presentation, IX Szkoła Analizy Termicznej (SAT'2019), Zakopane, 22-25.09.19.
4. M. Nadolska, M. Prześniak-Welenc, M.Łapiński K. Żelechowska, Synthesis and physicochemical properties of nanodiamonds with phosphonic groups, oral presentation, 7th International Conference “Nanotechnologies and Nanomaterials” NANO-2019, Lwów, 27-30.08.19
5. M. Nadolska, B. Cieślik, K. Żelechowska, Zastosowanie fosfonowanych materiałów węglowych do oczyszczania wody, Oral presentation, IV Krajowa Konferencja "Grafen i inne materiały 2D", Szczecin, 24-26.09.18.
6. M. Nadolska, Funkcjonalizowane adsorbenty węglowe do efektywnego usuwania jonów metali z wody, Oral presentation, Nowe wyzywania dla Polskiej nauki Edycja III, Gdańsk, 8.09.18.
7. M. Nadolska, B. Cieślik, D. Sobota, K. Żelechowska, Modyfikowane materiały węglowe do efektywnego usuwania jonów metali ciężkich z wody, Oral presentation, III Interdyscyplinarna Akademicka Konferencja Ochrony Środowiska (IAKOŚ), Gdańsk, 13-1 5.04.18.- *2nd prize for the best oral presentation.*

Poster presentations:

8. M. Nadolska, A. Nowak, K. Sadowska, J. Ryl, M. Prześniak-Welenc, Ammonium vanadate/reduced graphene oxide composites: correlation between the synthesis parameters and physicochemical properties, poster, 32nd International Conference on Diamond and Carbon Materials, Portugal, Lisbon, 4-8.09.22.
9. M. Nadolska, J. Pośpiech, T. Sobczyk, M. Chmielewski, I. Szpunar, S. Wachowski, 3D-Printing of Proton Conducting Ceramics, poster, 239th ECS Meeting with the 18th International Meeting on Chemical Sensors (IMCS), Digital meeting, 30.05-03.06.21.
10. M. Nadolska, J. Pośpiech, T. Sobczyk, M. Chmielewski, I. Szpunar, S. Wachowski, 3D - printing of ceramic electrode materials, poster, 14th International Symposium on Systems with Fast Ionic Transport, on-line, 7- 9.07.21.
11. M. Nadolska, P. Harispuru, G. Menassol, A. Zebda, K. Sadowska, Biofuel cells implanted into the living body as power source for other implantable devices. Optimization study, poster, Polsko-Francuskie Forum Nauki I Innowacji-5 edycja, Warszawa, 19.11.19.
12. M. Nadolska, M. Prześniak-Welenc, M. Łapiński, M. Sawczak, K. Żelechowska, Free-radical phosphonylation of carbon nanomaterials, Poster, 30th International Conference on Diamond and Carbon Materials, Seville, 8- 12.09.19.
13. M. Nadolska, M. Prześniak-Welenc, A. Nowak, K. Żelechowska, Hydrothermal synthesis of vanadium ammonium compounds – the crucial role of the pressure, Poster, NanoTech Poland 2019, Poznań, 5-8.06.19.
14. M. Nadolska, B. Cieślik, K. Żelechowska, Phosphonated carbon materials for effective mercury ions removal from aqueous solutions, Poster, 13th NANOSMAT Conference, Gdańsk, 12-1 4.09.18.
15. M. Nadolska, Wpływ parametrów syntezy na strukturę i morfologię wanadanów amonu, Poster, Nowe wyzywania dla Polskiej nauki Edycja III, Gdańsk, 8.09.18.

Experience in projects

01.2021-01.2023	Principal Investigator in scientific grant carried out under PRELUDIUM program, National Science Center, 2020/37/N/ST5/03697. Project title: „Ammonium vanadate/rGO composites: synthesis, physicochemical characterization and electrochemical properties".
03-12.2022	Scholar in National research project entitled „ Electrochemical Au-Minecraft: a new approach towards the impedimetric biosensing system", OPUS, National Science Center, 2020/37/B/ST7/03262, PI: dr hab. inż. Jacek Ryl.
03-12.2022	Investigator in the research project entitled "Thermoplastics/ground tire rubber/carbon fillers systems - novel approach for development of low-cost flexible electronics with tailored performance properties", PLATINUM ESTABLISHING TOP-CLASS RESEARCH, IDUB Politechnika Gdańska, DEC-1/2021/IDUB/I.1./Pt. PI: dr Mohammad Reza Saeb.
01.2020-06.2021	Scholar in European research grant M-ERA.NET 3 entitled „Functional Grading by Key doping in Catalytic electrodes for Proton Ceramic Cells", 2018/30/Z/ST5/00915, PI: dr inż. Sebastian Wachowski.
01.2018-12.2019	Contractor in National research project entitled „Synthesis and properties of carbonaceous nanomaterials functionalized with phosphonic groups", SONATA, National Science Center, 2016/23/D/ST5/02800. PI: dr hab. inż. Kamila Sadowska.

Research Internships

12.2022 11.2021 04-08.2021 02.2020 10.2019	University of Grenoble Alps, TIMC-IMAG Laboratory